The Effects of Wakes on Separating Boundary Layers in Low Pressure Turbines

Rory Douglas Stieger

Peterhouse

A dissertation submitted for the degree of doctor of Philosophy

Cambridge University Engineering Department

February 2002

Abstract

An experimental investigation into wake-induced transition in separating boundary layers was conducted. Measurements were made on a flat plate with an imposed pressure distribution and on a 2D cascade of LP turbine blades. The unsteady effects of wakes were simulated in both facilities by wake generators consisting of cylindrical bars traversed across the inlet flow.

Single component LDA measurements were made on the flat plate with a technique developed to measure the ensemble averaged Reynolds stresses by making measurements at multiple probe orientations. These measurements allowed the boundary layer dissipation to be determined thus providing experimental proof of the loss reducing mechanisms arising from wake induced unsteady transition processes. Evidence of a deterministic natural transition processes by Tollmein-Schlichting waves was also identified in the boundary layer between wake passing events. The frequency of these waves matches that of the most amplified disturbance in a Falkner-Skan profile of the same displacement thickness.

The convection of a turbulent wake through a LP turbine cascade was measured using 2D LDA. The resolution of these measurements is unprecedented and the measurements will provide a database for future CFD validation. The wake turbulence was found to be anisotropic. The production of turbulent kinetic energy was calculated from the 2D LDA measurements and found to increase the levels of turbulent kinetic energy of the wake fluid at approximately mid chord.

Unsteady blade surface pressures were measured on the suction surface of the T106 LP turbine cascade. Large amplitude pressure oscillations were observed to arise as the wake passed over the region that was occupied by a separation bubble in steady flow conditions. The source of these pressure oscillations was identified to be vortices embedded in the suction surface boundary layer.

Preface

The work reported in this thesis was performed at the Whittle Laboratory, Cambridge University Engineering Department between October 1999 and January 2002. Except where specifically stated to the contrary, this dissertation is my own work and includes nothing that is the result of collaboration. No part of this dissertation has been submitted to any other academic establishment.

This thesis comprises eight chapters and four appendices, which total approximately 51 000 words and 80 figures.

Rory Stieger

Acknowledgement

Although the preface says that this work is all my own it is very clear to me that it was in fact made possible by a great number of people.

G. D. J Smith and J.P. Bindon were instrumental in instilling in me a fascination with turbomachinery. I am indebted to them not only for this but also their efforts to pave the way for my further study. AECI Ltd was also generous in releasing me from contractual obligations thereby allowing me to follow a dream.

I am indebted for the financial support provided by a Peterhouse Research Studentship, the ORS trust, and the EPSRC.

The staff of the Whittle Laboratory workshops have always produced work of unrivalled calibre. I am particularly indebted to the nimble fingers and endless patience of T. Chandler, while I am also particularly grateful for the assistance of J. Saunders, B. Taylor and K. Bryant.

Colleagues of the Whittle Lab have not only provided a fun working environment but have been a valuable source of assistance, encouragement and friendship.

It has become quite plain to me that any person gaining further sight or greater understanding has done so by standing on the shoulders of a giant. Prof. H. Hodson has been such a giant in his supervision of this work. I am most grateful for his guidance and the opportunities he has afforded me.

It is right that the ultimate acknowledgement be to my parents, for their unending love and support.

Nomenclature

Symbols

φ	analysing wavelet
ω	angular frequency
α	anisotropy; probe angle
Γ	circulation
ρ	density
β	Falkner-Skan pressure gradient parameter
ϕ	flow coefficient $\phi=V_x/U_b$
ν	kinematic viscosity $\nu=\mu/\rho$
θ	momentum thickness $\theta = \int_{y=0}^{\delta} \frac{u}{U_\infty}\left(1-\frac{u}{U_\infty}\right)dy$
λ	Pohlhausen pressure gradient parameter $\lambda = \frac{\delta^2}{\nu}\frac{dU_\infty}{dx}$
ψ	principal stress direction
μ	viscosity
Ω	vorticity $\Omega = \frac{\partial V}{\partial x} - \frac{\partial U}{\partial y}$
λ_θ	Thwaites pressure gradient parameter $\lambda_\theta = \frac{\theta^2}{\nu}\frac{dU_\infty}{dx}$
δ^*	displacement thickness $\delta^* = \int_{y=0}^{\delta}\left(1-\frac{u}{U_\infty}\right)dy$
δ'	Blackwelder Parameter $\delta' = \frac{1}{U_{98}{}^2}\int_{y=0}^{\delta_{98}} \tfrac{1}{2}(\overline{u'^2}+\overline{v'^2})dy$
τ	time constant
τ_0	bar passing period
τ_{conv}	convective time scale
δj	wavelet scale resolution
τ_{visc}	viscous time scale
τ_{yx}	shear stress in boundary layer
C	chord
$C_{D\ non\text{-}turb}$	non-turbulent component of dissipation coefficient
$C_{D\ turb}$	turbulent component of dissipation coefficient
C_D	dissipation coefficient
C_p	Coefficient of pressure $C_p=(P_{01}-P)/(P_{01}-P_{2s})$
d	diameter
D_{TKE}	dissipation of *TKE*
f	frequency
f_r	reduced frequency $f_r=fC/V_{2is}$
H_{12}	shape factor $H_{12}=\delta^*/\theta$
M	measured component of velocity vector
P	pressure

P_{TKE}	production of TKE
Q	velocity vector magnitude $Q=\sqrt{U^2+V^2}$
r	radius
Re_θ	momentum thickness Reynolds number
$Re_{\delta*}$	displacement thickness Reynolds number
Re_{2C}	Reynolds number based on isentropic exit velocity and blade chord
s	surface distance; wavelet scale
s_0	suction surface length
s_b	bar pitch
s_c	cascade pitch
St_θ	Strouhal number based on momentum thickness $St_\theta=f\theta/U$
T	temperature
t	time
TKE	Turbulent kinetic energy
t_r	residence time of LDA sample
Tu	turbulence intensity
U_∞	freestream velocity
U^*,V^*	non-dimensional velocity; $U^*=U/V_{2is}$, $V^*=V/V_{2is}$
$\overline{u'^2}\,,\overline{v'^2}$	Reynolds normal stresses
$\overline{u'v'}$	Reynolds shear stress
U_b	bar speed or blade speed
V	velocity
v_θ	radial velocity
V_x	axial velocity
x	distance
x^*, y^*	non-dimensional distance $x^*=x/C$, $y^*=y/C$

Subscripts

0	total
1	inlet
2	exit
ψ	aligned to principal stress direction
f	fluid
is	isentropic
p	perturbation; particle
s	static
t	transition

Superscripts

$*$	non-dimensional
$\bullet$	complex conjugate

Other

$\overline{X}$	time average of X
$\langle X \rangle$	ensemble-average of X
$W(X)$	continuous wavelet transform of X
$\hat{X}$	Fourier transform of X

Contents

Chapter 1: Introduction

1.1 Research motivation

Gas turbines are suited to aero-engine applications due to a combination of high power-to-weight ratio and high efficiency. Most of the thrust of modern high by-pass ratio turbofan engines, such as that shown in Figure 1-1, comes from the fan, which is driven by the low-pressure (LP) turbine.

Due to the high power requirements of the fan, the LP turbine consists of several stages. Furthermore, the low rotational speed imposed by the fan leads to large diameters. As a result, the LP turbine is heavy, up to a third of the total engine weight, and expensive to manufacture.

The efficiency of the gas turbine engine is critically dependant on the LP turbine efficiency. Typically, a *1%* increase in the polytropic efficiency of the LP turbine will improve the engine's fuel consumption by *0.5%* (Hodson, 1998). For this reason much effort has been devoted to developing highly efficient LP turbines and current aero-engines have LP turbines efficiencies of *90% - 93%*. In the last *50* years of development, the LP turbine efficiency has only improved by about *13%* and further increases in efficiency are increasingly difficult to achieve.

The primary concern for aero-engine operators is the total cost of engine ownership, which considers not only the capital cost but also the operating costs that are influenced by efficiency, weight and reliability. Recent development (Cobley at al, 1997) has shown that the blade count of an LP turbine can be reduced by *20%* without significant efficiency penalties by capitalising on unsteady transition phenomena found on LP turbine blade boundary layers. Reducing the number of blades in this way reduces both the weight and manufacturing cost of the engine. This provides a substantial reduction to the total cost of engine ownership.

1.2 Unsteady aerodynamics in LP turbines

LP turbine blades have a large aspect ratio, typically in the range *3-7:1* and as a result secondary flows occupy only a small fraction of the blade span. The profile loss thus contributes most significantly to the lost efficiency. The profile loss is made up of contributions from the boundary layers of the suction and pressure surfaces, mixing losses and base pressure losses. The relative magnitudes of these components for a typical thin profile are shown in Figure 1-2 from which it is apparent that the suction surface boundary layer is the most significant source of lost efficiency and thus the most likely candidate for the attention of researchers.

The blade chord Reynolds numbers in LP turbines range from approximately $4{\times}10^4$ for the rear stages of small business jets at cruise to approximately $5{\times}10^5$ for the largest turbofan engines at sea-level take-off. Furthermore, between take-off and cruise the Reynolds number may drop by up to a factor of four. The low Reynolds number conditions mean that a significant portion of the blade surface boundary layers may be laminar and so laminar separation may be experienced in the regions of deceleration over the rear of the suction surface. Figure 1-4 shows the possible flow structures on an LP turbine blade over a range of Reynolds numbers. Historically, turbomachinery blading has been designed using a combination of steady cascade measurements and steady computational tools. These design procedures lead to design rules that limited boundary layer deceleration to avoid laminar separation and the associated loss penalties. Thus for steady flow arguments, with the back surface diffusion limited to avoid separation, the blade loading was capped and LP turbine blading was designed by methods such as controlled diffusion (Hourmouziadis, 1989). A typical blade surface velocity distribution is shown in Figure 1-5. The effects of unsteadiness were assumed to increase losses in LP turbines. For boundary layers that were designed to remain attached, the turbulent wake shed from upstream bladerows induced bypass transition upstream of the natural transition point. This earlier transition increased the turbulent wetted area and therefore the losses (Hodson, 1984).

However, measurements by Schlichting and Das (1969) showed that turbulence generated by an oscillating turbulence grid reduced the losses of a compressor cascade due to the suppression of a separation bubble. Gibson (1970) also showed a reduction in profile loss occurred when a turbine cascade with a separation bubble was subject to increased turbulence from a moving grid. Schulte and Hodson (1994) showed that the periodic passing of turbulent wakes affected the separation bubble on a modern LP turbine blade and reported a reduction in profile loss due the wake passing for some flow conditions. This was later explained by Schulte and Hodson (1996) who presented hot film measurements showing that turbulent spots induced by the wake upstream of the separation point prevented the boundary layer from separating. The calmed regions that follow the turbulent spots were also shown to be responsible for suppressing separation due to their elevated shear and full velocity profiles.

Loss reductions are thus intimately linked to the relative portions of the blade surface covered by laminar, turbulent, calmed and separated flow. These phenomena are all Reynolds number dependant and as a result, the profile loss depends on the Reynolds number. This is true for steady and unsteady flows as shown in Figure 1-3. For this profile, it is apparent that below a critical Reynolds number the unsteady flow has lower losses than the steady flow. As the Reynolds number decreases, the steady flow losses rise due to the increased extent of separation. In the wake passing case, the separation is periodically suppressed by the turbulent and calmed flow. In the time average, the losses generated during the turbulent and calmed periods contribute less than the steady separation and this leads to loss reduction.

Armed with this improved understanding of unsteady transition, the traditional steady flow design rules that limited boundary layer diffusion were challenged. A new generation of blade profiles was designed based on the extensive experimental work of Curtis et al (1996) and Howell et al (2000). These ‘high lift’ LP turbine blade profiles, of which a typical velocity distribution is shown in Figure 1-5, were reported to reduce the blade count of the LP turbine by *20%* (Cobley et al, 1997) thus achieving the ultimate goal of reducing the cost of ownership by simultaneously reducing weight and manufacturing costs while providing little efficiency penalty. A further reduction in blade count of *11%* was reported by Haselbach et al. (2001) with the advent of ‘Ultra High Lift’ blades. The resulting blade surface velocity distribution shown in Figure 1-5 can be seen to have still higher levels of diffusion on the rear of the suction surface. However, such increases in blade loading were only possible when accompanied by the extensive experimental validation of Brunner et al (2000), Howell et al (2000) and Howell et al (2001).

Despite drastic reductions in blade count and significant savings to manufacturers and operators, the fundamental transition mechanisms involved in reducing losses are not fully understood and unsteady design tools are in the early stages of development, primarily due to inadequacies in understanding of the unsteady transition phenomena associated with highly decelerated and separated boundary layers.

1.3 Thesis overview

The work reported in this thesis seeks primarily to identify the mechanism by which boundary layer transition occurs when the wake shed from an upstream bladerow interacts with the highly decelerated boundary layer on the suction surface of a highly loaded LP turbine blade. In particular, the interaction between the turbulent wake and the unsteady separation bubble that re-establishes between wake passing events is investigated.

Chapter 2 presents a review of the literature pertaining to boundary layer transition and separation bubbles. Details of the experimental methods used in the course of research are presented in Chapter 3 together with a description of the experimental facilities employed.

A fundamental study, conducted on a flat plate with a pressure gradient matched to that measured on the T106 LP turbine cascade, is presented in Chapter 4. Evidence of deterministic natural transition phenomena between wake passing events was found and the boundary layer dissipation was measured thereby providing experimental proof of the loss reducing mechanism exploited by modern high lift LP turbine blade designs.

Chapter 5 presents detailed measurements of the wake convection through the T106 LP turbine cascade. The use of 2D LDA and a very fine measurement grid provides unprecedented detail and resolution of the turbulent quantities.

The unsteady blade surface boundary layer on the T106 LP turbine cascade is then investigated. Chapter 6 presents measurements of the unsteady blade surface pressures that reveal large amplitude pressure oscillations that arise as the wake passes over the location of the steady separation bubble. The source of the pressure oscillations is identified to be vortices embedded in the boundary layer. Chapter 7 presents evidence of these vortices in ensemble averaged 2D LDA boundary layer measurements. The vortices are identified to form in the separated shear layer of the separating boundary layer by an inviscid Kelvin-Helmholtz breakdown that is triggered by wake passing. Finally, conclusions and recommendations for further work are presented in Chapter 8.

Co-ordinates of the T106 profile investigated are presented in Appendix I, while a novel technique for the measurement of 2D Reynolds stresses with 1D LDA is presented in Appendix II. An algorithm for the wavelet transform of randomly sampled data is presented in Appendix III while Appendix IV presents details of the calculation of derivatives and the calculation of the dissipation of turbulent kinetic energy used in the thesis.

1.4 Figures

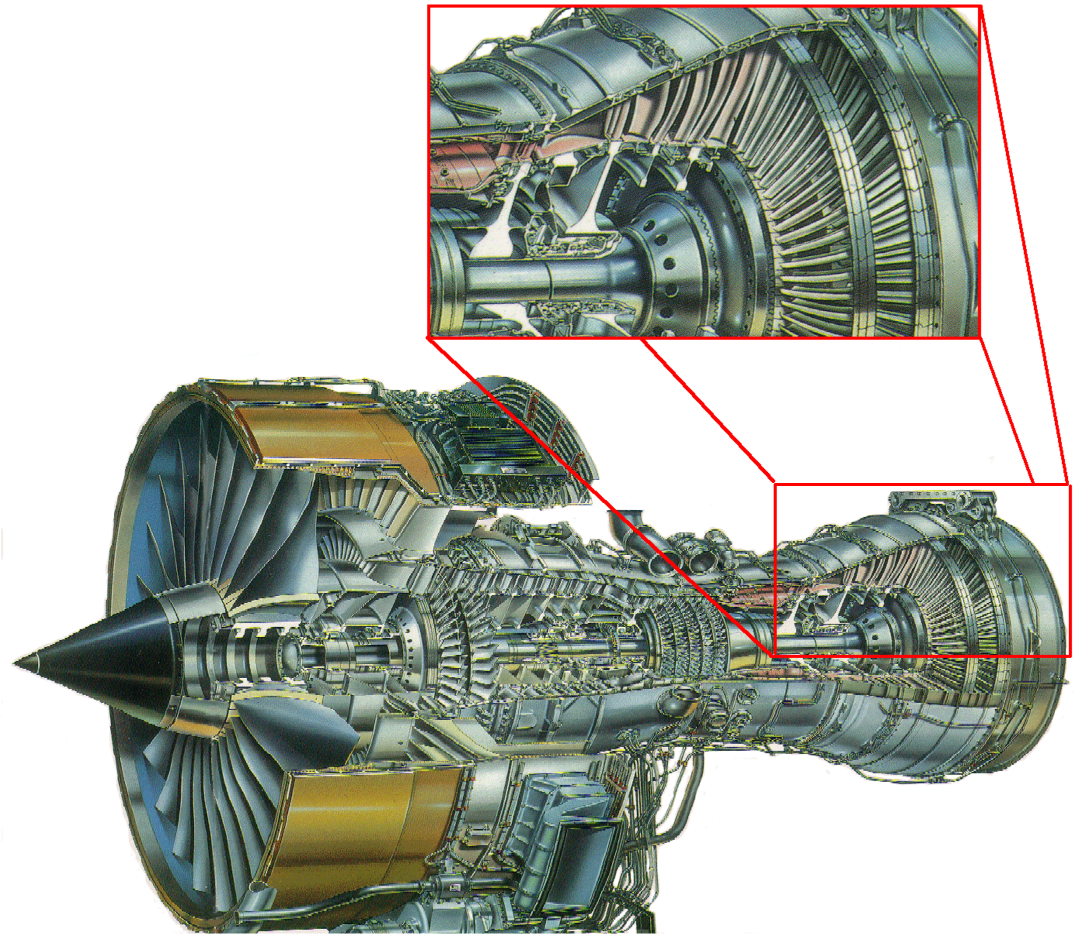

Figure 1-1: Cutaway section of a modern high bypass civil aircraft engine. Detail shows the LP turbine. Reproduced from Howell (1999)

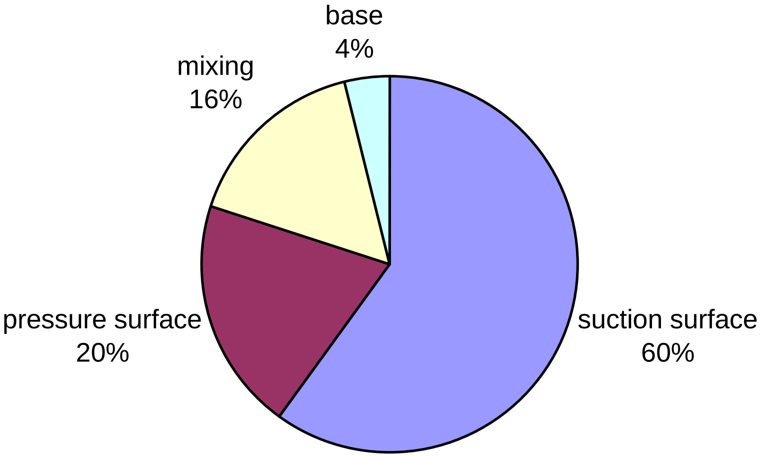

Figure 1-2: Estimated profile loss breakdown for a typical thin LP turbine blade from Banieghbal et al. (1995)

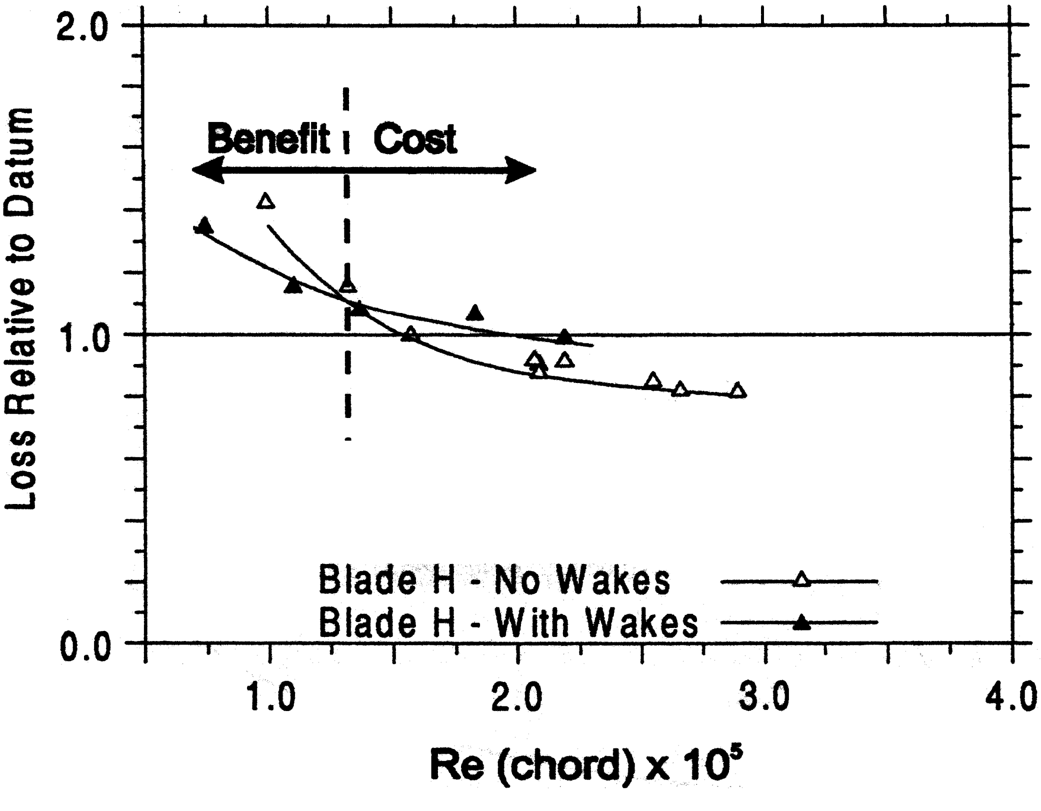

Figure 1-3: Reynolds number dependence of profile loss with steady and unsteady inflow. Based on Curtis et al (1996).

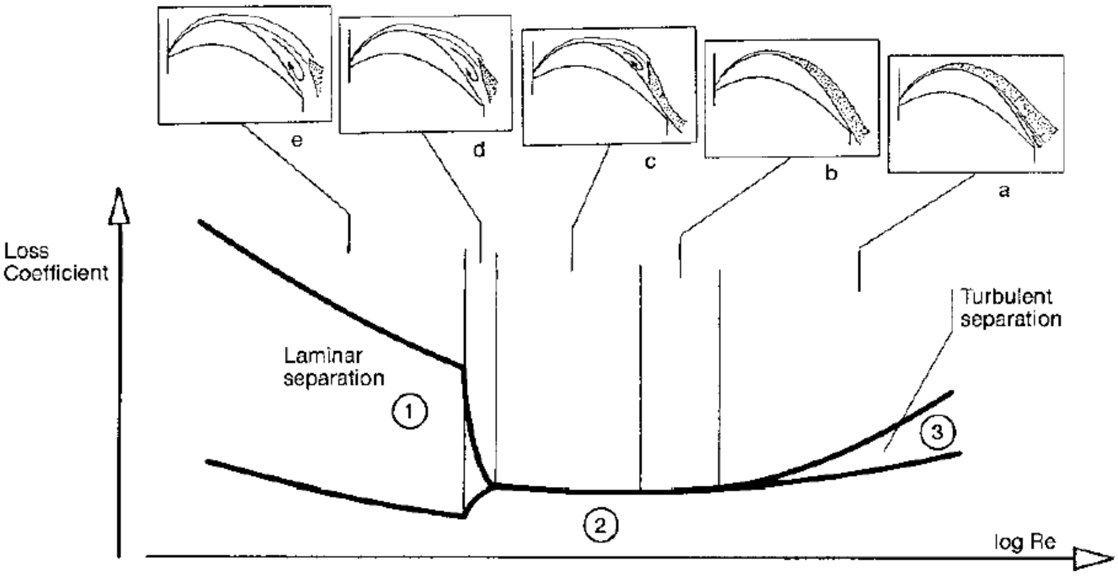

Figure 1-4: Schematic showing variation with Reynolds number of the flow structure on the suction surface of LP turbine blades. Reproduced from Hourmouziadis (1989)

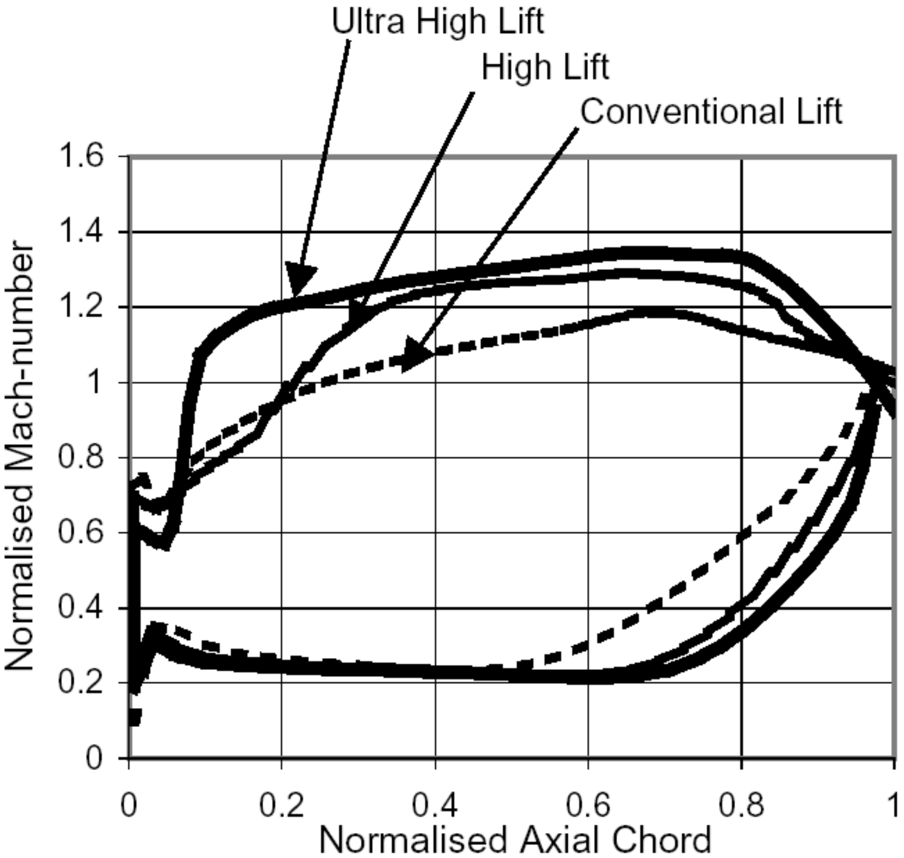

Figure 1-5: Blade surface velocity distributions representative of conventional, high lift and ultra high lift LP turbine blades. Reproduced from Haselbach et al (2001)

Chapter 2: Literature Review

2.1 Introduction

The development of highly loaded blading for LP turbines has come about primarily due to an improved understanding of pertinent unsteady boundary layer transition phenomena. LP turbines typically operate with a blade chord Reynolds number in the range 4×10^4-5×10^5. This dictates that significant portions of the blade surface boundary layers are transitional. For this reason, the field of boundary layer transition has received much attention in recent years. The calculation of both laminar and turbulent boundary layers is routinely possible in turbomachine environments. However, the transitional region, which is highly complex, is not yet fully understood. This has led to the development of numerous correlations to facilitate its calculation. The theory of boundary layer transition and its associated correlations however fail to adequately describe the transition process resulting from the unsteady interaction of a wake and inflexional boundary layer profile. This thesis addresses this aspect of boundary layer transition and presents a mechanism by which the interaction of a convected turbulent wake and an inflexional boundary layer profile causes transition thus paving the way for future wake-induced transition modelling efforts.

This chapter presents an overview of the literature describing the current understanding of boundary layer transition that is relevant to LP turbine design. Intermittency models for transition in steady and unsteady boundary layers are reviewed together with a range of correlations necessary for their implementation. In addition, the literature describing separation bubbles is considered. Although this body of literature is primarily concerned with steady flows, it provides valuable insight into flow structures and transition mechanisms found in highly decelerated flows.

2.2 Boundary layer transition

2.2.1 Natural transition in steady flow

Perhaps he most famous experiment in fluid mechanics is that of Reynolds who observed the motion of dye streaks in water pipes. He noted that the breakdown of orderly laminar flow to turbulence was in some instances intermittent in character. The generally accepted model of transition, including boundary layer, transition, which resulted from these observations, was that of an instantaneous change between laminar and turbulent states. From a one-dimensional viewpoint, this model matches the experimental observations of Reynolds.

For many years, the results of inviscid stability theory suggested that all boundary layer flows were only unstable if the velocity profile contained a point of inflexion. The existence of viscous instability waves, or Tollmein-Schlichting waves was, however, predicted physically by Prandtl and then proven mathematically by Tollmein, but the experiments of the day were too noisy and the results were treated with scepticism until Schubauer and Skramstad (1947) documented their existence. Klebanoff et al (1962) later showed the unexpected existence of three-dimensional disturbances that rapidly developed from the two-dimensional Tollmein-Schlichting waves. These three dimensional instability waves form into patterns of Λ-vortices under the influence of non-linear effects.

Emmons (1951) presented the next significant step in describing the transition zone. He observed isolated spots of disturbed flow (commonly called turbulent spots) appearing on a water table experiment. Experiments performed by Schubauer and Klebanoff (1955) confirmed the existence of turbulent spots and showed the spots to be approximately triangular in plan view and to spread at a constant rate in a zero pressure gradient flow. The same authors also observed a region following the artificial turbulent spot in which the disturbances were attenuated. These regions of reduced turbulent activity are termed calmed regions and are characterised by full laminar like velocity profile.

A schematic of boundary layer transition on an idealised zero pressure gradient flat plate (as described by White (1991)) is presented in Figure 2-1. The stable laminar boundary layer flow near the leading edge develops until at a certain critical Reynolds number it becomes unstable and develops linear oscillations of a well-defined frequency. These are two-dimensional Tollmein-Schlichting waves. These two-dimensional disturbances convect downstream with a typical speed of 0.3 - $0.35U_\infty$ in a zero pressure gradient flow. They grow in an increasingly non-linear manner as they convect and develop unstable three-dimensional waves, which form into hairpin vortices. Vortex breakdown then occurs in regions of highly localised shear resulting in three-dimensional fluctuations. Turbulent spots form at the locally intense fluctuations. As the turbulent spots propagate, they spread until they coalesce into fully turbulent boundary layer flow.

If the disturbance levels are high or the pressure gradient is strongly adverse a bypass transition may occur. In such a case the process of formation, growth and breakdown, of the instability waves occurs very rapidly or is bypassed entirely and turbulent spots form immediately in the laminar boundary layer.

2.2.2 Intermittency methods for transition

From his observations on a water table, Emmons (1951) was able to conclude that transition occurs by the formation of turbulent spots within a laminar boundary layer. The turbulent spots form randomly in time and space through a transition region. Each spot grows as it propagates downstream until the spots coalesce into a turbulent boundary layer. The process of transition is random in time and space and can best be described by a probability function specifying the fraction of time that the flow at a point in the transition zone is covered by turbulent flow. This fraction of time that the flow is turbulent is known as the intermittency, γ, and has values ranging from $\gamma=0$ for a laminar boundary layer to $\gamma=1$ for a fully turbulent boundary layer. Based on his observations, Emmons developed a ‘Probability Transition Theory’ to determine the intermittency distribution based on the rate of formation of turbulent spots per unit area and knowledge of how the spots propagate in the flow.

With insufficient information at his disposal Emmons went on to determine the chordwise intermittency distribution for a flat plate by assuming a constant turbulent spot formation rate and a simple model for the spot propagation.

The data of Schubauer and Klebanoff (1955) highlighted the failing of Emmons’ assumptions to correctly describe the transition zone. However, the necessary agreement between experiment and theory was provided by Narasimha’s (1957) concentrated breakdown hypothesis. Based on experimental observations that spots formed only in a narrow band, Narasimha hypothesized that the spot production rate could be represented by a Dirac delta function. Dhawan and Narasimha (1958) showed that this hypothesis adequately predicted all the mean flow properties in the transition zone.

Although the concentrated breakdown hypothesis provided the necessary agreement between experiment and theory, no explanation for its success was provided for almost 40 years. Schulte (1995) described how spot formation is suppressed in the calmed region that follows a turbulent spot. The genesis of spots occurs at a particular location, but downstream of that location, spot formation is suppressed due to the influence of existing spots and their calmed regions. Based on this observation Schulte went on to describe a corrected spot production rate by accounting for the effect of existing spots and calmed regions.

A more thorough development of the concepts proposed by Schulte (1995) was given by Ramesh and Hodson (1999) who presented a closed form solution for the corrected spot production rate in a zero pressure gradient flow. By approximating the calmed region behind each spot by a rectangular shape, they showed excellent agreement with the intermittency distribution of Narasimha. This provided an important physical explanation of the success of the concentrated breakdown model.

Application of the model of Ramesh and Hodson (1999) showed excellent agreement with that of Narasimha, where under adverse pressure gradients the spot production is limited to a narrow band by both models. Under zero pressure gradient flow, however, the spot production in the new model occurred over a wider range with the resulting intermittency distribution being delayed. This offset is, however, small compared to the transition zone length and could be accounted for by modifications to the transition onset location. No comparison with experimental results was presented.

The suppression of spot formation by existing turbulent spots was previously documented by Johnson and Fashifar (1994) who conducted a series of measurements in a transitional boundary layer on a zero pressure gradient flat plate. Using an intermittency routine to distinguish between laminar and turbulent flow, they proceeded to calculate statistics of the burst-length, gap-length and spacing between turbulent events and found that new turbulent spots were not formed randomly but were suppressed within a recovery period adjacent to existing turbulent spots.

2.2.3 Transition onset correlations

Transition is known to be affected by a wide range of parameters including: Reynolds number, Mach number, acoustic radiation, surface roughness, surface temperature, surface curvature and flow history. However, the dominant parameters in the turbomachinery environment are the streamwise pressure gradient and the free stream turbulence and it is upon these two parameters that most correlations are based.

In order to apply the intermittency model in the transition zone one requires knowledge of the spot production and propagation rates as well as the onset location of transition. Current understanding of the transition process is, however, insufficient to allow the prediction of the necessary parameters. This has necessitated the development of correlations to determine transition onset, spot production rate and transition length in terms of flow conditions at transition onset.

2.2.3.1 Transition onset

Linear stability theory for laminar boundary layers indicates that transition is predominantly brought about by the amplification of disturbances in the boundary layer. At a critical displacement thickness Reynolds number, the boundary layer becomes susceptible to disturbances that grow and lead to transition. This process is however not fully understood and as a result experimental data and correlations must be used to facilitate the prediction of transition. In the turbomachinery environment, where disturbances abound from a range of sources, primarily turbulence, the use of experimental data and correlations is vital for engineering calculations.

An extensive experimental study on transition in attached boundary layers representative of turbomachinery environments was performed by Abu-Ghannam and Shaw (1980). Based on a combination of published data and their own, they provided a correlation for transition onset as a function of turbulence level and pressure gradient. It was noted that the pressure gradient has a less significant effect on transition onset at higher turbulence levels. Although Abu-Ghannam and Shaw noted the importance of turbulent length scale, they found that it had little effect on transition onset.

Mayle (1991) correlates transition onset with turbulence in zero pressure gradient flows and arrives at an expression similar to that previously suggested by Hourmouziadis (1989). He notes that Abu-Ghannam and Shaw’s correlation forced data to fit at low turbulence and to level out at the minimum stability criteria. These measures are seen as unnecessary in light of the influence of acoustic disturbances at very low turbulence levels[1]. Although insufficient data was available for a reliable

---

[1] The irrelevance of stability theory to by-pass transition is cited by Mayle as a reason to dismiss the need for the minimum limit imposed by Abu-Ghannam and Shaw. Walker (1993), however comments that stability theory and its governing parameters are applicable and relevant to estimating transition length.

correlation, Mayle suggests the use of Taylor's turbulence parameter[2] to account for the effect of turbulent length scale, using momentum thickness as a length parameter. Based on the assumption that turbulence far outweighs the influence of pressure gradient in gas turbine environments, Mayle (1991) proposes his zero pressure gradient correlation for transition onset as sufficient for all conditions with turbulence level above *3%*.

In an attempt to add physical insight to the transition onset problem, Johnson (1993) argued that the start of transition could be inferred from laminar fluctuations of the near wall velocity that are induced by freestream turbulence. He argues that if the near wall velocity drops below half the mean local velocity then the near wall flow will stall and separate instantaneously, a mechanism that is consistent with the formation of hairpin vortices known to precede breakdown. Johnson's simplistic argument was able to show that this condition corresponds to a local turbulence level of *23%*, which agrees with near wall measurements at the start of transition for a range of freestream turbulence intensities and pressure gradients. A complementary physical argument suggests that the local turbulence level is a measure of streamline distortion and that the streamline distortion corresponding to a turbulence level of *23%* is the maximum that can be tolerated prior to breakdown. By assuming a Pohlhausen velocity profile, Johnson was able to produce a semi-empirical formula to predict the start of transition as a function of pressure gradient and turbulence. However, the results do not show a significant improvement over those of Abu-Ghannam and Shaw (1980).

Mayle and Schulz (1997) present a separate analysis for calculating fluctuations in the laminar boundary layer resulting from a turbulent freestream. Their analysis, based on that of Lin (1957), derived an equation for the kinetic energy of fluctuations in a laminar boundary layer. It was found that the only link between the fluctuations in the freestream and the boundary layer was through the production of laminar kinetic energy in the boundary layer by the work of imposed fluctuating pressure forces in the freestream. After formulating models for the production and dissipation of the laminar fluctuations, calculations were performed to predict

---

[2] $Ta = Tu\sqrt[5]{\frac{\theta}{L}}$ where Ta is Taylor's turbulence parameter, Tu is the turbulence intensity, θ the momentum thickness and L the turbulence length scale.

transition onset. Limited success was attributed to inadequacies in the models for production, dissipation and the absence of a suitable universal onset criterion.

2.2.3.2 Transition length

The transition length in turbomachinery flows has usually been determined by one of two approaches, namely the minimum transition length concept introduced by Walker (1989) or the spot formation rate concept of Narasimha (1985) [3]. Both approaches depend primarily on correlations for pressure gradient and turbulence level but these correlations are applied to different views of the fundamental mechanism whereby spots are formed. The separate views are however, seen to describe the same underlying mechanism in that they share a common functional relationship between transition length and transition onset Reynolds numbers (Walker, 1993).

Spot formation rate correlations

The approach of Narasimha begins by determining an appropriate non-dimensional parameter for spot production rate. By correlating the transition length and onset location Reynolds numbers, he found the most appropriate non-dimensional parameter for breakdown to be $N = n\sigma\theta_t^3/\nu$, which he termed “crumble”. Narasimha proposed that N was a constant in zero pressure gradient flows. Furthermore, using Blasius’ boundary layer thickness to interchange θ_t and δ_t Narasimha showed that $n\delta_t^3/\nu$ is approximately constant and therefore the breakdown rate scales primarily with the ratio of boundary layer thickness (δ_t) to viscous diffusion time (δ_t^2/ν).

Another correlation for spot production rate is proposed by Mayle (1991), but in terms of different parameters. He provided a best fit to available zero pressure gradient data for spot production rate ($n\sigma$) and turbulence level, but dismissed a correlation for pressure gradient and turbulence in terms of the acceleration parameter, K, due to insufficient data.

With more data available, Gostelow, Blunden and Walker (1994) showed that N was dependant on pressure gradient and turbulence level. By making a series of measurements of intermittency distributions for a range of turbulence levels, Gostelow showed that the spot formation rate parameter decreases monotonically with

---

[3] Narasimha (1985) also defines a transition length but this is different to the minimum possible transition length concept of Walker.

increasing freestream turbulence and presented a correlation for N in terms of turbulence level. Measurements made at a complete range of pressure gradients showed that the spot formation rate parameter increased rapidly with the increased severity of the adverse pressure gradient. An order of magnitude increase was observed from the zero pressure gradient case as laminar separation is approached. A correlation for the spot formation rate parameter is presented in terms of the pressure gradient parameter at transition onset ($\lambda_{\theta t}$) and the turbulence level.

The effect of changes in pressure gradient on transition length was accounted for by the method of Solomon, Walker and Gostelow (1996). It had previously been assumed that the spot spreading angle (α) and propagation parameter (σ) did not vary significantly with pressure gradient through the transition zone. However, the measurements of Gostelow, Melwani and Walker (1996) showed a strong variation of these parameters in an adverse pressure gradient. A correlation for these parameters was developed in terms of the pressure gradient parameter, however insufficient data was available to extend the correlations to account for turbulence. The calculation method of Solomon, Walker and Gostelow (1996) used the concentrated breakdown hypothesis of Narasimha with the spot inception rate assumed to depend only on the local conditions at transition onset. The spreading rate of the turbulent spots was then allowed to vary as a function of the local pressure gradient parameter based on the laminar boundary layer, thereby accounting for the effect of a rapidly changing pressure gradient. The model of Chen and Thyson (1971) was adapted to incorporate this new model, which was demonstrated for typical turbine aerofoil test cases.

The correlation used by Solomon, Walker and Gostelow (1996) only covered a limited range of adverse pressure gradients and limited the spot spreading angle and spot propagation parameter for strong adverse pressure gradients. Believing that limiting α and σ for strong adverse pressure gradients lead to over predictions of transition length, Johnson and Ercan (1996) presented a correlation for a wider range of pressure gradients by extrapolating the data of Gostelow, Melwani and Walker (1996). He noted that the leading and trailing edge celerities of the turbulent spots corresponded to the velocities at particular heights in a boundary layer with a Pohlhausen velocity profile and was able to correlate the celerities with the pressure gradient parameter over the range of pressure gradients presented by Gostelow, Melwani and Walker (1996). Assuming that the leading and trailing edge of the spot always travelled at these particular heights in the boundary layer, Johnson provided a new correlation for the spot spreading angle and spot propagation parameter's dependence on pressure gradient. His correlations fit the data of Gostelow, Melwani and Walker (1996) but have a different shape to those used by Solomon, Walker and Gostelow (1996). In particular, the predicted values of α and σ for strong adverse pressure gradients are far higher than the Solomon, Walker and Gostelow (1996) correlations.

The determination of the spot spreading parameters over a wider range of pressure gradients was attempted computationally by Johnson (1998). The time mean flow was assumed inviscid and parallel, with a Pohlhausen velocity profile. Taking lead from Li and Widnall (1989), who showed that the characteristics of a linearly disturbed region are very similar to those of a turbulent spot for Poiseuille flow, Johnson (1998) calculated the flow due to the 'spot' as a small linear perturbation to the time mean flow. Although linear, the perturbation was treated as three-dimensional and viscous. The 'spot' was initiated by introducing a pulse at a point on the wall. The calculated flow patterns captured the geometrical features of artificial turbulent spots observed in flow visualisation studies. The calculated flow was, of course, not a turbulent spot, as no turbulence was calculated. The effect of pressure gradient on the 'spots' was calculated by tracking the flow structures in mean flows with a range of Pohlhausen pressure gradient parameters (λ). For favourable and mild adverse pressure gradients, the calculated properties agree favourably with the data of Gostelow, Melwani and Walker (1996). In strong adverse pressure gradients, the calculated properties follow the correlation of Johnson and Ercan (1996). However, the calculation and correlation are both based on the Pohlhausen velocity and provide no mechanism for the interaction of the 'spot' with the mean flow.

D'Ovidio, Harkins and Gostelow (2001 a & b) provided a further series of measurements to extend the range of the correlations used by Solomon, Walker and Gostelow (1996). The propagation of an artificially triggered turbulent spot was tracked through an incipient laminar separation and a laminar separation bubble to derive α and σ. The new data points thus obtained suggested that the correlation for α remained unchanged, however, the measured values for σ fell significantly below the previous correlation, which was modified to better describe all the available data.

The data of D'Ovidio, Harkins and Gostelow (2001 a & b) disproves the extended correlation of Johnson and Ercan (1996) and points to the shortcomings in the model used for the calculations of Johnson (1998). Both the correlation and the calculations of Johnson assume that the mean flow in which the spot propagates is described by the Pohlhausen velocity profile, which is not altered by the presence of the 'spot'. The agreement between Johnson's correlation and his subsequent calculations can thus be attributed to this common element. Furthermore, the discrepancies between these calculations and the measurements of D'Ovidio, Harkins and Gostelow (2001 a & b) may be attributed to effects associated with non-linearity, the turbulence and the interaction of the mean velocity profile and the 'spot'.

Minimum transition length correlations

Walker (1975) encountered problems with an over predicted transition length when using the arbitrary pressure gradient model of Chen and Tyson (1971). This provided the stimulus for developing a model for determining the minimum possible transition length. This model was later extended and used as the basis of a correlation for predicting transition length.

Knapp and Roache (1968) observed the breakdown of laminar instability (Tollmien-Schlichting) waves to occur in sets interspersed by laminar flow. With increased adverse pressure gradients, the sets of waves occurred at higher frequencies. Considering this observation, Walker (1989) postulated that the minimum possible transition length would occur with spot formation occurring once per Tollmien-Schlichting wave cycle. He obtained the Tollmien-Schlichting frequency from the locus of the maximum amplification ratio of a Falkner-Skan profile and used this period in conjunction with simple spot kinematics to estimate the minimum length necessary for such spots to coalesce. From this, a relationship between minimum possible transition length and transition inception Reynolds number was established. Substituting a Blasius profile, the functional relationship between transition length and onset Reynolds numbers was found to match that of Narasimha. The physical basis of this relationship is the correlation of dominant disturbance frequencies with local boundary layer parameters from linearized stability theory.

The minimum transition length as described above will underestimate transition length. However, Walker and Gostelow (1989) found they were able to correlate the ratio of observed transition length to the minimum theoretical transition length for different pressure gradients. Later Gostelow, Blunden and Walker (1994) extended this correlation with a curve fit for data in terms of the pressure gradient parameter at transition onset ($\lambda_{\theta t}$) and the turbulence level[4].

A further model for transition length presented by Mayle (1998) borrows ideas from Walker's minimum transition length hypothesis to predict spot production rates for bypass transition in zero pressure gradient flow. Walker's minimum transition length model was formulated based on a continuous breakdown of Tollmien-Schlichting waves (natural transition). In contrast to this approach, Mayle formulated his model in terms of a bypass transition model (Mayle and Schulz, 1997).

Following Walker, Mayle argues that the maximum possible spot production frequency is related to the frequency of turbulence that is most effective in producing pre-transitional boundary layer fluctuations. The actual spot production rate is thus arguably a fraction of the maximum number of spots that can form. Mayle argued that the initial spot size must be related to a length scale of the flow and the boundary layer thickness at transition onset was found to correlate best. Further, using the proportionality of the integral length scales in zero pressure gradient flows Mayle was able to find an expression correlating spot production rate with $Re_{\theta t}$, the Kolmogorov velocity scale and the freestream velocity. By substituting a correlation for turbulence intensity and Re_{θ}, the correlation was adapted to include the effects of turbulence intensity and length scale. This second correlation allowed Mayle to postulate that the scatter in published data for transition onset may be caused by length scale, about which information is not typically available.

2.2.4 Direct simulation of bypass transition

Direct numerical simulations of bypass transition have been performed by Jacobs and Durbin (2001). Their simulations, performed for a zero pressure gradient flow with a freestream turbulence intensity of about *1%*, provide sufficient detail to identify the mechanism by which turbulent spots are formed in the boundary layer under the influence of freestream turbulence. The precursor to the formation of a turbulent spot was found to be a long backward jet extending into the upper region of the boundary layer. This backward jet is a region whose instantaneous velocity is below the mean velocity and does not imply flow reversal. These backward jets occur

---

[4] This correlation is based on the same data as the previous correlation for N by the same authors.

throughout the boundary layer in response to the low frequency eddies in the freestream turbulence. However, it is only when the backward jets are in the upper portion of the boundary layer that they interact with the fine scale disturbances of the freestream turbulence. In this way, the backward jets act to overcome the sheltering effect of the boundary layer shear, which prevents the high frequency fluctuations from penetrating the boundary layer. With the shear layer of the backward jet in the outer region of the boundary layer, small-scale motions develop under the influence of the fine scale freestream turbulence and a Kelvin-Helmholtz breakdown occurs. Turbulent spots ensue when the irregular motion at the edge of the boundary layer cascades towards the wall. Breakdown occurs only near the top of the boundary layer. External disturbances do not penetrate the boundary layer, rather the backflow jet rises to the edge of the boundary layer where it breaks down. Not all backflow jets result in turbulent spots and Jacobs and Durbin (2001) were unable to identify a definite qualitative signature to predict which of the backward jets would lead to the formation of a turbulent spot.

2.2.5 Comments on the presented correlations

One of the most striking features of the correlations presented for transition onset and transition length is the variety of parameters used by different authors. Most notable is the use of the acceleration parameter, K, by Mayle as opposed to Thwaites' pressure gradient parameter, $\lambda_{\theta t}$, used by Abu-Ghannam and Shaw, Walker and Gostelow.

Mayle chose the acceleration parameter, K, based on the belief that it was more appropriate for accelerating flows where transition is predominantly of the bypass mode. He presents a correlation of $n\sigma$ in terms of K and free stream turbulence. However, for flows with adverse pressure gradients, where the transition physics is more representative of natural transition (Walker and Gostelow (1989) and D'Ovidio et al (2001 a)), $\lambda_{\theta t}$ is more appropriate as it is directly proportional to the curvature of the velocity profile near the wall and is thus an indicator of flow stability. Gostelow, Blunden and Walker (1994) found a strong correlation for N in terms of freestream turbulence and $\lambda_{\theta t}$.

The parameter used for spot production rate is also found to vary between correlations. The form of Narasimha's crumble (N) is physically more appealing as it has as its basis the scaling between diffusion time and boundary layer thickness. The parameter of Mayle ($n\sigma$), originally suggested by Narasimha, lacks this feature.

It is also worthy of note that the intermittency distribution predicted by Narasimha’s concentrated breakdown model is found to hold even in separated flow transition (Malkiel and Mayle, 1995). The universal intermittency distribution is based entirely on three assumptions, namely: Poisson birth, linear propagation and concentrated breakdown (Narasimha, 1998). The observed conformity to the intermittency distribution thus suggests that these assumptions hold into the separated region. As such, suitable correlations for transition onset and transition length should allow the extension of the currently employed intermittency methods into regions of separated flow. This however assumes that transition occurs by a bypass mechanism in separated flows.

Results from the DNS calculation of Jacobs and Durbin (2001) illuminate many aspects of the bypass transition induced by freestream turbulence. In particular, the mechanism by which turbulent spots are initiated is highlighted as the breakdown of backward jets lifted to the outer boundary layer by low frequency eddies in the freestream. The attempts of Johnson (1993) and Johnson and Dris (2000) to determine spot inception as either the point where the instantaneous near wall velocity fluctuated to half its mean value or where an instantaneous separation is induced, are seen to be inappropriate. Although the precursor to a turbulent spot is a backward jet and therefore reduced velocity, it is necessary for the jet to be in the outer boundary layer before breakdown to a turbulent spot can ensue in the absence of shear sheltering. The method of Mayle and Schulz (1997) uses the concept of an effective frequency. In light of the mechanism described by Jacobs and Durbin (2001) this may be associated with the low frequency eddies responsible for the formation of the backward jets. The lack of a suitable transition criterion is reported by Mayle and Schulz (1997). It is unfortunate that the DNS of Jacobs and Durbin (2001) did not provide this criterion.

A further concern over the correlations developed for transition length predictions is raised by the DNS of Jacobs and Durbin (2001). The propagation of turbulent spots forms the basis for all bypass transition theories. These theories have assumed the spot shape as described by Emmons (1951) and confirmed by Schubauer and Klebanoff (1955) as having a downstream pointing arrowhead. However all such turbulent spots have been generated by forcing at the wall. Even the spots observed by

Emmons (1951) must have originated from the wall, as there was no forcing applied to the edge of the boundary layer in his experiment. Such spots are termed bottom-up spots. However, for bypass transition the calculations of Jacobs and Durbin (2001) show that the spots form in the outer region of the boundary layer and do not have the typical shape of a downstream pointing arrowhead. These spots are termed top-down spots. All available correlations for spot spreading and propagation used for transition length predictions have been based on data collected on artificially generated bottom-up spots. It has not been confirmed that top-down spots, appropriate for bypass transition predictions, have the same spreading angle and propagation parameters as bottom-up spots, nor that the dependence of these parameters on pressure gradient and turbulence level are valid.

2.3 Unsteady transition in turbomachines

2.3.1 *Introduction*

The process of boundary layer transition that occurs in real turbomachines is more complex than the steady model described above due to the presence of unsteadiness.

Transition on a zero pressure gradient flat plate with the freestream disturbed in a sinusoidal manner was investigated experimentally by Obremski and Fejer (1967). They found that the unsteady transition could be classed broadly into two regimes based on the unsteady Reynolds number, $Re_{NS}=N_A/(\omega\nu/U_0^2)$. For Re_{NS} below $25\ 000$ the Reynolds number based on transition onset length, Re_{ts}, was independent of the amplitude ratio of the disturbance ($N_A=\Delta U_0/U_0$), and for Re_{NS} above $27\ 000$, Re_{ts} dropped linearly with increasing N_A. In both regimes, the turbulent bursts were preceded in space and time by disturbance wave packets that originated at the minimum velocity during the cycle. For the high Re_{NS} cases, rapid amplification of the wave packets occurred prior to turbulent breakdown and the transition onset depended on the amplitude of the freestream disturbance. For the low Re_{NS} cases, where the transition onset was not dependant on the initial disturbance amplitude, the wave packet moved along the accelerating portion of the measured velocity trace before bursting into turbulence near the wave crest. The wave packets continued to grow upstream of the newly formed turbulent bursts until at a certain time during the cycle the interface between the turbulent burst and the growing wave packet moved upstream.

A quasi-steady model for this unsteady natural transition process was presented by Obremski and Morkovin (1969). The stability characteristics were calculated for modelled unsteady boundary layer velocity profiles at a number of locations and time instants on the flat plate. Obremski and Morkovin were able to determine the amplification ratio of a particular disturbance frequency by following the trajectory of the local group velocity for that particular disturbance frequency using a graphical integration method. In this manner, they were able to determine the most amplified frequency at a given point at different times through the cycle. Their calculated frequencies were found to be in reasonable agreement with the measured values of Obremski and Fejer (1967). The stability characteristics of the unsteady profiles change through the cycle and as a result, the boundary layer is only susceptible to the critical disturbances for a short period in the cycle. Only disturbances that arise during this window are subsequently amplified and this results in a well-defined wave train present for only a short duration in the cycle.

In agreement with the observations, this simple model was able to predict a wave packet forming at the minimum velocity and advancing through the cycle. The calculated amplification ratios at transition were, however significantly below those expected for the e^n method[5] in steady flow. An explanation for the two regimes of unsteady transition is presented. For the low Re_{NS} conditions, the most amplified disturbance is unable to attain sufficient amplification in a single cycle before the stabilising effect of the accelerating part of the cycle occurs. In such a case, transition is delayed and the unsteady transition becomes independent of the initial amplitude.

Although the investigations of Obremski and co-workers point to the added complexity of unsteady transition, they do not include all the features relevant to the turbomachinery environment where the unsteadiness is primarily a result of the wakes shed from upstream bladerows. Fluid in the wake is turbulent and when convecting over the blade surface boundary layer may cause bypass transition to occur. The unsteady transition process thus retains the nature of bypass transition and its

---

[5] The e^n method is used to predict transition onset by determining the total amplification ratio of Tollmein-Schlichting waves. Transition onset is correlated to a certain value of n representing the total amplification ratio equal e^n. See White (1991).

associated random nature and this necessitates the use of a statistical model with suitable correlations as developed for steady bypass transition.

A number of models to describe the wake-induced transition on turbomachine blades have been developed. These models have achieved differing levels of success in determining the unsteady transition onset front and predicting the time averaged boundary layer properties.

2.3.2 Unsteady wake induced transition in attached boundary layers

The first observation of the behaviour of transition under the influence of incident turbulent wakes was that of Pfeil and Herbst (1979). They observed that the global structure of the wake flow behind a cylinder and a turbomachine blade of equal drag are nearly the same. Using wakes from cylindrical bars upstream of a flat plate, Pfeil and Herbst (1979) observed that at a point on the flat plate the boundary layer became turbulent for the duration of the wake disturbance. Intermittently laminar and turbulent states of the boundary layer were thus observed. The measurements of Pfeil and Herbst showed that for a given bar the wake passing frequency had no effect on the location of earliest transition onset.

Pfeil, Herbst and Schröder (1982) present a model for the unsteady transition process on a flat plate subjected to wakes from cylindrical bars. In the case of steady, unperturbed, inflow, the transition process begins with the formation of Tollmein-Schlichting type disturbances at the point of neutral stability (x_{ns}). The Tollmein-Schlichting waves then grow until turbulent spots are formed at the transition onset location (x_{0tr}). The spots propagate and grow in the intermittently turbulent boundary layer until they merge into the fully turbulent boundary layer at the end of transition (x_{0Tr}). Becalmed regions trail the turbulent spots as the trailing edges of the turbulent spots propagate faster than the Tollmein-Schlichting waves and so no disturbances can penetrate the calmed region. This transition process is presented schematically in Figure 2-3 (a).

For the case with incident turbulent wakes, Pfeil, Herbst and Schröder (1982) present a modified S-T diagram as shown in Figure 2-3 (b). As the increased turbulence of the wake convects over the plate, the laminar boundary layer is intermittently disturbed. At the forced start of transition (x_{ftr}), depicted as occurring after the neutral stability point, turbulent spots are periodically formed. These turbulent spots then propagate as those formed at the natural transition point. If the spacing between wakes is large, then turbulent spots are also formed at the natural transition point as for the case with no wake passing. However, no turbulent spots can form at this natural transition point during the passage of the calmed region formed after the wake induced turbulent spots. This has the effect of delaying the point at which transition is complete as shown in Figure 2-3 (b). Depending on the wake passing frequency, the end of transition can thus range from the wake induced transition onset location to a point after the end of natural transition.

The observations of Pfeil, Herbst and Schröder (1982) were applied to a simple model for wake-induced transition by Doorly (1988). During each wake passing cycle, the boundary layer was considered turbulent beneath the wake. By determining the location and extent of the wake through the wake passing cycle, the time averaged intermittency was calculated as the fraction of time each surface location was covered by wake fluid. This was then used to determine the time averaged flow from separate laminar and turbulent calculations. The agreement with experimental data was only qualitative. The model of Doorly did not consider the mechanism by which wake induced transition occurs. The flow under the wake was assumed fully turbulent, with no consideration of the transitional flow characterised by the formation and growth of turbulent spots responsible for the transition process.

Addison and Hodson (1990 a) conducted unsteady measurements on a rotating rig together with complementary measurements on a linear cascade. The unsteady velocity fluctuations due to the velocity defect in the wake were discounted as being responsible for inducing unsteady transition as the unsteady Reynolds number of their experiments was well below the critical value reported by Obremski and Fejer (1967). With the additional argument that at elevated turbulence levels the effect of pressure gradient on boundary layer stability is small, they discarded the direct effect of the wake velocity defect on transition. Furthermore, they showed that wake boundary layer interactions could be considered quasi steady for the range of reduced frequencies representative of turbomachinery environments and thus assumed the steady correlations for bypass transition to hold in the quasi-steady environment.

Addison and Hodson (1990 b) went on to show that the onset location of transition could be found from the level of free stream turbulence, which varied along the blade surface and through the wake passing cycle. They showed the onset location to be well modelled by assuming the wake turbulence to decay in proportion to the decay of grid turbulence measured in their linear cascade. However, simple models for wake convection were found inadequate in predicting the spread of wake turbulence in the boundary layer as inviscid calculations showed that the kinematics of wake convection did not produce significant spreading of wake turbulence.

A further model for wake-induced transition was presented by Mayle and Dullenkopf (1989). They considered wake-induced transition to result from two possible sources of turbulent spot production in an Emmons type bypass transition formulation. A constant spot formation rate due to natural transition was assumed independent of and linearly superposed upon time varying spot production induced by the passage of wakes. The spot formation was thus a function of time and space. The wake turbulence was assumed an intense source of spots that immediately formed into spanwise strips of turbulence, which propagated and grew as they convected downstream. The need to calculate the position of the wake was thus avoided as, once formed, the turbulent spots in the boundary layer convected independent of the wake position. By approximating these turbulent strips with a series of square waves and solving the resultant intermittency distribution, Mayle and Dullenkopf were able to arrive at a formulation for the time average intermittency. They reported good agreement when comparing their predicted intermittency to the ratio

$$\gamma(x) = \frac{f_{measured} - f_{la\min ar}}{f_{turbulent} - f_{la\min ar}} \qquad (2\text{-}1)$$

where the quantity (*f*) was taken from measured results together with laminar and turbulent predictions.

Another model for determining the wake induced transition process was presented by Addison and Hodson (1992). The instantaneous transition onset location was specified in space and time and the spot formation rate was then found from correlation with a steady value of λ_θ. The unsteady intermittency distribution was found by integrating Narasimha's concentrated breakdown formulation over the unsteady dependence volume. The time mean intermittency was then obtained from the unsteady intermittency distribution. This calculated time mean intermittency was used to prescribe the effective eddy viscosity according to

$$\upsilon_{eff} = \upsilon_{lam} + \bar{\gamma}(s)\upsilon_{turb} \qquad (2\text{-}2)$$

The use of a steady boundary layer code and a time mean intermittency was justified in terms of previous observations (Hodson, 1989) that it is the wake turbulence and not the velocity fluctuations that cause transition.

The model of Addison and Hodson (1992) required the instantaneous transition onset location to be specified. No model for this was used in their calculation, but their previous model (Addison and Hodson, 1990 b) was suggested as a likely starting point.

Unsteady wake induced transition was modelled by Hodson et al (1992) by calculating an ensemble averaged intermittency distribution and thereby allowing the state of the boundary layer to vary with time and space. After specifying the start of transition as a function of time and space, the unsteady spot production rate was determined from correlations and a steady laminar boundary layer calculation. A numerical Emmons style integration of the spot production over the unsteady dependence volume was then performed to determine the unsteady intermittency as a function of time and space. The unsteady intermittency was used to determine the effective eddy viscosity according to

$$\upsilon_{eff}(s,y,t) = \upsilon_{lam} + \tilde{\gamma}(s,t)\upsilon_{turb}(s,y,t) \qquad (2\text{-}3)$$

where $\upsilon_{turb}(s,y,t)$ is determined through a turbulence model using the instantaneous velocity profile.

Two models for the transition onset were presented. For cases where the wake is wide and the wake turbulence is high, the transition onset location is not sensitive to the freestream turbulence it is possible to model the spot formation to occur for a portion of the wake passing cycle at a fixed chordwise location. Alternatively, for thin wakes, the wake may be considered a source of high turbulence travelling at the velocity of the freestream. At a location, determined from steady experiments, turbulent spots form randomly along the span beneath the wake. The spot formation rate is again determined from steady experiments. The spots thus formed, grow and convect, as they do in steady flow, until they merge into a fully turbulent strip. The wake moves ahead of the turbulent spots and may thus cause spots to be formed further downstream.

2.3.3 Direct simulation of unsteady transition

The bypass transition induced by turbulent wakes convecting over a flat plate has been studied by the direct numerical simulations of Wu et al (1999) who aimed to compute the experiments of Liu and Rodi (1991). Predating Jacobs and Durbin (2001), Wu et al (1999) found that turbulent spots induced by the turbulent wake were preceded by longitudinal puffs that were selectively intensified under certain conditions of local forcing by the turbulent eddies in the wake above the boundary layer. The mechanism for wake induced bypass transition is thus the same as for steady bypass transition induced by a turbulent freestream.

Wu et al (1999) also found the shape of their turbulent spots to differ from the classic Emmons spots, however remarkable agreements was found between visualisations of their computed turbulent spots and those visualised using liquid crystals by Zhong et al (1998). Their comparison is presented in Figure 2-4. Wu et al (1999) explained the differences in observed spot shapes in terms of the position in the boundary layer where the spots originate.

2.3.4 Comments on unsteady transition

The unsteady wake-induced transition process for attached boundary layers is well modelled by the unsteady intermittency methods of Hodson et al (1992). However, while accounting adequately for the unsteady wake passing processes, the model is based on and limited by steady flow transition correlations. As a result, substantial effort has been directed to providing and extending correlations for transition onset and spot propagation parameters.

The prescription of an unsteady intermittency distribution also relies on the ability of the turbulence model to adequately model the resulting turbulent portion of the flow and assumes the final flow to be a linear combination of the laminar and turbulent components. The unsteady intermittency approach has proved successful for the calculation of unsteady transition in attached boundary layers, however the shortfalls of simple turbulence models and transition correlations for highly decelerated flows limit its application as a reliable design tool.

2.4 Separation bubbles

2.4.1 Structure of a separation bubble

A laminar boundary layer may separate if the near wall fluid has insufficient momentum to overcome an imposed adverse pressure gradient. The stagnation of near wall fluid causes a blockage and forces the streamlines away from the wall.

The conventional view of the time-averaged structure of a separation bubble is shown in Figure 2-5. After separation, the shear layer detaches from the surface forming a separated shear layer. Although initially laminar, the inflexional velocity profiles of the separated shear layer are unstable and transition results. The resulting turbulent entrainment re-energizes the flow causing the streamlines to turn toward the surface and the boundary layer to reattach. This forms a laminar separation bubble with turbulent reattachment.

The streamline dividing the free shear layer and the dead air region at first rises almost linearly from the surface at the separation point and reaches its maximum displacement above the centre of the reverse flow region. The displacement of the shear layer from the surface causes a rapid increase in the thickness of the boundary layer, which in turn modifies the local pressure distribution that was originally responsible for the separation. There is thus an inherent feed back mechanism controlling the structure of a separation bubble.

Separation bubbles are broadly classed as short or long with the distinction based on the effect of the bubble on the surface pressure distribution. Tani (1964) described bubbles as being short if they had only a local effect on the pressure distribution, which outside of the separated region closely followed the inviscid pressure distribution. Separation bubbles were considered long if the pressure distribution was appreciably affected together with the velocity peak and circulation of the aerofoil.

A further quantitative classification of bubbles was proposed by Hatman and Wang (1998 a) based on the boundary layer state at separation. Accordingly, separation bubbles were broadly classed transitional or laminar. Laminar bubbles were further classed short if the reverse flow vortex (see Figure 2-5) was intermittently ejected or long otherwise.

2.4.2 Previous research on separation bubbles

Early research was primarily concerned with determining flow conditions under which a separation bubble would burst. Gaster (1967) conducted experiments at a range of Reynolds numbers and pressure gradients. He found the bursting of bubbles depended on a unique relationship between the momentum thickness Reynolds number at separation and a pressure gradient parameter. His investigation was however conducted at low freestream turbulence with the intended application being in external aerodynamics.

A semi-empirical correlation for the length of a separation bubble was proposed by Horton (1969). He considered the bubble to consist of an initial laminar region followed by a region of turbulent reattachment. The laminar length was given by a constant length Reynolds number and the reattachment zone length was found from an empirical correlation. The shape factor and the momentum thickness at the start of the ensuing turbulent boundary layer were also provided by the model. Again, these results are for low turbulence levels.

Dunham (1972) added to the model of Horton by considering the effects of freestream turbulence. He provided a speculative correlation for the dependence of the laminar length on freestream turbulence. Further additions to the model of Horton were made by Roberts (1980). His prediction of the laminar shear length of the bubble accounted for turbulence intensity and length scale by means of Taylor’s turbulence factor. Adjustments were also made to the turbulent boundary layer properties at reattachment.

All the models discussed thus far considered the break down to turbulence to be at a fixed point. However, this contradicts even the data of Gaster (1967) who observed intermittent turbulent bursts in the shear layer of experiments conducted at low Reynolds numbers.

2.4.3 Transition in separation bubbles

An early attempt to model the transition process in separation bubbles on compressor blades was presented by Walker (1975). This model, again an adaptation of Horton’s model, allowed the transition process to begin in the attached boundary layer. It was considered that transition in the bubble was not controlled by the conditions at separation alone. Walker’s model did not include any effects of freestream turbulence, though his correlation was fitted to data from a range of turbulence intensities.

The conditions at reattachment measured by Walker disagreed with those predicted by Horton’s method. This was because the reattaching boundary layer was not yet fully turbulent.

Later work by the same author proposed a greatly reduced transition length in separation bubbles. Walker (1989) hypothesized that the transition length in an adverse pressure gradient (of which a separating flow is the worst case) will approximate the minimum possible transition length in forced transition. The zero pressure gradient transition length of Dhawan and Narasimha was reduced in proportion to Walkers minimum transition length obtained from an instability analysis. Using this modified transition length in the model of Chen and Thyson (1971), reasonable agreement was achieved between measured data and predictions from a viscous-inviscid coupling scheme on a low Reynolds number calculation of an isolated aerofoil.

Mayle (1991) analysed published data to arrive at a correlation for transition length in a separation bubble. Adopting a model like that of Horton, Mayle further divided the laminar region of the bubble into two regions. The unstable laminar shear layer was taken to begin at separation and terminate with the formation of spots and the transition region made up the remainder of the previously laminar region of the bubble. Mayle developed a correlation for each of these lengths. He further assumed that transition occurred mostly in the constant pressure region of the bubble and concluded that the correlation for zero pressure gradient attached flows could thus be used in separated flow transition. Walker (1993) pointed out that Mayle’s assumption that transition was complete by the end of the constant pressure region was inappropriate. Both the experimental results of Walker (1975) and the computational results of Walker et al (1988) showed that transition might only be complete after the time mean reattachment location.

Malkiel and Mayle (1995) conducted an experimental investigation into transition in the separated shear layer of a generic leading edge bubble at low turbulence levels. They detected Kelvin-Helmholtz waves shortly after separation. Both the frequency and wavelength of the measured disturbances was in good agreement with predictions from the stability analysis on a *tanh* velocity profile (Michalke, 1991), which was matched to the measured velocity profile just after separation.

Malkiel and Mayle further presented measurements of intermittency through the separated shear layer. These measurements showed good agreement with the universal intermittency distribution of Narasimha and yielded non-dimensional spot production rates of the order of those in strong adverse pressure gradients. Their measurements also served to confirm the correlation of transition length presented by Mayle (1991), which was based on intermittency distributions inferred from turbulence measurements.

A later study of separation bubble transition was conducted by Hatman and Wang (1998 a, b, c & d). Their study was of a more fundamental nature and included an extensive experimental program conducted on a flat plate at low turbulence levels. The experimental arrangement provided control over the relative transition and separation onset locations.

Hatman and Wang (1998 d) proposed a model for calculating separated flow transition based on their experimental observations and hypotheses. The calculation procedure consisted of a number of steps: firstly, separation onset was determined either from the established correlation of Thwaites ($\lambda_{\theta s} = -0.082$) or from a fourth order polynomial fit between K_s and Re_{xs}. The transition mode was then determined by comparing attached flow transition onset with separation location. If separation occurred in the laminar boundary layer then transition onset is taken as the location of maximum bubble height, which was found from a linear correlation of Re_{xMD} with Re_{xs}. However, if separation occurred in the transitional boundary layer then the onset location of attached flow transition was used. The reattachment location and mid transition point (maximum streamwise fluctuation) were found from correlations in terms of Re_{xs} depending on the bubble length. The end of transition was then determined either from the correlation of Cebeci (see Walker, 1989) or from a correlation of Re_{xT} and Re_{xs}.

The correlations presented by Hatman and Wang did not make use of traditional parameters. Reynolds numbers based on distance from separation and a local pressure gradient parameter rather than $Re_{\theta s}$ and $\lambda_{\theta s}$ were used. Motivation for their choice of parameters lay in the difficulty of determining θ in separated flow coupled with their hypothesis that the mechanism by which transition occurred in separated flows was the inviscid Kelvin-Helmholtz instability (Hatman and Wang, 1998 c). This assumption denies the physical significance of $Re_{\theta s}$ and $\lambda_{\theta s}$ in specifying the momentum deficit and pressure gradient which are responsible for boundary layer separation. However, it is reported that after separation a correlation based on Re_θ was no longer possible. The concern for inaccuracies in determining Re_θ is suspicious as traditional correlations relied on $Re_{\theta s}$, which would be free from inaccuracies associated with determining θ in a region of separated flow.

The data used by Hatman and Wang was from flat plate experiments at low turbulence levels. The correlations suffer in that they, like the correlations of Mayle (1991), are of a mathematical form that does not allow the bubble length or height to vanish continuously (Walker, 1993). In calculations with small or incipient separations, this may lead to the bubble appearing and disappearing in successive iterations thus preventing convergence of the solution.

Understanding of the transition mechanisms occurring in short laminar separation bubbles has been greatly enhanced by the direct numerical simulation of Alam and Sandham (2000). Their simulations of a flat plate with a Gaussian suction distribution imposed on the upper wall lead to a short laminar separation bubble. The natural transition process occurring in a separation bubble is by means of amplifying disturbances naturally occurring in the flow. These natural disturbances are absent from direct simulations and so disturbances were injected into the solution ahead of the separation point with a frequency unstable to both the laminar profile and the separated shear layer.

The transition region resulting from the applied disturbances was characterised by a series of staggered Λ-vortices as shown in Figure 2-6. The Λ-vortex shown in Figure 2-6 was observed to pump fluid away from the wall and thereby form a shear layer above the Λ-vortex. This shear layer subsequently rolled up into a series of smaller vortices perpendicular to the original, which then decays. This process of vortex stretching provides a mechanism for the cascade of vortices to smaller scales.

2.4.4 Unsteady effects on separation bubbles

Separation bubbles are inherently unsteady structures and as such, no truly steady bubbles exist. At best, the time mean structure of a bubble may be steady. Besides the DNS of Alam and Sandham (2000), all the studies presented thus far have considered only steady bubble models. In turbomachines, however, the flow is far from steady. In particular, the passage of wakes shed from upstream blade rows makes the flow highly turbulent and unsteady. In such an environment, steady analyses of separated flow and its transition are highly simplified.

The time scales associated with the re-establishment of a separation bubble are of a similar order to the time scale of the disturbances (Schulte, 1995). The re-establishment of the bubble is thus a truly unsteady process. Schulte (1995) has shown that wake passing causes periodic suppression of the bubble. His measurements showed the high turbulence intensity of the wake induces transition in the attached boundary layer at a location upstream of separation. The fuller turbulent or calmed velocity profiles, which result, are able to withstand greater adverse pressure gradients and thus the boundary layer remains attached. As the influence of the wake decays, and the velocity profiles return to their undisturbed state, the separation bubble re-establishes. Further observations from the experimental results of Schulte (1995) show that the length of the bubble initially grows at a rate governed by the trailing edge of the calmed region. However, the mechanism controlling the re-establishment and growth of the bubble is not fully understood.

Howell (1999) investigated the interaction of an artificial turbulent spot with a separation bubble formed on a flat plate. The spots were generated at a similar location and frequency as they would have been if they had been formed by a passing wake. In the early laminar region of the bubble, the arrival of the artificial disturbance caused the boundary layer profile to become attached. The period of influence of the perturbation was however short and the profile was separated again within 13% of the spot passing period. Further downstream in the bubble, where the amplification of disturbance in the free shear layer caused a fully developed turbulent spot, the duration of the calmed effects increased to *45%* of the period.

D’Ovidio et al (2001 a) performed a study similar to that of Howell (1999), and generated artificial disturbances in the decelerated boundary layer of a flat plate. The aim of their investigation was to determine the propagation of turbulent spots in highly decelerated boundary layers. For the case of a laminar separation bubble, the artificial disturbance first formed a wave packet. The wave packet grew as it propagated and subsequently formed a turbulent spot. However, the turbulent spot was preceded by wave packet activity showing a strong link to natural transition phenomena in highly decelerated flows. Regions of calmed flow were reported to follow not only the turbulent spots, but also the wave packets. This had not previously been observed. By increasing the Reynolds number, the flow structure changed and the steady flow exhibited incipient separation. Artificial spots generated in this flow were found to form turbulent spots more rapidly than for the laminar separation case and the wave packet activity preceding the turbulent spot was less pronounced.

The investigation of Howell (1999) and D’Ovidio et al (2001 a) studied the effect of artificial disturbances on separated boundary layers. The approach of Lou and Hourmouziadis (2000) differed in that the unsteadiness was introduced by a sinusoidal perturbation to the freestream. Their investigation was conducted on a flat plate with a short laminar separation bubble and the unsteady freestream perturbation was introduced by a rotating throttle downstream of the test section in their suction wind tunnel. A sample of their unsteady results is reproduced in Figure 2-7. Upstream of the separation bubble (A) the velocity shows the sinusoidal velocity oscillation with no turbulent fluctuations. However, along the separated shear layer regions of instability waves evolve just prior to the minimum velocity in the cycle (B). The packets of instability waves grow in amplitude and occupy an increasing portion of the cycle (B – E) until the velocity signals are turbulent throughout the cycle after the time mean reattachment location (F). The ‘dead air’ region of the separation bubble is characterised by intermittently turbulent flow with velocity traces similar to what would be expected for the passing of turbulent spots.

A phase shift was identified between the freestream and boundary layer fluid. The phase shift was reported to reduce with reducing Strouhal number showing a slower response to higher frequencies as expected from the analysis of Lin (1957) for attached boundary layers. Lou and Hourmouziadis (2000) report that the separation location does not change through the wake passing cycle, however, few details of the measurement grid are presented and it is impossible to deduce the resolution of their measurements about the separation location. However, the transition onset and reattachment locations as well as the size of the bubble were found to vary with the freestream oscillation. Unlike the attached boundary layer with an oscillating freestream as investigated by Obremski and Fejer (1967), there is no phase of the cycle in which laminar flow was measured downstream of turbulent flow.

2.4.5 Unsteady transition with separated boundary layers

A hypothetical description of the unsteady transition process involving the interaction of wakes and separation bubbles was presented by Schulte (1995). Considering a space time view of the process he mapped transition onset location as all points having combinations of Re_θ, λ_θ, and turbulence that instantaneously satisfy a relevant transition onset correlation.

Based on experimental observations, Schulte postulated that the boundary layer separated when the influence of the calmed region ceased. It was initially assumed that the re-establishment of the separation bubble was controlled by the trailing edge of the calmed region[6]. After a certain critical bubble length was achieved, transition was assumed to occur in the separated shear layer. After this initial transition, the transition onset location in the bubble and the resulting reattachment location are governed by the currently unknown physics of the re-establishing bubble. The growth of the bubble continues under the influence of these unknown mechanisms until it reaches its natural size. The bubble then retains its “steady” features until being suppressed by the next wake cycle.

This model is implemented in the calculations of Howell (1999). The unsteady intermittency was calculated by the code of Schulte and Hodson (1999) and was used to modify the eddy viscosity in the algebraic turbulence model as described by Addison and Hodson (1992). The calculations of Howell (1999) highlighted shortfalls of current transition modelling in separated flows. He showed that by modifying the damping factor in the algebraic turbulence model reasonable agreement between measurements and calculations could be achieved. However, no suitable explanation for the success of this approach was provided.

2.4.6 Comments on separation bubble literature

Much of the experimentation conducted on separation bubbles has been performed at conditions more representative of external aerodynamics than of

---

[6] During this portion of the cycle, there is no transition in the separated region. No explanation is provided as to how the separated boundary layer reattaches during this phase.

turbomachinery environments. Low turbulence levels are typically used, and bubbles have typically been at the leading edge rather than on the rear surface as found in low-pressure turbines. Additionally little attention has been paid to measurements of the transition process in the shear layer with the only appropriate measurements being those of Malkiel and Mayle (1995).

The effects of wake passing on separation bubbles has been investigated by Schulte (1995) and Howell (1999) who highlighted the importance of the wake passing in reducing the losses as a result of suppressing the separation bubble. The re-establishment of the bubble and transition processes that occurs in the unsteady bubble and re-establishing bubble has not been investigated.

2.5 Concluding remarks

The body of literature concerning unsteady transition in turbomachines is growing rapidly, however, understanding of basic transition processes in engineering applications remains incomplete. The advent of direct simulations of simple turbulent and transitional processes promises to provide data of unprecedented resolution and detail, however the interpretation, understanding and translating of this data into practical engineering design correlations remains a challenge which must be based on an understanding of the fundamental physics governing the transition process.

This thesis seeks to unveil the dominant mechanisms that govern the transition process that results from the interaction of a turbulent wake and highly decelerated, separating, boundary layer. It does not intend to add to the list of transition correlations, but rather through a series of experimental investigations to describe the interaction mechanism thereby paving the way for future modelling efforts.

2.6 Figures

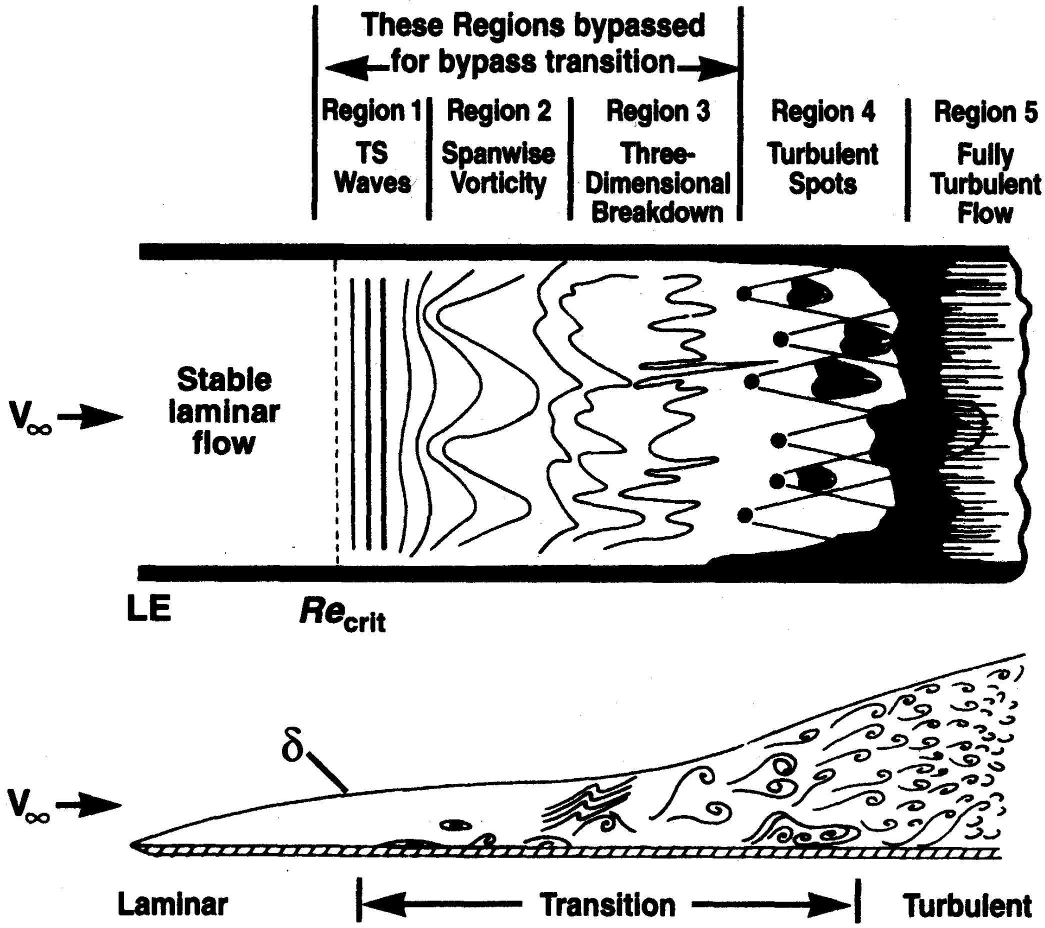

Figure 2-1: Natural boundary layer transition after White (1991)

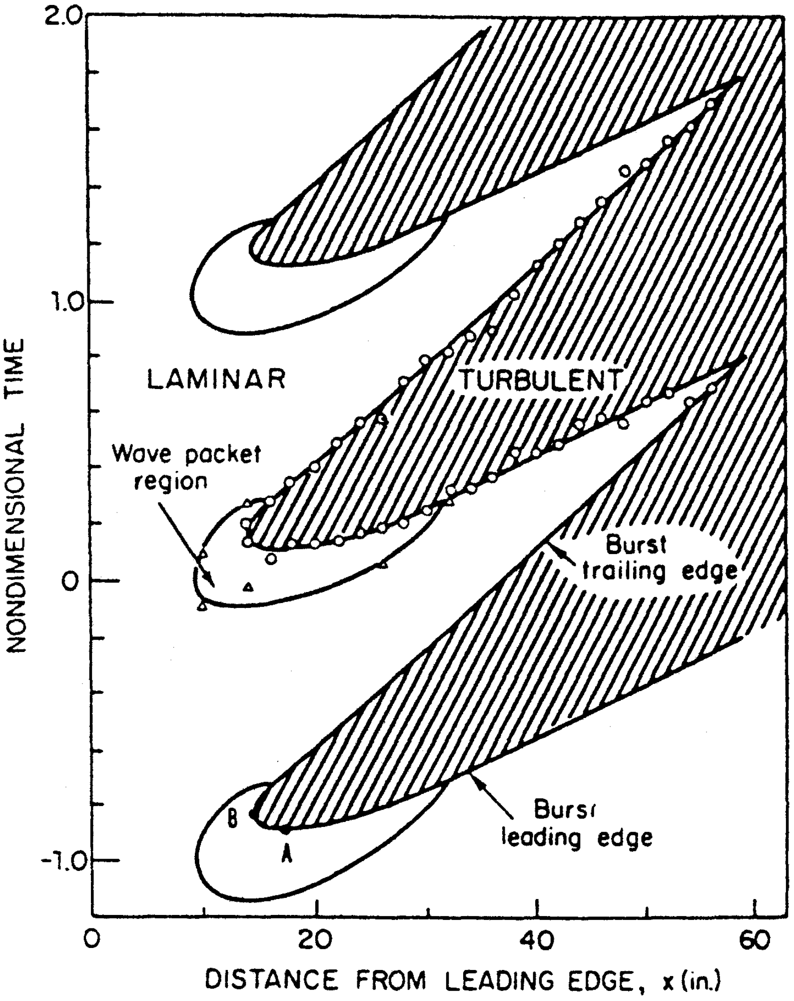

Figure 2-2: Unsteady natural transition process as depicted by Obremski and Morkovin (1969)

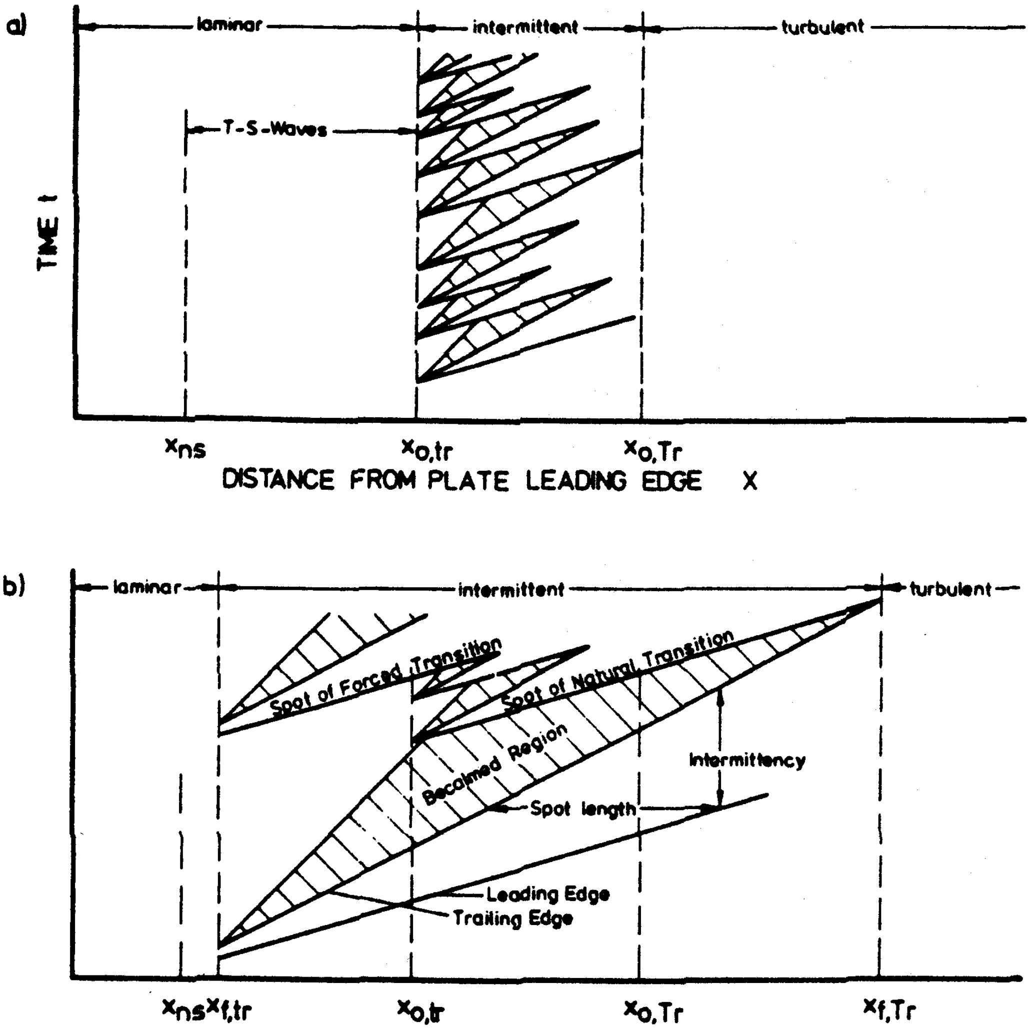

Figure 2-3: S-T description of steady flow transition and wake induced transition after Pfeil, Herbst and Schröder (1982)

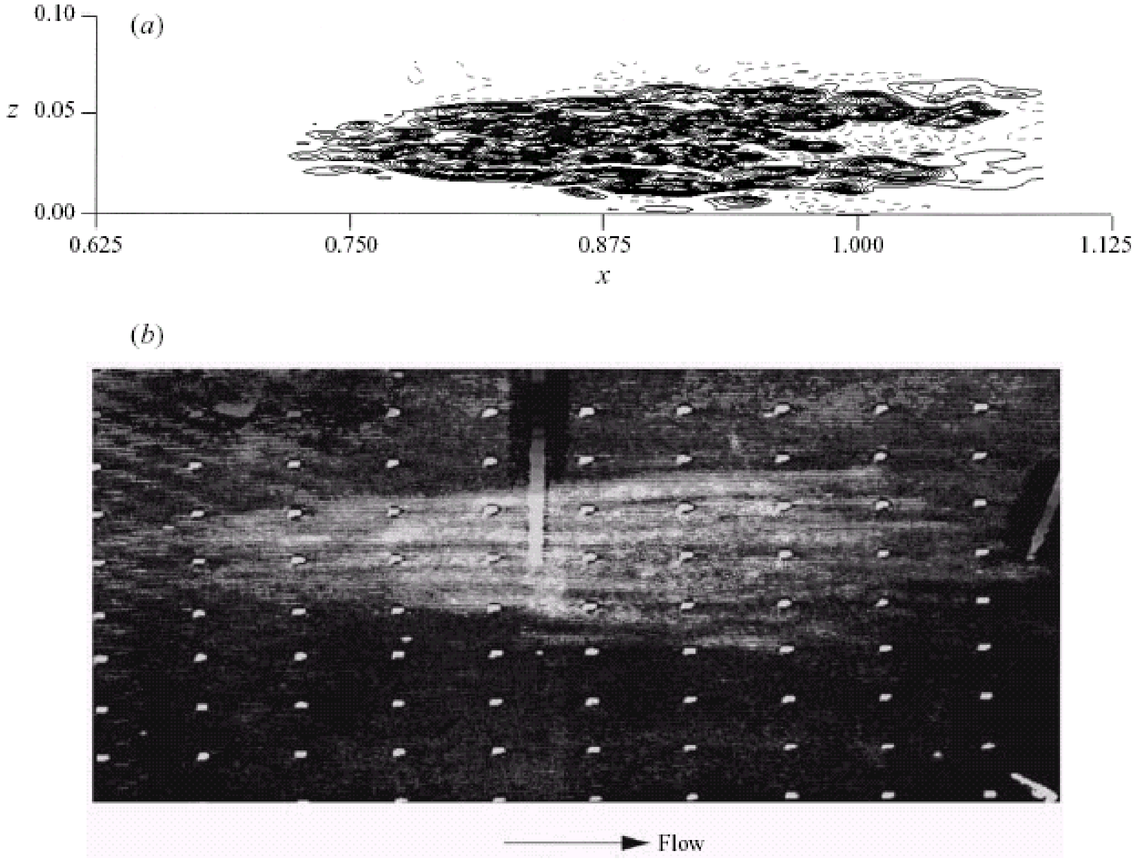

Figure 2-4: Visualisation of a wake induced turbulent spot. DNS calculations of Wu et al (1999) and liquid crystal visualisation of Zhong et al (1998)

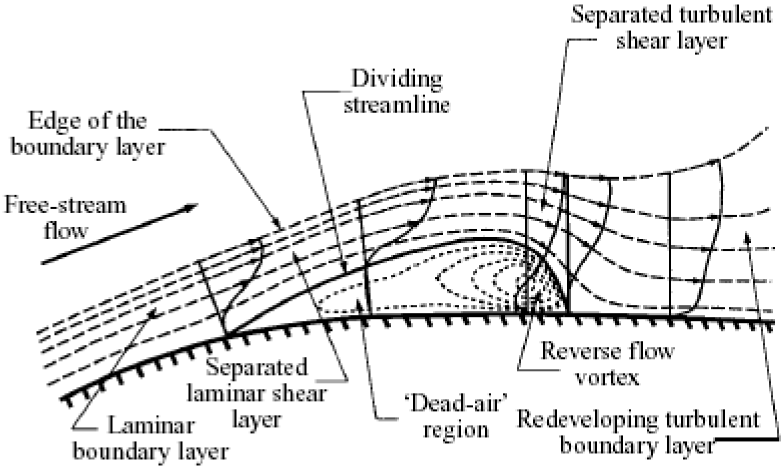

Figure 2-5: The time-average structure of a laminar separation bubble after Horton (1969)

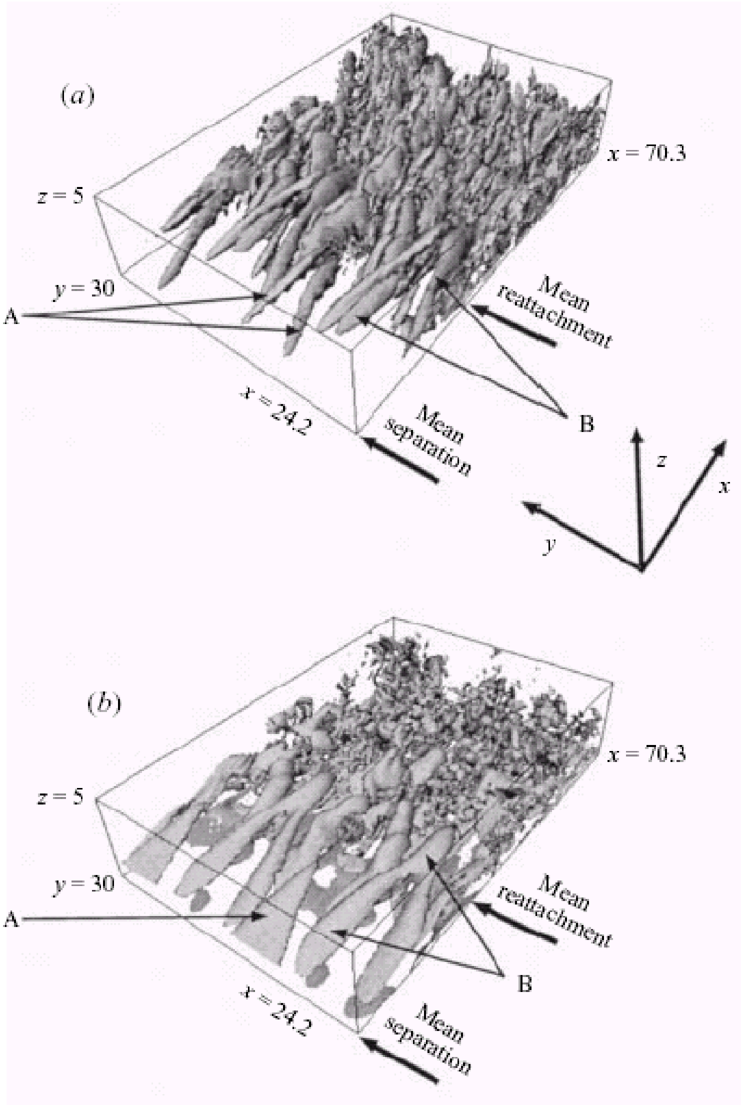

Figure 2-6: Detail of the natural transition mechanism as calculated by Alam and Sandham (2000) showing separated flow transition occurring by Λ-vortices

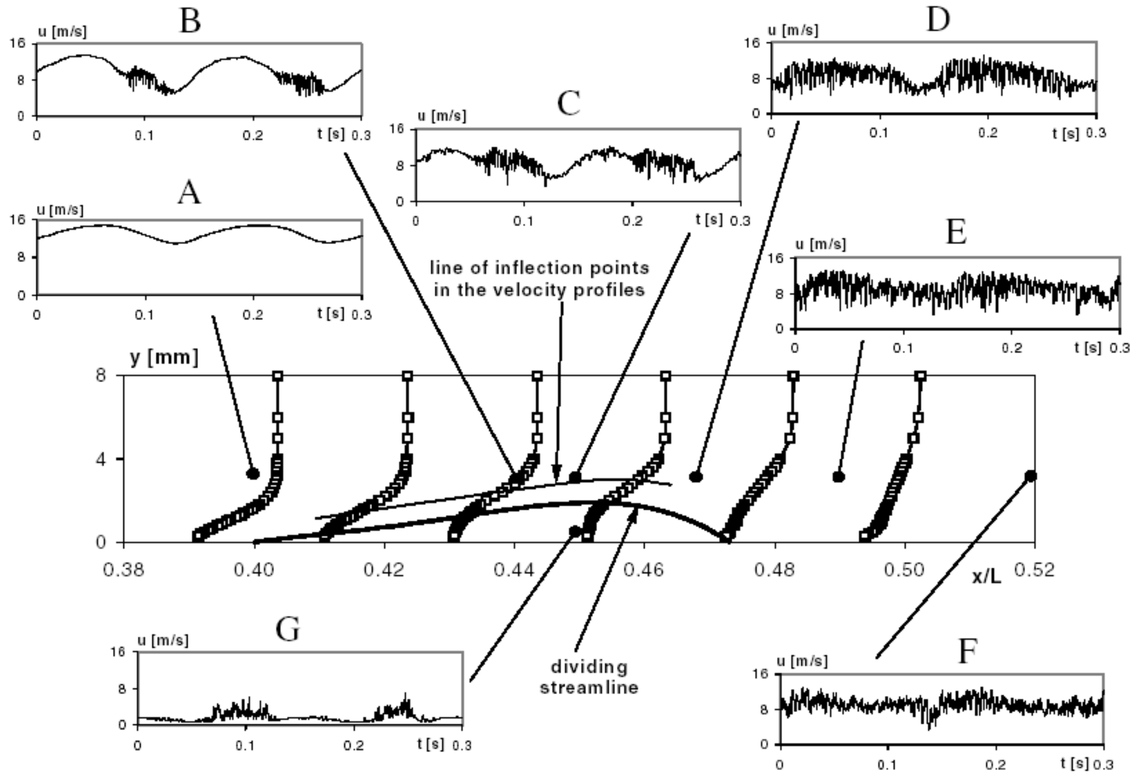

Figure 2-7: Velocity traces during the unsteady transition of a separation bubble. From Lou and Hourmouziadis (2000)

Chapter 3: Experimental Methods

3.1 Introduction

The experimental facilities, instrumentation and measurements techniques used in obtaining the experimental results presented in subsequent Chapters of this thesis are described here. Experimental work was performed on two experimental configurations. The first, a flat plate with an imposed pressure distribution and the second a low-pressure (LP) turbine cascade designated T106. Both these configurations were subjected to wakes shed from moving bar wake generators and were attached to an exit of the Duplex wind tunnel in the Whittle Laboratory of Cambridge University Engineering Department.

The data logging equipment is described together with details of the instrumentation. The measurements techniques used included conventional and fast-response static pressure measurements together with a single hot wire anemometer, a laser Doppler anemometer and a particle image velocimetry system.

3.2 Experimental facilities

3.2.1 Wind tunnel

The Duplex wind tunnel, sketched in Figure 3-1, is of an open return design and has two exits. Air is drawn in from the laboratory by a centrifugal fan. It then diffuses over a series of splitter plates into a constant area duct where it is diverted to one of the two exits. Each of the ducts contains a series of grids, gauzes and honeycombs to smooth and settle the flow before passing through a *3.7:1* area ratio contraction and discharging into the test section.

The centrifugal fan is driven by a *75 BHP* AC motor. Control of air speed is achieved by a combination of fan speed and inlet throttle position.

3.2.2 Bar passing flat plate

The experimental facility, shown in Figure 3-2, consists of an aluminium plate *545mm* long by *458mm* wide and *30mm* thick. A *8:3* ellipse was used for the leading edge and the trailing edge of the plate was blunt. A splitter plate *100mm* in length was attached to the centre of the trailing edge to suppress vortex shedding. The flat plate was mounted in a wooden box of constant span with a glass window to provide optical access for the LDA measurements. A pair of contoured walls was mounted in the box to impose a pressure distribution on the flat plate. A symmetrical arrangement was chosen to ensure zero incidence at the leading edge. The shape of the contoured walls was designed using a simple one-dimensional continuity argument to match the pressure distribution measured on the flat plate to that measured by Cicatelli (1998) on the T106 LP turbine cascade.

A moving bar wake generator was used to create unsteady wake passing conditions. Carbon fibre bars of *7.8mm* diameter were attached to a pair of reinforced nylon belts. The belts of the wake generator were driven by a speed controlled *2 HP* DC motor. The belts travelled on *4* sets of pulleys so that the bars passed across the inlet of the test section and then around the outside of a wooden box containing the flat plate and contoured end-walls. The return path of the bars was well downstream of the test section so that no downstream effect of the bar passing was generated. The bars passed *250mm* in front of the plate leading edge. As the bars passed across the inlet of the test section, they shed wakes, which convect over the flat plate and simulate the wake passing conditions in a turbomachine.

3.2.3 Bar passing cascade

The bar passing cascade facility, shown in Figure 3-3, is a cascade analogue of a multi-stage turbomachine. The facility has previously been described by Banieghbal et al (1995) and Schulte (1995).

The wakes shed from upstream blade rows in a real machine are simulated by an array of cylindrical bars moving across the inlet plane of the cascade. Pfeil and Eifler (1976) have shown that the far wake region of a cylindrical bar ($x/d>80$) is representative of the wakes in a real turbomachine. The bar passing cascade provides no means of representing the correct potential filed of adjacent blade rows.

The bars are held between two nylon belts that run on two sets pulleys. The pulley system is driven through a belt drive by a *2.0 HP* DC motor, the speed of which is manually controlled by a variac. The range of reduced frequencies that the rig is capable of simulating is limited by the positioning of the lugs on the nylon belts.

The configuration of the bar passing cascade required that the top and bottom walls of the cascade be slotted to permit the passage of wake generator bars (Figure 3-4). These slots provide two additional passages to the flow. The slot on the top wall does not present a problem, as it requires the flow to change direction, however, the slot on the bottom wall was more closely aligned with the flow. Moreover, the pressure gradient due to the incidence of the cascade forces flow out of the bottom slot. The result is an effective increase of incidence on the cascade and a non-uniform inlet static pressure. In order to minimise this problem and maintain inlet periodicity, an additional dummy passage was created on the suction side of the cascade as shown in Figure 3-4. This was achieved by adding a straight flap to the bottom wall. The throat of this dummy passage was then adjusted so that the combined throat of the end wall gap and the dummy passage matched that of one of the cascade passages. The flap of the dummy passage was set while monitoring the inlet static pressure and thereby ensuring periodicity. The periodicity of inlet static pressure was maintained within a *2.5%* range of inlet dynamic head.

3.2.4 T106 low pressure turbine cascade

The cascade investigated is designated T106. The profile is that of an aft-loaded low-pressure turbine blade. Blade co-ordinates together with blade static pressure tapping locations are presented in Appendix I. The cascade used consisted of *5* blades of chord *198mm*. Details of the cascade are presented in Table 3-1.

The bar passing conditions were chosen to represent a repeating stage of the T106 profile at *50%* reaction. The flow coefficient for this condition is $\phi=0.83$. The Reynolds number based on chord and exit velocity for the datum test case was $Re_{2C}=1.6\times10^5$.

Number of blades		5
Chord	[mm]	198
Axial chord	[mm]	170
Blade stagger	[°]	59.3
Pitch	[mm]	158
Span	[mm]	375
Suction surface length	[mm]	264.7
Pressure surface length	[mm]	230.0
Inlet flow angle	[°]	37.7
Design exit flow angle	[°]	63.2
Bar diameter	[mm]	2.05
Bar Pitch	[mm]	158 & 316
Axial distance: bars to LE	[mm]	70
Flow Coefficient ($\phi=V_x/U_b$)		0.83

Table 3-1: Specification of T106 cascade.

3.2.5 Artificial disturbance generator

Artificial disturbances were generated in the boundary layer of one of the T106 turbine blades by a puff of air emerging through a small hole in the blade surface. The disturbance generator, sketched in Figure 3-5, consisted of a signal generator, a 30*W* power amplifier and a *40W, 4Ω* loudspeaker attached to a sheet of Perspex as shown in the sketch. A stainless steel tube was mounted through the Perspex sheet so that when the diaphragm of the speaker moved a jet of air would be forced out of the tube. A PVC tube was used to connect the outlet of the disturbance generator to a *0.3mm* hole drilled in the surface of the turbine blade.

The disturbance generator was driven by a square wave of $5\mu s$ duration that was generated at the desired frequency by a Thandar TG503 Function generator. The jet emerging from the blade surface was sufficient to disturb the boundary layer.

3.3 Instrumentation

3.3.1 Data logging

All data logging was controlled by a PC running LabVIEW software. Voltages were acquired using a National Instruments PCI-MIO-16E-1 card, which consisted of a *12* bit A/D converter with a maximum throughput of *1.25 MS/s* multiplexed onto *16* analogue input channels. A National Instruments BNC 2090 connector panel was used to connect BNC cables to the data acquisition board.

The traverse gear consisted of Unislide traverse slides driven by McLennan stepper motors. The stepper motors were driven by Digiplan CD25 stepper motor drivers and controlled by a Digiplan IFX indexer system. The PC communicated with the Digiplan system by a RS232 serial network.

A Scanivalve DSA 3017 with $\pm 10\ inH_2O$ range was used to provide up to *16* simultaneous pressures measurements to monitor the experimental flow conditions. The PC communicated with the DSA over a network using TCP/IP communication.

Tunnel total temperature was logged with a total temperature probe and a T-type thermocouple. A Farnell DTT2 Digital Thermocouple Thermometer was used to precondition the thermocouple output. The PCI-MIO-16E-1 card measured the thermometer’s analogue output voltage. Atmospheric pressure was measured using a Druk DPI250 absolute pressure indicator the analogue output voltage was again logged by the PCI-MIO-16E-1 card. Bar passing speed was monitored with a reflective opto-switch. The frequency of bar passing was measured by the PCI-MIO-16E-1 card.

3.3.2 Pressure measurements

3.3.2.1 Conventional blade static pressure measurements

Blade static pressure measurements were made on both the flat plate and the T106 cascade. Conventional surface static pressure tappings were used. These consisted of *0.3mm* holes drilled normal to the blade surface. The pressure tappings were connected to a Scanivalve fluid switch by *1.0mm I.D.* PVC tubing. Pressures were measured using a Druck PDCR *22* pressure transducer with *37mbar g* range. The transducer output voltage was amplified before being measured by the PCI-MIO-16E-1 A/D card. Calibration of the transducer was performed against a Druck DPI520 ATE Pressure Controller. A simple linear calibration was deemed adequate.

Surface pressure distributions were non-dimensionalised by the isentropic exit dynamic head and where appropriate converted to surface velocity distributions according to

$$C_p = \frac{P_{01} - P}{P_{01} - P_{s2}} = \left(\frac{V}{V_{2is}} \right)^2 \qquad (3\text{-}1)$$

3.3.2.2 Unsteady blade surface pressure measurements

Conventional static pressure measurements provide only steady or time averaged information. In general, the large volume between the transducer and the pressure tapping prevents time accurate measurements being made. Moreover, it is atypical to use a fast response transducer in such applications. In order to resolve temporal fluctuations of pressure it is thus necessary not only to use a transducer with good frequency response, but also to mount the transducer so that the volume within the tapping is minimised.

The unsteady blade surface pressures were measured at mid span of the T106 cascade using Kulite XCS-062 ultra-miniature pressure transducers mounted flush with the blade surface. The suction surface of the T106 blade was instrumented at *21* locations. The diameter of the Kulite is *1.6 mm*, which is *0.6%* of the suction surface length. At each of these locations, the blade surface was drilled with a *1.95mm* hole. This was then back drilled and threaded. The transducer was mounted in a brass sheath, which was screwed into the holes in the blade until the transducer was flush with the surface as shown in Figure 3-6. Brass plugs were made for each of the unused tapping locations and were polished flush with the surface of the blade. Conventional static pressure tapings located at *25%* span and the same surface location were used to measure the mean pressure levels at each of the Kulite locations.

Up to four Kulite transducers were used simultaneously, each powered by a Fylde 492BBS bridge with *12V* excitation. The bridge output signals were amplified by Fylde 254GA amplifiers with a gain of *1000*. The voltage out of the amplifiers was measured by the PCI-MIO-16E-1. The input range was set to *±0.2V*. The Kulites were used to measure only the pressure fluctuations and not mean levels. It was thus possible to use a Fylde 294-OA auto-zero control unit to zero the bridge outputs before each acquisition thereby minimising thermal drift.

Calibration of the transducers, bridges and amplifiers of all four Kulites was performed simultaneously using the DPI520 as a common pressure source. The calibration thus included a calibration of the amplifiers and bridges. The response of the transducers and amplifiers was linear and, as the mean level was not required from the Kulites, only the slope of the calibration curve was retained. The system described above resulted in a sensitivity of approximately *500Pa/V* with a discretisation error of *0.05Pa*. Each measurement consists of *256* ensembles of *4096* points logged at *10Khz*.

The mean pressure level was measured using a Scanivalve DSA 3017 array with a ± 10 in H_2O range and 16-bit A/D. The discretisation error on this measurement is thus *1.0 Pa* which corresponds to *1.0%* exit dynamic head at $Re_{2C}=1.6\times 10^5$.

Processing of the resulting signals to achieve a pressure trace required the mean and fluctuating components of the signals to be combined. The fluctuating component was obtained by applying the linear calibration to each voltage ensemble. The mean level was then subtracted to provide a zero-mean pressure ensemble. These were then ensemble averaged before adding the mean level measured by the DSA to give the final ensemble averaged pressure trace. The results were non-dimensionalised by isentropic exit dynamic head to give the ensemble averaged pressure coefficient.

3.3.3 *Hot wire measurements*

Hot wire boundary layer traverses were performed on the T106 cascade using a Dantec 55P15 single wire boundary layer probe with $5\mu m \times 1mm$ tungsten element set to an overheat ratio of *1.8*. A Dantec 56C01 constant temperature anemometer was used in conjunction with a Dantec 56C17 bridge and a Dantec 55N22 signal-conditioning unit.

The raw unfiltered output of the anemometer was typically between *1.4V* and *2.5V*. This signal was logged by the PCI-MIO-16E-1 with a range of *0-5V* to provide a mean DC signal level. The AC component of the signal was obtained separately by band pass filtering the signal between *1Hz* and *10KHz*. The resulting signal was in the range *±0.5V* and was logged by the PCI-MIO-16E-1. The signal was then reconstructed by adding the DC level to the zero-mean filtered output thereby enhancing the signal resolution. The hot wire measurements presented in this thesis consists of *128* ensembles of AC data and *16* ensembles of DC data. Each ensemble consists of *4096* points logged at *10KHz*.

Positioning of the probe in the stream wise direction was performed manually. The location of the wall was then found by measuring the electrical contact between the probe[7] and the blade surface using a circuit as shown in Figure 3-7. To do this a voltage source was connected between the probe and the blade surface. With no contact, the full supply voltage was measured between the probe and the blade surface, whereas upon contact the measured output voltage was zero. The surface locating procedure was performed automatically by traversing the probe towards the surface in steps of *0.05mm* until the average measured voltage dropped to *90%* of the no-contact value. This location was then taken to be the blade surface. Probe and rig vibration were accounted for by performing the wall location procedure at the operating condition.

Calibration of the hot wire probes described above was performed in a suction calibration facility. In order to account for temperature drift effects the flow temperature was measured at each calibration point. Ten calibration points,

---

[7] In order to prevent damage to the probe the anemometer was switched off during this process. The wire element demonstrates greater strength when cold.

encompassing the velocities to be measured, were used in the calibration. A best-fit calibration for King's law was then found.

The correction of Cox (1957) was applied to the measured data to account for the effects of heat transfer to the metal surfaces. To achieve this a unique no-flow traverse was performed at each measurement location. The correction of Bearman (1971) was applied to account for drift in air temperature using the measured inlet flow temperature.

3.3.4 Laser Doppler anemometry

The Doppler effect is a frequency shift in radiation received from one body moving relative to another. Laser Doppler Anemometry (LDA) uses this effect to measure the velocity of particles suspended in a fluid. If the particles follow the fluid faithfully then the velocity of the particle is a reliable measure of the flow velocity.

For measurements of incompressible airflow, the Doppler effect is not used directly as the comparatively small velocity of the particles relative to that of the incident light means that the technique is insensitive. Rather, two coherent laser beams, typically from the same source, are focused to a common point. Particles passing through the intersection volume scatter light from each beam at a slightly different frequency due to the differences in angles of the incident light on the particle. The beat frequency[8] can then be used to find the velocity of the particle. The velocity measured by LDA is the component of velocity in the plane of the intersecting beams

The measurements reported in Chapter 4 of this thesis used a single component LDA system. However, upon the acquisition of a second component, the 2D system, consisting of two pairs of intersecting beams and two signal processors, was used. Two components of the velocity vector can thus be simultaneously measured when a particle passes the common intersection volume of the two pairs of beams.

The LDA system is sketched in Figure 3-8. Light was supplied by a *5W* Argon-Ion laser (Coherent Innova 70C). The transmitting optics consisted of a Dantec FibreFlow® unit incorporating a colour separator and Bragg cell. A 2D *85mm* Dantec

---

[8] The beat frequency is the interference frequency resulting from the difference in frequency between light scattered from the two beams.

probe was used with a *1.95* beam expender and a focal length of *500mm*. A backward scatter configuration was used and the receiving optics included a Dantec 55X35 colour separator and two Dantec 9057X0081 photo-multiplier tubes. Details of the optical system are presented in Table 3-2.

		Beam 1	Beam 2
Wavelength	[nm]	514.5	488
Focal length	[mm]	500	500
Beam Separation	[mm]	74.5	74.5
Intersection Angle	[°]	4.31	4.31
Beam Diameter	[mm]	2.2	2.2
Expander Ratio		1.95	1.95
dx	[mm]	0.077	0.073
dy	[mm]	0.076	0.072
dz	[mm]	1.016	0.963
Number of Fringes		22	22

Table 3-2: Optical parameters of LDA system.

The photo-multiplier outputs were processed by Dantec BSA signal processors (BSA Enhanced 57N21 Master for *514.5nm* and BSA Enhanced 57N35 Model S for *488nm*). The signal processor conducted a spectral analysis of the photo-multiplier input to detect the Doppler frequency and hence the particle velocity. Details of the operation of the BSA processor can be found in BSA Installation and User’s guide (Dantec, 1999). Data from the BSA was transferred to a PC by a GPIB interface. Control of the BSA and data acquisition was handled by the BSA Flow Software (Dantec).

Seeding of the flow was by means of smoke generated by a Dantec SPT smoke generator using Shell Ondina oil. The smoke was injected into the constant area section of the Duplex wind tunnel through the trailing edge of a streamlined injector tube. The point of injection was approximately *3m* upstream of the honeycomb and final screen of the wind tunnel. The effect of the injector on the flow was thus immaterial.

PDA measurements conducted by Williams (1999) showed the characteristic size of the smoke particles used to be $1.5\mu m$. Assuming the drag coefficient of the smoke particle is given by Stokes Law, Merzkirch (1974) shows the equation of motion for the particle to be

$$\frac{du_p}{dt} = \frac{18\mu_f (u_f - u_p)}{\rho_p d_p^{\ 2}} \tag{3-2}$$

Following the analysis of presented by Saathoff and Melbourne (1997), assuming a constant fluid velocity and the particle to be at rest initially, the step response of the particle to the flow can be found as

$$u_p = u_f (1 - e^{-t/\tau}) \tag{3-3}$$

where

$$\tau = \frac{\rho_p d_p^{\ 2}}{18\mu_f} \tag{3-4}$$

Using a conservative estimate of the particle density as the density of the oil ($\rho_p \approx 850kg/m^3$), the particle reaches *99.97%* of the fluid velocity in 8τ and will faithfully follow fluctuations up to *20KHz*.

Data was collected in Dead Time mode with a minimum interval between samples of *0.1ms*. At each traverse point a maximum of *100000* samples were collected in up to *60* seconds. This corresponded to a maximum of approximately *2500* wake passing cycles of the T106 cascade at datum test conditions. Data rates typically varied from *1.5* to *5Khz*. Two component measurements were made with both processors acting as coincidence masters. Final coincidence filtering was performed by software with a coincidence interval of *0.005ms* corresponding to twice the sample record length.

Unlike thermal anemometry techniques, LDA does not produce a continuous output signal because a velocity can only be measured when a seeding particle passes through the intersection volume of the two beams. This is an inherently random process. Furthermore, LDA statistics suffer from velocity bias. During periods of higher velocity, more samples are recorded due to a higher volume flow rate through the measurement volume. These samples have a shorter residence time, t_r, in the measurements volume. To remove this bias from resulting statistics a residence time weighting factor, η_i, defined as

$$\eta_i = \frac{t_{r\,i}}{\sum_{j=1}^{N} t_{r\,j}} \tag{3-5}$$

was employed (George, 1975). Ensemble averaging of the LDA data was performed by first dividing the wake passing period into a number of time bins (typically *128* were used). The weighting factor, mean, variance and cross moments were then assembled for each of these time bins according to

$$\bar{u} = \sum_{i=1}^{N} \eta_i u_i \tag{3-6}$$

$$\overline{u'^2} = \sum_{i=1}^{N} \eta_i (u_i - \bar{u})^2 \tag{3-7}$$

$$\overline{u'v'} = \sum_{i=1}^{N} \eta_i (u_i - \bar{u})(v_i - \bar{v}) \tag{3-8}$$

Positioning of the measuring volume in the stream-wise direction was performed manually. The location of the surface was then found in a manner similar to that described for the hot wire boundary layer measurements. The probe was traversed towards the surface in steps of *0.05mm*. The pedestal signal[9] of the BSA was then logged by the PCI-MIO-16E-1. The wall was identified as the position where the pedestal signal reached a peak value. This corresponds to the position where the photo-multiplier receives the most reflected light due to the measuring volume intersecting the wall. Locating the wall was performed with the laser at low power to prevent the anode limiter[10] from becoming active.

3.3.5 Digital particle image velocimetry

Particle image velocimetry (PIV) is essentially a quantitative flow visualisation technique. Two images of a seeded flow are captured at a known time interval. By tracking the movement of the seeding particles between the two images it is possible to calculate the velocity of the particles and from this, assuming that the particles faithfully follow the fluid, to measure the fluid velocity field.

---

[9] The pedestal signal is a low pass filtered version of the photo-multiplier signal available at a BNC connector on the front of the BSA signal processor.

[10] The anode limiter limits the current supplied to the photo-multiplier to prevent damage to the receiver. This is a hardware feature of the BSA

The digital PIV technique used here uses a digital video camera to acquire images of the seeded flow that is illuminated by a laser light sheet. Two lasers are used and their pulses are synchronised with the ‘shutter’ of the digital camera so that the laser pulses are captured by successive frames of the digital camera. This greatly reduces the time between images allowing higher speed flows to be captured.

A commercial TSI PIV system was used consisting of a pair of *50mJ* New Wave Nd-YAG lasers, a synchroniser and a Kodak digital camera with 1024×1024 CCD array. A *105mm* Nikon lens was used and zoomed to provide a *19.0mm* square field of view. The Nd-YAG laser light was transmitted to the light sheet optics through an articulated delivery arm. The light sheet was generated at the end of the articulated arm by a *25.4mm* focal length negative cylindrical lens and a *500mm* focal length spherical lens. This arrangement provided a light sheet between *0.5mm* and *1.5mm* thick on the blade surface, which was approximately *500mm* from the light sheet optic. The light sheet covered approximately half a blade passage.

The layout of the experiment is shown in the sketch of Figure 3-9. The light sheet was positioned downstream of the cascade pointing upstream and onto the rear portion of the suction surface. The position of the light sheet optic was chosen so that shadows from the returning bars of the wake generator were not present at the phases of interest. The light sheet optic was also positioned out of the main exit flow to minimise blockage effects. The camera was positioned to look parallel to the blade surface through the glass sidewall that was used for the LDA measurements.

The flow was seeded with a mist of groundnut oil generated by a pair of TSI Six-Jet Atomisers used in parallel. The seeding was introduced into the wind tunnel approximately *3m* upstream of the bar passing cascade, at the same point in the wind tunnel as the smoke used for the LDA.

The inter frame delay was set to $\Delta t=3\mu s$, which gave particle displacements in the range -3 to 6 pixels. The maximum data rate of the PIV system was *15Hz* so it was not possible to capture a sequence of images within one bar passing cycle. The acquisition of images was thus triggered. The trigger used for the LDA measurements was passed through a delay generator thereby allowing the PIV images to be acquired at different phases relative to the trigger.

Processing of the acquired image pairs was done with LaVision's DaVis V.6.03 software (LaVision, 2001)[11]. An adaptive multi-pass technique was used with the initial cell size of 64×64 pixels decreasing to a final cell size of 16×16 pixels with a spatial resolution of $304\mu m \times 304\mu m$. The final cells were overlapped by *50%* effectively increasing the data yield and giving a vector grid spacing of $152\mu m$.

---

[11] Processing of the acquired image pairs was not done by the author but by Mr D Hollis of Loughborough University. His assistance is gratefully acknowledged.

3.4 Figures

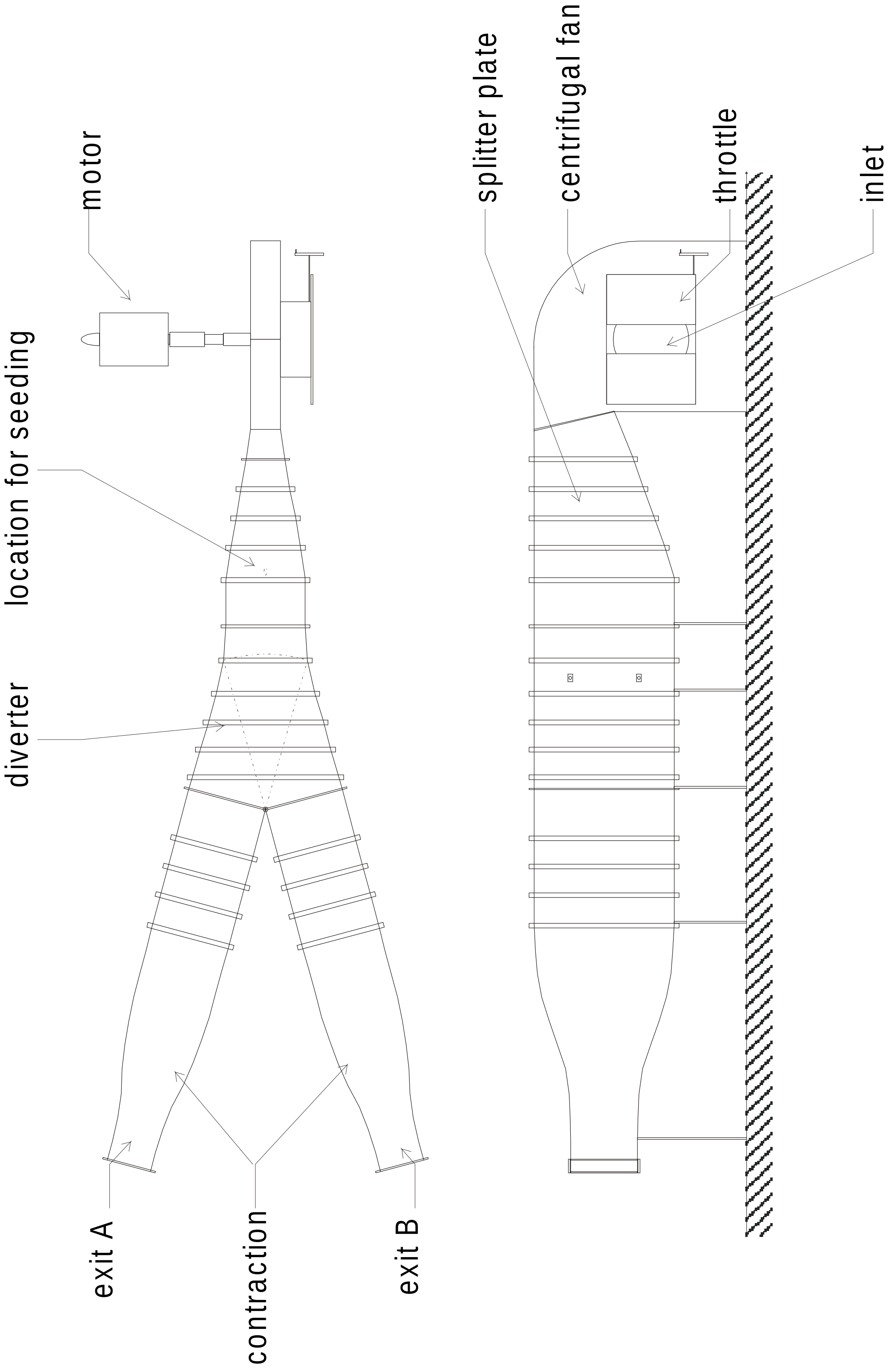

Figure 3-1: Duplex wind tunnel

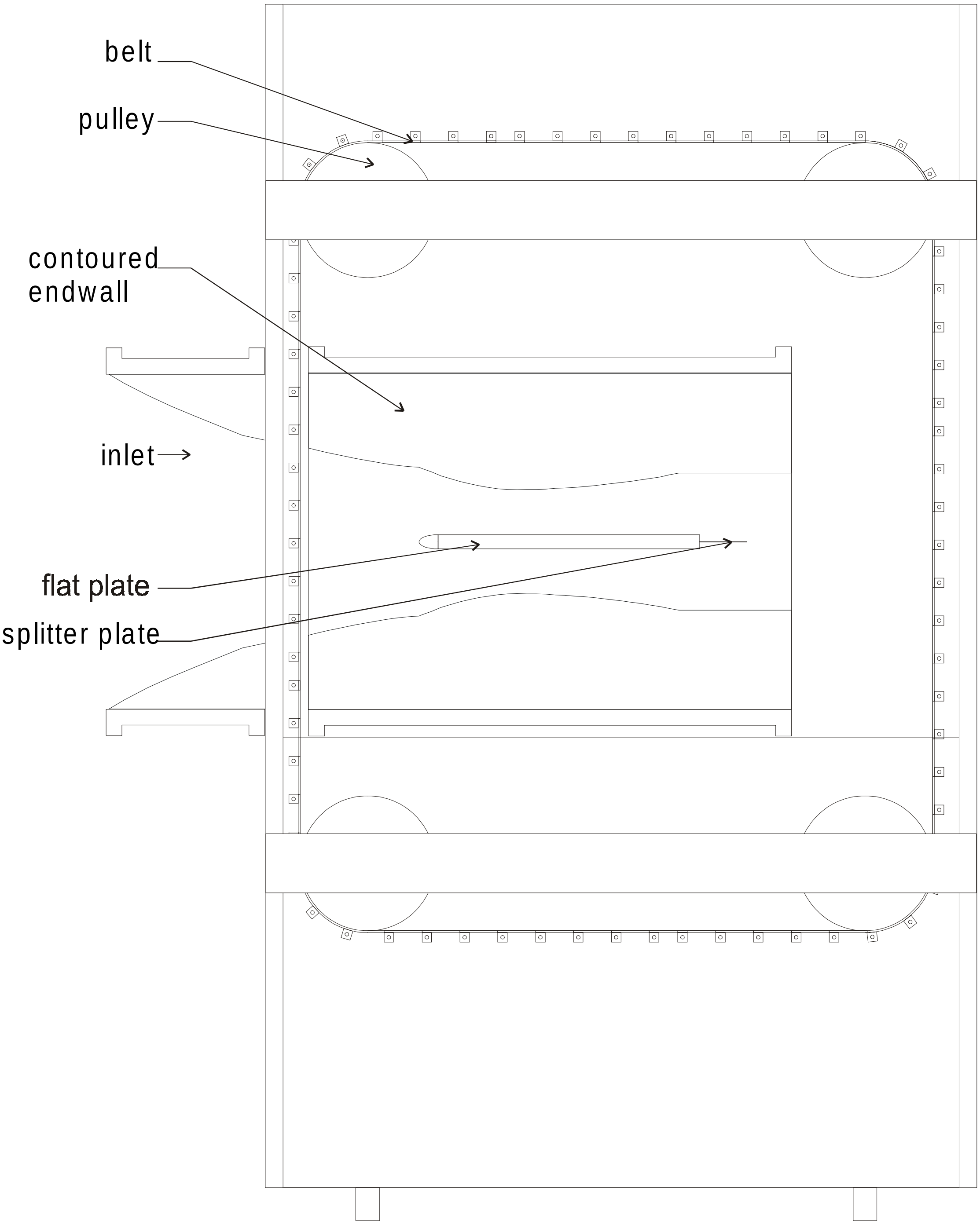

Figure 3-2: Flat Plate bar passing rig.

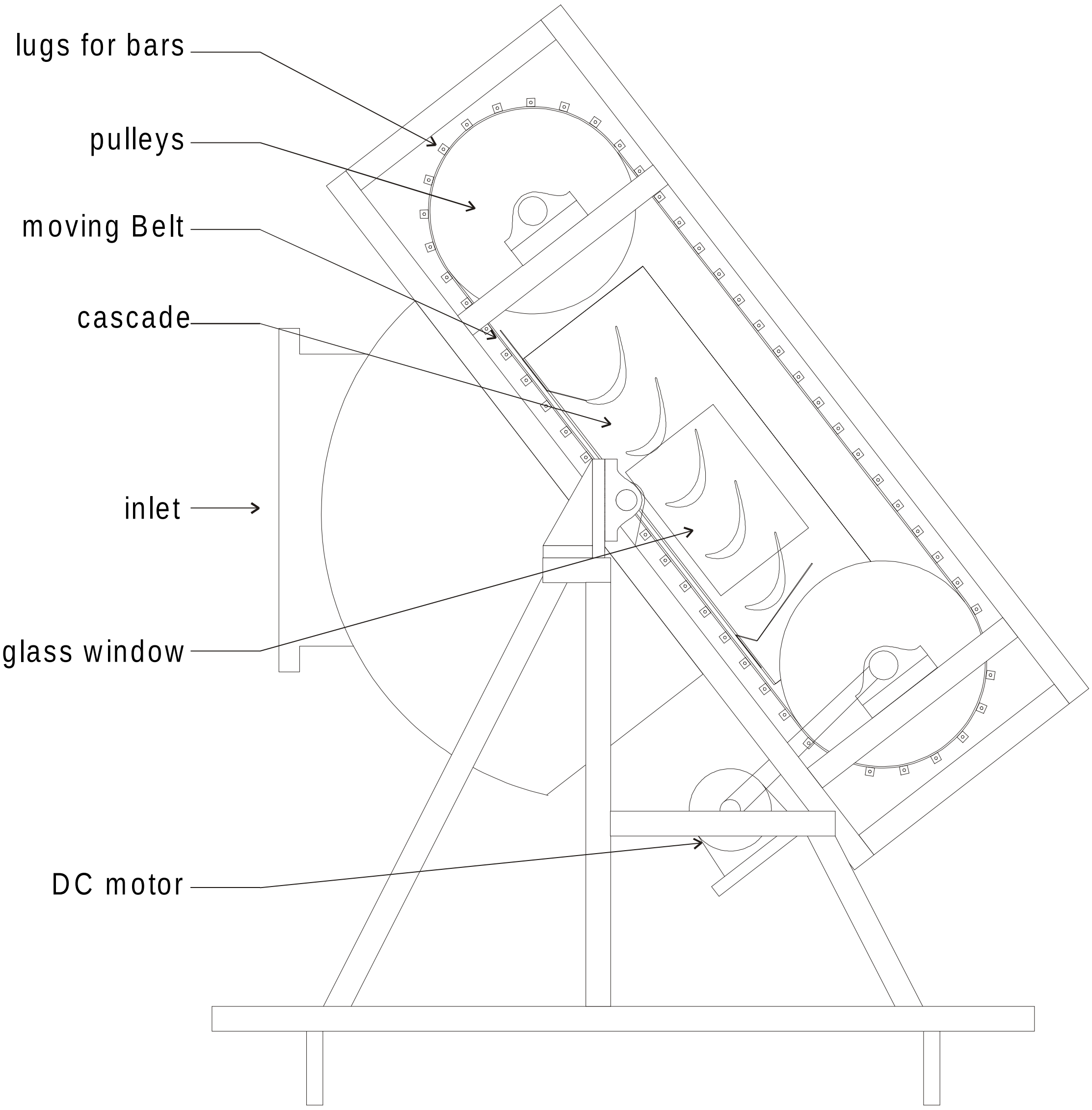

Figure 3-3: Bar passing cascade facility consisting of wake generator and cascade.

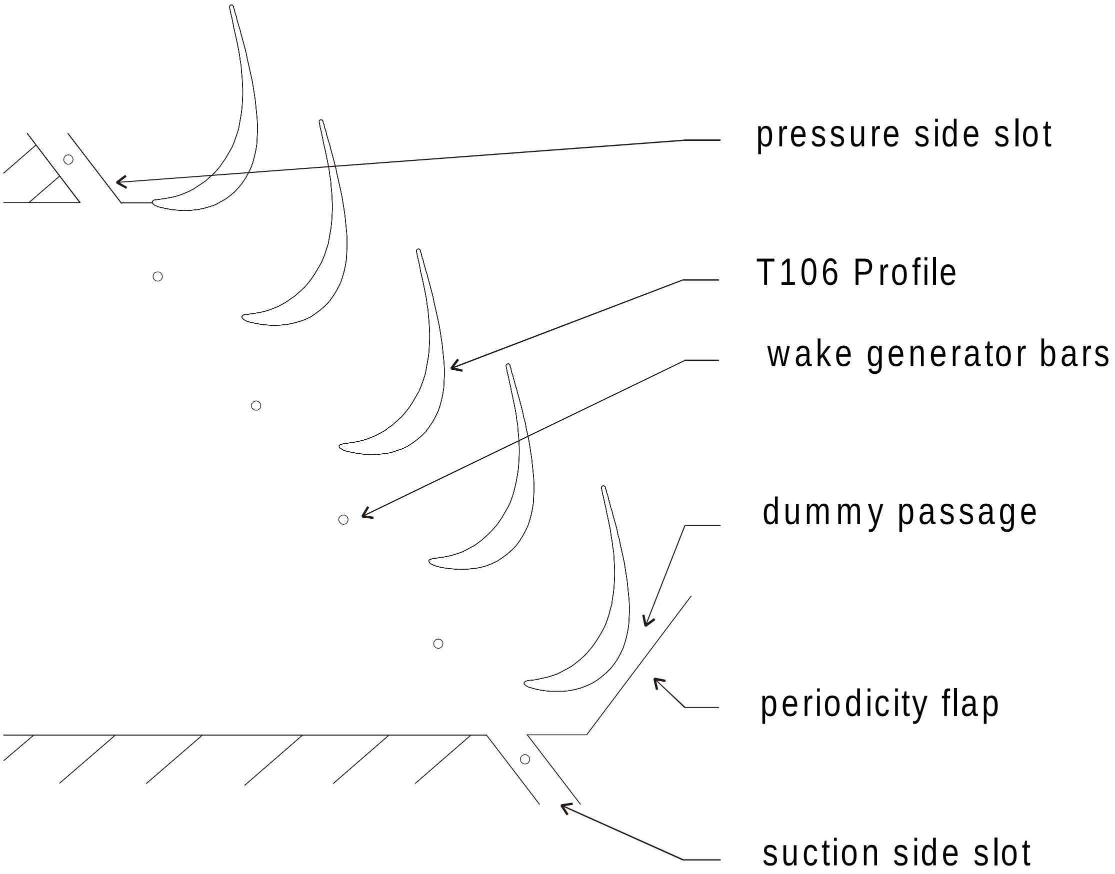

Figure 3-4: Detail of periodicity flap for bar passing cascade.

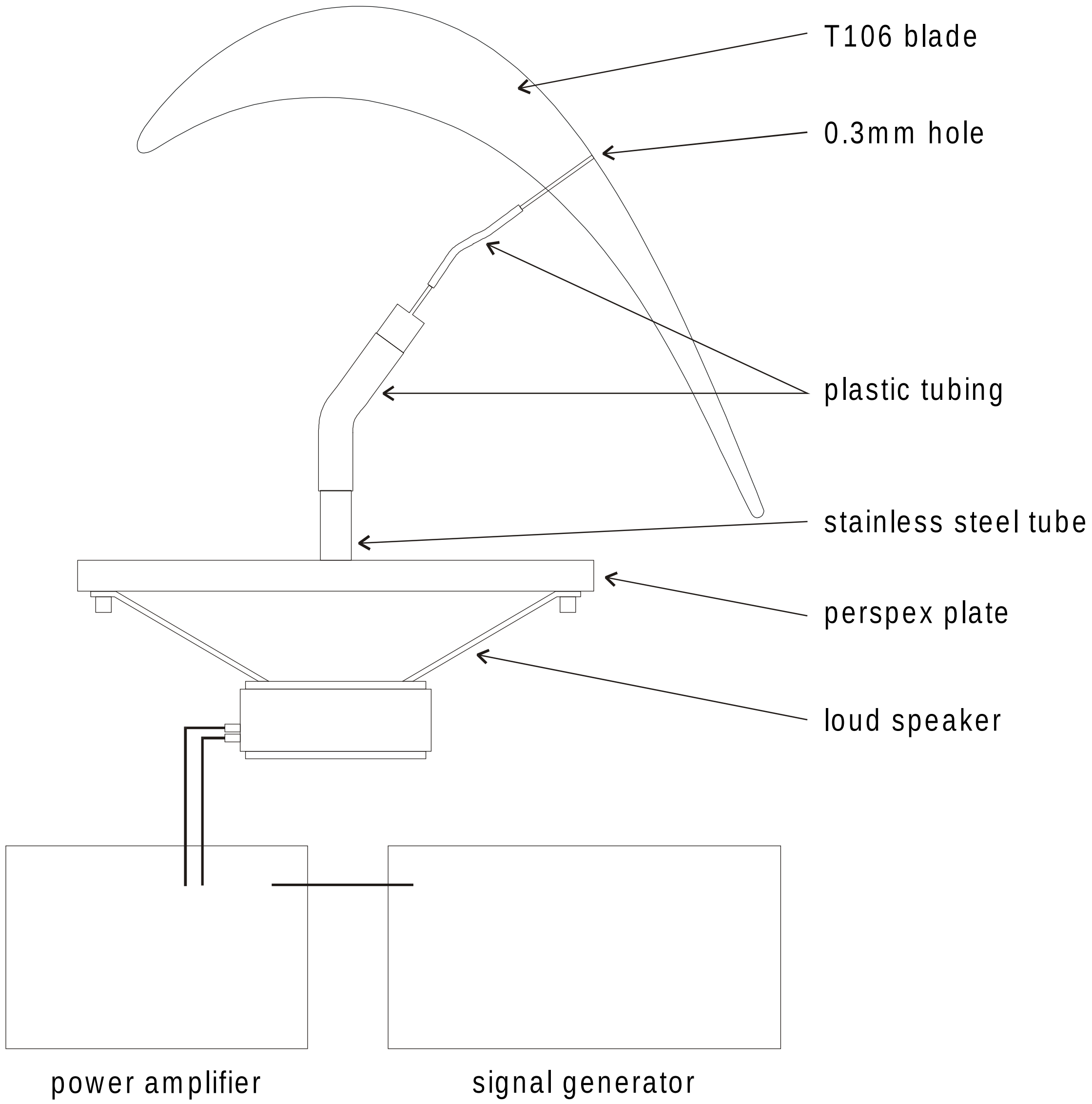

Figure 3-5: Artificial disturbance generator

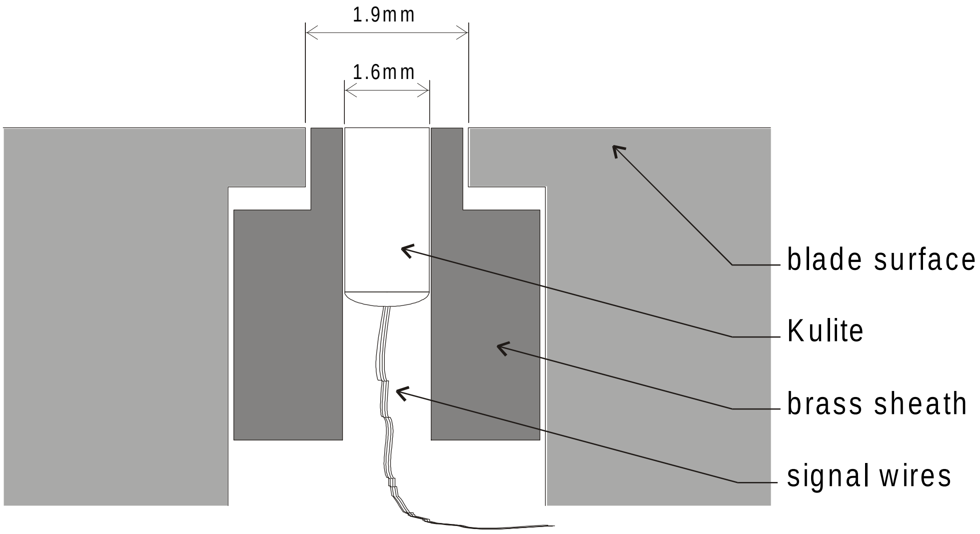

Figure 3-6: Mounting of Kulite pressure transducers.

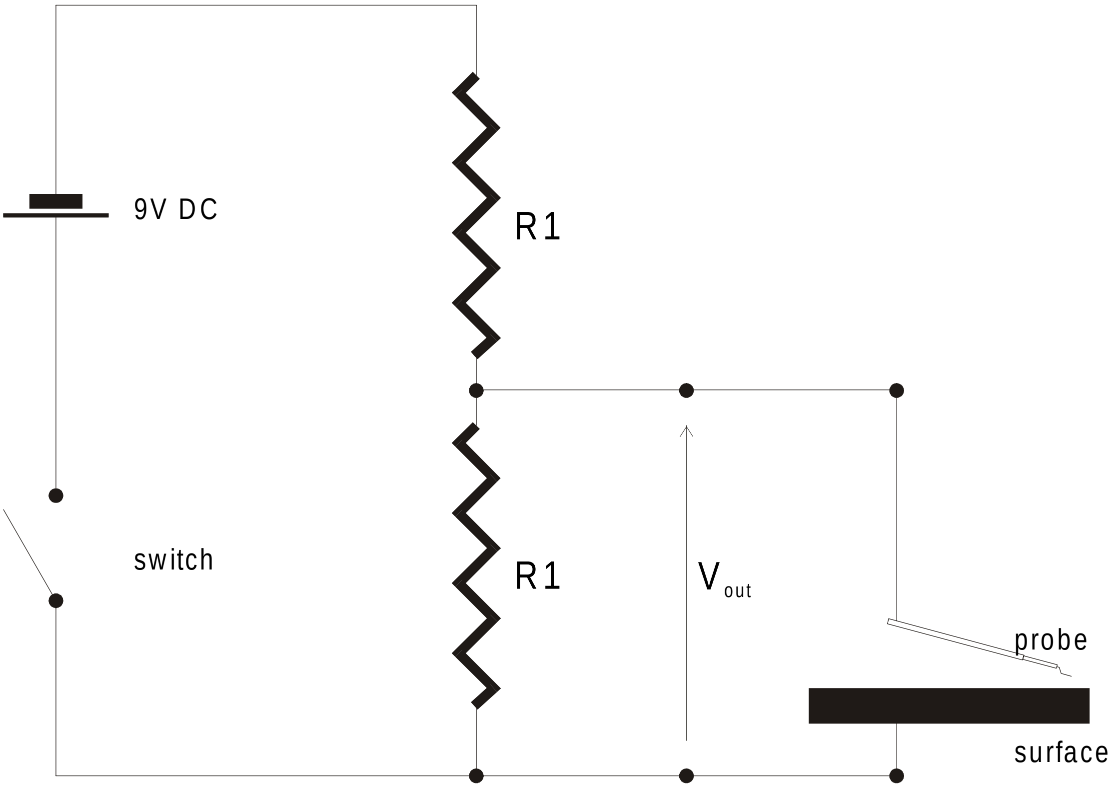

Figure 3-7: Circuit for measuring surface contact.

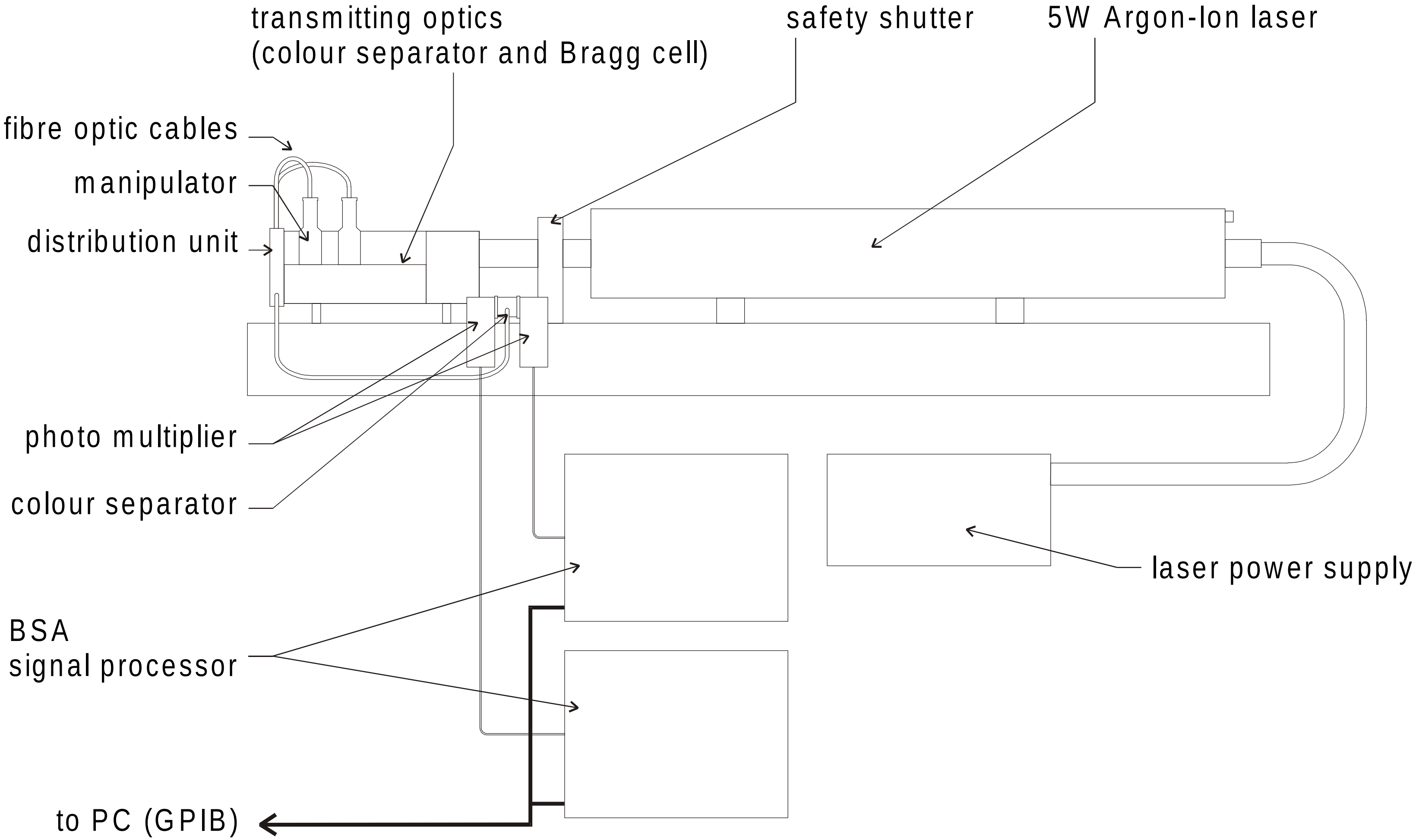

Figure 3-8: LDA system.

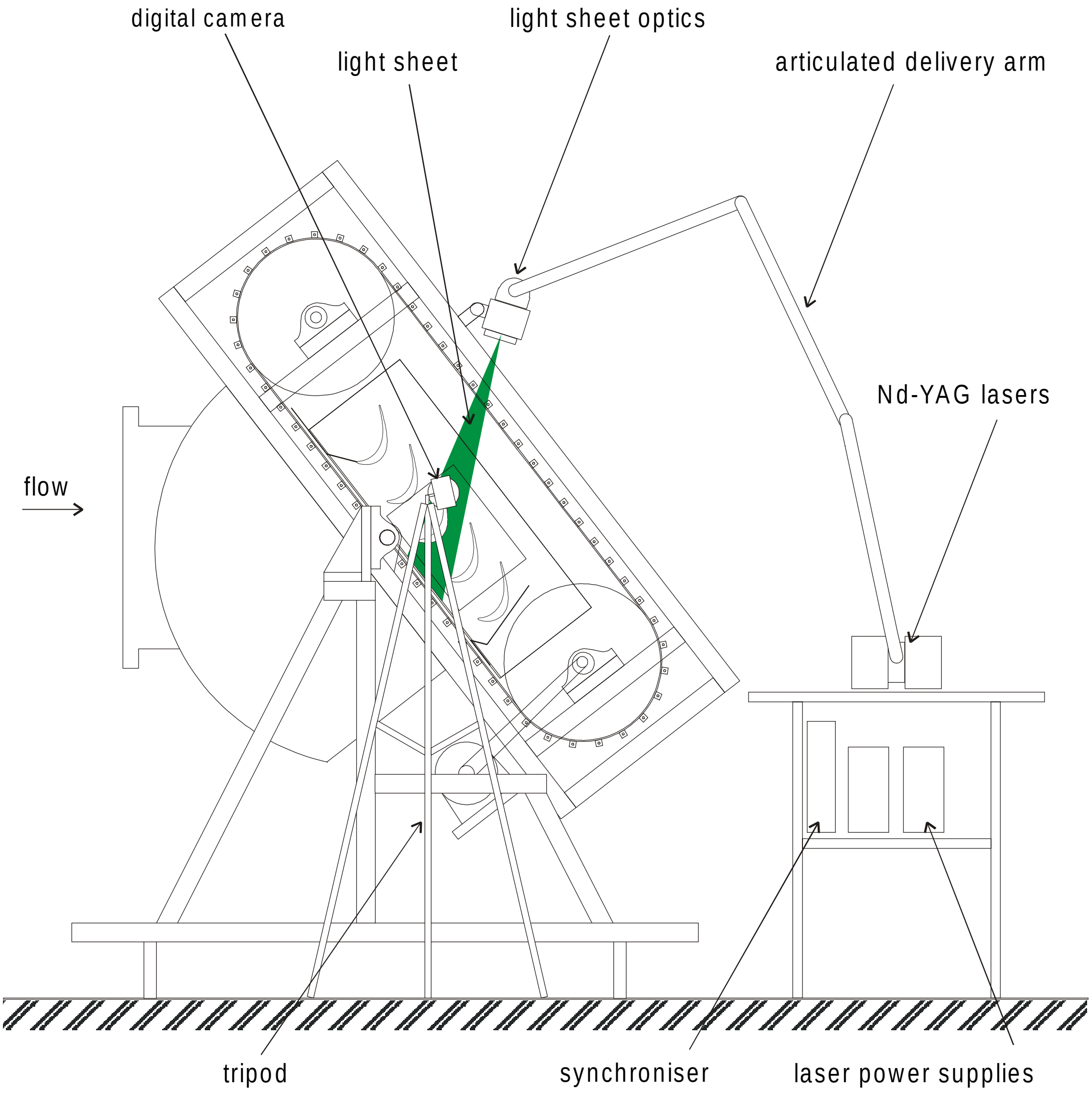

Figure 3-9: Layout of PIV experiment showing position of light sheet and came

Chapter 4: The interaction of wakes with the separating boundary layer on a flat plate

4.1 Introduction

This chapter presents ensemble averaged boundary layer measurements made using the rotated 1D LDA technique detailed in Appendix II. The measurements were performed on a flat plate subject to wakes from a moving bar wake generator. The pressure distribution on the flat plate was matched to that measured on the T106 LP turbine cascade.

This chapter first establishes the extent to which the flat plate is able to simulate the cascade boundary layer. Thereafter, the unsteady boundary layer results are presented in terms of space-time (S-T) diagrams of the integral boundary layer parameters. All such diagrams present one period of ensemble-averaged data copied onto two or three periods to aid interpretation. The S-T diagrams summarise the boundary layer measurements and allow a description of the boundary layer parameters as a function of both time and surface distance. The boundary layer measurements are then analysed to identify the transition mechanisms between wake passing events. The measured Reynolds stresses are also used to calculate the boundary layer dissipation allowing the loss generating and loss reducing mechanisms associated with unsteady transition to be identified.

Between wake passing events the boundary layer profiles slowly relax from their turbulent shape. The calmed region that follows the turbulent boundary layer gives way to a separating boundary layer under the influence of an adverse pressure gradient. The transition process that occurs during this stage of the wake passing cycle is identified to be by means of deterministic wave-like structures having a frequency that is characteristic of Tollmien-Schlichting waves. The measurements presented provide experimental evidence of ensemble-averaged natural transition phenomena arising in the unsteady wake-induced transition cycle.

The boundary layer dissipation is calculated from the measurements of Reynolds stresses and ensemble average velocity profiles. Previous claims of the benign character of the calmed region are supported. The calmed region is found to persist through the early stages of the separating boundary layer. Elevated levels of loss in the unsteady wake induced turbulent boundary layer were also measured. The measured dissipation coefficient provides an unprecedented description of the loss associated with the different phases of the wake separation bubble interaction from experimental data.

4.2 Experimental details

4.2.1 Matching flat plate and cascade boundary layers

The boundary layer that forms on the surface of a turbine blade is most strongly influenced by the velocity distribution along the blade surface and the balance of inertial to viscous forces as characterised by the Reynolds number. The effect of surface curvature on the blade boundary layer is to introduce wall normal pressure gradients, but these may be neglected if the boundary layer thickness is much smaller than the radius of curvature of the surface (White, 1991). This is indeed the case for LP turbine blades. Thus to reproduce the boundary layer of the turbine cascade on a flat plate it is necessary to match the Reynolds number of the flow and the surface velocity distribution.

The surface velocity distribution measured on a turbine blade results from the combined effect of changes in flow area and curvature as the flow is accelerated and turned by the blade row. Thus to reproduce a turbine blade velocity distribution on a flat plate, where there is no curvature, it is necessary to use variations in flow area. This may be achieved in practice by applying a simple one-dimensional continuity argument to vary the area between the flat plate and a contoured end wall and thus to achieve the desired velocity distribution. This simple argument, with no modifications for the effects of blockage due to the boundary layer growth or curvature of the upper wall, was used to design the shape of a pair of symmetrical end walls used to impose a pressure gradient on the flat plate described in Chapter 3. The validity of this method is confirmed by results presented in section 4.2.3 below.

4.2.2 Modelling the unsteady flow conditions for the flat plate

The flow in real turbomachines is unsteady with convected disturbances from upstream components and potential disturbances from both upstream and downstream. The predominant unsteady effects on the blade surface boundary layers are due to the convection of wakes shed from upstream blade rows. This unsteady interaction is termed a rotor-stator interaction and may be simulated in a cascade environment by a moving bar wake generator (Schulte (1995), Banieghbal et al (1995), Curtis et al (1996)).

The kinematics of the rotor-stator interaction is primarily governed by the velocity triangles and, according to Schulte and Hodson (1998), may be simulated in a cascade by matching the flow coefficient

$$\phi = \frac{V_x}{U_b} \tag{4-1}$$

In converting the geometry of a bar passing cascade experiment to a flat plate, it is not possible to correctly match the wake kinematics over the whole plate due to differences in the angle between the convecting wake and the plate surface. The symmetrical arrangement of the flat plate experiment also lacks the circulation due to the blade loading. However, the region of interest for this investigation is the rear of the suction surface where the separation bubble is located. In LP turbine blade profiles, this region has little curvature. Thus for the flat plate, the flow coefficient was based on bar speed and exit velocity and was chosen to be representative of a repeating stage of the T106 profile so that $\phi=0.83$.

The reduced frequency

$$f_r = \frac{fC}{V_{2is}} \tag{4-2}$$

is the ratio of the convection time scale ($t=C/V_{2is}$) to the wake passing time scale ($t=1/f$) and provides an indicator of the unsteadiness of the flow. This parameter must be matched if a representative flow is to be obtained. The matching of the boundary layer is achieved through the Reynolds number. This sets the flow velocity. Matching the flow coefficient then sets the bar speed. Thus to match the reduced frequency the remaining parameter to be set is the bar passing frequency which, for a given bar speed, is achieved by selecting the spacing between the bars.

Pfeil and Eifler (1976) showed that the far wake ($x/d>80$) of an aerofoil is almost the same as that of a cylindrical body having the same drag. The structure of the convected wake is thus matched by choosing the size of the bars. However, for the measurements reported here it was believed to be more important to match the turbulence levels at the leading edge of the flat plate to those measured by Howell

(1999) in the bar passing cascade. The bar diameter was therefore chosen using the relation suggested by Schlichting (1979)

$$Tu = \sqrt{\frac{857x}{d}} \tag{4-3}$$

A summary of the parameters chosen for the flat plate experiment is presented in Table 4-1.

		Flat Plate	Cascade
Re_{2s}		214000	214000
Suction surface length	[mm]	552.0	264.7
Chord	[mm]	546.0	170.0
Inlet flow angle	[°]	0.0	37.7
Design exit flow angle	[°]	0.0	63.2
Bar diameter	[mm]	7.8	2.0
Bar Pitch	[mm]	960.0	316.0
Axial distance: bars to LE	[mm]	245	70
Reduced frequency (f_r)		0.67	0.68
Flow Coefficient ($\phi = V_x/U$)		0.83	0.83

Table 4-1: Comparison of unsteady flow parameters for Flat Plate and T106 Cascade

4.2.3 Details of boundary layer measurements

The boundary layer measurements presented in this Chapter were made using the single component LDA system as described in Chapter 3. A novel technique, based on the method of Fujita and Kovasznay (1969), was developed to enable the measurement of the ensemble averaged 2D Reynolds stress tensor with a single component LDA. This was achieved by making measurements at multiple probe orientations. Details of this technique are given by Stieger and Hodson (2001) and are included in Appendix II. For the measurements presented here, *7* probe orientations were used ranging from *+45°* to *–45°* at intervals of *15°*.

The boundary layer was traversed at *13* locations evenly distributed along the blade surface between *50* and *94* % surface length. Each traverse consisted of *25* points exponentially distributed normal to the wall with the first point *0.1 mm* and the final point *25.0 mm* above the surface of the plate. The ensemble average of the randomly sampled LDA data was calculated as described in Chapter 3 using *128* time bins through the wake passing cycle.

4.2.4 Validation of the flat plate pressure distribution

Figure 4-1 compares the velocity distribution measured on the flat plate with steady inflow and bar passing to the measurements of Cicatelli et al (1998) for the T106 cascade with bar passing. From this it is apparent that for the case of bar passing, when the separation bubble is suppressed, excellent agreement was achieved between the flat plate and cascade velocity distributions. However, for the flat plate with steady inflow, agreement was only achieved up to the separation location and the velocity distribution in the separated region was not perfectly matched.

The discrepancies between the flat plate and cascade velocity distributions for steady inflow may be explained in terms of the differences in geometry between the two cases. The displacement thickness of attached boundary layers varies slowly with streamwise distance; however, upon separation there is a sharp increase in boundary layer thickness. It is impossible to accurately predict the boundary layer growth after separation. The increase in boundary layer thickness increases the boundary layer blockage. This accelerates the freestream flow due to the change in area. Differences between cascade and flat plate geometry do not allow the ratio of flow area to blockage from the separated boundary layer to be conserved. The feedback mechanisms responsible for the bubble formation are thus not reproduced. This may account for differences.

For the case with wake passing, the time mean pressure distribution measured on the flat plate was found to be in excellent agreement with that measured on the T106 cascade as shown in Figure 4-1. The improvement in agreement over the steady case is due to the periodic suppression of the separation bubble due to the wakes. This reduces the blockage effect responsible for discrepancies in the steady flow case.

4.2.5 Validation of flat plate boundary layer

Further validation, in this case using the steady pre-separation boundary layer, is presented in Figure 4-2. High levels of agreement were achieved between integral parameters calculated from boundary layer traverses and those calculated by the integral method of Thwaites (see White, 1991). The integral calculation was based on the velocity distribution measured with a tripped boundary layer to better approximate the inviscid pressure distribution. The method of Thwaites is inaccurate near and invalid beyond the point of laminar separation and for that reason the integration was not continued to the trailing edge.

4.3 Ensemble averaged measurements for wake boundary layer interaction

4.3.1 Unsteady freestream disturbance environment

The convection of a wake over an aerofoil surface has been described by Meyer (1958). His simplified model, known as the negative jet, describes the interaction of a moving wake with a blade surface. The flow is described as the superposition of a jet pointing towards the wake source (negative jet) on a uniform stream. As the wake convects with the freestream, it is chopped by the blade. The resulting wake segments behave as negative jets, which impinge on the blade suction surface. The effect of the impinging action at a fixed location is observed first as an acceleration of the boundary layer edge velocity as the wake approaches from upstream. This is due to the addition of the freestream and perturbation velocity components. After the centre of the wake passes, the perturbation component from the impinging jet changes direction. This causes the boundary layer edge velocity to decrease to a level below that of the undisturbed flow. As the wake continues to convect, the impingement effect reduces and the edge velocity returns to its undisturbed state.

The negative jet effect described above is evident in Figure 4-3. Here time traces of the measured boundary layer edge velocity[12] are plotted at several points along the surface of the flat plate. The vertical scale is non-dimensional surface distance at which the measurement was made. The amplitude of the traces is arbitrary but consistent from trance to trace. Prior to the arrival of the wake, the boundary layer edge velocity is seen to increase above the time mean value and after the passage of the wake velocity decreases below the time mean before recovering to its undisturbed level. This agrees with the above description of the negative jet.

The trajectory of the freestream flow is depicted in Figure 4-3 by lines *A* and *B*. These lines were calculated from the measured time-mean velocity distribution. The alignment of the peaks and troughs in the boundary layer edge velocities with these trajectory lines show that the wake is simply convected with the local freestream.

---

[12] The boundary layer edge is defined as the point where the ensemble average velocity is *98%* of the maximum measured ensemble averaged velocity in the boundary layer profile. The boundary layer edge velocity is the velocity at this point and the turbulence intensity at the boundary layer edge is the turbulence intensity at this point.

The time delay between the peak and the trough is indicative of the wake width. From Figure 4-3, it is apparent that the wake width is almost constant along the length of the flat plate in the current measurements.

The boundary layer edge turbulence intensity, based on the local boundary layer edge velocity, is plotted as an S-T diagram in Figure 4-4. Line *A* and line *B* from Figure 4-3 have been transferred onto this plot. It is apparent that the maximum turbulence level coincides with the center of the wake, a point approximately half way between line *A* and line *B*. Upstream of *60%* surface length the level of wake centre line turbulence is seen to reach levels of about *5%*. The undisturbed flow in the same region has turbulence levels as low as *0.5%*. After *65%* surface length, the turbulence level between wakes increases to levels of up to *3%*, however the dominant region of high turbulence is still confined to the wake centreline. A further region of high turbulence, labelled *C*, arises in the region following the wake and downstream of *65%* surface length. This is the result of boundary layer transition induced by the wake passing.

4.3.2 Response of the boundary layer through a wake passing cycle

Ensemble averaged velocity profiles measured at *76*% surface length are shown in Figure 4-5 and the boundary layer integral parameters calculated from the measured ensemble average profiles through the wake passing cycle are presented in Figure 4-6. The displacement thickness, δ^*, momentum thickness, θ, and Blackwelder thickness, δ', which is a measure of the turbulence in the boundary layer, were calculated according to

$$\left\langle \delta^* \right\rangle = \int_{y=0}^{\langle \delta_{98} \rangle} \left(1 - \left\langle \frac{u(y)}{U_\infty} \right\rangle \right) dy \tag{4-4}$$

$$\left\langle \theta \right\rangle = \int_{y=0}^{\langle \delta_{98} \rangle} \left\langle \frac{u(y)}{U_\infty} \right\rangle \left(1 - \left\langle \frac{u(y)}{U_\infty} \right\rangle \right) dy \tag{4-5}$$

$$\left\langle \delta' \right\rangle = \frac{1}{\left\langle U_{98} \right\rangle^2} \int_{y=0}^{\delta_{98}} \tfrac{1}{2} \left(\left\langle u'^2 \right\rangle + \left\langle v'^2 \right\rangle \right) dy \tag{4-6}$$

The eight profiles of Figure 4-5 are equally spaced through one wake passing cycle and their positions in the cycle are marked on Figure 4-6.

Profile *1* of Figure 4-6 corresponds to a turbulent profile that results from wake-induced transition. The relaxation of this turbulent profile, to a laminar state, under an adverse pressure gradient, is shown by the sequence of profiles *2* through *6*. After the passage of the wake, the turbulence in the boundary layer decays. This is indicated by the drop of the Blackwelder parameter, δ', between positions *1* and *3*. The unsteady response of the boundary layer results in calmed profiles of which *3* is a typical example.

At *76* % surface length, there is an adverse pressure gradient sufficient to cause laminar separation. The profiles *4* to *6* show the thickening of the boundary layer profile as the near wall fluid slows down under the combined effect of viscosity and pressure gradient. The profiles become progressively more inflexional and the change in the boundary layer shape is accompanied by a more rapid increase in δ^* than θ. This results in an increase in the shape factor to levels approaching *3.5* indicative of a laminar separation for steady flow.

The effect of the negative jet on the boundary layer is evident from the fluctuation in boundary layer edge velocity. The trace at *76%* surface length in Figure 4-3 is repeated in Figure 4-6 for reference. The dashed line drawn through the maximum edge velocity in Figure 4-6 corresponds to the dashed profile in Figure 4-5. Similarly, the dash-dot lines are for the minimum edge velocity. A comparison of these two profiles in Figure 4-5 shows that the negative jet penetrates the outer *90%* of the boundary layer.

At the centre of the wake, midway between the dashed and dash-dot lines, the displacement and momentum thickness begin to increase rapidly. This is a result of the wake-induced transition. Finally, profile *8* is the result of this transition process. It is characterised by a rapidly decreasing shape factor with rapidly rising momentum and displacement thickness. The turbulence intensity in the boundary layer is also increasing at this point as indicated by δ'.

4.3.3 Space Time description of boundary layer state

The shape factor (H_{12}) gives a clear characterisation of the boundary layer profile and is a measure of the boundary layer state. Turbulent boundary layer profiles are fuller than laminar profiles and so typically have lower values of shape factor. Laminar profiles have shape factors ranging from *2.6* for a Blasius profile to approximately *3.5* at separation. In steady flow, there is a unique relationship between shape factor and pressure gradient parameter λ_θ as highlighted in the integral method of Thwaites. In steady flow, a zero pressure gradient turbulent boundary layer has a shape factor of 1.3. As in the case of laminar boundary layers, the shape factor is a function of the pressure gradient. The literature suggests that turbulent separation occurs over a wide range of shape factors from *1.8* to *2.4* (Schlichting, 1979).

In order to identify the ensemble average boundary layer state in time and space an S-T diagram of H_{12} is plotted in Figure 4-7. In addition to lines *A* and *B* showing the trajectory of the wake (copied from Figure 4-4) are lines showing the trajectory of the leading edge of the turbulent spots (line *D*), the trajectory of the trailing edge of turbulent spots (line *E*) and the trajectory of the trailing edge of the calmed region (line *F*). The celerities of lines *D*, *E* and *F* were calculated from measured time average boundary layer integral parameters and the correlation of Gostelow et al (1996). The lines were then calculated from the time averaged boundary layer edge velocity and the calculated celerities.

The region of low shape factor bounded by lines *D* and *E* is a classical wake induced turbulent wedge. The high levels of turbulence in the wake intermittently induce turbulent spots in the attached boundary layer upstream of the separation point by a bypass transition mechanism. Due to the adverse pressure gradient the spots grow rapidly in the spanwise direction and coalesce into a spanwise turbulent strip. This is indicated by low H_{12} measured under the wake as far upstream as the first measurement location. The leading edge of the turbulent strip travels faster than the trailing edge, thus as the turbulent strip convects downstream it's streamwise extent increases. This results in a characteristic wedge shape on an S-T diagram. The elevated turbulence and full boundary layer profiles of the turbulent strip convect into the separated region and suppress the separation bubble that has been developing since the previous wake-passing event. This suppression of the separation bubble by turbulent spots formed upstream of the separation location was described by Schulte and Hodson (1996).

The region between the wake passing events shows the relaxation of the turbulent boundary layer under an adverse pressure gradient. Following the wake-induced turbulent wedge is a calmed region bounded by the lines *E* and *F*. The calmed region may be described as the unsteady response of the boundary layer to the decay of turbulent shear behind a turbulent spot (Schulte, 1995). Immediately after the passage of the spot the boundary layer profile is full with a low shape factor, as the influence of the turbulent shear decays, the profile relaxes back to the laminar like profile with high shape factor as determined by the local pressure gradient.

In Figure 4-7, the effect of the calmed region is apparent. Upstream of *65* % surface length, the calmed region has only a short duration and the boundary layer quickly returns to high levels of shape factor. This region is predominantly steady as indicated by the vertical contours of H_{12} in Figure 4-7. Around *70* % surface length the laminar boundary layer begins to become inflexional and to separate prior to the arrival of the next wake induced turbulent strip. The downstream edge of the high H_{12} region is seen to coincide with line *F*. This indicates that the fuller profiles of the calmed region resist separation and thus control the separating boundary layer.

The interaction of the negative jet and the separating boundary layer is evident between lines *A* and *B*. In the region *65* to *70* % surface length, the shape factor is seen to increase beneath the centre of the wake (midway between lines *A* and *B*). This is the result of the outer region of the boundary layer responding to the wake more rapidly than the portion near the wall where viscous effects dominate. This distortion of the boundary layer results in higher values of displacement thickness, δ^*, with little effect on the momentum thickness, θ and thus H_{12} increases.

4.4 Transition between wake passing

4.4.1 Introduction

In general, the range of Reynolds numbers found in LP turbines means that the blade surface boundary layers are transitional. During the wake passing cycle the boundary layers are alternately subjected to turbulent wake flow and relatively undisturbed flow from the upstream blade row. Thus, although rapid bypass transition may be induced under the wake passage, the portion of the cycle between wake passing events may result in a transition process more akin to natural boundary layer transition.

The investigation of Hughes and Walker (2000) presents evidence of such natural transition phenomena in hot-film signals measured on a 1.5 stage axial compressor. By high-pass filtering the raw hot-film signals, Hughes and Walker were able to remove the large amplitude fluctuations in quasi-wall shear stress associated with the laminar to turbulent transition. After the high pass filtering, evidence of Tollmein-Schlichting wave activity was visible in highly amplified raw hot-film signals. After excluding turbulent portions of the signal using the intermittency algorithm of Solomon and Walker (1995), a wavelet analysis of the remainder of the high-pass filtered signal revealed significant regions where the frequency content was within *±10%* of that predicted for Tollmein-Schlichting waves. The Tollmein-Schlichting waves were identified over a wide range of operating conditions, even when turbulence levels were as high as *8%*. This evidence highlights the importance of natural transition phenomena in a real turbomachinery environment.

4.4.2 Evidence of Natural transition phenomena in ensemble average measurements

A close inspection of Figure 4-7 in the region labelled *G* shows that the ensemble averaged H_{12} displays regular temporal oscillations. The oscillations arise along a line parallel to line *F*. The onset of the oscillations is therefore controlled by the calmed region. Figure 4-8 indicates the source of these oscillations of H_{12}. A series of ensemble average time traces of streamwise velocity measured at different heights in the boundary layer and at *80* % surface length are plotted. The spread in velocity level is a result of measurements at different heights and the temporal variations are the result of the wake passing described in section 4.3.2 above.

At *60* % of the cycle phase, a series of velocity fluctuations are evident in the ensemble average velocity traces. These fluctuations appear in the near wall region where the velocity is below half the freestream value. The fluctuations are in phase throughout the region in which they are observed and their character appears to be that of sinusoidal oscillations superimposed on a temporally decaying velocity. The amplitude of the fluctuations remains small compared to those resulting from the wake-induced transition and the frequency does not change significantly with time. The existence of these oscillations in ensemble-averaged data indicates they are deterministic and caused by some coherent structure in the boundary layer.

The development of the velocity fluctuations in time and space can be seen in Figure 4-9, where the ensemble average time traces of the first five traverse points from the wall are plotted at each of the streamwise measurement locations along the surface of the flat plate. More than one of the near wall traces is shown at each streamwise location. At all surface locations the velocity fluctuations emerge after the influence of the calmed region. The disturbance amplitude grows towards the trailing edge but the frequency is observed to be approximately constant at all surface locations. From the period of the velocity fluctuations, the frequency was found to be approximately *80Hz*.

The trajectory of the wave packets is marked in Figure 4-9 by the peaks and troughs in the velocity traces. At the time of each peak and trough, a circle is drawn at the appropriate surface distance (red for peak and blue for trough). Also drawn in Figure 4-9 are trajectories calculated for the trailing edge celerity of a turbulent spots from the correlation of Gostelow et al (1996). The circles lie very nearly on these trajectory lines of which the celerity is approximately $0.5U_\infty$. Solutions of the Orr-Sommerfeld equations for the Falkner-Skan profile on the verge of separating ($\beta=-0.1988$) show that this is in good agreement with the calculated phase speed or celerity of the most amplified wave (see Obremski et al (1969)).

4.4.3 Simple correlation for wave frequency

The experimental observations of §4.4.2 are characteristic of the growth and propagation of wave packets that occur in natural boundary layer transition. Experimental investigations have shown that the dominant disturbance frequency at breakdown is well predicted by the Tollmein-Schlichting wave frequency having the maximum amplification ratio (Walker, 1989). The frequency of the Tollmein-Schlichting waves may be predicted by linear stability theory. However, this involves a search for eigenvalues of the Orr-Sommerfeld equation.

It has been observed that the stability characteristics of a boundary layer are most strongly influenced by the shape of the velocity profile (Obremski et al, 1969). For the purposes of approximating the stability characteristics, the velocity profiles measured on the flat plate may be approximated by the Falkner-Skan family of boundary layer profiles (see Figure 4-5). A stability analysis on such profiles was performed by Obremski et al (1969). Based on these calculations, Walker (1989) derived a correlation for the frequency of the most amplified Tollmein-Schlichting waves in terms of the displacement thickness Reynolds number according to

$$f = \frac{3.2 U_\infty{}^2 \, \mathrm{Re}_{\delta^*}{}^{-3/2}}{2\pi\upsilon} \tag{4-7}$$

From this correlation and the ensemble average displacement thickness measured on the flat plate, it is possible to calculate the distribution of the most amplified Tollmein-Schlichting wave frequencies. Figure 4-10 shows the results of this calculation. The trajectories drawn on Figure 4-9 are copied to Figure 4-10. The observed frequency of about *80Hz* is seen to correspond to the region labelled *H*. From the trajectory lines, it is apparent that the waves observed are Tollmein-Schlichting waves that originate in the region of *H* and convect downstream while being amplified by the viscous instability mechanisms associated with the boundary layer.

4.4.4 Implications for transition modelling between wake passing

The agreement between measured and predicted frequency indicates that the transition mechanism occurring between wake passing events in a highly decelerated boundary layer is characteristic of natural boundary layer transition. The measured ensemble averaged oscillations indicate that the transition mechanism is deterministic.

Between wake passing events the flow is similar to that investigated by Obremski and Morkovin (1969) where a flat plate boundary layer was subjected to an oscillating freestream. They observed well-defined wave packets prior to transition and explained the repeatability of the measured wave packets in terms of the unsteady flow. At a particular point in the unsteady cycle, the boundary layer is most susceptible to disturbances. Disturbances arising at this point in the cycle are amplified by the boundary layer. In this way, the unsteady flow acts to filter the initial disturbances. This same phenomenon occurs in the unsteady flow between wake passing. The boundary layer velocity profile changes from the full turbulent profile, through the calmed profiles and tends towards the separated profiles that would exist in steady flow. Background disturbances first amplify at a point when the velocity profile becomes unstable and the disturbance spectrum continues to amplify according to the local linear stability characteristics of the boundary layer.

The mechanism where disturbances are amplified in a quasi-steady manner by the local boundary layer characteristics was described by Obremski and Morkovin (1969) who achieved reasonable success in predicting the developing wave packets on their flat plate subject to an oscillating freestream. They used a quasi-steady adaptation of the e^n method to predict the frequency of observed wave-packets and to calculate the amplification ratio spectrum. Traditional steady flow values of n in the e^n

method were found to be inadequate for describing the transition onset location. However, as in all transition prediction methods this could be accounted for by an appropriate correlation. The evidence of deterministic instability waves presented above suggests that a quasi-steady e^n method such as that of Obremski and Morkovin could be applicable to describing the transition between wake passing in turbomachinery environments.

4.5 Boundary Layer Dissipation

4.5.1 Introduction

The ultimate measure for loss of efficiency in turbomachinery is the creation of entropy (Denton, 1993). In turbomachinery, entropy creation occurs in fluid dynamic processes involving viscous dissipation, heat transfer across finite temperature differences and non-equilibrium processes associated with very rapid expansions such as shock waves or rapid condensations. Of these phenomena, viscous dissipation in the blade surface boundary layers is the primary source of loss in LP turbines.

4.5.2 Calculation of Dissipation

It is possible to determine the non-dimensional viscous dissipation per surface area, C_D, in a boundary layer by evaluating the integral

$$C_D = \frac{1}{\rho U_\infty{}^3}\int_0^\delta \frac{1}{T}\tau_{yx}\,dV = \frac{1}{\rho U_\infty{}^3}\int_0^\delta \frac{1}{T}\tau_{yx}\frac{du}{dy}\,dy \qquad \text{(4-8)}$$

where the shear, τ_{yx}, consists of laminar and turbulent components and is given in terms of the fluid viscosity, μ, density, ρ, velocity gradient, du/dy and Reynolds shear stress, $\overline{u'v'}$ by,

$$\tau_{yx} = \mu\frac{du}{dy} - \rho\overline{u'v'} \qquad \text{(4-9)}$$

The dissipation integral is equally applicable for steady and unsteady flows if thermodynamic equilibrium is maintained and temporal gradients of internal energy can be neglected. These conditions are satisfied for the current measurements.

With ensemble average measurements of mean velocities and Reynolds stress through the boundary layer, it is possible to calculate the ensemble average viscous boundary layer dissipation directly. In accordance with the derivation presented by

Denton (1993), the values of Reynolds stress used in the calculation are transformed to align with the local flow direction.

4.5.3 Space time description of boundary layer dissipation

Figure 4-11 shows the dissipation coefficient, C_D, over the flat plate as calculated from the boundary layer measurements and equation (4-5). Also included on Figure 4-11 are the trajectory lines and labels from previous S-T diagrams.

Immediately evident is the fact that high levels of viscous dissipation are predominantly confined to the wake induced turbulent wedge between line *B* and line *E*. The peak levels of C_D occur as the high shape factor boundary layer along line *D* undergoes transition.

Another region of elevated C_D is evident at the location where Tollmein-Schlichting waves were observed (between labels *G* and *F*). These elevated levels of dissipation arise due to the mean flow transferring energy to the velocity oscillations (Betchov and Criminale, 1967), however the levels of C_D associated with this energy transfer are about half the peak levels measured.

The calmed region between line *E* and line *F* has low levels of C_D. The magnitude is comparable to that of the undisturbed laminar boundary layer. This is in agreement with the numerical model of Schulte (1995).

Separated flows are typically associated with high levels of loss. However, the measurements presented here show that the regions of high shape factor in Figure 4-7, which are indicative of the initial stages of the formation of a separation bubble, have laminar levels of dissipation.

These findings provide experimental proof of the loss reducing mechanism exploited in the design of high lift LP turbine blading. The highly dissipative separation bubble formed in the adverse pressure gradient of the steady flow is replaced between wake passing events initially by calmed flow and then the initial stages of the formation of a separation bubble which are characterised by low levels of dissipation. Although the wake induced turbulent strip has high levels of dissipation, in the time average the losses are reduced by the longer durations of the calmed region and then the initial stages of separation.

4.5.4 Observed mechanisms of viscous dissipation

Unlike traditional steady separation bubbles, the high shape factor flow between wake passing events does not have high levels of Reynolds stress and this is the reason for the low levels of dissipation that were measured. In steady separation bubbles, high levels of Reynolds stresses arise due to the instability of the separated shear layer that leads to vortex shedding. However, in the case of an establishing separation bubble the shear layer instabilities do not have time to develop.

The two-dimensional calculations of Pauley et al (1990) showed that separation bubbles shed vortices with an effectively constant Strouhal number of $St_{\theta s}=6.86\times 10^{-3}$ based on momentum thickness at separation. For the presented measurements, this gives the period of vortex shedding as about *12ms*[13]. By contrast the time for the development of the separating boundary layer, determined for example from Figure 4-6, is about *40%* of the wake passing period which corresponds to approximately *50ms*. The vortex shedding that would result if the separation bubble were fully established would thus be significantly faster than the time taken for the separation bubble to establish. The low levels of Reynolds stresses do not result from insufficient time for vortex shedding to occur. The low levels of Reynolds stresses measured suggest that the conditions leading to the instability and subsequent vortex shedding do not have sufficient time to establish prior to the arrival of the next wake.

A more detailed understanding of the mechanisms responsible for viscous dissipation in the unsteady boundary layer flow can be obtained by assessing the non-turbulent and turbulent contributions to the production of entropy in the boundary layer.

If the laminar and turbulent components of the shear, τ_{yx}, are separated, the dissipation coefficient may be written as the sum of the non-turbulent and turbulent components, which, for isothermal flows, are given by

---

[13] It should be noted that this period is very close to the observed frequency of Tollmein-Schlichting waves. Indeed Pauley et al (1990) note that the vortex shedding occurs at the most unstable frequency of the inflexional profile associated with the separation. The velocity traces in Figure 4-8 and Figure 4-9 show that the oscillations are in phase through most of the boundary layer. This is characteristic of a sinusoidal wave superimposed on the flow throughout the boundary layer. It is proposed that if the oscillations were due to vortices shed from the separation the phase change through the boundary layer would be more obvious with the velocity above the centre of the vortex increased and the velocity below the centre of the vortex decreased.

$$C_{D\,non-turb} = \frac{1}{\rho T U_\infty^3} \int_0^\delta \mu \frac{du}{dy}^2 dy \qquad (4\text{-}10)$$

$$C_{D\,turb} = \frac{1}{\rho T U_\infty^3} \int_0^\delta - \rho \overline{u'v'} \frac{du}{dy} dy \qquad (4\text{-}11)$$

Thus, the non-turbulent contribution to dissipation arises from the shape of the boundary layer profile alone, while the turbulent contribution contains contributions from the shape of the boundary layer and the Reynolds stresses. In general, the Reynolds stresses dominate the boundary layer dissipation in turbulent regions.

This is highlighted by Figure 4-12 where the component due only to the Reynolds stress, $C_{D\ turb}$, is calculated. Differences between Figure 4-12 and Figure 4-11 are thus due to the laminar contribution to dissipation, $C_{D\ non\text{-}turb}$, which is only dependent on the shape of the velocity profile. It is immediately apparent that the majority of viscous dissipation for the wake boundary layer interaction arises from the Reynolds stresses. The regions where there are noticeable differences between the two plots are under the footprint of the wake in region *I* and in the turbulent wedge well after the passage of the wake such as at *J*. In these regions, the shape of the boundary layer contributes to the boundary layer dissipation. The peak levels of dissipation associated with the laminar to turbulent transition along line *D* are seen to be almost entirely from the Reynolds stress while the dissipation due to the Tollmein-Schlichting waves is more evenly divided between the profile shape and the Reynolds stress.

More insight into the dissipation mechanism may be gained by looking at the profiles of velocity and Reynolds stress at selected points through a wake passing cycle at *87* % surface length. Five sets of profiles are plotted in Figure 4-13. The locations of these profiles are marked by numbered crosses on Figure 4-12.

Profile *1* is associated with the calmed region and low levels of dissipation. The velocity profile is typical of the calmed region and has no strong velocity gradients. The measured Reynolds stresses are low throughout the boundary layer at this location and so low levels of dissipation prevail.

The region of observed Tollmein-Schlichting waves between *G* and *F* has islands of moderate and low dissipation. Two profiles are considered from this region to aid the explanation and show the source of the differences. Profile *2* is associated with higher levels of dissipation than profile *3* yet the velocity profiles are very similar and inflexional in character. The differences in dissipation result from the difference in the level of Reynolds stress. Profile *2* has a peak in Reynolds stress at the mid boundary layer height while *3* has lower levels more uniformly distributed and confined to the inner half of the boundary layer height.

The peak levels of C_D are associated with profile *4* and result from the laminar to turbulent transition. The boundary layer profile is not yet full like a typical turbulent profile, nor is it inflexional like profiles *2* and *3*. The contribution from the profile shape is thus minor. The peak values of C_D are thus achieved primarily by the very high levels of Reynolds stress. However, due to the shape of the profile, the velocity gradients in the region of high Reynolds stress are also higher. Therefore, the peak levels of C_D are achieved through the combined effect of very high Reynolds stresses, and the relative location of the velocity gradients within the boundary layer.

The profile *5* taken from within the wake induced turbulent wedge is associated with a high level of C_D but with a noticeable non-turbulent contribution. The velocity profile at this location has a full turbulent shape. The near wall velocity gradient is thus very high and this accounts for the non-turbulent contribution to C_D. The Reynolds stresses are high throughout the boundary layer height, although in the outer part of the boundary layer, the velocity gradients are low and thus the contribution to dissipation is diminished in this region.

4.5.5 Comparison of measured and expected levels of dissipation

The general level of dissipation for a turbulent boundary layer is given by Schlichting (1979) as an experimentally based correlation. For a turbulent boundary layer with $1.2<H_{12}<2.0$ and $10^3<Re_\theta<10^5$ the dissipation may be correlated as

$$C_D = 0.0056\,\mathrm{Re}_\theta^{-1/6} \qquad (4\text{-}12)$$

Denton (1993) shows that a Cebeci boundary layer calculation with a mixing length turbulence model produces similar results to this correlation for zero pressure gradient. The same calculation predicts diffusing flows to have elevated dissipation and accelerating flows to have reduced dissipation. However, these results are simply a measure of the ability of the mixing length turbulence model to determine boundary layer dissipation.

In laminar boundary layers, C_D is more strongly dependent on the boundary layer thickness and Truckenbrodt (1952) provides the correlation

$$C_D = \beta \,\mathrm{Re}_\theta^{-1} \qquad (4\text{-}13)$$

and an analytic solution for a zero pressure gradient laminar boundary layer gives a coefficient $\beta=0.173$. Denton (1993) suggests accounting for pressure gradients by considering the Pohlhausen velocity profiles. For a highly accelerated boundary layer with $\lambda=+12$ the coefficient is $\beta=0.220$ while for the separating Pohlhausen profile with $\lambda=-12$ the coefficient is $\beta=0.151$.

The correlations for turbulent and laminar boundary layers are presented in Figure 4-14. Also shown on Figure 4-14 are data of the ensemble-averaged measurements of dissipation and Re_θ. Each measured data point is indicated by a circle and the scatter indicates the range of values measured. The points of highest Re_θ correspond to the wake-induced strip and have levels of C_D significantly higher than predicted by the correlation of Schlichting. The greatest density of measurement points lie in the range $200< Re_\theta<300$ where the levels of C_D are laminar and in reasonable agreement with the correlation of Truckenbrodt. The time average of the measured ensemble average Re_θs and C_D is shown by the heavy line. These values lie between the expected laminar and turbulent levels from the first measurement point until $Re_\theta=450$ which is at *83 %* surface length. Thereafter the levels marginally exceed the correlation of Schlichting as anticipated in a decelerating flow.

The time average measurements of C_D are thus in reasonable agreement with anticipated levels which credits the validity of the measurements. However, the levels of C_D and Re_θ that occur during the wake-induced transition are significantly higher than anticipated and the correlation of Schlichting, which is based on steady experimental data, is unable to capture any of the unsteady effects of wake-induced transition.

4.6 Conclusion from Flat Plate measurements

The results presented in this chapter demonstrate that it is possible to simulate the boundary layers of LP turbine blades on a flat plate by imposing a representative pressure distribution.

The interaction of a wake and a boundary layer was dominated by the unsteady wake induced transition phenomena. Wake turbulence resulted in periodic early bypass transition. This prevented the formation of a steady separation bubble. The turbulent to laminar relaxation of the boundary layer that occurred between wake passing events was governed by the calmed region.

A deterministic natural transition mechanism was identified in the boundary layer as it relaxed from turbulent to laminar between wake passing events. The frequency of velocity fluctuations observed towards the trailing edge was found to be in good agreement with the frequency predicted from the most amplified Tollmein-Schlichting waves in a Falkner-Skan profile of the same displacement thickness.

Ensemble averaged measurements of velocity profiles and Reynolds stress profiles along the surface of the flat plate facilitated the calculation of the boundary layer dissipation coefficient. Experimental proof of the loss reducing mechanism associated with the calmed region following the wake induced turbulent boundary layer was thus provided.

4.7 Figures

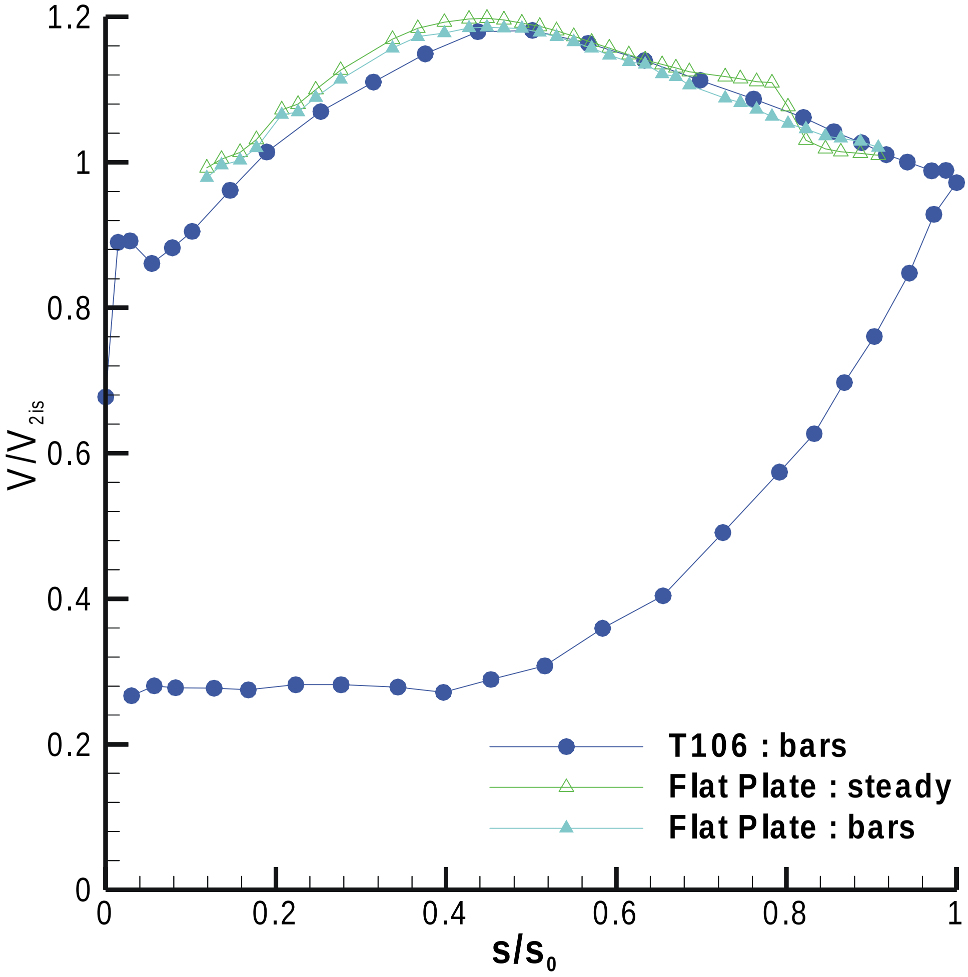

Figure 4-1: Comparison of the velocity distribution measured on the T106 cascade with moving bars to that measured on the flat plate with and without moving bars

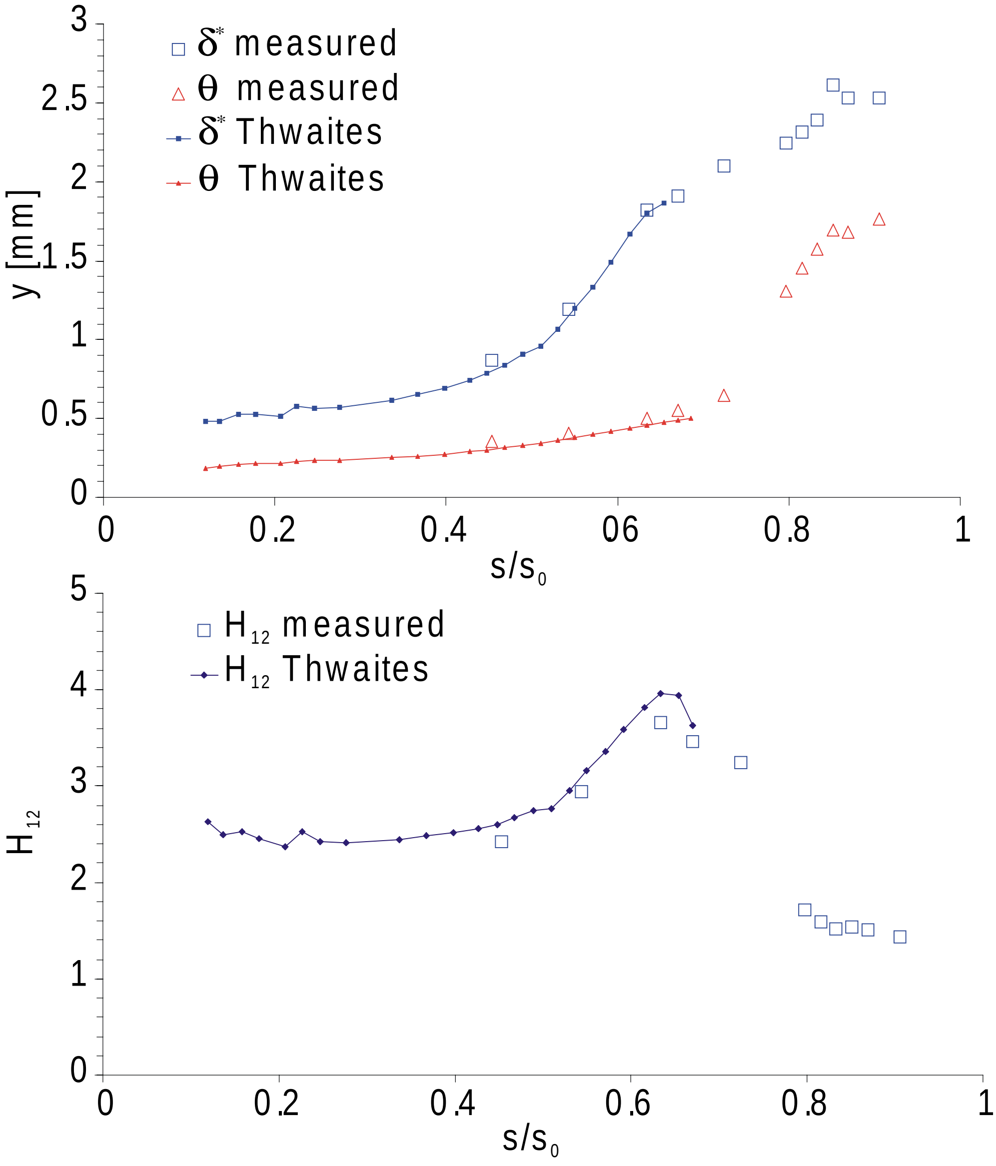

Figure 4-2: Comparison of steady integral parameters calculated from measured boundary layer traverses and predicted from a Thwaites calculation based on the measured velocity distribution. ***Re_{2s}=214000, steady flow***

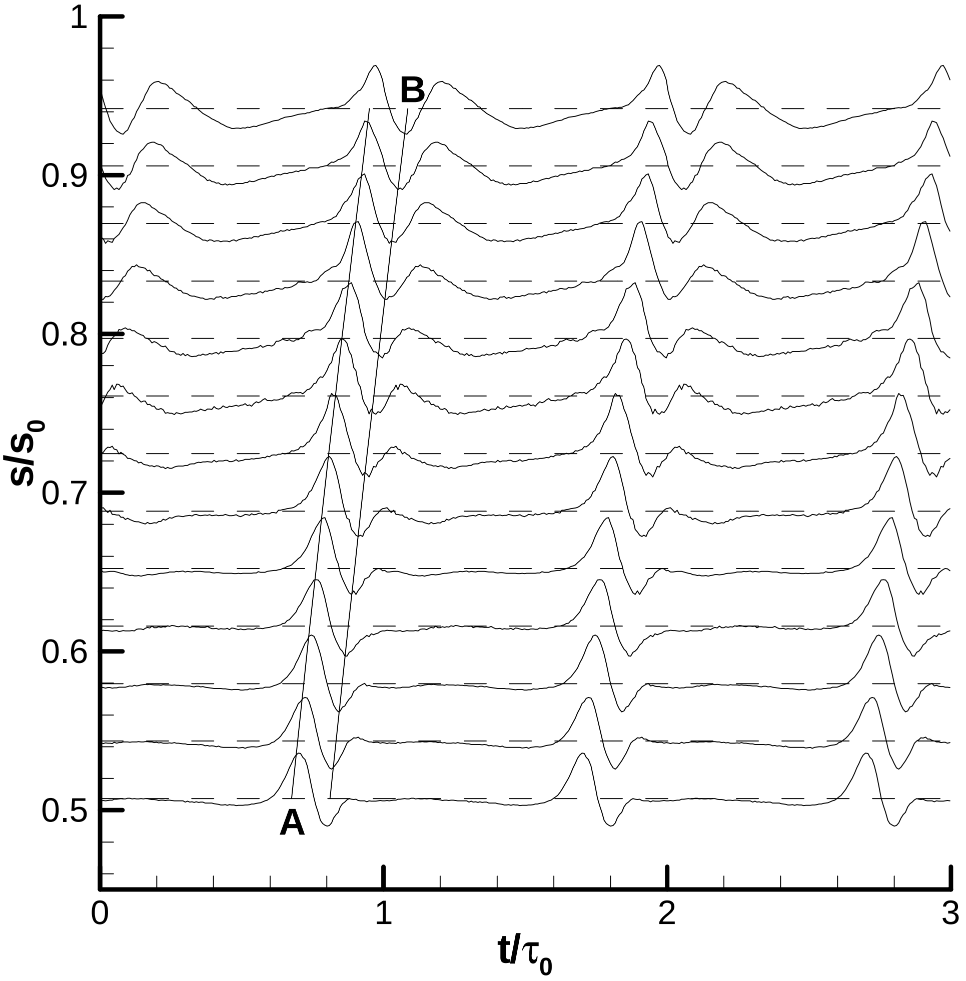

Figure 4-3: Ensemble average time traces of boundary layer edge velocity showing the negative jet effect and the convection of the wake with the local freestream velocity. ***Re_{2s}=214000, ϕ=0.83, f_r=0.67***

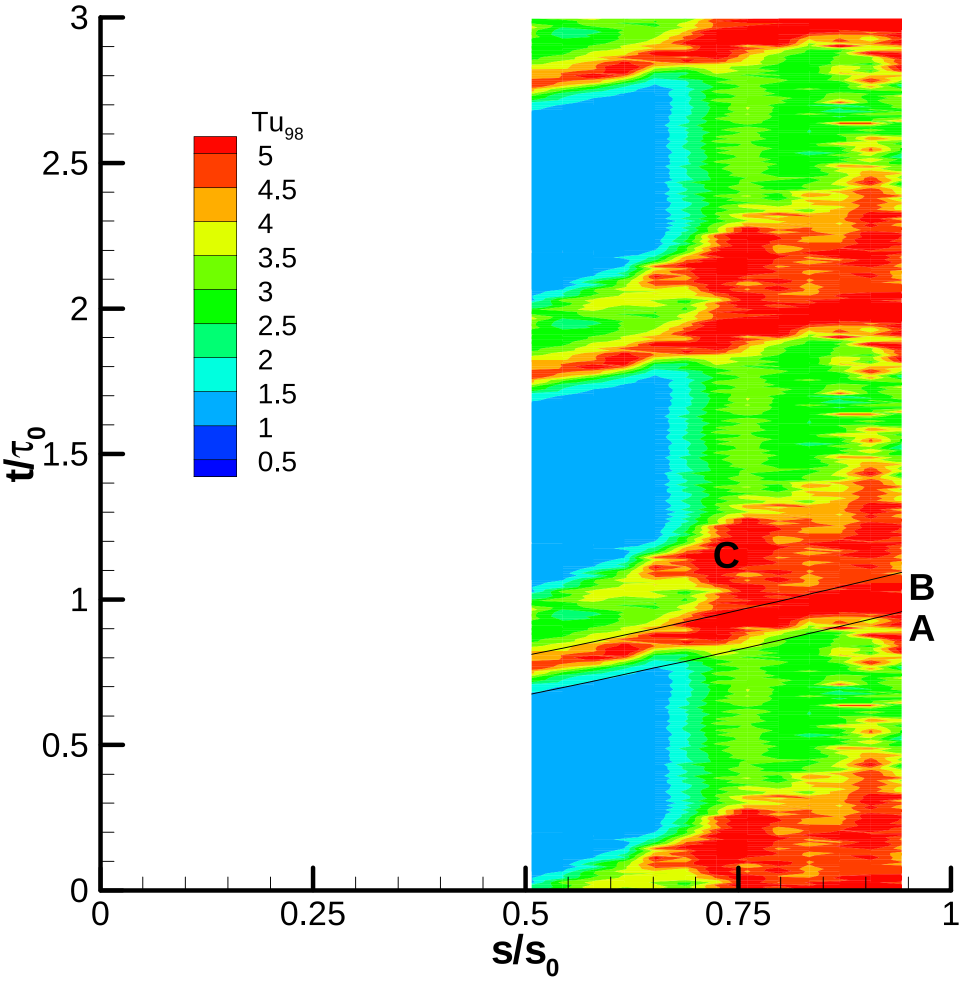

Figure 4-4: S-T diagram of turbulence intensity at boundary layer edge. ***Re_{2s}=214000, ϕ=0.83, f_r=0.67***

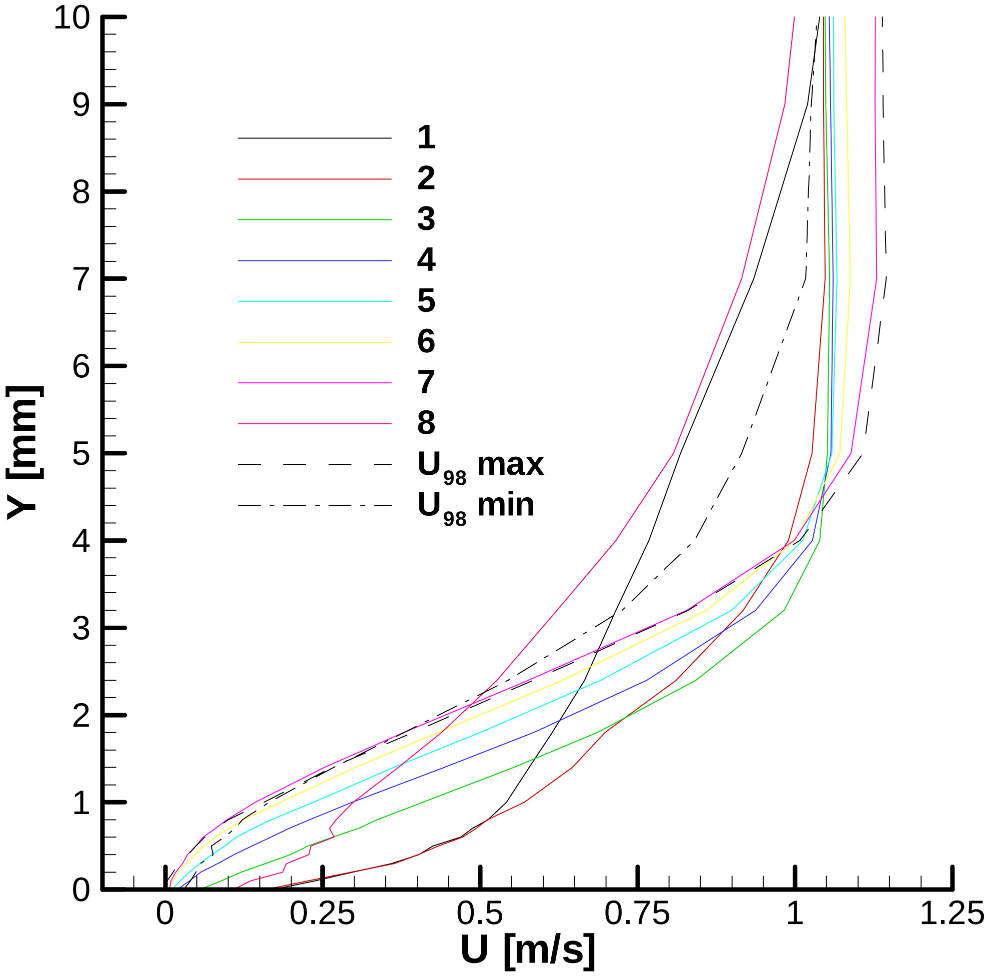

Figure 4-5: Measured ensemble averaged boundary layer velocity profiles at *76* % surface length through one wake passing cycle. Re_{2s}=*214000*, ϕ=*0.83*, f_r=*0.67*

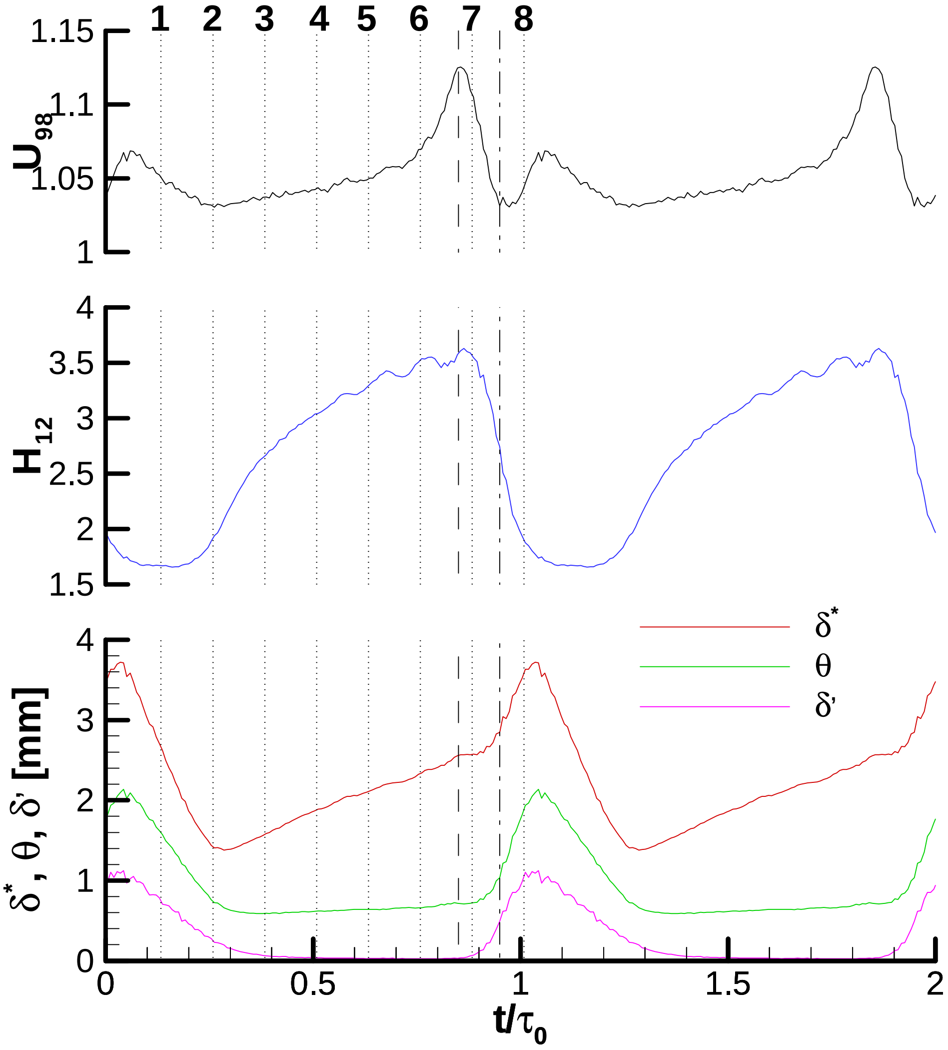

Figure 4-6: Ensemble average integral parameters at *76* % surface length as calculated from the measured boundary layer velocity profiles. ***Re_{2s}=214000, ϕ=0.83, f_r=0.67***

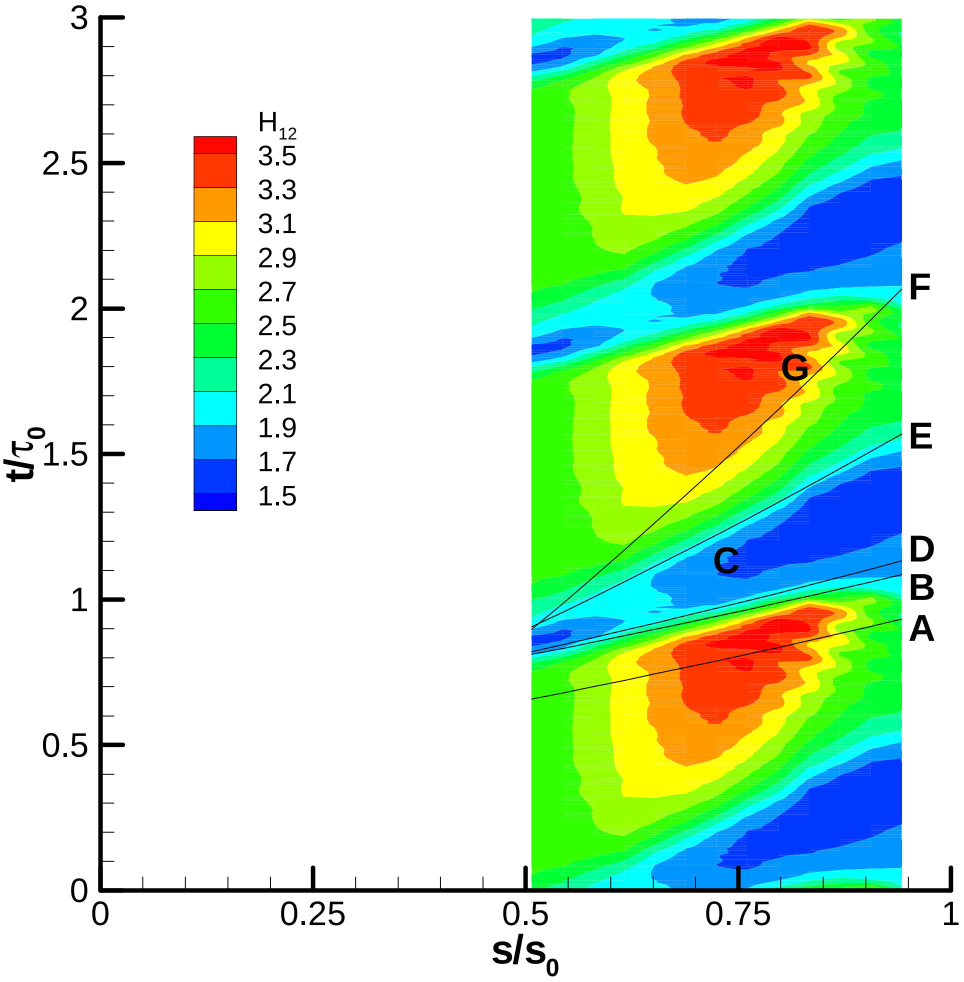

Figure 4-7: S-T diagram of ensemble averaged boundary layer shape factor H_{12} as calculated from measured velocity profiles. $Re_{2s}=214000$, $\phi=0.83$, $f_r=0.67$

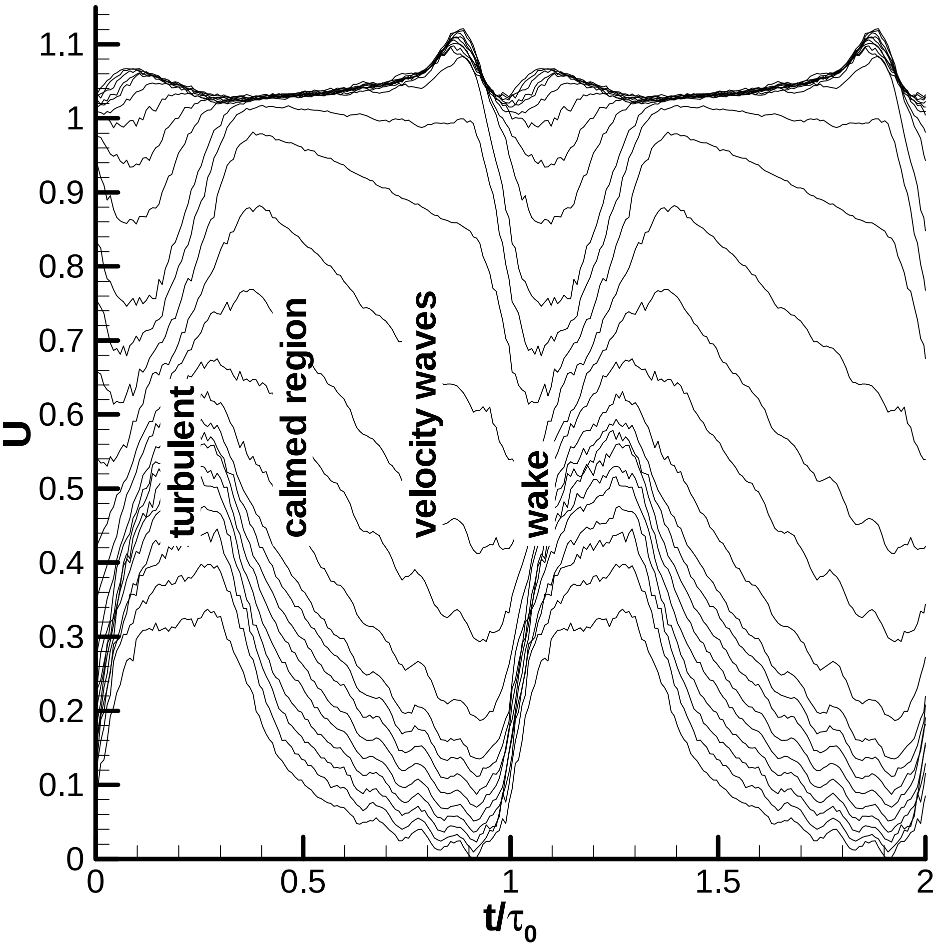

Figure 4-8: Ensemble averaged velocity traces measured at different heights through the boundary layer at *80* % surface length. *Re_{2s}=214000, ϕ=0.83, f_r=0.67*

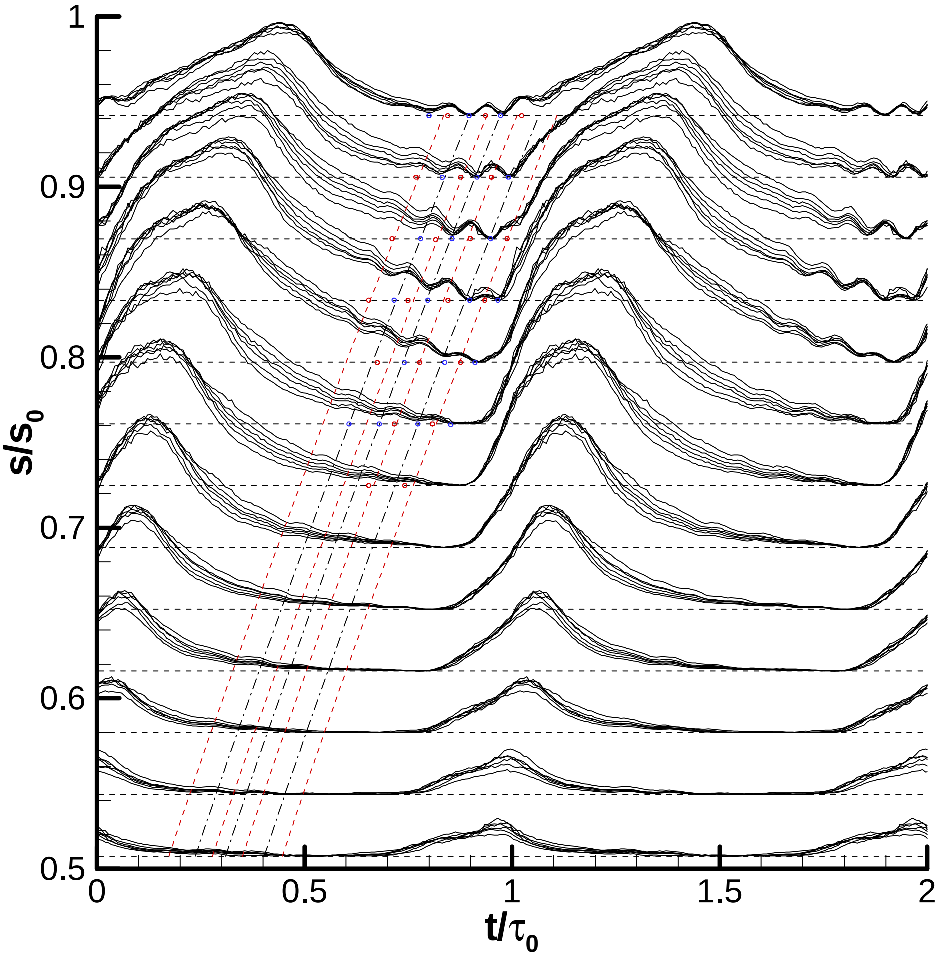

Figure 4-9: The development of near wall velocity fluctuations in space and time over the flat plate. ***Re_{2s}=214000, ϕ=0.83, f_r=0.67*****. At each surface position traces are shown for** ***y=0.1mm*** **to** ***y=0.6mm*** **in steps of** ***0.1mm*****.**

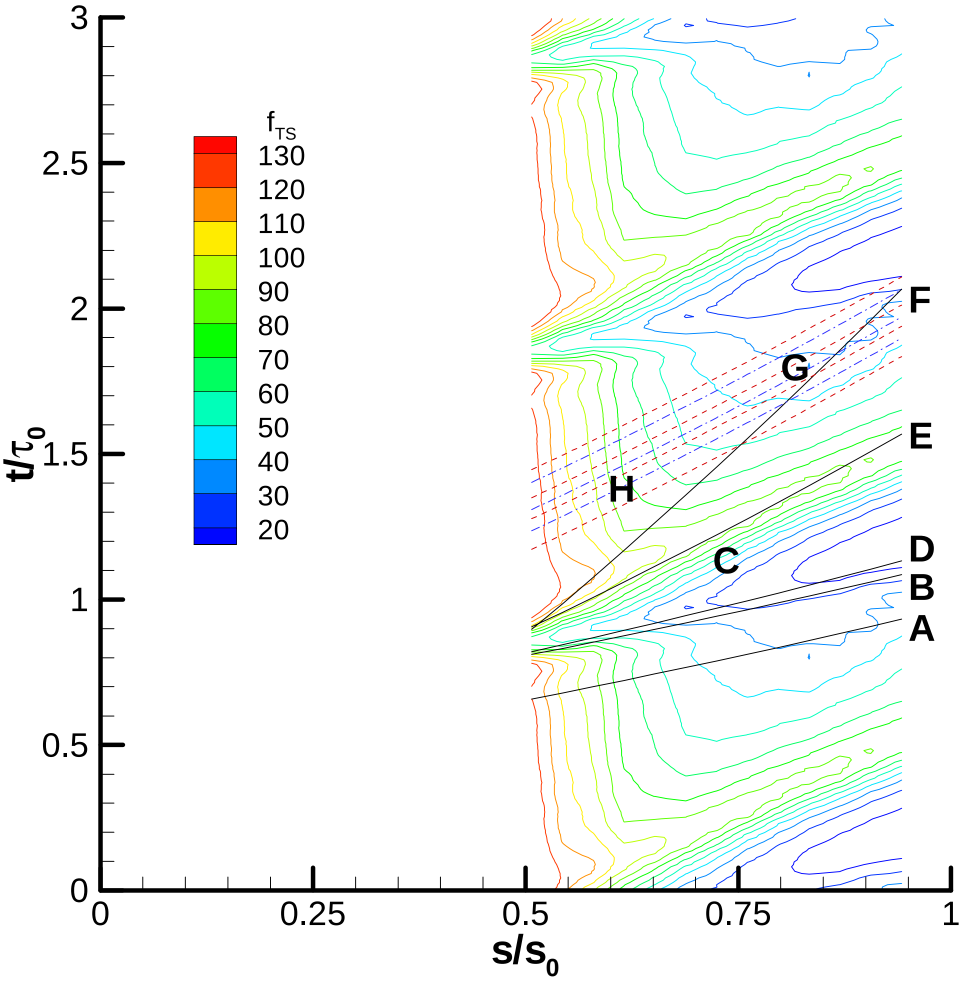

Figure 4-10: The frequency of the most amplified Tollmein-Schlichting waves as predicted from the correlation of Walker (1989) applied to the ensemble averaged boundary layer measurements. ***Re_{2s}=214000, ϕ=0.83, f_r=0.67***

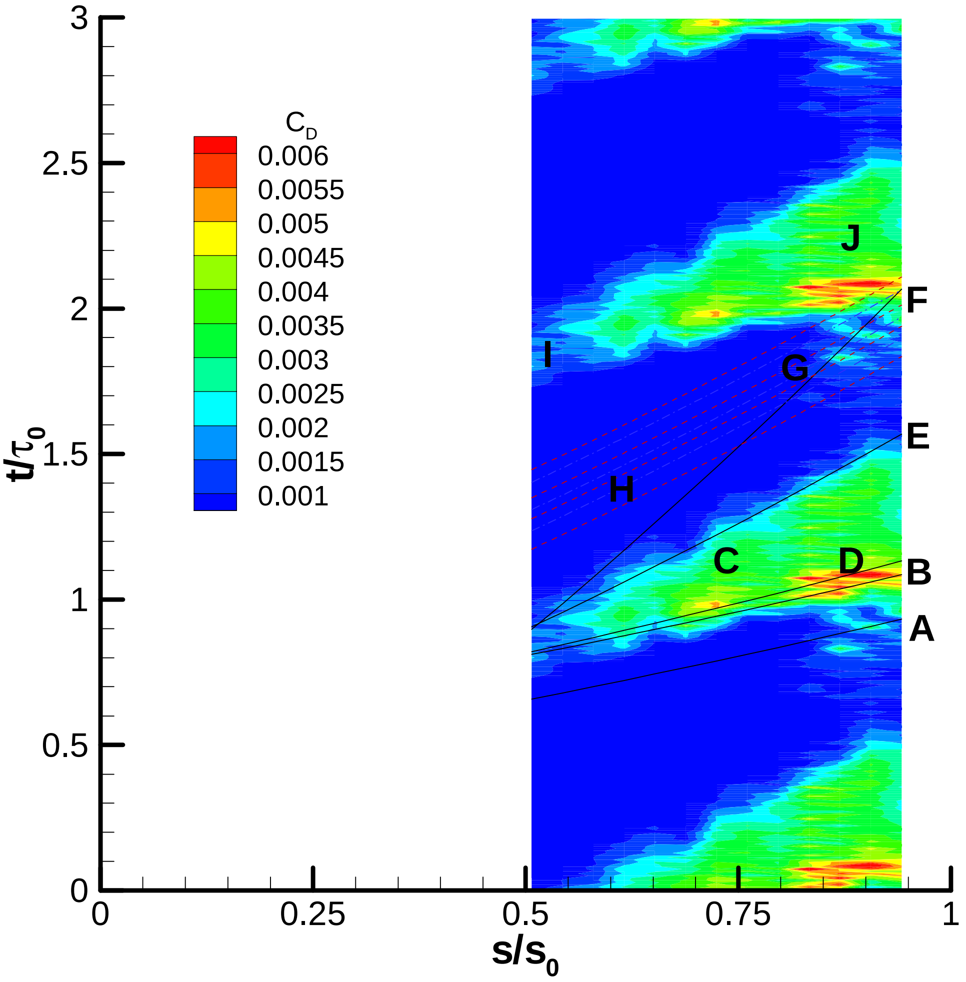

Figure 4-11: S-T diagram of boundary layer dissipation coefficient, C_D, calculated from measured ensemble average profiles of mean velocity and Reynolds stresses. $Re_{2s}=214000$, $\phi=0.83$, $f_r=0.67$

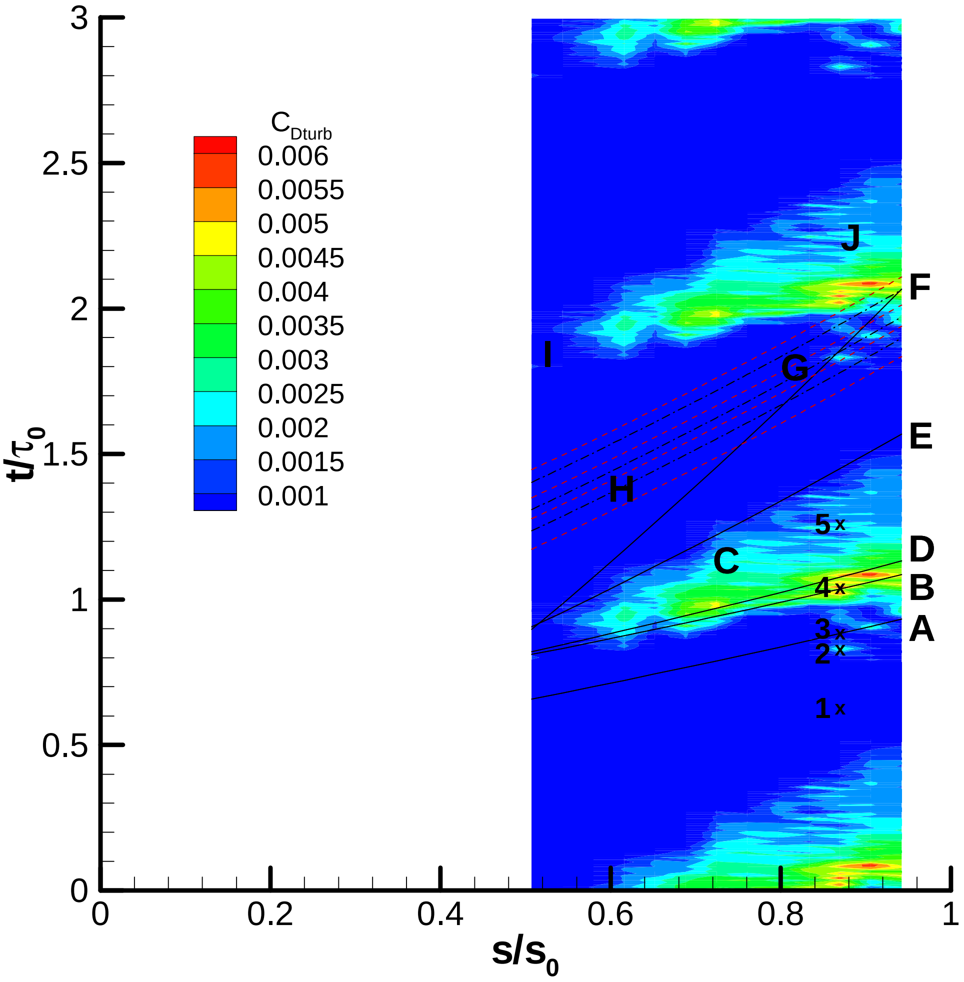

Figure 4-12: S-T diagram showing the contribution to boundary layer dissipation of the turbulent Reynolds stresses, $C_{D\,turb}$. Re_{2s}=214000, ϕ=0.83, f_r=0.67

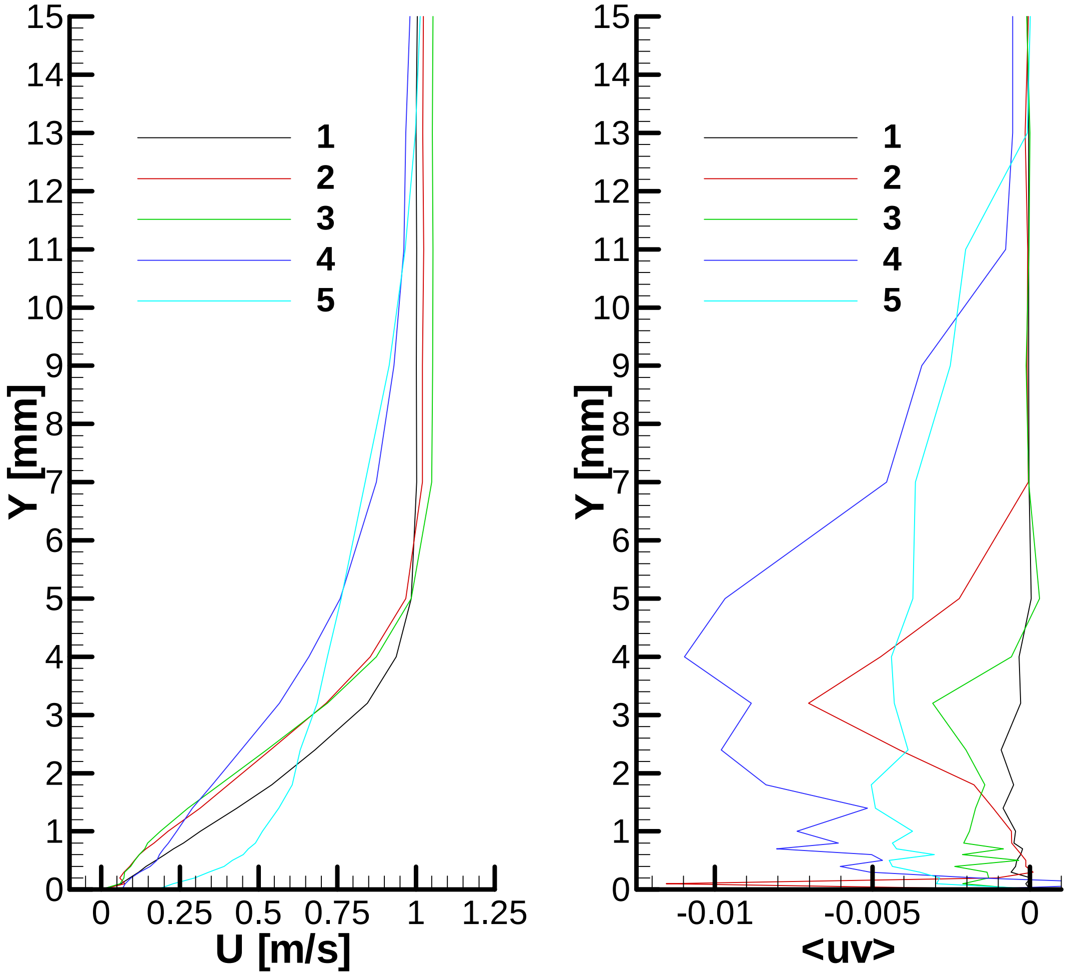

Figure 4-13: Measured ensemble averaged profiles of mean velocity and Reynolds stress at selected phases through the wake passing cycle. Profiles at *87* % surface length, $Re_{2s}=214000$, $\phi=0.83$, $f_r=0.67$

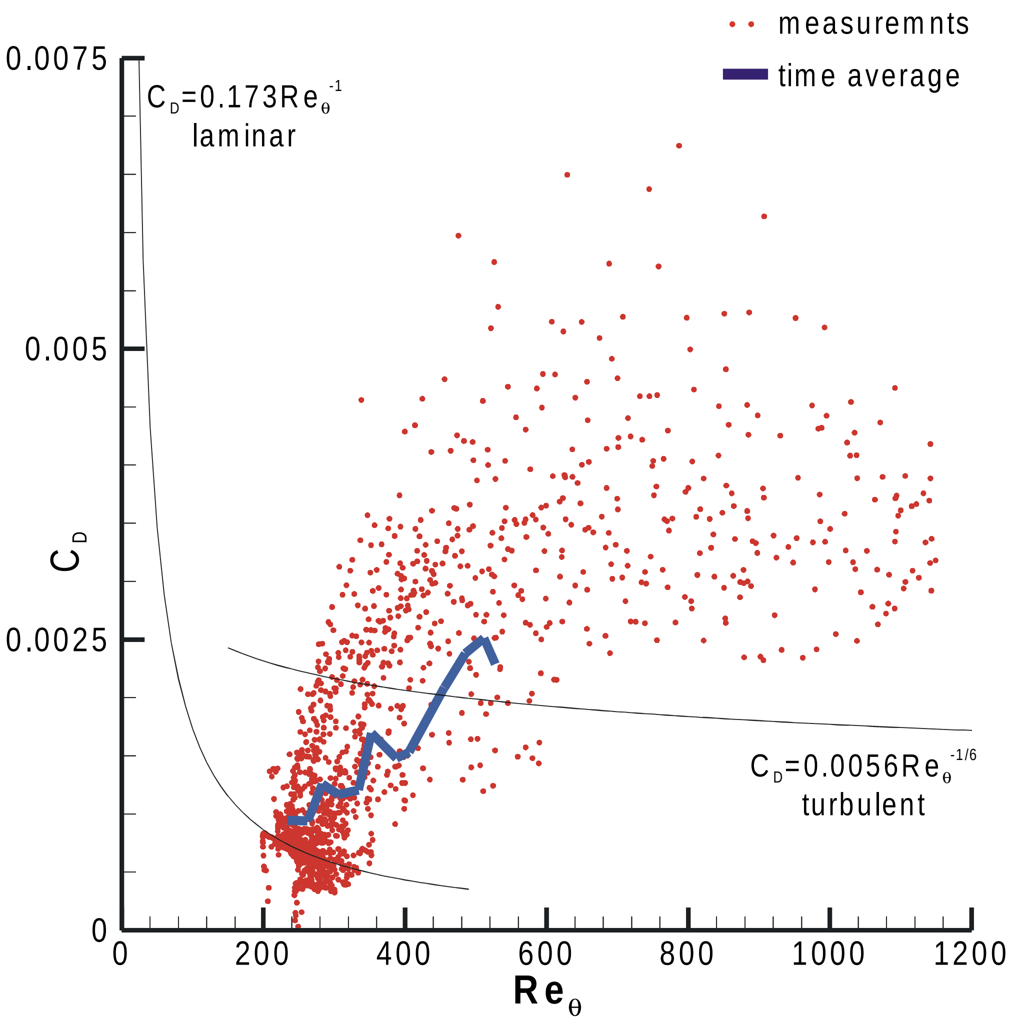

Figure 4-14: Comparison of measured and predicted levels of C_D. The scattered data are the ensemble average measurement points. The heavy line indicates the time average of the boundary layer dissipation. $Re_{2s}=214000$, $\phi=0.83$, $f_r=0.67$

Chapter 5: Measurement of turbulent wake convection through an axial turbine cascade

5.1 Introduction

The unsteady flow field in LP turbines is governed by a combination of potential and convective interactions (Hodson, 1998). Of these, the convected wakes from upstream blade rows play the most significant role due to their effect upon the blade surface boundary layers.

A number of researchers have described the kinematics governing the convection of a wake through a cascade. Early work by Meyer (1958) used potential flow solutions and resulted in the negative jet model. Numerous numerical studies have further shown that the wake convection is primarily a kinematic phenomenon (e.g. Hodson, 1985 and Giles, 1987).

However, the kinematics of the wake convection is only partly responsible for the effects of the wake on the blade surface boundary layer. The primary effect of the wake convection is to dictate boundary layer transition and so it is the turbulence of the wake and the convection of the turbulent quantities through the blade row that is of prime importance. Indeed, the transition models of Addison and Hodson (1992), Doorly and Oldfield (1985) and La Graff et al (1989) all neglect the negative jet effect. These models use the wake convection simply to transport wake turbulence, which acts as a transition onset front.

To date, few measurements exist of the unsteady wake convection through a turbine blade row. The measurements of Schulte (1995) provide a guide to the mean flow through a LP turbine passage, however these measurements lack resolution and detail of the turbulent quantities.

This chapter presents 2D LDA measurements of the wake convection through the T106 LP turbine cascade. Not only is the spatial resolution of the measurements unprecedented but also the direct measurement of Reynolds stresses provides a valuable database for comparison of numerical predictions. Based on the measured mean and turbulent quantities, the production of turbulent kinetic energy is calculated. A novel wavelet analysis of the 2D LDA data is also presented at representative points within the blade passage. This provides understanding of the contributions of the different scales to the turbulent quantities during the wake passing cycle.

The measured ensemble-averaged velocity field confirmed the previously reported kinematics of wake convection. Measurements of the turbulent quantities showed the wake fluid to be characterised by elevated levels of turbulent kinetic energy (*TKE*) and to have an anisotropic structure. Production of *TKE* within the blade passage elevated the *TKE* levels and resulted in a more isotropic turbulent flow above the suction surface at about mid-chord.

5.2 Measurement details

The convection of wakes shed from a moving bar wake generator through the T106 LP turbine cascade was measured using 2D LDA as described in Chapter 3. The measurement grid consisted of *35* tangential traverses evenly spaced in the axial direction within the bladerow. A further 4 traverses were performed upstream of the leading edge of the cascade. Each tangential traverse consisted of *48* points. The beam pairs of the LDA intersect at a half angle of $4.3°$ so in order to make measurements close to the blade surfaces it was necessary to incline the probe so that neither of the beams was obstructed by the blade. The traverses in the axial planes were thus performed in two stages with *24* points equally spaced from the suction surface and then, after altering the probe inclination, *24* equally spaced from the pressure surface. The suction side traverses were performed at a marginally smaller spacing than those from the pressure side. The velocity measured with the inclined LDA probe is insignificantly different from that measured with a normal probe (less than *0.5%*) and for this reason it was considered unnecessary to apply a correction to the measurements.

The blade surface was painted matt black to minimise flare from the intersecting beams. However, a narrow strip at mid span was left unpainted to avoid contaminating the mid-span static pressure tappings. For this reason all measurements were performed at *45%* span. The measurement grid with the blades and bars superimposed together with the definitions of the co-ordinate directions and velocity components is shown in Figure 5-1.

A trigger signal was supplied on every bar passing and was used to ensemble average the LDA data using the methods described in Chapter 3. Each bar passing cycle was divided into 128 time bins, which provided adequate temporal resolution of the ensemble averaged flow physics.

5.3 The kinematics of wake convection through a turbine cascade

5.3.1 Mean flow

The ensemble average velocity magnitude measured at a series of six time instants through the wake passing cycle is shown in Figure 5-2. Although more easily identified by the perturbation velocity vectors of Figure 5-3, the position of the wake may be detected in Figure 5-2 by the velocity deficit, which causes the contour lines to form ‘V’ shapes pointing along the wake centreline.

The effect of wake passing on the position and magnitude of peak velocity can be determined from Figure 5-2. The suction surface is not directly affected by the wake in Figure 5-2 (a) and peak suction is identified by the maximum velocity, which occurs at label *A*. The strength of peak suction increases through Figure 5-2 (b) & (c) while remaining at the same location on the blade surface. During this time, only the magnitude of the wake induced perturbation velocity increases. By the time of Figure 5-2 (d), the wake centre has passed location *A*. The direction of the perturbation velocity has reversed and as a result, the local velocity at *A* drops. Peak suction moves downstream to label *B* and then *C* ahead of the wake. However, by Figure 5-2 (f) peak suction has returned to its original position, *A*, due to the decreased magnitude of the wake induced perturbation velocity.

It is apparent that the wake passage does not simply raise or lower the peak suction as it convects through the passage; rather the velocity distribution is altered. The surface velocity gradient, and thus the pressure gradient imposed on the blade surface boundary layer, is affected and this, in turn, will influence the unsteady boundary layer separation process.

5.3.2 Perturbation flow

The unsteady flow can be more easily visualised by the perturbation velocity, which is defined as the difference between the ensemble average and the time average velocities according to

$$\left\langle U_p^* \right\rangle = \left\langle U^* \right\rangle - \overline{U^*} \qquad (5\text{-}1)$$

$$\left\langle V_p^* \right\rangle = \left\langle V^* \right\rangle - \overline{V^*} \qquad (5\text{-}2)$$

The perturbation velocity vectors are shown at the same six time instants in Figure 5-3. The location and shape of the wake is easily identified.

5.3.2.1 Kinematic wake convection

The convection of the wake segment within the bladerow is characterised by bowing, re-orientation, elongation and stretching (see Hodson, 1998). All these processes are visible in Figure 5-2 but are clearer in the perturbation vectors shown in Figure 5-3.

Bowing of the wake fluid is most evident in Figure 5-3 (a) & (b) and originates near the leading edge plane where the mid passage velocities are higher than the velocities near the blade surfaces. The wake fluid convects with the local velocity and distorts into the bowed shape. The re-orientation of the wake segment occurs due to the circulation of the blade. The velocities near the suction surface are higher than near the pressure surface and so fluid near the suction surface convects through the passage more rapidly than the fluid near the pressure surface resulting in a re-orientation of the wake segment. This is most clearly seen by comparing the angles of the two wake segments towards the pressure side of the passage in Figure 5-3 (e). The difference in convection velocities also causes the wake segment to elongate and this in turn decreases the wake width to conserve the circulation of the wake fluid. Comparing the wake width in Figure 5-3 (a) and (e), the decrease in wake width is only apparent on the pressure side of the passage. Near the suction side of the passage the width of the wake increases. As the first part of the wake reaches the leading edge, it is accelerated over the suction surface of the blade and moves away from the upstream edge of the wake thus increasing the wake width on the suction side of the passage. This stretching process is visible along the suction surface in Figure 5-3 (c) & (d). The velocity gradients along the leading half of the pressure surface are not as strong as on the suction surface and so this stretching effect is less pronounced on the pressure surface. The combined effect of all the above results in the wake fluid building up on the suction surface with a tail pointing upstream and towards the pressure side as seen most clearly in Figure 5-3 (e).

5.3.2.2 Negative jet

The velocity perturbation vectors of Figure 5-3 provide a clear picture of the negative jet effect described by Meyer (1958). The wake segment within the bladerow is clearly identified as a perturbation jet pointing towards the source of the wake. This negative jet has a component of velocity across the blade passage that causes the wake fluid to convect towards, and impinge upon, the suction surface. This is apparent in

Figure 5-3 (d)-(f). As the wake fluid impinges on the surface, it splits into two perturbation streams, one pointed downstream along the blade and the other upstream along the blade. Thus, downstream of the wake centre the perturbation from the negative jet is in the same direction as the main flow, while upstream of the wake centre it opposes the mean flow.

5.3.2.3 Vorticity

The negative jet, trapped between two solid blades, establishes a pair of counter rotating vortices. These counter rotating vortices, with centres marked ‘D’ and ‘E’ in Figure 5-3 (c) - (f), are clearly visible in the perturbation velocity vector plots as they convect through the blade passage.

The flow area reduces as the flow accelerates through the bladerow. According to Kelvin’s theorem, the vorticity must therefore increase to conserve angular momentum. Evidence of this is seen by the increase in the magnitude of the perturbation vectors through the blade passage. The vortex pair also convects towards the suction surface under the influence of the cross passage transport. The interaction of the vortex pair with the blade surface may be explained by considering an imaginary image system to be formed through the blade surface. As the suction surface is approached, the interaction of the vortex pair with the image system causes the separation between the vortex centres to increase and further magnifies the perturbation velocity magnitude.

Figure 5-4 presents contours of non-dimensional vorticity, Ω^*, calculated as

$$\left\langle \Omega^* \right\rangle = \frac{\partial \left\langle V^* \right\rangle}{\partial x^*} - \frac{\partial \left\langle U^* \right\rangle}{\partial y^*} \qquad (5\text{-}3)$$

where the derivatives were determined using Green’s theorem as described in Appendix IV. The position and shape of the wake is again evident from the shear layers either side of the wake centre. It is apparent that the wake velocity distribution can be represented by a vorticity distribution as suggested by Smith (1966). The counter rotating vortex pair is evident in the build-up of vorticity at mid pitch. As the wake reaches the rear portion of the blade passage (Figure 5-4 (d)-(f)), the unsteadiness of the flow increases the random error of the measured velocities, which are amplified in the calculation of vorticity. Along the forward region of the suction surface and along the pressure surface the wake centre line is stretched. The stretching of the wake centre line reduces the magnitude of vorticity in the wake according to Kelvin's theorem.

5.4 Convection of wake turbulence through a turbine cascade

The use of 2D LDA allows the simultaneous measurement of both components of the velocity vector in the measurement plane. From these measurements it is possible to calculate the ensemble averaged flow velocity and the 2D Reynolds stresses.

5.4.1 *Turbulent kinetic energy*

The turbulent kinetic energy, *TKE*, is defined as (Tennekes and Lumley, 1987)

$$TKE = \tfrac{1}{2}\overline{u'_i\, u'_i} \qquad (\text{5-4})$$

The ensemble-average non-dimensional *TKE* for the 2D flow was calculated from the 2D LDA measurements according to

$$\left\langle TKE^* \right\rangle = \tfrac{1}{2}\left\langle \left\langle u'^{2^*} \right\rangle + \left\langle v'^2 \right\rangle^* \right\rangle \qquad (\text{5-5})$$

and is presented at a series of six time instants through the wake passing cycle in Figure 5-5. As described in §5.3 above, the kinematic wake convection is apparent, with the wake clearly distinguished from the undisturbed flow by high levels of *TKE*.

The response of the boundary layer to the wake passing can be seen in Figure 5-5 (f) where very high levels of turbulent kinetic energy are observed near the rear of the suction surface. The boundary layer response to wake passing is discussed in Chapter 6 and Chapter 7.

Along the pressure side of the channel, the *TKE* of the wake fluid is observed to drop as it convects through the bladerow. A combination of elongation of the wake centre line and the convective transport away from the pressure surface is responsible for this reduction in *TKE*. Similarly, the stretching that results as the blade chops the wake causes the *TKE* to reduce over the forward part of the suction surface. This is evident in Figure 5-5 (c) & (d).

The highest levels of *TKE* outside of the boundary layer occur in Figure 5-5 (d) and (e). These high regions of *TKE*, labelled *G* and *H*, occur where the wake fluid accumulates near the suction surface. The perturbation velocity vectors, a few of which are superimposed in Figure 5-5 (d), indicate that the peak *TKE* occurs slightly below the centres of the counter rotating vortex pair. The elevated *TKE* does not penetrate to the boundary layer. In this region the turbulence intensity based on isentropic exit velocity is *Tu=7%* where the wake centreline turbulence intensity at the leading edge plane is *Tu=5%*. The increase in the level of *TKE* is seen to begin in Figure 5-5 (c) at label *F* and continue through Figure 5-5 (d)-(f), although it is the extent and not the level that increases between *G* and *H*.

The production of *TKE*, P_{TKE}, is given by Tennekes and Lumley (1987) as

$$P_{TKE} = -\overline{u'_i u'_j}\frac{\partial U_i}{\partial x_j} \tag{5-6}$$

The measured ensemble averaged Reynolds stresses were used together with the ensemble average velocity derivatives calculated from Green's theorem, as described in Appendix IV, to evaluate the ensemble averaged non-dimensional production of *TKE* in the blade-to-blade plane according to

$$\left\langle {P_{TKE}}^{*}\right\rangle = -\left\langle u'^{2^*}\right\rangle\frac{\partial\left\langle U^*\right\rangle}{\partial x^*} - \left\langle v'^{2^*}\right\rangle\frac{\partial\left\langle V^*\right\rangle}{\partial y^*} - \left\langle u'v'^*\right\rangle\left(\frac{\partial\left\langle U^*\right\rangle}{\partial y^*} + \frac{\partial\left\langle V^*\right\rangle}{\partial x^*}\right) \tag{5-7}$$

The results are presented in Figure 5-6 with the labels copied from Figure 5-5. It is apparent that the increased levels of *TKE* are a direct result of *TKE* production. The highest production levels occur at labels *F* and *G* in Figure 5-6 (c) & (d) and it is these regions of high production that subsequently lead to regions of high *TKE* at *G* and *H*.

The production of *TKE* occurs when the turbulence extracts work from the mean flow and this occurs in regions having high turbulent stresses and high spatial velocity gradients. The turbulent stresses are confined to the wake fluid and so production occurs when the wake fluid enters regions of high spatial velocity gradients. However, it is not only the magnitudes, but also the directions that are important. If the turbulent stresses and velocity gradients are aligned, the turbulent production is enhanced.

Throughout the wake passing cycle, it is apparent that the production of *TKE* occurs in the wake fluid. This is due to the coexistence of turbulent stresses and the wake shear layers. Very high levels of *TKE* production are measured in the boundary layers on the rear part of the suction surface. This is considered in Chapter 7.

5.4.2 Anisotropy

An isotropic turbulent flow is one having the same characteristics of turbulence in all directions. For any turbulent flow, it is possible to define the principal stress direction, ψ, as that orientation having zero shear stress according to

$$\langle\psi\rangle = \tfrac{1}{2}\tan^{-1}\left(\frac{2\left\langle u'v'^{*}\right\rangle}{\left\langle u'^{2^*}\right\rangle - \left\langle v'^{2^*}\right\rangle}\right) \qquad (5\text{-}8)$$

The principal normal stresses may then be found by a co-ordinate transformation to align the measured turbulent quantities to the calculated principal directions

$$\left\langle u_{\psi}'^{2^*}\right\rangle = \left\langle u'^{2^*}\right\rangle\cdot\cos(\langle\psi\rangle) - \left\langle v'^{2^*}\right\rangle\cdot\sin(\langle\psi\rangle) \qquad (5\text{-}9)$$

$$\left\langle v_{\psi}'^{2^*}\right\rangle = \left\langle u'^{2^*}\right\rangle\cdot\sin(\langle\psi\rangle) - \left\langle v'^{2^*}\right\rangle\cdot\cos(\langle\psi\rangle) \qquad (5\text{-}10)$$

A measure of the anisotropy, α, may then be inferred by taking the modulus of the ratio of these principal turbulent stresses

$$\begin{aligned}\langle\alpha\rangle &= \left|\frac{\left\langle u_{\psi}'^{2^*}\right\rangle}{\left\langle v_{\psi}'^{2^*}\right\rangle}\right| \quad \cdots \quad if \quad \left\langle u_{\psi}'^{2^*}\right\rangle > \left\langle v_{\psi}'^{2^*}\right\rangle \\ &= \left|\frac{\left\langle v_{\psi}'^{2^*}\right\rangle}{\left\langle u_{\psi}'^{2^*}\right\rangle}\right| \quad \cdots \quad if \quad \left\langle v_{\psi}'^{2^*}\right\rangle > \left\langle u_{\psi}'^{2^*}\right\rangle\end{aligned} \qquad (5\text{-}11)$$

so that the ratio is greater than unity with a value of unity indicating isotropy

Figure 5-7 shows contours of α and it is apparent that the wake fluid is anisotropic while the undisturbed fluid is essentially isotropic with low turbulent stresses magnitudes. As the wake fluid reaches the point of peak *TKE* production, identified by label ‘F’ in Figure 5-6 (c), the level of anisotropy of the wake fluid falls. This drop in anisotropy continues and by Figure 5-7 (e), the wake fluid, identified as having high *TKE* at label ‘H’ in Figure 5-5 (e), is seen to be essentially isotropic in the measurement plane[14]. The *TKE* production described in §5.4.1 thus results in isotropic turbulence. The wake fluid near the pressure surface can also be seen to become

---

[14] Strictly speaking, isotropy can only be inferred once the out of plane component of the Reynolds stress is known. The 2D LDA measurements do not provide any information about the third component and the reference to isotropy is purely in a two-dimensional sense.

isotropic as it convects through the bladerow. This is the same region identified as having low *TKE* due to stretching of the wake centre line in Figure 5-5.

A possible reason for the high production regions labelled *F* and *G* arises due to the change in flow direction through the bladerow. The turbulent stresses in the wake are oriented along the wake centreline. As the main flow is turned in the bladerow, the velocity gradients and turbulent stresses align thereby enhancing the production of *TKE*. It is proposed that the turbulent stresses in the wake do not orientate themselves to the mean flow instantaneously and *TKE* production may occur in the bladerow as a result.

5.5 Ensemble average wavelet analysis of LDA data

The wavelet transform provides a time–frequency decomposition of a signal and is thus able to provide information about the scales of turbulence in an unsteady flow. However, wavelet analysis is traditionally applied to evenly sampled data using FFT techniques to reduce the computational time. Moreover, for fine scale resolution high data rates are required. For these reasons, LDA data is not generally suited to wavelet analysis. However, at certain locations in the current data set the mean data rate was sufficient to permit a continuous wavelet analysis of limited frequency resolution.

The wavelet analysis was conducted using a novel adaptation of traditional wavelet algorithms as described in Appendix III. The discrete Fourier transform of the unevenly sampled data was calculated directly rather than using traditional FFT techniques. The convolution of the data and the analysing wavelet was performed in the frequency domain by taking the product of the discrete Fourier transform and analysing wavelet. Finally, due to careful selection of the number of frequencies at which the discrete Fourier transform was calculated, it was possible to obtain the wavelet transform as the inverse FFT of this product. The wavelet transforms were ensemble averaged.

The discrete Fourier transform required for the wavelet transform was calculated at $N=128$ frequencies per wake passing. This was the maximum resolution that was permitted by the available data. To ensure that adequate data was present in each wake passing cycle, the wavelet transform was only counted in the ensemble average if there were more than $NL=128$ LDA samples in the ensemble (i.e. $NL > N$).

The complex valued Morlet wavelet, defined as

$$\varphi_0(\eta) = \pi^{-1/4} e^{i\omega_0\eta} e^{-\eta^2/2} \qquad (5\text{-}12)$$

and shown in Figure 5-8 was used for the wavelet analysis. This wavelet was selected due to its resemblance to a travelling wave packet such as those measured in Chapter 4. The value $\omega_0=6.0$ was selected to approximate admissibility (see Farge (1992)). Following Torrence and Compo (1998), the smallest scale was taken as *1/64* of the wake passing cycle and the scale resolution was chosen as $\delta j=0.125$ thus providing *48* wavelet scales.

5.5.1 Ensemble average wavelet description of Reynolds stresses

The wavelet analysis was performed at three locations as shown in Figure 5-1. Point *I* is representative of the flow in which the wake has not been significantly distorted, while *J* is located at the point where peak *TKE* production levels were observed in Figure 5-6 (c). Finally, point *K* is representative of the high turbulence flow over the rear of the suction surface, which results from the production of isotropic turbulence at locations such as *J*.

Due to the change in the mean flow direction through the turbine passage, the velocities at each location were aligned to the local time average flow direction before performing the wavelet transforms. This allows comparison of the streamwise and cross-stream velocity components at the different locations. The streamwise velocity component is referred to with subscript *1*, while the cross-stream component is referred to with subscript *2*. The shear stress component is referred to with mixed subscripts.

Following Volino (1998) the wavelet transforms of the Reynolds stresses were calculated from the wavelet transforms of the velocity components according to

$$\begin{aligned}
\left\langle W({u_1}'^{2^*})\right\rangle &= \left\langle W({u_1}'^{*})\cdot W({u_1}'^{*})^{\bullet}\right\rangle \\
\left\langle W({u_2}'^{2^*})\right\rangle &= \left\langle W({u_2}'^{*})\cdot W({u_2}'^{*})^{\bullet}\right\rangle \qquad (5\text{-}13) \\
\left\langle W({u_1}'{u_2}'^{*})\right\rangle &= \left\langle W({u_1}'^{*})\cdot W({u_2}'^{*})^{\bullet}\right\rangle
\end{aligned}$$

and the wavelet spectra were then calculated as the time average of the ensemble average wavelet transforms according to

$$\begin{aligned}
\overline{W(u_1'^{2^*})} &= \sum_{t=0}^{t_0} \left\langle W(u_1'^{2^*}) \right\rangle dt \\
\overline{W(u_2'^{2^*})} &= \sum_{t=0}^{t_0} \left\langle W(u_2'^{2^*}) \right\rangle dt \qquad (5\text{-}14) \\
\overline{W(u_1'u_2'^{*})} &= \sum_{t=0}^{t_0} \left\langle W(u_1'u_2'^{*}) \right\rangle dt
\end{aligned}$$

The results of the ensemble averaged wavelet transforms of the Reynolds stress components are presented in Figure 5-9 to Figure 5-11. The time average wavelet spectra are shown on log-log plots, much the same as traditional Fourier spectra[15]. The top left plot in Figure 5-9 to Figure 5-11 shows a superposition of all three wavelet spectra to aid comparison. The unsteady contributions to the wavelet spectra are presented on the adjacent contour plots sharing a common abscissa. These show the ensemble averaged wavelet coefficients non-dimensionalised at each scale by the time average wavelet spectra. Data presented in this way reveals the periodic content of the wavelet transform at each scale. The time was non-dimensionalised by the wake passing period and data was duplicated onto two wake passing periods to emphasise periodicity. Frequency was non-dimensionalised by the inverse of the flow time scale, given by the time mean isentropic exit velocity and the blade chord length ($f_{ref}=C/V_{2is}$). All velocities were non-dimensionalised by the time mean isentropic exit velocity prior to the calculation of the wavelet transforms.

Figure 5-9 shows the wavelet transform of the Reynolds stresses at position *I*. The streamwise component of Reynolds stress shown in Figure 5-9 (a)(i) has the greatest magnitude over the whole frequency range, with the highest energy concentrated at the blade passing frequency and its first harmonic. The cross-stream component shown in Figure 5-9 (b)(i) does not share the same spectral distribution. It decays more slowly above $f^*=2.4$. This is indicative of the anisotropy of the wake turbulence at this position. The shear stress component shown in Figure 5-9 (c)(i) has the same spectral distribution as the streamwise component, however the level is typically an order of magnitude less than the normal component.

The unsteady contribution to the streamwise component of the normal Reynolds stress at position *I* is shown in Figure 5-9 (a)(ii). The wake passage is clearly identified by the large contributions to the mean spectrum at high frequencies.

---

[15] Volino (1998) presents a comparison of Fourier and wavelet spectra.

Increasing contour levels at a given t/τ_0 indicate a very shallow slope to the instantaneous spectrum and it can be concluded that a range of frequencies above $f^*=5.0$ contribute to the instantaneous spectrum of the wake fluid. The wake passing is thus not characterised by a single eddy size (frequency) but rather by a whole range of eddies of $f^*>10.0$ $(\log_2 f^*>3.32)$.

At position *I*, the counter rotating vortex pair is not yet evident (see §5.3.2 and Figure 5-3). Wake passing is thus a single event characterised by a cross-stream velocity component followed by a streamwise fluctuation. This behaviour may be inferred from the high frequency content of Figure 5-9 (a)(ii), (b)(ii) & (c)(ii) as the peak of the cross-stream spectra precedes the streamwise component. The peak of Reynolds shear stress occurs at the centre of the wake.

The Reynolds stress components at position *J* are shown in Figure 5-10. The *TKE* at this location is higher than at *I* and so the levels of all Reynolds stress on the time average spectra are elevated. The streamwise component retains the basic shape, with the highest time mean energy levels at the blade passing frequency and its first harmonic. The spectral decay is however not as steep as at *I*. Moreover, the cross-stream component exceeds the streamwise component for $2.3<f^*<20.0$. The increased duration of the high frequency contributions to all the Reynolds stress components at position *J* (Figure 5-10 (a)(ii), (b)(ii) &(c)(ii)), show that the temporal extent of the wake has increased. This is due to the stretching of the wake over the suction surface as described in §5.3.2.1 and evident in Figure 5-3.

The effect of the counter rotating vortex pair can be seen in the high frequency content of the wavelet maps. At $t/\tau_0=0.35$, the streamwise component has a high contribution corresponding to the increased velocity due to the approaching wake (see Figure 5-3 (c)). By $t/\tau_0=0.45$, the streamwise component has diminished, but the cross-stream component has increased to a peak level. This corresponds to the centre of the vortex pair where there is a strong cross-stream velocity component directed towards the blade. As the vortex pair convects past point *J*, the cross-stream component of Reynolds stress decreases and the streamwise component increases to a maximum level. The distribution of Reynolds shear stress mimics the streamwise component. The Reynolds shear stress is thus low at the centre of the counter rotating vortex pair, but high under the influence of each of the vortices.

Finally, at position *K* the wake turbulence is nearly isotropic according to Figure 5-7 and the spectral distributions of the streamwise and cross-stream components of Figure 5-11 (a)(i) & (b)(i) have similar levels. The broadening of the wake is seen to continue and the passage of the counter rotating vortex pair is again evident: the streamwise component of Reynolds stress has a trough at $t/\tau_0=0.84$ while the cross-stream component has a peak corresponding to the centre of the vortex pair. By contrast to position *J*, the Reynolds shear stress is characterised by three peaks at high frequency in Figure 5-11 (c)(ii).

The wavelet transforms of the Reynolds stress components at position *I*, *J* and *K* show the development of the Reynolds stress spectra through the cascade. At positions *I* and *J*, the wake passing significantly alters the shape of the spectra with greater components from the higher frequencies during the wake passing. However, by position K where the turbulence is more isotropic due the production of *TKE* within the passage, the spectral distribution of the Reynolds stress components shows less variation through the cycle.

5.5.2 Ensemble average wavelet description of turbulent kinetic energy

From the traditional definition of *TKE*, it is possible to define the wavelet transform of *TKE* according to

$$W(TKE) = \tfrac{1}{2} W(u'_i) \cdot W(u'_i)^{\bullet} \tag{5-15}$$

The non-dimensional ensemble average wavelet transform of *TKE* can thus be calculated from the measured 2D LDA data according to

$$\left\langle W(TKE^{*}) \right\rangle = \left\langle \tfrac{1}{2} \left(W(u'^{*}) \cdot W(u'^{*})^{\bullet} + W(v'^{*}) \cdot W(v'^{*})^{\bullet} \right) \right\rangle \tag{5-16}$$

Moreover, as the ensemble average spatial velocity gradients are independent of frequency, it is possible to define the wavelet transform of the production of *TKE* according to

$$W(P_{TKE}) = -W(u'_i) \cdot W(u'_j)^{\bullet} \cdot \left\langle \frac{\partial U_i}{\partial x_j} \right\rangle \tag{5-17}$$

As for *TKE*, the non-dimensional ensemble average production of *TKE* may be calculated form the 2D LDA measurements according to

$$\left\langle W(P_{TKE}{}^{*})\right\rangle = \left\langle -W(u'^{*})\cdot W(u'^{*})^{\bullet}\cdot\frac{\partial\left\langle U^{*}\right\rangle}{\partial x^{*}} - W(v'^{*})\cdot W(v'^{*})^{\bullet}\cdot\frac{\partial\left\langle V^{*}\right\rangle}{\partial y^{*}} - W(u'^{*})\cdot W(v'^{*})^{\bullet}\cdot\left(\frac{\partial\left\langle U^{*}\right\rangle}{\partial y^{*}}+\frac{\partial\left\langle V^{*}\right\rangle}{\partial x^{*}}\right)\right\rangle \qquad (\text{ 5-18})$$

With the time-frequency decomposition of the turbulent quantities it is possible to examine which of the scales contain the turbulent energy and which scales are responsible for the production of *TKE* at different times in the wake passing cycle.

The wavelet transform of *TKE* at all three positions is presented in Figure 5-12. These plots have the same layout as Figure 5-9 to Figure 5-11 with the time average spectra on the left and the ensemble average contours on the right. The time average spectra show all three positions overlaid with the bold line indicating the spectra at the relevant location. At position *I*, Figure 5-12 (a)(i), the level of *TKE* is low and most of the spectral energy is concentrated at low frequencies. The wake passing increases the high frequency contributions to *TKE* and flattens the spectrum, as was the case for the Reynolds stress components at this position.

Position *J* corresponds to the location of highest *TKE* and this is evident from the elevated levels of *TKE* throughout the spectrum in Figure 5-12 (b)(i). The slope of the spectra is not significantly different to that at position *I* for frequencies above *f=6.0*, however, below this the spectrum at *J* has a greater slope. As at position *I* the slope of the instantaneous spectrum is reduced under the wake as indicated by the contour levels increasing with frequency under the wake in Figure 5-12 (b)(ii).

It was noted previously that the turbulence of the wake fluid at position *K* is nearly isotropic. The contributions of the wake fluid to the *TKE* spectrum are characterised by their uniformity across the frequency range in Figure 5-12 (c)(ii). Thus although the level of the *TKE* spectrum increases under the wake, the shape does not alter as is did at positions *I* and *J*. At this location, *K*, the *TKE* is slightly lower than at position *J* and this deficit in *TKE* can be attributed to the lower contributions from frequencies below $f^{*}=2.8$.

The spectra of *TKE* production are shown in Figure 5-13. The layout of this figure is the same as Figure 5-12. At position *I*, *TKE* production is low and concentrated entirely within the wake. The unsteady contributions at high frequency occur at the time corresponding to the peak Reynolds shear stress. The high levels at high frequencies again indicate a flattening of the spectrum under the wake due to increased contributions from higher frequencies.

Position *J* is the location of peak *TKE* production. The spectrum of Figure 5-13(b)(i) shows an elevated level over the complete frequency range. Again, the unsteady contributions cause the spectrum to flatten. Production at higher frequencies is related to the passage of the counter rotating vortex pair, with an initial region of elevated production followed a second higher peak after the passing of the vortex pair.

The wavelet transform of the production of *TKE* at the final point, *K*, is shown in Figure 5-13 (c). This point exhibits the lowest level of *TKE* production as indicated by the low levels of the time average spectrum of Figure 5-13 (c)(i). The ensemble average spectrum shows smaller variations in the levels of *TKE* production through the wake passing cycle. Furthermore, as in the case of *TKE* at this location, there is no significant variation in the contributions from different scales.

In summary, the wavelet transforms show that a wide range of frequencies contribute to the turbulence and that no isolated frequency is responsible for elevated levels of *TKE* or *TKE* production. The spectral distributions of the wake and non-wake fluid were observed to be different. The spectra within the anisotropic wake, at positions *I* and *J*, have a greater contribution from the higher frequency components. This has the effect of changing the shape of the *TKE* and *TKE* production spectra at different times during the wake passing cycle. However, the *TKE* and *TKE* production spectra of the more isotropic turbulence at position *K* showed less variation in shape during the wake passing cycle.

5.6 Conclusions

Measurements of the wake convected through a turbine blade row were made using 2D LDA. The unprecedented resolution of the measurement grid and the availability of the Reynolds stress components of the 2D flow provide a detailed description of the ensemble averaged mean and turbulent flow fields.

The measurements confirm that the wake convection may be described by simple kinematics with the wake fluid being bowed, re-orientated, elongated and stretched as it passes through the blade passage. The counter rotating vortices pair established by the wake in the blade passage was clearly visible in plots of perturbation vectors.

Measurements of the convected wake turbulence showed increased levels of *TKE* due to the production of *TKE* by the interaction of the Reynolds stresses and the strain rate field of the flow through a turbine blade. The wake fluid was shown to be anisotropic until the point of peak *TKE* production was reached. The turbulence production within the blade row was observed to produce a more nearly isotropic turbulence and to increase the levels of *TKE*.

A novel algorithm for the wavelet analysis of unevenly sampled data was used to perform the ensemble average wavelet analysis at three positions in the bladerow. The Reynolds stress components were shown to be composed of a complete spectrum of eddies with no particular eddy size responsible for any of the Reynolds stress components, or the *TKE* or production of *TKE*. The wake fluid was characterised by a flatter spectrum than the non-wake fluid.

5.7 Figures

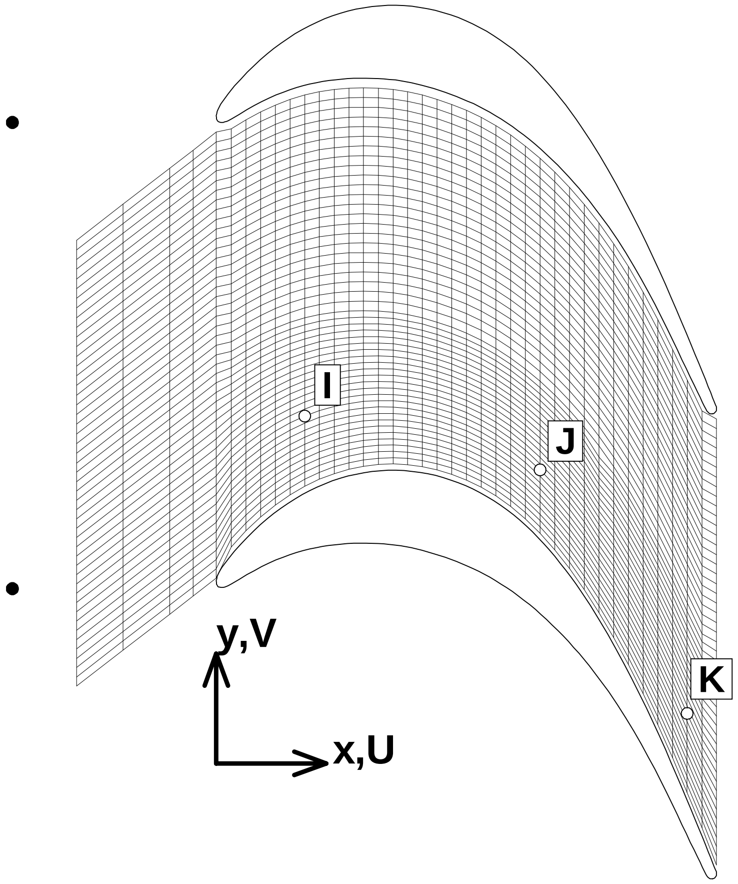

Figure 5-1: Measurement grid for 2D LDA measurements of the convection of a bar wake through the T106 LP turbine cascade

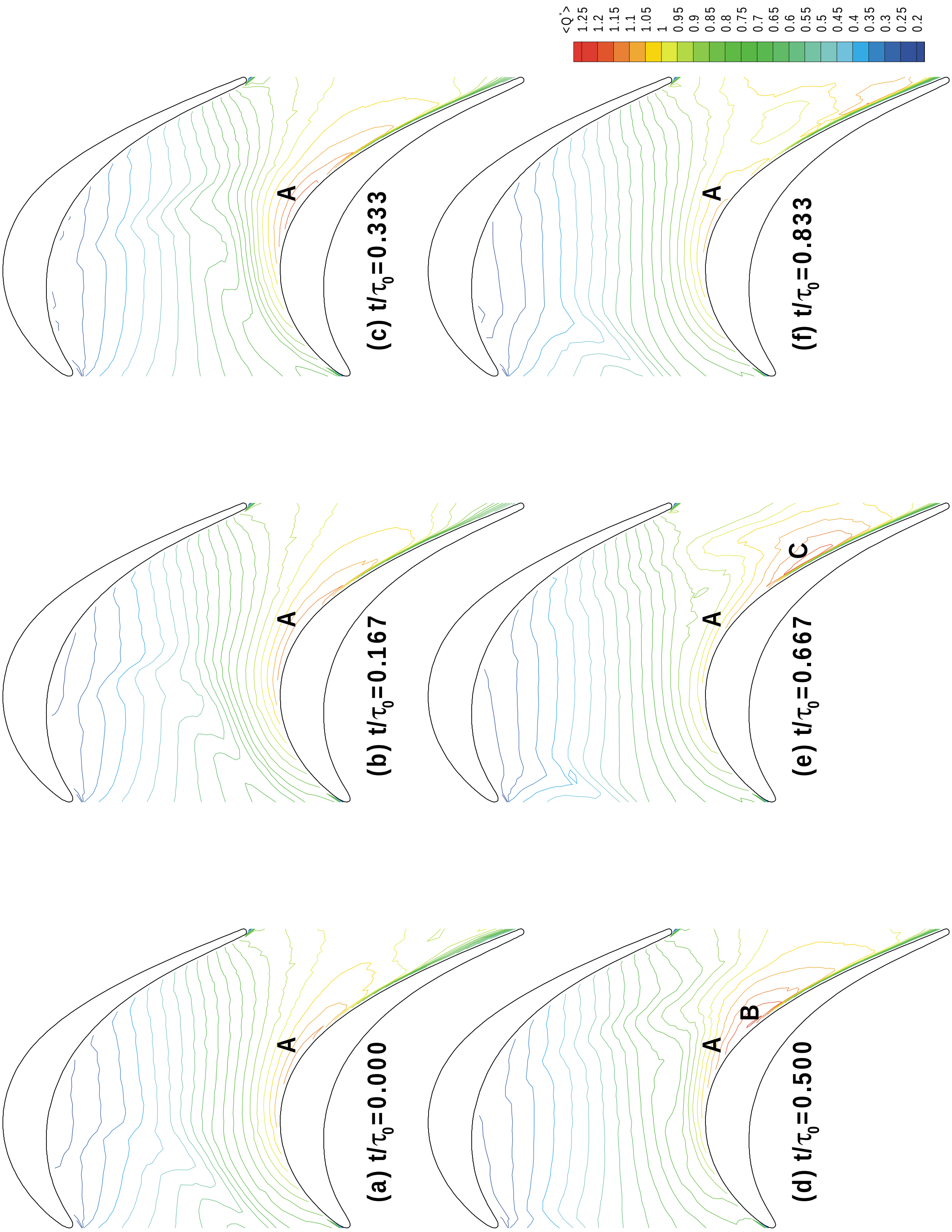

Figure 5-2: Measured ensemble average non-dimensional flow velocity at six equal time intervals through the wake passing cycle. ***T106, $Re_{2c}=1.6\times10^5$, $\phi=0.83$, $s_b/s_c=1$, $f_r=0.68$***

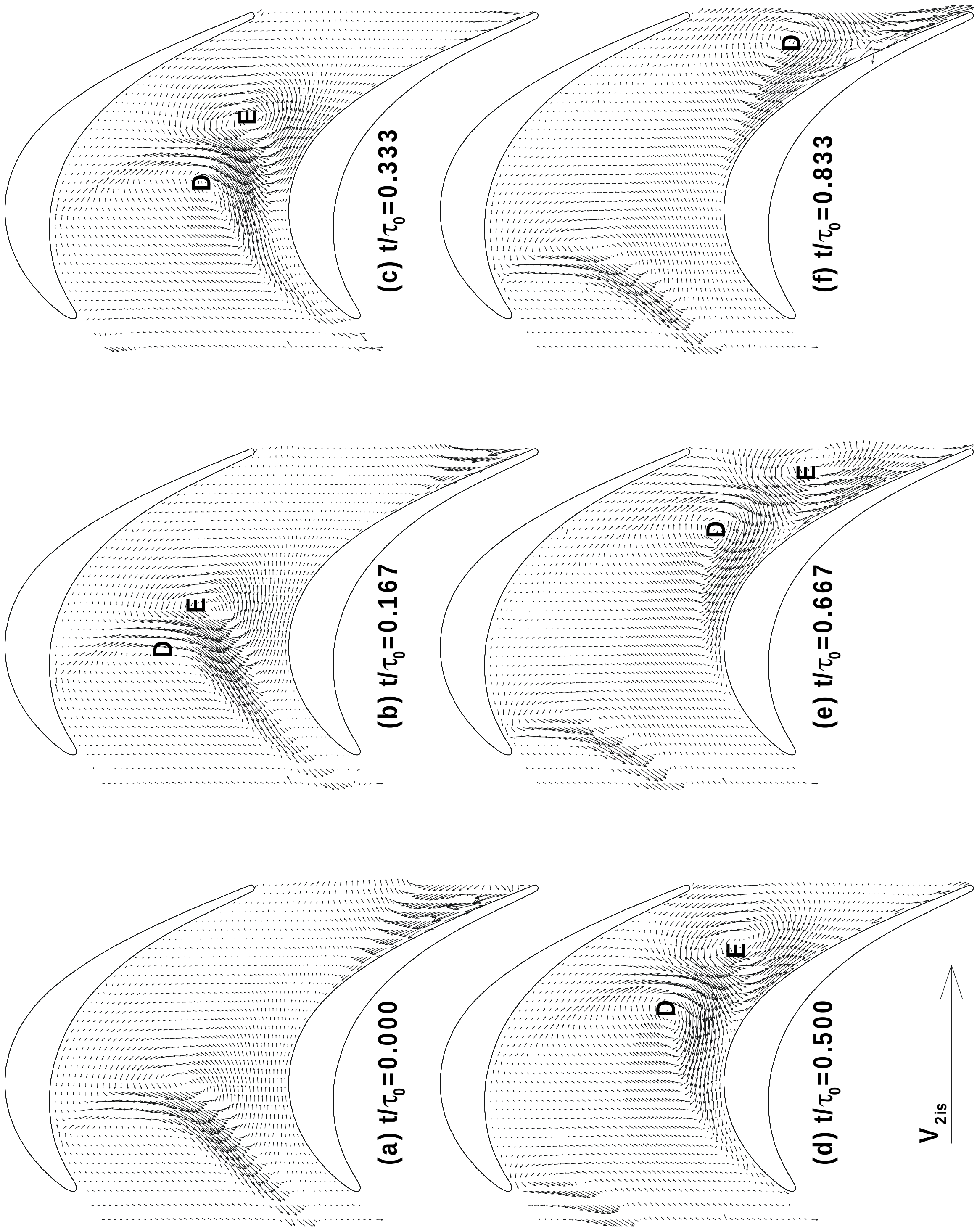

Figure 5-3: Measured ensemble average perturbation velocity vectors. ***T106, $Re_{2c}=1.6\times10^5$, $\phi=0.83$, $f_r=0.68$***

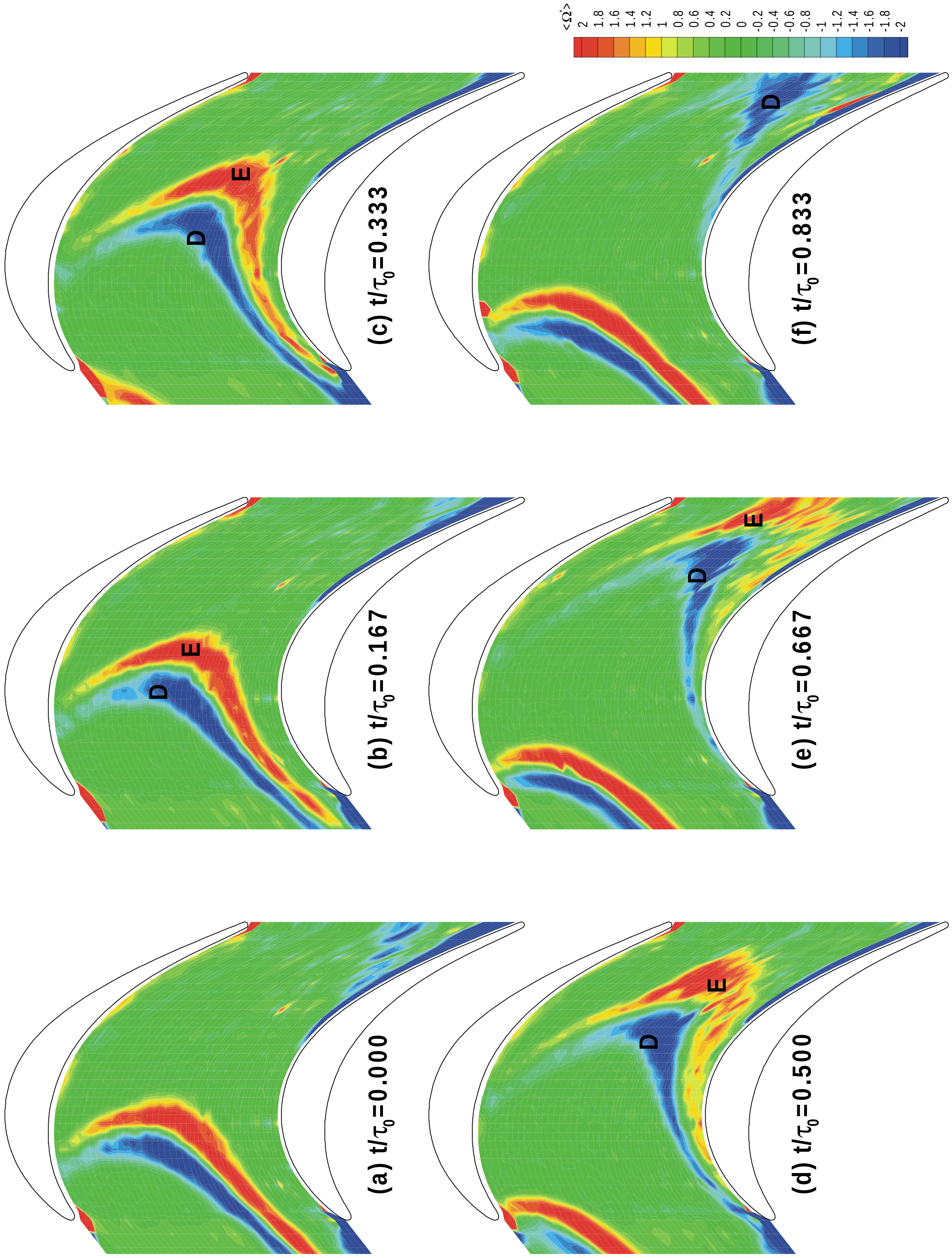

Figure 5-4: Ensemble average non-dimensional vorticity distribution calculated from measured velocities. ***T106, Re_{2c}=1.6×10^5, ϕ=0.83, s_b/s_c=1, f_r=0.68***

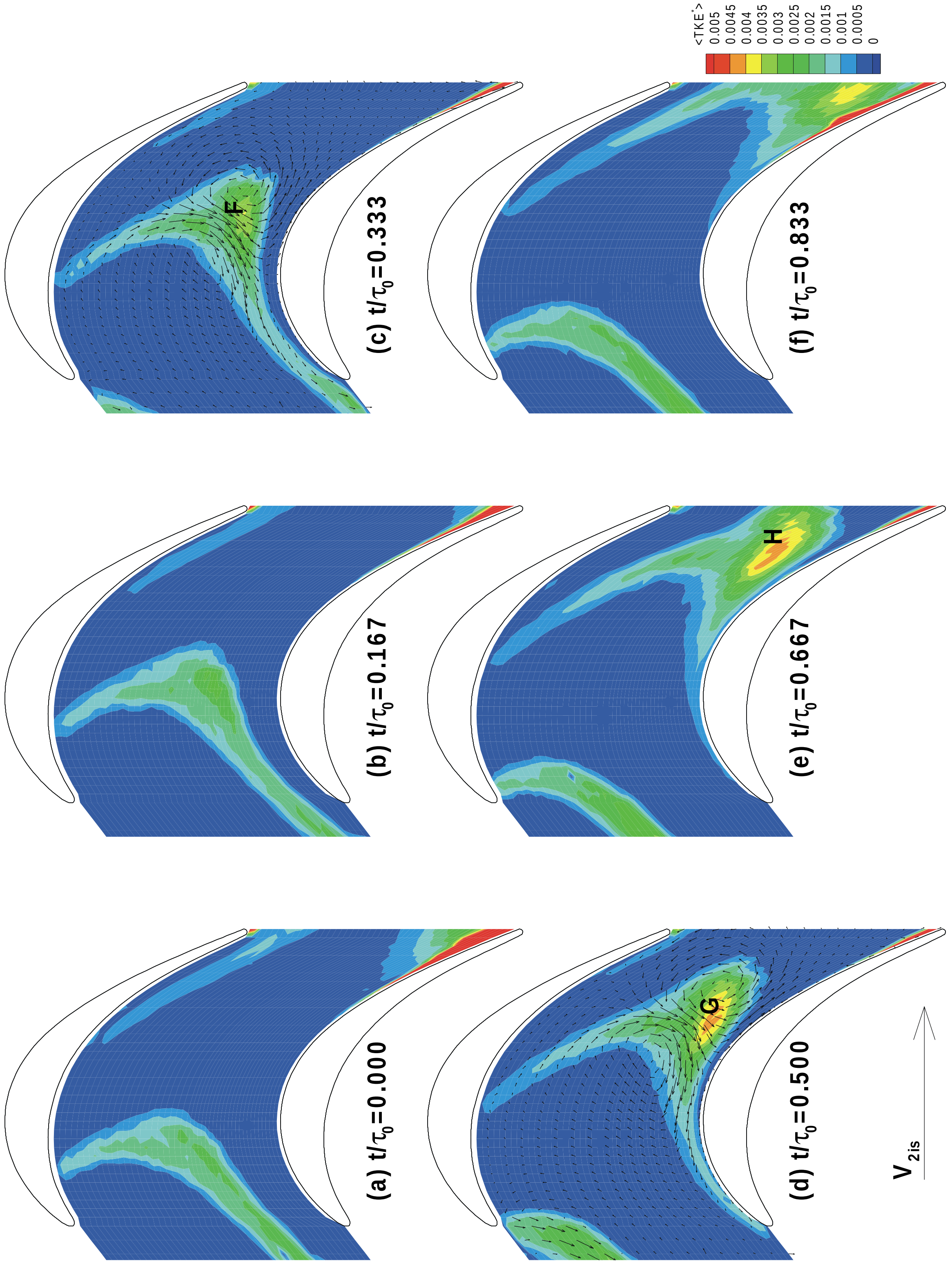

Figure 5-5: Measured ensemble average non-dimensional turbulent kinetic energy. ***T106, $Re_{2c}=1.6\times10^5$, $\phi=0.83$, $s_b/s_c=1$, $f_r=0.68$***

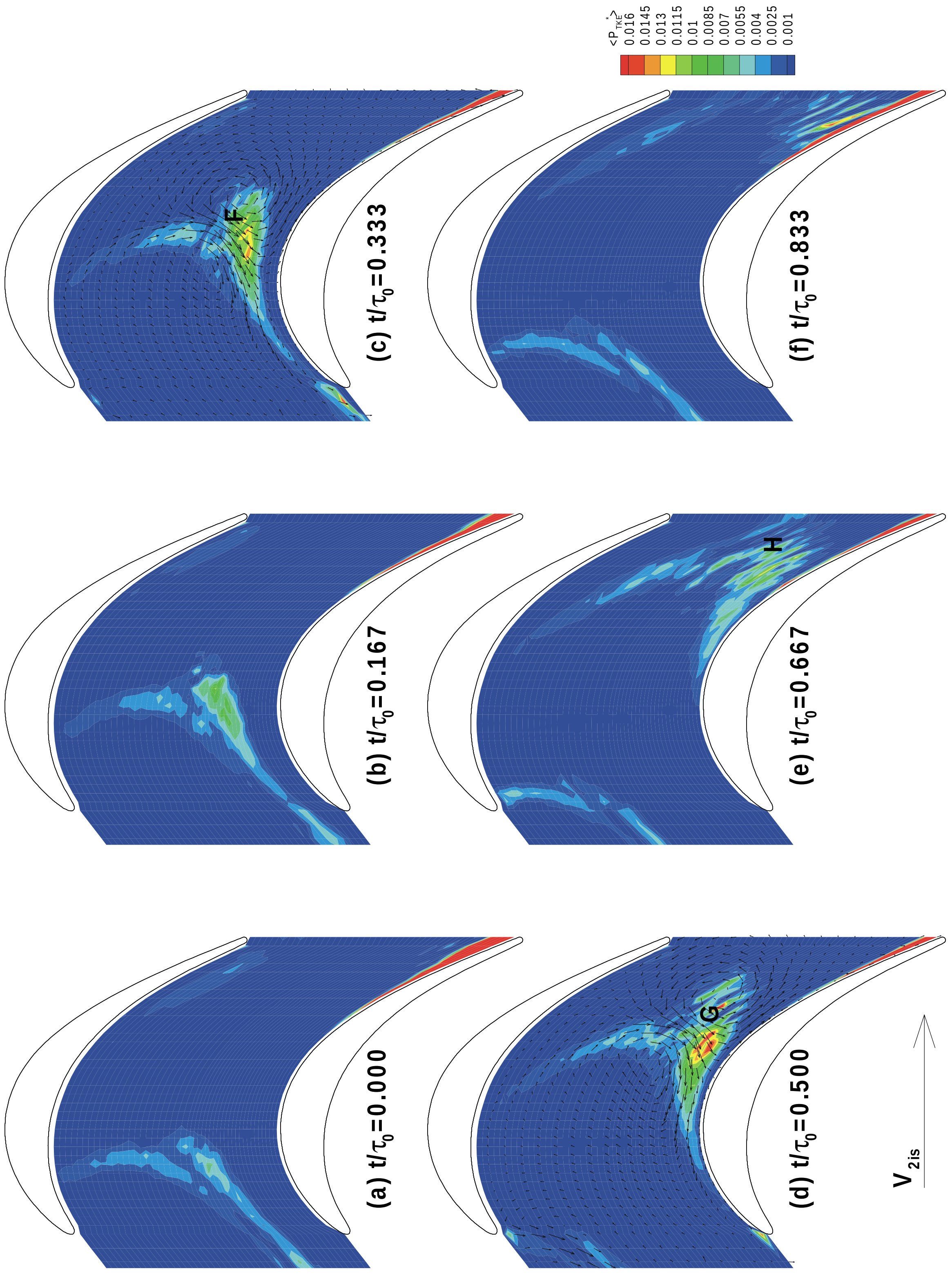

Figure 5-6: Measured ensemble average non-dimensional turbulent kinetic energy production. ***T106, $Re_{2c}=1.6\times10^5$, $\phi=0.83$, $s_b/s_c=1$, $f_r=0.68$***

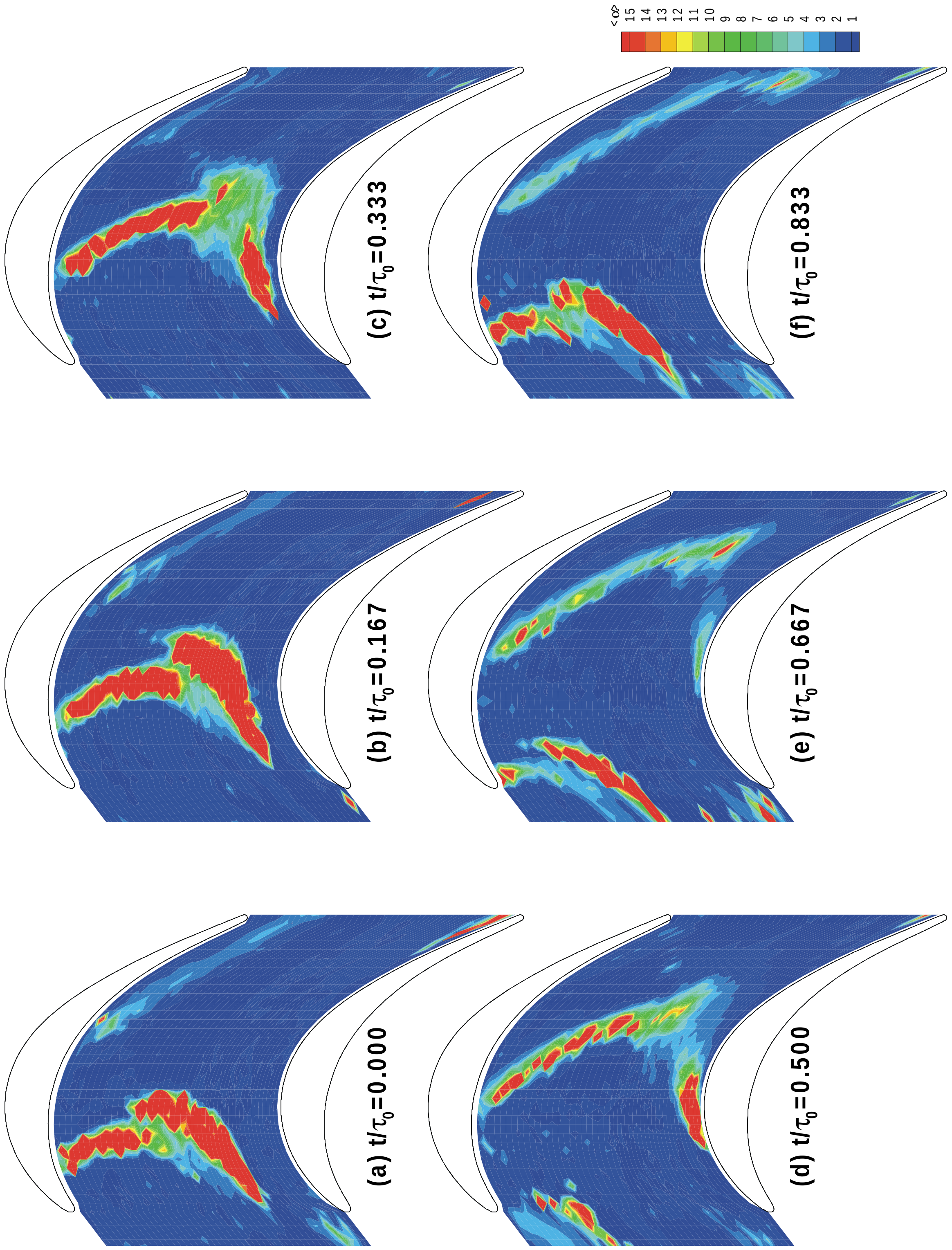

Figure 5-7: Ensemble average anisotropy of measured turbulent stresses. ***T106, Re_{2c}=1.6×10^5, ϕ=0.83, s_b/s_c=1, f_r=0.68***

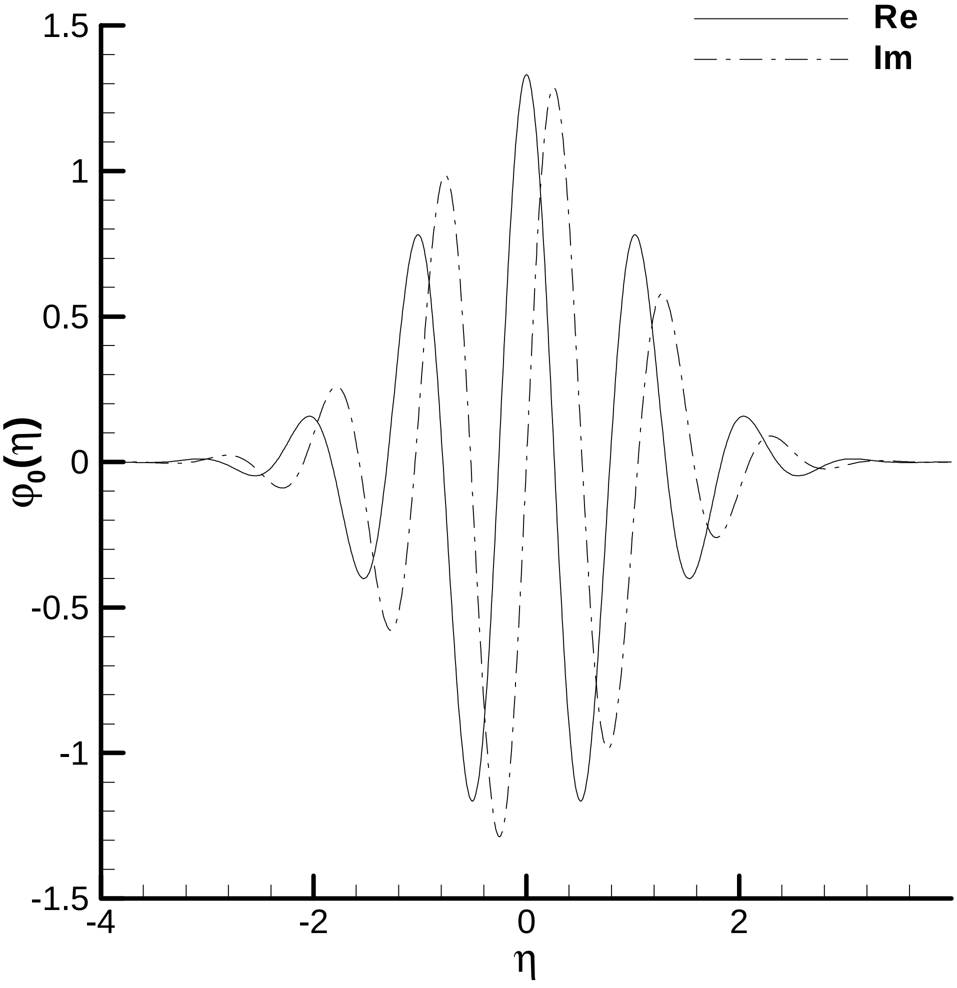

Figure 5-8: Real and imaginary components of the Morlet wavelet (*ω_0=6.0*) used for the analysis of LDA data.

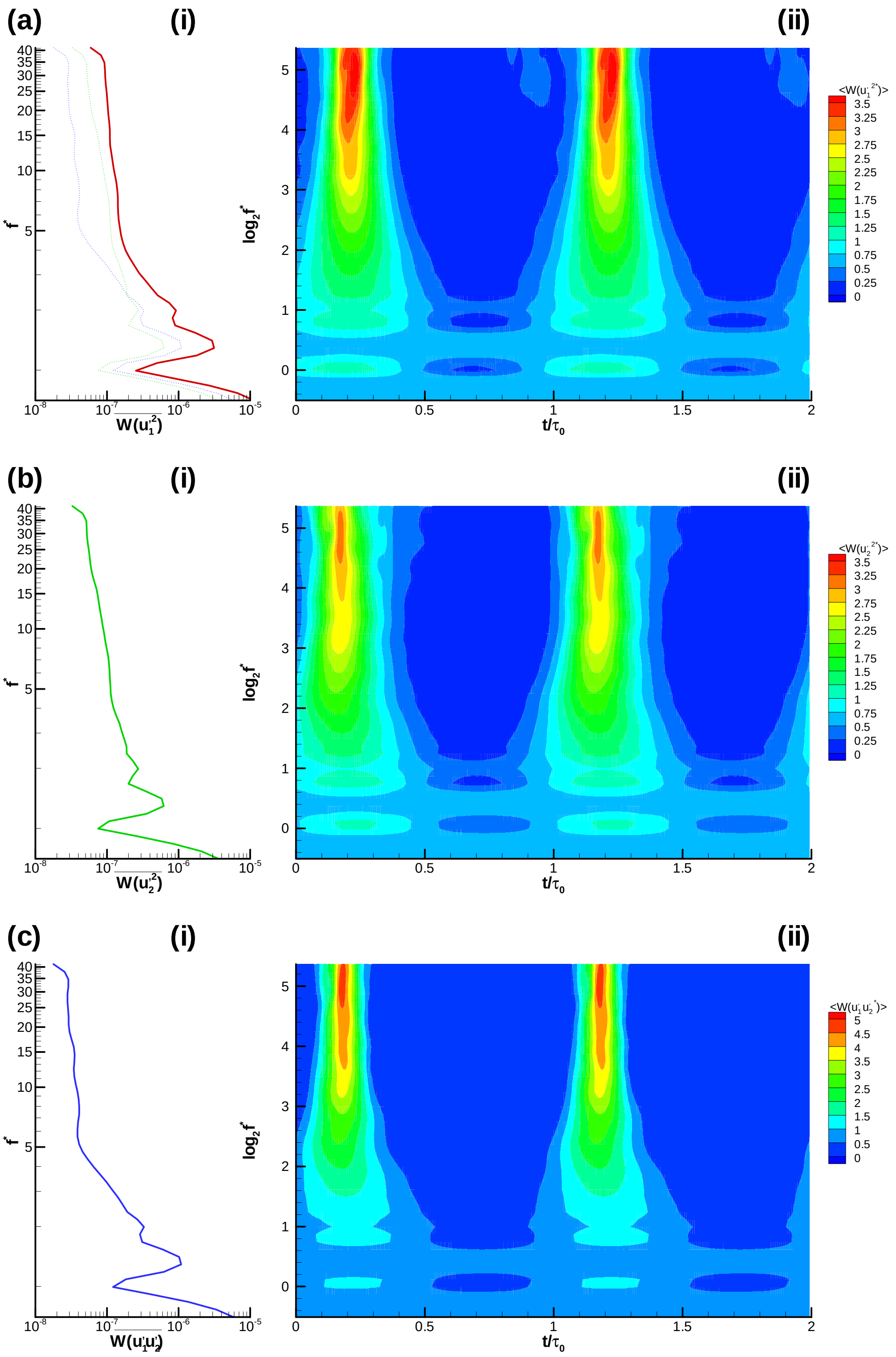

Figure 5-9: Wavelet transform of non-dimensional Reynolds stress components at position *I*, (a) streamwise component, (b) cross-stream component, (c) Reynolds shear stress. In all cases (i) is the non-dimensional time average wavelet spectrum and (ii) shows the non-dimensional ensemble average wavelet coefficients. *T106, Re_{2c}=1.6×10^5, ϕ=0.83, s_b/s_c=1, f_r=0.68*

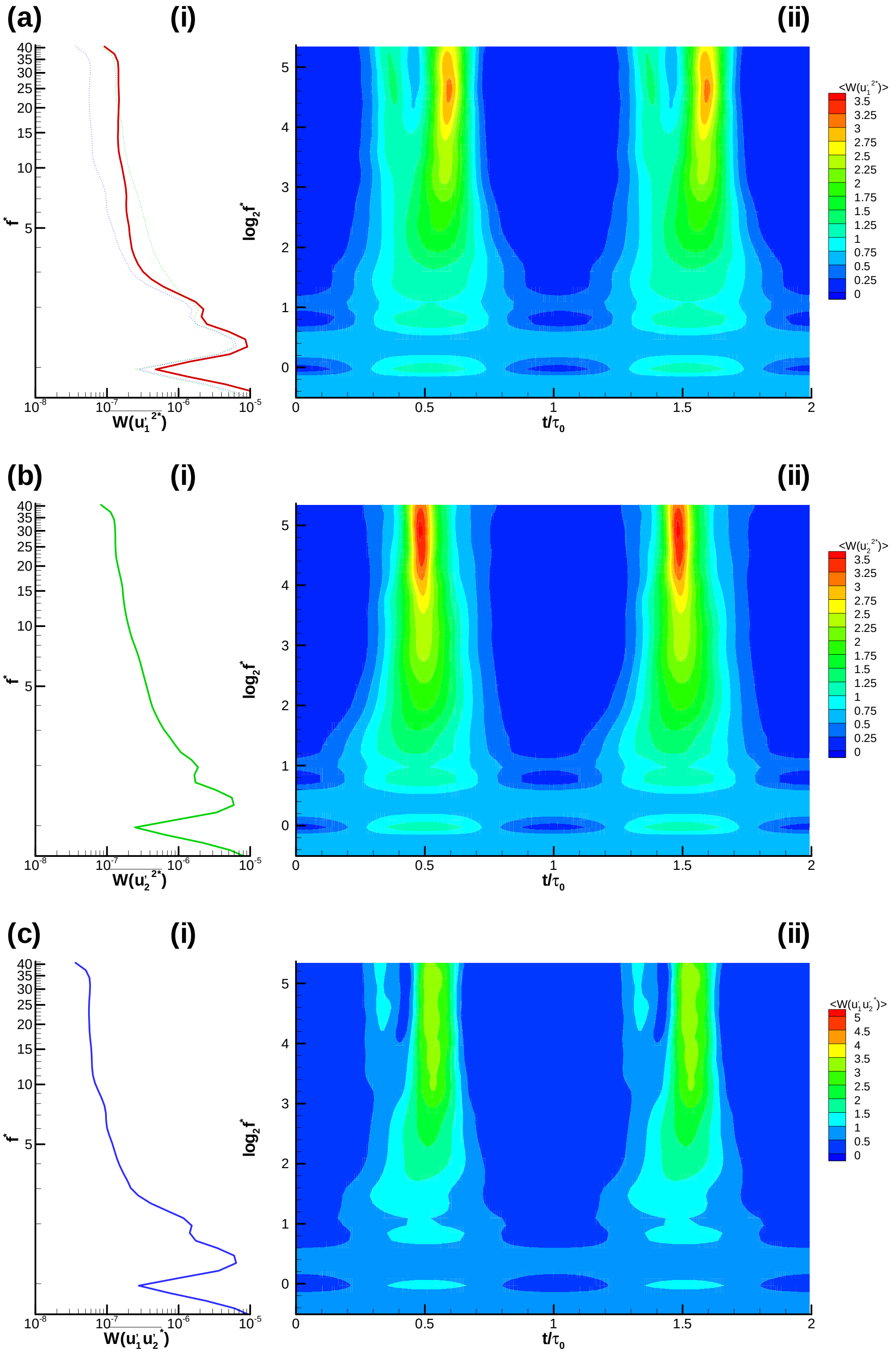

Figure 5-10: Wavelet transform of non-dimensional Reynolds stress components at position *J*, (a) streamwise component, (b) cross-stream component, (c) Reynolds shear stress. In all cases (i) is the non-dimensional time average wavelet spectrum and (ii) shows the non-dimensional ensemble average wavelet coefficients. *T106, $Re_{2c}=1.6\times10^5$, $\phi=0.83$, $s_b/s_c=1$, $f_r=0.68$*

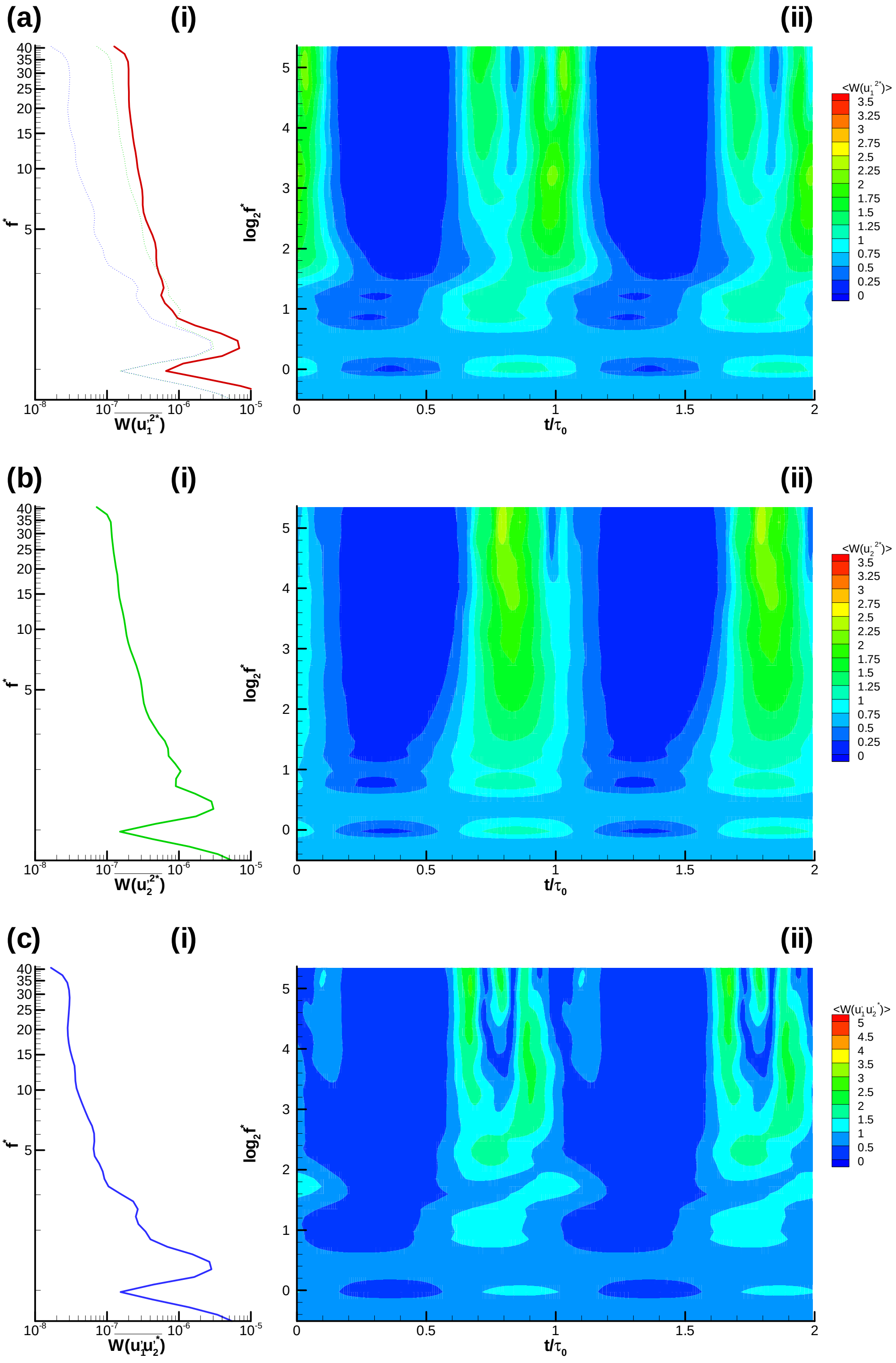

Figure 5-11: Wavelet transform of non-dimensional Reynolds stress components at position *K*, (a) streamwise component, (b) cross-stream component, (c) Reynolds shear stress. In all cases (i) is the non-dimensional time average wavelet spectrum and (ii) shows the non-dimensional ensemble average wavelet coefficients. *T106, $Re_{2c}=1.6\times10^5$, $\phi=0.83$, $s_b/s_c=1$, $f_r=0.68$*

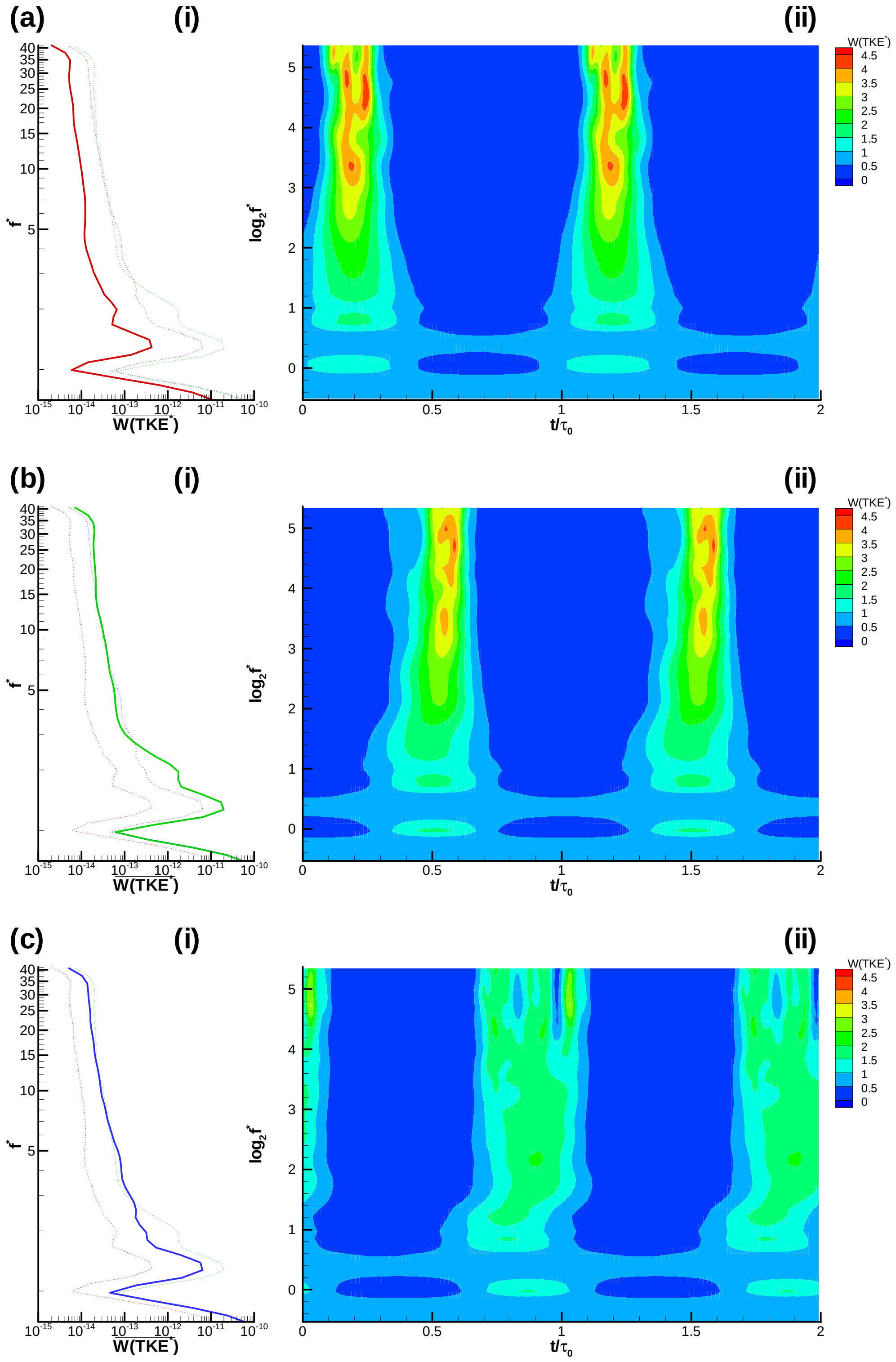

Figure 5-12: Wavelet transform of non-dimensional *TKE* at three locations in the bladerow. (a) Position *I*, (b) Position *J*, (c) Position *K*. In all cases (i) is the non-dimensional time average wavelet spectrum and (ii) shows the non-dimensional ensemble average wavelet coefficients. *T106*, $Re_{2c}=1.6\times10^5$, $\phi=0.83$, $s_b/s_c=1$, $f_r=0.68$

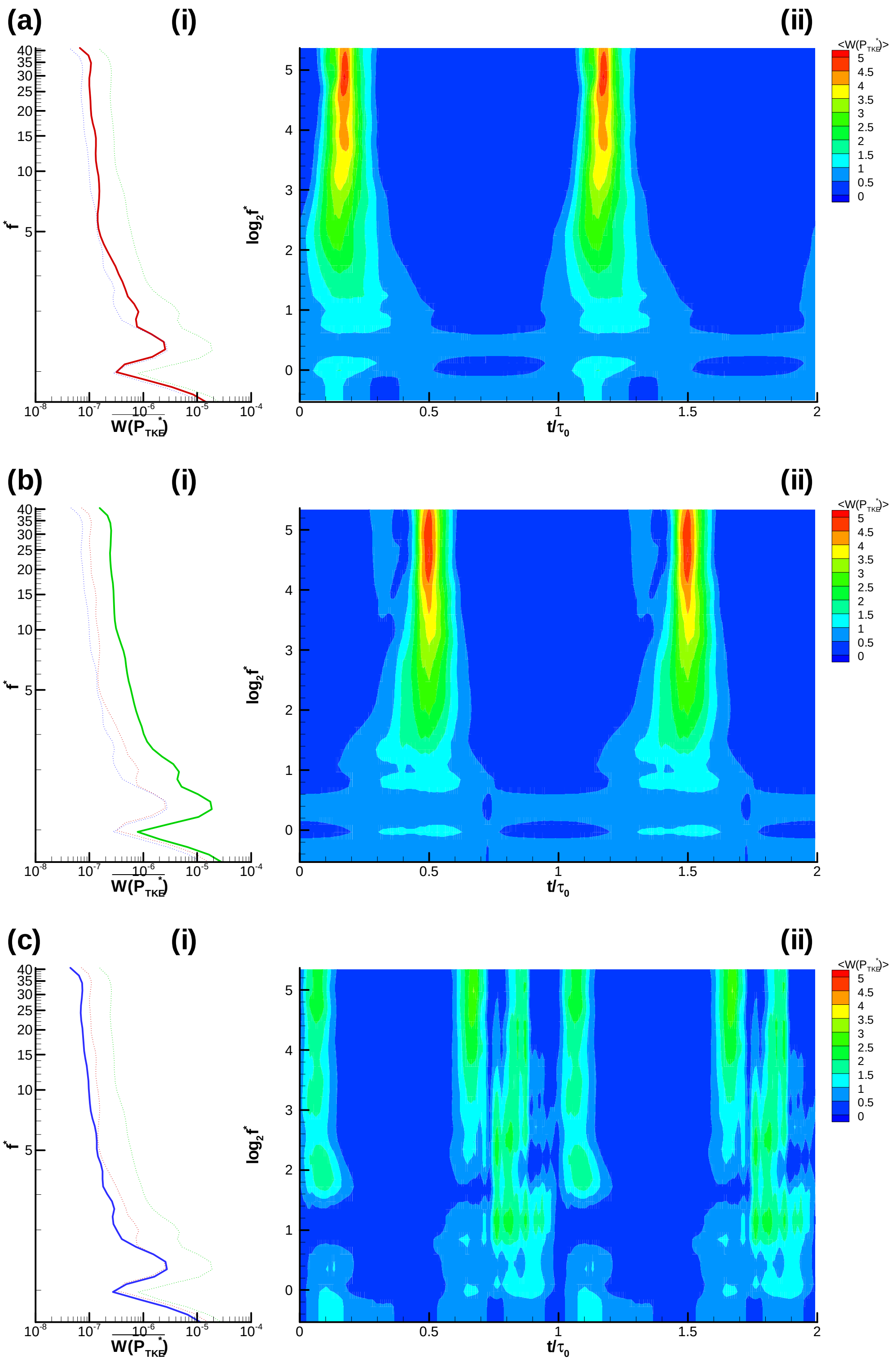

Figure 5-13: Wavelet transform of non-dimensional *TKE* production at three locations in the bladerow. (a) Position *I*, (b) Position *J*, (c) Position *K*. In all cases (i) is the non-dimensional time average wavelet spectrum and (ii) shows the non-dimensional ensemble average wavelet coefficients. *T106*, $Re_{2c}=1.6\times10^5$, $\phi=0.83$, $s_b/s_c=1$, $f_r=0.68$

Chapter 6: Unsteady pressures measured on the suction surface of the T106 LP Turbine cascade

6.1 Introduction

This Chapter presents unsteady surface pressures measured on the suction side of the T106 LP turbine cascade. The surface pressures measured under the laminar boundary layer upstream of the steady flow separation point were found to respond to the wake passing in a quasi-steady manner as would be expected from the wake convection measurements presented in Chapter 5. By contrast, in the region of the steady flow separation bubble the arrival of the convecting wake produced high frequency, short wavelength fluctuations in the ensemble averaged blade surface pressure with a peak-to-peak magnitude of *30%* of the exit dynamic head and a period equal to approximately *20%* of the bar passing period.

The existence of fluctuations in the ensemble averaged pressure traces indicates that they are deterministic and are produced by coherent structures. Indeed, the onset of the pressure fluctuations was found to lie beneath the convecting wake. The coherent structures thus formed, propagate along a trajectory line drawn at half the local freestream velocity.

The period of the oscillations depends on the Reynolds number, but not on the bar passing frequency. An artificial disturbance generator was used to excite the boundary layer and the pattern of ensemble average pressure traces thus measured was found to be dissimilar to those measured with bar wakes. From these observations, it is concluded that the coherent structures responsible for the pressure fluctuations do not evolve purely from the periodic disturbance of random turbulent fluctuations associated with the wake. Measurements performed with the boundary layer tripped ahead of the separation point showed no oscillations in the ensemble average pressure traces.

It is proposed that the coherent structures responsible for the large amplitude pressure fluctuations are rollup vortices that form in the boundary layer as the wake passes over inflexional velocity profiles and that the rollup of the separated shear layer associated with the inflexional velocity profiles occurs by an inviscid Kelvin-Helmholtz mechanism.

6.2 Time mean surface pressure distribution

Ensemble averaged unsteady surface pressure measurements were made at mid span on the suction surface of the T106 LP turbine cascade by the methods described in Chapter 3. The Kulite pressure transducers, *1.6 mm* in diameter (*0.6%* surface length), were mounted flush with the blade surface and were located at *21* positions along the mid span of the suction surface of the blade. The locations of the measurements are indicated by circles in Figure 6-1 (a).

The time averaged C_p distributions are shown in Figure 6-1(b). These surface pressure measurements were made by traditional static pressure tappings located at the same surface positions as the Kulites but a *25%* span. The surface pressure distribution measured at *25%* span matches that measured at mid span in the absence of the Kulites. For steady inflow, the pressure distribution is shown for both the suction and pressure surface. Peak suction is located at $s/s_0=0.45$. A separation bubble is evident over the rear portion of the suction surface with separation at $s/s_0=0.60$. The pressure plateau, typically associated with the shear layer of a steady separation bubble, extends to $s/s_0\approx0.82$. At this location, pressure recovery begins as the separated shear layer undergoes transition and reattaches the boundary layer as turbulent by $s/s_0=0.88$.

For all cases with incoming wakes, only the suction surface C_p distribution is shown. For the case of $s_b/s_c=1$ ($f_r=0.68$) the time-mean surface pressure distribution shows no sign of the separation bubble. In the time-mean, the separation bubble has been suppressed by the wakes (Schulte, 1995). For the case of $s_b/s_c=2$ ($f_r=0.34$), where the blade surface boundary layer has longer to re-establish between wakes, the time average surface pressure distribution indicates the presence of a separation bubble. The separation and reattachment point for this case are indistinguishable from the case for steady inflow; however, the pressure plateau is not as prevalent as in the steady flow case. This is due to the time averaging of a flow, which is periodically attached by the passing wake. The final surface pressure distribution on Figure 6-1 (b) is for the case of $s_b/s_c=2$ with the boundary layer tripped by a 0.056 mm diameter wire attached to the blade surface at $s/s_0\approx0.44$. The resulting turbulent boundary layer does not separate. The C_p distribution is altered by the presence of the trip wire, with a deceleration before and an over-acceleration after the trip-wire.

Near the leading edge of the suction surface, the C_p distributions differ for the steady inflow case and the cases with bar passing. The differences are due to an effective change in incidence of the incoming flow due to the bars of the wake generator turning the inlet flow. This alteration of incidence is small and does not significantly alter the pressure distribution downstream of peak suction.

6.3 Ensemble average suction surface pressures

The ensemble averaged unsteady surface pressures measured on the suction surface for the case of $s_b/s_c=1$ are presented as contours of C_p on an ST diagram in Figure 6-3. The surface distance is non-dimensionalised by the suction surface length and the time is non-dimensionalised by the bar passing period for the case $s_b/s_c=1$ ($f_r=0.68$). The convection of the wake is evident and, upstream of the separation point, is explained in terms of the negative jet model of Meyer (1958). The negative jet, incident on the suction surface, causes the surface pressure to increase locally as the wake convects over the suction surface. The increase in surface pressure corresponds to the reduction in C_p observed in Figure 6-2.

As the wake arrives at the steady inflow separation location, a series of large amplitude high frequency pressure oscillations arises. At $s/s_0=0.76$ the peak-to-peak amplitude of these pressure fluctuations is $\Delta C_p=0.3$. The contours suggest that these pressure waves travel with infinite celerity, however this is an anomaly of the contouring algorithm and results from insufficient spatial resolution of the measurements. These very large surface pressure fluctuations are the subject of §6.3.1.

The distribution of C_p is shown at a series of five time instants through the wake passing cycle in Figure 6-3. The time mean C_p distribution is shown for comparison together with a series of vertical bars indicating the envelope of the unsteady pressures at each sensor location. At $t/\tau_0=0.0$ the C_p distribution is very similar to that of the time mean distribution. As the wake convects along the suction surface, C_p is seen to reduce first over the forward part of the blade ($t/\tau_0=0.2$) under the negative jet effect as described above. As the wake reaches mid chord ($t/\tau_0=0.4$), the peak suction is reduced by $\Delta C_p=0.15$. The pressure gradient at $s/s_0=0.6$ is seen to increase at this time. This has consequences for boundary layer separation. By $t/\tau_0=0.6$ the wake has arrived at the separation location ($s/s_0=0.60$) and the C_p

distribution over the rear of the blade is drastically altered. The C_p distributions at $t/\tau_0=0.62$ and $t/\tau_0=0.67$ are included to demonstrate the magnitude of these pressure oscillations. After the passage of the wake the C_p distribution returns to a state similar to that of the time mean distribution as shown at $t/\tau_0=0.8$.

6.3.1 Unsteady surface pressures

As remarked in §6.3 above, the nature of the pressure traces in the region where the wake passes the steady flow separation bubble is markedly different from upstream where the boundary layer is attached. Figure 6-4 shows a selection of raw Kulite signals measured at $s/s_0=0.70$ together with the ensemble-averaged calculated from 256 ensembles. The ensemble averaging process can be seen to reduce the random fluctuations between the wake passing events, however the large amplitude pressure fluctuations are preserved in the ensemble average trace. The fact that these pressure fluctuations are evident in the raw and the ensemble-averaged pressure traces indicates that they are formed by deterministic coherent structures in the flow.

Ensemble averaged pressure traces measured over the rear half of the suction surface, are shown in Figure 6-5. The data is the same as that presented in Figure 6-2. The vertical axis indicates the surface location non-dimensionalised by the suction surface length, and the horizontal axis is time, non-dimensionalised as before. The dash-dot lines indicate the surface location of each Kulite while the solid lines are the ensemble-averaged traces of the measured surface pressure fluctuation. The magnitude of the pressure traces is arbitrary but consistent between the traces. At $s/s_0=0.76$ the peak-to-peak amplitude of the pressure fluctuations is *30%* of exit dynamic pressure and the period is approximately *20%* of the bar passing period ($f_r=0.68$).

The line, labelled *A*, in Figure 6-5 is a trajectory line drawn at the freestream velocity as calculated from the C_p distribution presented in Figure 6-1 (b). The onset of the large amplitude pressure oscillations in Figure 6-5, fall along line *A*. From this it is possible to conclude that the onset of the pressure oscillations is dictated by the wake, which convects with the freestream velocity. The onset is not controlled by the convection of turbulent spots nor instability waves within the boundary layer as these convect slower than the freestream. Similarly, the onset is not controlled by an acoustic mechanism as for a low Mach number flow this would travel ahead of the convecting wake.

The pressure fluctuations are observed to originate between the traces at $s/s_0=0.57$ and $s/s_0=0.63$. Thereafter, intense amplification occurs up to $s/s_0=0.70$ and after that the amplitude of the oscillations remains approximately constant. The period of the oscillations is also constant downstream of $s/s_0=0.70$. The amplitude of the fluctuations reduces slightly downstream of $s/s_0=0.82$. This region corresponds to the pressure recovery region of the steady separation bubble and is typically associated with transition in a separation bubble. With increased levels of turbulence and turbulent mixing that result from transition, the ensemble-average pressure fluctuations decrease in amplitude.

The pairs of trajectory lines labelled *C*, *D* and *E* are drawn at half the local freestream velocity as calculated from the C_p distribution of Figure 6-1 (b). These lines are positioned to trace the convection of the maxima and minima of the pressure fluctuations. The trajectory lines do not pass through the pressure traces at these points, but rather pass through the corresponding s/s_0 lines at the same time as the maxima or minima occur. From Figure 6-5, it is apparent that all the maxima and minima have the same trajectory and that this trajectory is half the freestream velocity. The coherent structures responsible for the pressure fluctuations thus travel at half the freestream velocity except in the region indicated by trajectory lines *B* that are drawn by hand to track the pressure maxima and minima between $s/s_0=0.63$ and $s/s_0=0.70$. The slope of lines *B* is lower than that of lines *C*, *D* and *E*. This indicates that the coherent structures convect slower than half the freestream velocity in this region.

The number of maxima and minima in the ensemble averaged pressure traces is not the same at every sensor location in Figure 6-5. At $s/s_0=0.7$ there is only one maxima and one minima observed, however, at $s/s_0=0.82$ there are three sets of maxima and minima. The appearance of more than one coherent structure is due to the different trajectories of the onset and convection of these structures. Once formed the structures convect slower than the wake thus allowing the wake to generate new structures at points further downstream as it passes over the undisturbed inflexional profiles of the separating boundary layer.

By extending the trajectory lines *C* to intersect line *A*, the origin of structure *C* is seen to be at $s/s_0 \approx 0.60$. However, by $s/s_0 \approx 0.86$ structure *C* disappears. The convection speed of coherent structure *C* is lower than the convection speed of the leading edge of a turbulent spot. The disappearance of *C* is attributed to turbulent spots formed at an upstream[16] location overtaking the coherent structure. This turbulence destroys the coherence of structure *C*.

6.3.2 The effect of bar passing frequency

Figure 6-6 shows the ensemble averaged unsteady surface pressures for the identical flow condition in Figure 6-5, but with double the bar spacing so that $s_b/s_c=2$ ($f_r=0.34$). Both the time axis and the scale of the pressure traces are identical to that of Figure 6-5.

The pressure fluctuations are again observed as the wake passes over the region of the steady flow separation bubble. No change in the onset location is evident and the period of oscillation is the same as before. The period of the pressure fluctuations are thus independent of the bar passing frequency. The pattern of the pressure oscillations is also the same as for the higher bar passing frequency up to $s/s_0=0.86$ but their magnitude is larger for the current case with lower bar passing frequency.

The lower bar passing frequency gives the boundary layer more time to re-establish between wake passing events. In this time a series of pressure oscillations, smaller in magnitude and of lower frequency arise downstream of $s/s_0=0.88$. The pattern of these pressure traces is different to those resulting from the wake-separation bubble interaction. They are more nearly sinusoidal with similar positive and negative amplitudes. The fact that these oscillations may be ensemble averaged is remarkable and indicates that they too are caused by coherent structures in the re-establishing boundary layer. As in Chapter 4, oscillations of this type were attributed to natural transition phenomena.

---

[16] At this stage of the argument, no mechanism for the creation of turbulent spots has been suggested. This will be addressed in Chapter 7.

6.3.3 The effect of a boundary layer trip

The effect of a trip wire fixed to the surface of the blade is to cause transition of the boundary layer at the trip wire location. Downstream of the trip wire the boundary layer is turbulent and attached throughout the wake passing cycle.

Figure 6-7 shows ensemble averaged pressure traces for identical flow conditions to those presented in Figure 6-6, but with a trip wire at $s/s_0=0.44$. Immediately obvious is the absence of the pressure fluctuations downstream of $s/s_0=0.60$. The coherent structures responsible for the pressure fluctuations are thus only formed when the wake interacts with the separating boundary layer.

6.3.4 The effect of Reynolds number on pressure fluctuations

It was established in §6.3.2 that the period of the large amplitude pressure fluctuations is independent of the bar passing frequency. However, the period of the pressure fluctuations is dependent on Reynolds number. The pressure traces at a Reynolds number of $Re_{2C}=1.6\times10^5$ and at a Reynolds number $Re_{2C}=2.0\times10^5$, which is 125% higher, are shown in Figure 6-9. Pressure traces are shown at $s/s_0=0.63$ and $s/s_0=0.70$ for both Reynolds numbers. These surface positions are both within the laminar shear layer of the steady flow separation bubble. The vertical axis is surface location with the magnitude of the pressure traces arbitrarily scaled. The time axis in this plot is dimensional. The pressure traces are shown only for the time associated with large oscillations resulting from the wake-separation interaction. It is apparent that the period of the pressure oscillations is not the same at the different Reynolds numbers. The time offset between the two sets of pressure traces is due to difference in the absolute time of the trigger used for the ensemble averaging of the different Reynolds number flow conditions.

The period of the pressure oscillations for $Re_{2C}=2.0\times10^5$ is marked by the blue lines L_1 at $s/s_0=0.63$ and L_2 at $s/s_0=0.72$. Similarly, the period for $Re_{2C}=1.6\times10^5$ is marked by red lines. Two more blue lines are drawn with solid arrows. As labelled, these are *125%* of the length of L_1 and L_2. From this it is clear that the period of the oscillations at $s/s_0=0.63$ and $s/s_0=0.72$ are inversely proportional to the Reynolds number.

The convective time scale,

$$\tau_{conv} \propto \frac{C}{U} \tag{6-1}$$

and viscous diffusion time scale,

$$\tau_{visc} \propto \frac{\delta *^2}{\nu} \propto \frac{\left(\frac{x}{\sqrt{\mathrm{Re}_x}}\right)^2}{\nu} \propto \frac{x}{U} \tag{6-2}$$

are indistinguishable for a given velocity distribution as the ratio of x to C is constant. It is thus not possible to determine if the large pressure fluctuations are related to viscous or convective phenomena.

A correlation for the period of the disturbance with the maximum amplification rate in the Falkner-Skan velocity profiles over the whole range of pressure gradient parameter is given by Walker (1989) as

$$\tau_{crit} \propto \frac{1}{f_{crit}} = \frac{\nu}{3.2\,\mathrm{Re}_{\delta *}^{-3/2}\,U^2} \tag{6-3}$$

This correlation was shown to reliably predict the frequency of Tollmein-Schlichting waves[17] in Chapter 4. The period of a viscous instability in a highly decelerated boundary layer is thus expected to vary non-linearly with Reynolds number. The observed linear relationship between the period of the pressure fluctuations and Reynolds number demonstrates that a viscous stability mechanism is not responsible for the large amplitude pressure fluctuation. Villermaux (1998) showed that inviscid instability processes have a negligible Reynolds number dependence and so an inviscid instability mechanism is not excluded.

6.3.5 The interaction of a wave packet with the separating boundary layer

In order to separate the effects of wake turbulence and the negative jet effect a series of measurements were performed with the boundary layer periodically perturbed by the artificial disturbance generator described in Chapter 3. The artificial disturbance generator was driven with a square wave pulse to excite as broad a frequency spectrum as possible. Such a disturbance simulates the effect of the periodically applied disturbances associated with the wake turbulence but without the negative jet effect of the convected wake.

---

[17] Obremski et al (1969) state that matching of the vorticity distribution between $0.1<y/\delta<0.9$ is the most reliable way of reproducing nearly identical stability characteristics.

The disturbances were generated at $s/s_0=0.57$, this is in the decelerating boundary layer before the steady flow separation point. The frequency of the perturbations was set to match the bar passing frequency for $Re_{2C}=1.6\times10^5$ and $s_b/s_c=2$. The ensemble averaged surface pressure distribution measured downstream of this location is presented in Figure 6-8.

As for the case with bar passing, ensemble average pressure fluctuations are observed with strong amplification between $s/s_0=0.63$ and $s/s_0=0.70$. However the amplitude of these pressure fluctuations is smaller and the period is about half that of the wake passing case. The pattern of pressure fluctuations is different to the wake passing case as highlighted by the inset frame which shows the traces overlaid at $s/s_0=0.70$.

From these measurements, it is possible to conclude that the coherent structures responsible for the large amplitude pressure fluctuations are not only a result of the amplification of disturbances associated with wake turbulence by the velocity profiles of the steady flow separation region.

6.4 The formation of coherent structures in a separating shear layer

The evolution of artificial disturbances in boundary layers has been studied by researchers interested in boundary layer stability. The classical stability experiments, such as those of Schubauer and Skramstad (1947), were performed by using a vibrating ribbon to excite instability waves in a boundary layer. By varying the frequency of excitation and altering the flow speed to change the boundary layer thickness, the neutral stability curve was determined. Good agreement was found between the experimentally determined neutral stability curve and that predicted by linear stability theory.

The evolution of a wave packet in a zero pressure gradient boundary layer was studied experimentally and theoretically by Gaster (1981). An acoustic driver was used to introduce a disturbance into the boundary layer and the evolution of the resulting wave packet was measured by a probe at a fixed location downstream of the disturbance. Measurements in the boundary layer downstream of the disturbance location were made across the span of the plate and showed a wave packet to be formed. Gaster was able to calculate the convected wave packet. Linear stability theory was used to predict the behaviour of all the discrete modes excited in the boundary layer and this information was then used to compute the resulting wave packet by a summation over all the modes with only the dominant mode capable of amplification and a locally parallel flow approximation. The measurements and calculations of Gaster (1981) are reproduced in Figure 6-10. The agreement between the calculated and measured wave packets is good. The discrepancies between the two are attributed to non-linear effects.

In the experiment of Gaster (1981), the boundary layer was excited by an acoustic driver through a small hole in the flat plate. A square pulse was used to excite a broad spectrum of disturbances. The linear instability mechanism associated with the flat plate boundary layer profile lead to amplification of particular frequencies. The exponential amplification rate associated with linear instability rapidly lead to the dominance of the most amplified mode. Such a selective amplification process acts as a filter that leads to a single mode becoming dominant. This selective amplification mechanism resulted in a coherent structure being formed in the boundary layer, in this case a travelling wave packet.

The instability mechanism governing the evolution of a wave packet in a separation bubble was investigated experimentally by Watmuff (1999). A pressure gradient was imposed on a large flat plate so that a laminar separation bubble was formed. An artificial disturbance was periodically generated at the minimum pressure point (peak suction) and hot-wire measurements were made to track the evolution of the resulting wave packet. The disturbance was observed to decay in the boundary layer upstream of separation. After the separation location, the rate of decay reduced but the disturbances continued to decay. The character of the disturbance was also observed to change upon entering the separated region. At a later point after separation, the amplitude of the disturbances began to increase and the wave packet disturbance was observed to grow with the same exponential growth rate as background disturbances. This indicates linear behaviour, as the growth rate is independent of the initial amplitude of the disturbance. Dovgal and Kozlov (1990) also found the growth rate of two-dimensional waves in a separation bubble to be independent of their initial magnitude even when the amplitude of the disturbance reached *20%* of the freestream velocity. The end of the exponential growth region corresponds to the end of the linear region and this was found to coincide with a rapid increase in the boundary layer thickness.

The location of the maximum amplitude of the wave packet was observed to follow the trajectory of the inflexion points in the boundary layer velocity profile and contours of the spanwise vorticity revealed a cat's eye pattern, which is characteristic of a Kelvin-Helmholtz breakdown in the shear layer. This evidence allowed Watmuff to conclude that the instability mechanism governing the amplification of the wave packet in a separation bubble is predominantly inviscid.

Further measurements by Watmuff (1999) were performed with a flying X-wire probe and an exceptionally fine three-dimensional measurement grid. Figure 6-11 and Figure 6-12 are reproduced from Watmuff (1999). A series of contour plots of spanwise vorticity at the centre line of the wave packets (Figure 6-11) shows the cat's eye patterns reminiscent of the initial stages of rollups in a shear layer. The evolution of the cat's eye pattern into four regions of concentrated spanwise vorticity is apparent in Figure 6-11. However, the three-dimensional data, shown as a series of iso-vorticity surfaces in Figure 6-12, reveals the rollup is actually three-dimensional. The large amplitude three-dimensional waves resulting from the inviscid amplification mechanism in the separation bubble's shear layer can be seen to evolve into a group of large-scale vortex loops. The three-dimensional rollups develop legs, which move together. The coming together of the legs enforces the curvature of the central region. This in turn accelerates the central region away from the wall forming elongated vortex loops. These vortex loops remain as discernable coherent structures up to twenty boundary layer thicknesses downstream in the fully turbulent boundary layer.

The work of Gaster (1981) and Watmuff (1999) shows that the selective amplification associated with boundary layer stability, both viscid and inviscid, provides a mechanism able to form coherent structures. It is proposed that the deterministic coherent structures responsible for the measured pressure fluctuations are formed by the selective amplification of such an instability mechanism.

6.5 Visualisation of the instantaneous flow field using PIV

PIV is essentially a quantitative flow visualisation technique. Two images of a seeded flow are used to determine the fluid velocity by tracking the displacement of the suspended particles over a known time as described in Chapter 3. The PIV technique provides quantitative data of the instantaneous flow field, however, for the current purpose of identifying coherent structures, an instantaneous flow visualisation is sufficient.

The results of a PIV measurement for a small area on the suction surface of the T106 LP turbine cascade for the phase $t/\tau_0=0.85$ are shown in Figure 6-13. The position of the measurement relative to the blade is shown in Figure 6-13 (a) and corresponds to the region between $s/s_0=0.8$ and $s/s_0=0.9$. In order to achieve sufficient resolution in the boundary layer a large zoom factor was used permitting only a small section of the blade surface to be viewed.

The instantaneous vector map, calculated as described in Chapter 3[18], is shown in Figure 6-13 (c). Two vortices are visible in the boundary layer at labels *A* and *B*. Instantaneous streamlines calculated from the vector map are shown in Figure 6-13 (d) and confirm that the structures at *A* and *B* are vortices embedded in the boundary layer. A number of PIV measurements were made and not all showed identical features to the results of Figure 6-13. The vortices were not always present and their size and position varied at the same phase relative to the bar passing.

The vorticity of the vortices at A and B is of the same sense as the boundary layer vorticity. The vortex centres are separated by approximately *5%* of the suction surface length with their centres at approximately a third of the local time average boundary layer thickness. It is argued below that these vortices are responsible for the measured pressure fluctuations.

6.6 The source of surface pressure fluctuations

Saathoff and Melbourne (1997) conducted an investigation into the cause of large pressure fluctuations occurring near the leading edges of sharp-edged bluff bodies[19]. A long two-dimensional rectangular prism was mounted in a wind tunnel and the surface pressure was measured under the separation bubble that formed at the leading edge. Flow visualisation was performed with a laser light sheet with the flow seeded from the model’s leading edge with a fine powder consisting of a mixture of balsa and china clay. A high-speed cine camera was used to simultaneously capture flow visualisation pictures and an oscilloscope output from the pressure transducers.

---

[18] The author is indebted to Mr D Hollis for his assistance in acquiring the PIV data. The processing of the PIV images is the work of Mr Hollis.

[19] A major cause of damage in windstorms is large pressure fluctuations occurring near the leading edges of buildings. The sharp-edged bluff body is intended to simulate the leading edge of a building in wind.

The results, a sample of which are reproduced in Figure 6-14, showed that large surface pressure fluctuations were caused by vortices in close proximity to the surface of the model. The rollup of the separated shear layer, initiated by perturbations in the approaching flow, was identified as the source of these vortices.

The pressure trace during one roll up is shown in Figure 6-14. The pattern of this pressure trace matches that of the ensemble averaged pressure traces shown in Figure 6-5 and Figure 6-6. It is thus possible to identify the coherent structures responsible for the pressure traces to be vortices formed in the shear layer of the re-establishing boundary layer.

The interaction of a convected spanwise vortex and a Blasius boundary layer was investigated numerically by Luton et al (1995). The vortex, which entered the computational domain just above the boundary layer edge, was modelled as an Oseen vortex with a velocity field given by

$$v_\theta = \frac{\Gamma}{2\pi r}\left[1 - e^{-r^2/4\nu t}\right] \qquad (\ 6\text{-}4)$$

The incompressible unsteady two-dimensional Navier-Stokes equations for laminar flow were solved. The computed surface pressure distribution for the case of a vortex with vorticity of the same sign and similar magnitude as the boundary layer wall vorticity is shown in Figure 6-15. The pattern of surface pressure distribution matches that measured here and by Saathoff and Melbourne (1997). It should be borne in mind that the surface distribution must be reversed to match the time traces measured at a fixed point. The detail available in the computations of Luton et al (1995) showed the minimum pressure to coincide with the location of the vortex centre. The small disturbance upstream of the vortex centre was identified as corresponding to a region of negative vorticity upstream of the vortex that results from the interaction of the vortex and the boundary layer.

The magnitude of the pressure fluctuations associated with the vortex computed by Luton et al (1995) for the case shown in Figure 6-15 are only *5.5%* of the dynamic head of the flow. This is considerably smaller than the current measurements. However another calculation presented by Luton et al (1995) with the vorticity magnitude of the vortex an order of magnitude greater than the presented results show a maximum pressure fluctuation of *55%* of the dynamic head. The pressure fluctuation depends on the location of the distance of the vortex from the wall as well as the strength of vortex.

6.7 Description of Mechanism

6.7.1 Hot wire measurements

In order to establish the state of the boundary layer during the wake passing cycle, a series of hot wire traverses were performed at the same surface locations as the surface pressures were measured.

Figure 6-16 shows the traverse measured at s/s_0=0.70 for the case of the artificial disturbance. The contour plots of perturbation velocity show the wave packet. These results are very similar to those of Watmuff (1999). The adjacent ensemble average velocity profiles, shown at selected time instants, demonstrate the inflexional nature of the profiles in the shear layer of a separation bubble. The profile shape does not change much as the wave packet passes. The wave packet travels at the height of the inflexion point in the profiles. This agrees with the observations of Watmuff and indicates an inviscid instability mechanism.

The hot wire traverse results for the case of wake passing are shown in Figure 6-16 (b). The negative jet effect associated with the wake is apparent as an acceleration before and deceleration after the passing of the wake in the perturbation velocity contours and the ensemble average velocity profiles. Of primary interest are the velocity profiles before the wake arrival (purple and red line in Figure 6-16 (b)). These profiles are similar to those in Figure 6-16 (a) and have an inflexion point. The turbulent to laminar relaxation of the boundary layer under a strong adverse pressure gradient results in inflexional boundary layer profiles. The inviscid instability mechanism, found to be responsible for the amplification of the artificial wave packets, is thus applicable to the wake passing case. Moreover, the contours of perturbation velocity show the peak velocity perturbations at the height of the boundary layer inflexion. This again indicates an inviscid mechanism is dominant.

6.7.2 A schematic view of the origin of pressure fluctuations

A schematic view of mechanism responsible for the high amplitude pressure fluctuations is presented in Figure 6-17. The upper plot shows the measured mean pressure distribution over the rear suction surface of the T106 LP turbine cascade for steady flow. Also shown is an inviscid pressure distribution. The difference between the inviscid and measured pressure distributions is due to the presence of a separation bubble. The circular marks on the measured pressure distribution represent the locations of the unsteady surface pressure measurements and a short portion of the ensemble averaged time traces of surface pressure are shown for each of these locations. The lower plot shows a series of measured hot wire boundary layer profiles at different time instants through the wake passing cycle. The heavy lines correspond to the boundary layer profiles just before the arrival of the wake and the dotted line, drawn by hand, passes approximately through the inflexion points of these boundary layer profiles. Just before the arrival of the wake, the laminar shear layer extends from the steady separation point to the end of the pressure plateau (from $s/s_0 \approx 0.60$ *to* $s/s_0 \approx 0.82$). The final set of profiles at $s/s_0=0.88$ does not have an inflexion point at any time during the wake passing cycle. This is representative of the reattached boundary layer after a separation bubble. This description of the profiles prior to the arrival of the wake agrees with what would be expected for a separation bubble with in a steady flow.

Between $s/s_0=0.63$ and $s/s_0=0.70$ the peak-to-peak amplitude of the pressure fluctuation rises by about *750%* and the trajectory of the pressure fluctuations is slightly slower than half the freestream velocity as shown by trajectory line *B* in Figure 6-5. Prior to the arrival of the wake, the boundary layer profiles are inflexional over this region of the blade surface. The intense amplification of the pressure traces observed in this region is attributed to the amplification of disturbances through a instability mechanism resulting from the inflexional velocity profiles.

At $s/s_0=0.70$ the pressure trace matches the shape of those measured by Saathoff and Melbourne (1997) (see pressure trace of Figure 6-14) and those calculated by Luton et al (1995) for the vortex boundary layer interaction. This, together with the PIV measurements showing vortices embedded in the boundary layer suggests that the large pressure fluctuations measured in the region covered by the separation bubble in the case of steady flow are caused by rollup vortices that form in the shear layer at the points of inflexion in the boundary layer velocity profiles. This is further confirmed by Watmuff's (1999) measurements that showed that a wave packet amplified by an inviscid mechanism in a laminar separation bubble rolled up into a series of vortex loops. The point disturbances in Watmuff's work were observed to grow laterally in the adverse pressure gradient. For the case of wake passing, where the disturbance sources may be viewed as a two-dimensional strip of convecting wake fluid, the amplified disturbances would not break down into vortex loops, but rather a more two-dimensional spanwise rollup vortex. Rollup vortices formed in a shear layer convect at the mean velocity of the shear layer. For the shear layer of a separation bubble the mean velocity would be approximately half the freestream velocity as the wall velocity is zero. The coherent structures responsible for the pressure fluctuations were identified to convect at half the freestream velocity in §6.3.1above. This adds to the argument that the coherent structures responsible for the large amplitude surface pressure fluctuations are rollup vortices formed in the separated shear layer associated with the inflexional boundary layer velocity profiles.

The pressure traces for the artificial disturbance shown in Figure 6-8 do not have the same pattern as those for the case with wakes. The hot wire traverses highlighted the similarity between these measurements and those of Watmuff (1999) and indicate that the source of the pressure oscillations in this case is a wave packet rather than a rollup vortex. The pattern of the pressure fluctuations for the artificial disturbance is similar to that in the region of natural transition. The coherent structures in the natural transition region identified in §6.3.2 and Figure 6-6 can thus be identified as waves rather than vortices. This supports their identification as Tollmein-Schlichting waves arising during the turbulent-laminar transition as identified in Chapter 4.

6.8 Conclusions

Measurements of the unsteady surface pressure on the T106 LP turbine cascade showed unexpected large amplitude fluctuations in surface pressure as the wake convected over the location of the steady flow separation bubble. The pressure oscillations were suppressed when the boundary layer was tripped indicating that the unsteady decelerated laminar boundary layer was necessary for the development of the pressure oscillations. The pressure oscillations were found to be generated as the wake passed over the region covered by the separation bubble in the case of steady flow and to convect at half the local freestream velocity. The pressure oscillations were unaltered when the bar passing frequency was halved but were found to be inversely proportional to the Reynolds number. Artificial disturbances to the boundary layer were also found to trigger large amplitude pressure fluctuations, however the ensemble averaged pressure traces that resulted had a different character.

PIV measurements, used as a quantitative flow visualisation technique, identified vortices present in the boundary layer and it was shown by reference to literature that these vortices are responsible for the pressure oscillations.

In the ensemble-averaged measurements, the vortices appear as coherent and deterministic structures. Hot wire boundary layer traverses confirmed the existence of inflexional velocity profiles prior to the arrival of the wake. It is proposed that an inviscid instability mechanism associated with the inflexional boundary layer velocity profiles is responsible for the formation of the vortices that are responsible for the pressure fluctuations.

6.9 Figures

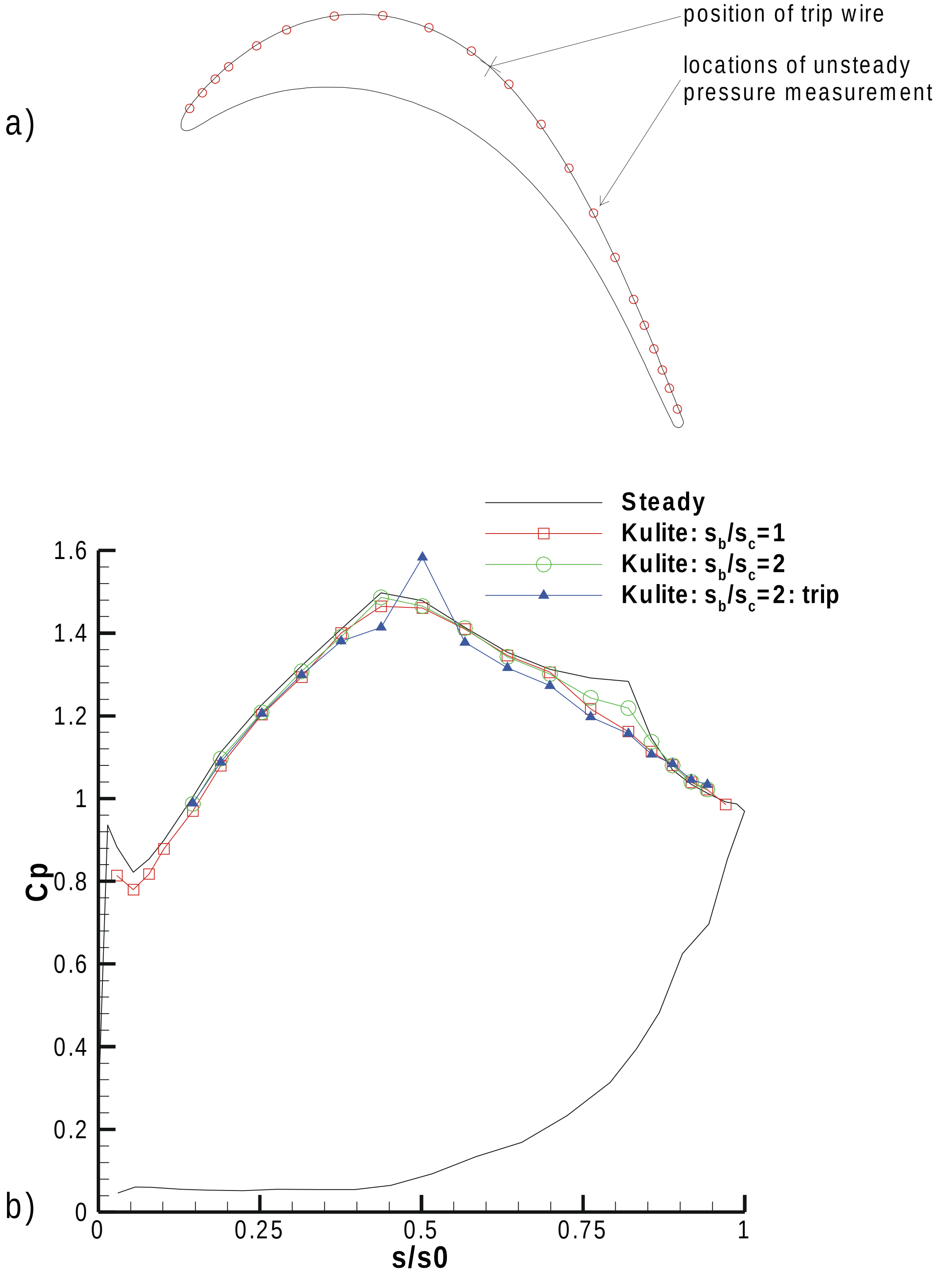

Figure 6-1: a) T106 LP turbine profile with locations of surface pressure transducers indicated by circles. b) Surface pressure distributions measured on the T106 LP turbine cascade. ***$Re_{2C}=1.6\times10^5$, $\phi=0.83$, $d_{bar}=2.05mm$.***

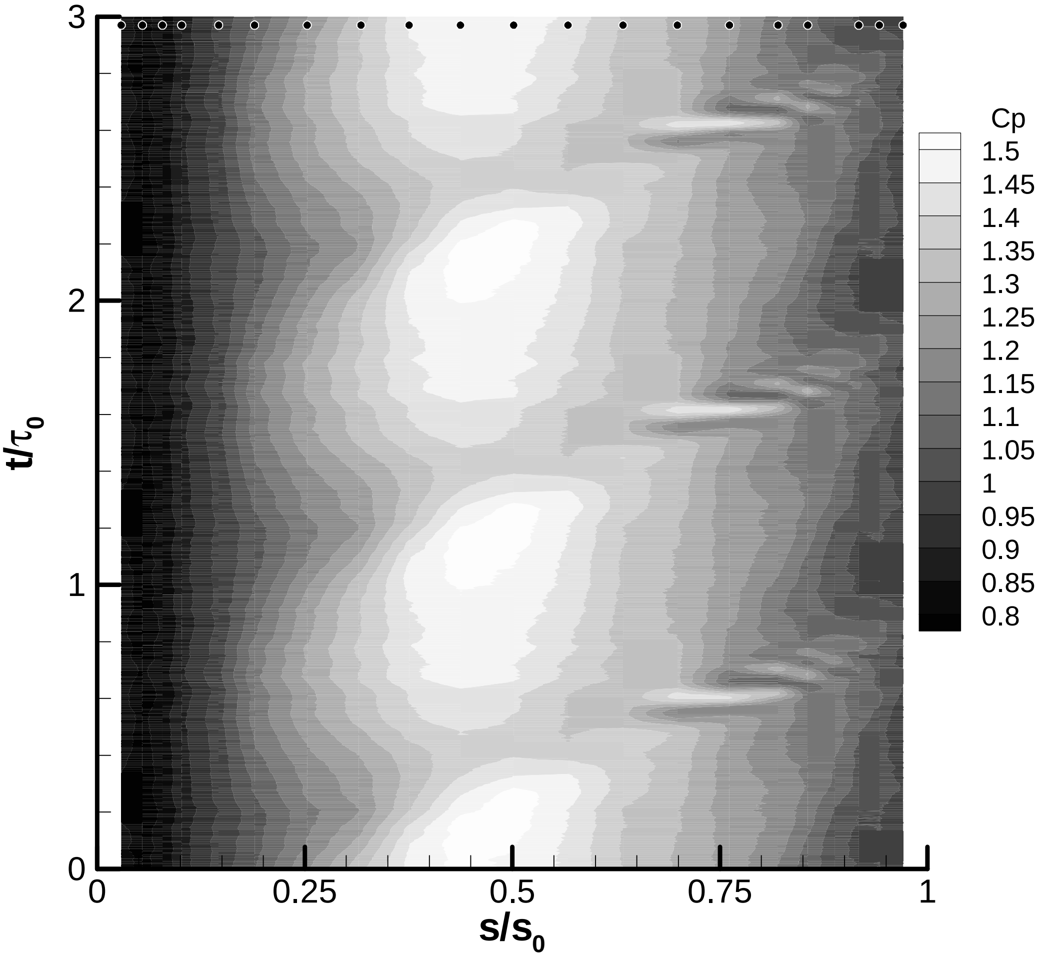

Figure 6-2: ST diagram of ensemble averaged C_p measured on the suction surface of the T106 LP turbine cascade. Symbols along the top of the plot indicate the measurement locations. ***$Re_{2C}=1.6\times10^5$, $\phi=0.83$, $d_{bar}=2.05mm$, $s_b/s_c=1$, $f_r=0.68$.***

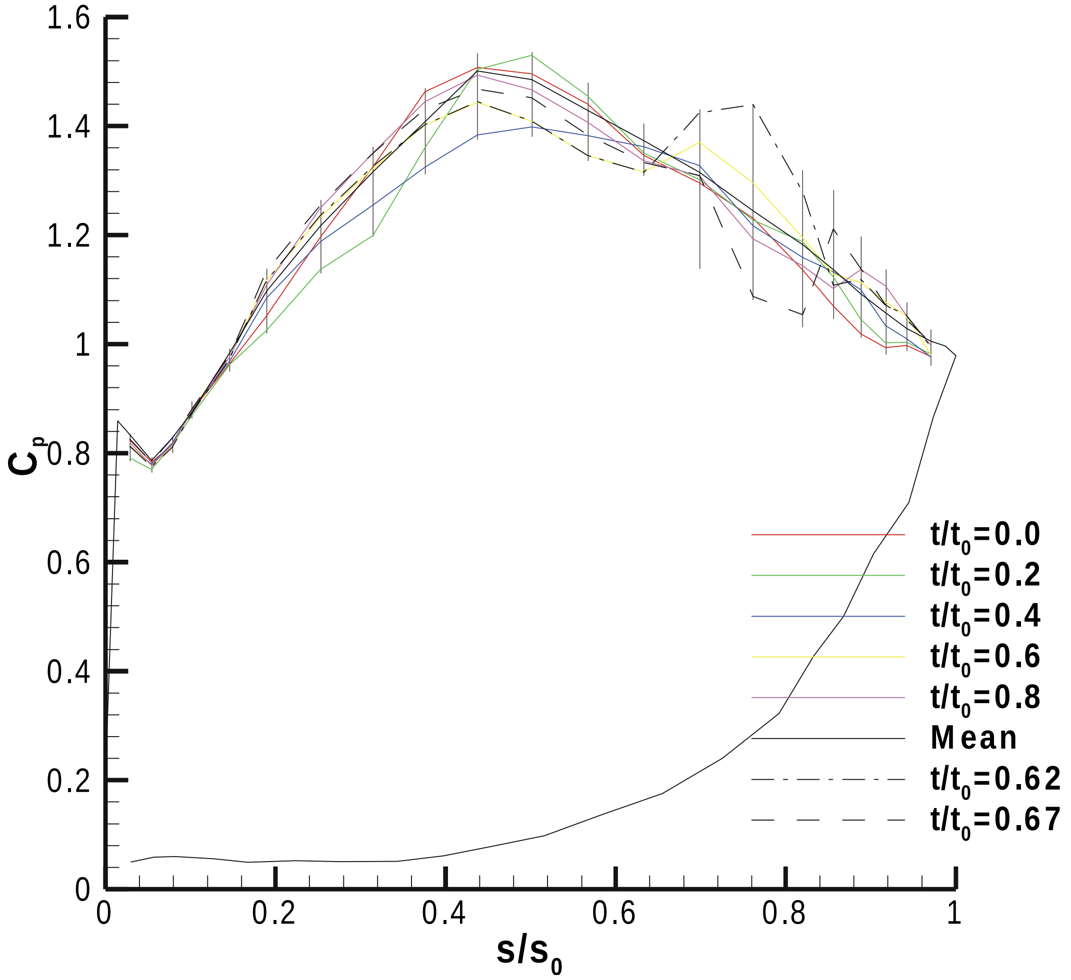

Figure 6-3: *C_p* distribution measured on the T106 LP turbine cascade at five points through the wake passing cycle. Also shown are the time mean *C_p* distribution repeated from Figure 6-1 (b) and the *C_p* distribution at two instants showing the magnitude of the pressure oscillations that result from the wake separation interaction. *$Re_{2C}=1.6\times10^5$, $\phi=0.83$, $d_{bar}=2.05mm$, $s_b/s_c=1$, $f_r=0.68$.*

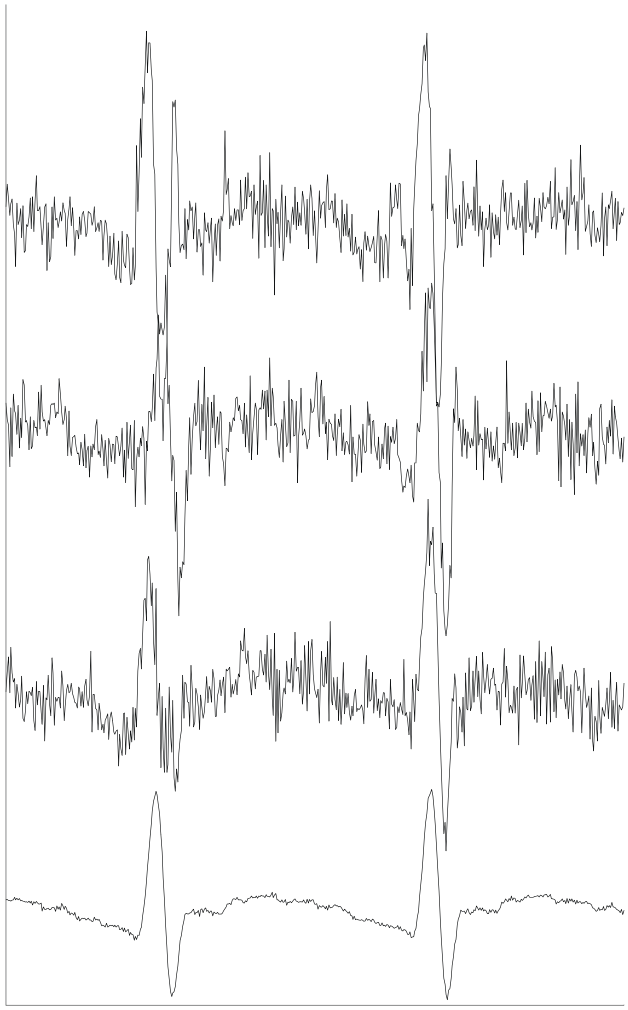

Figure 6-4: Top three traces are typical raw Kulite traces. Bottom trace is the ensemble average of 256 ensembles measured at $s/s_0=0.70$.

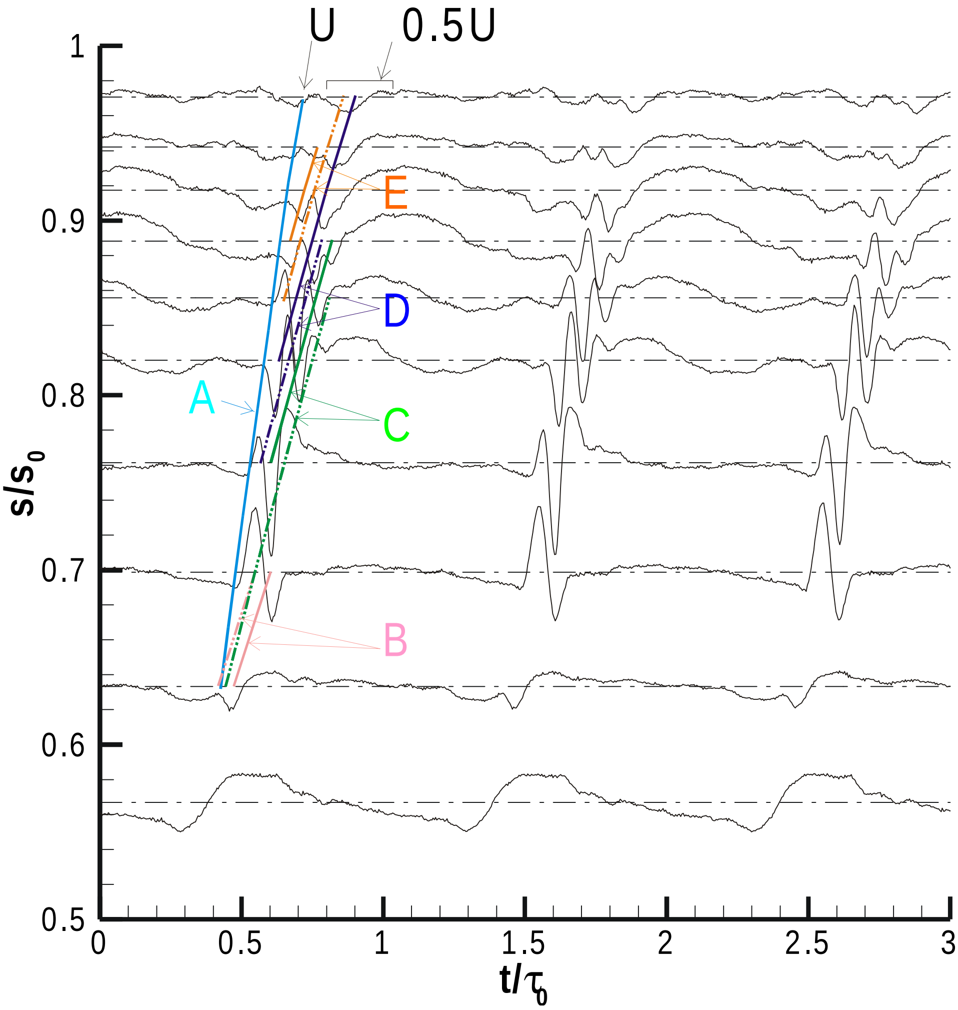

Figure 6-5: Measured ensemble averaged unsteady surface pressure distribution over rear suction surface of T106 LP turbine cascade. Trajectories drawn from measured surface velocity distribution at U∞ and 0.5U∞. Labels *A, B* & *C* indicate the trajectories of peaks (dash-dot-dot line) and troughs (solid line) of the pressure trace. $Re_{2C}=1.6\times10^5$, $\phi=0.83$, $d_{bar}=2.05mm$, $s_b/s_c=1$, $f_r=0.68$.

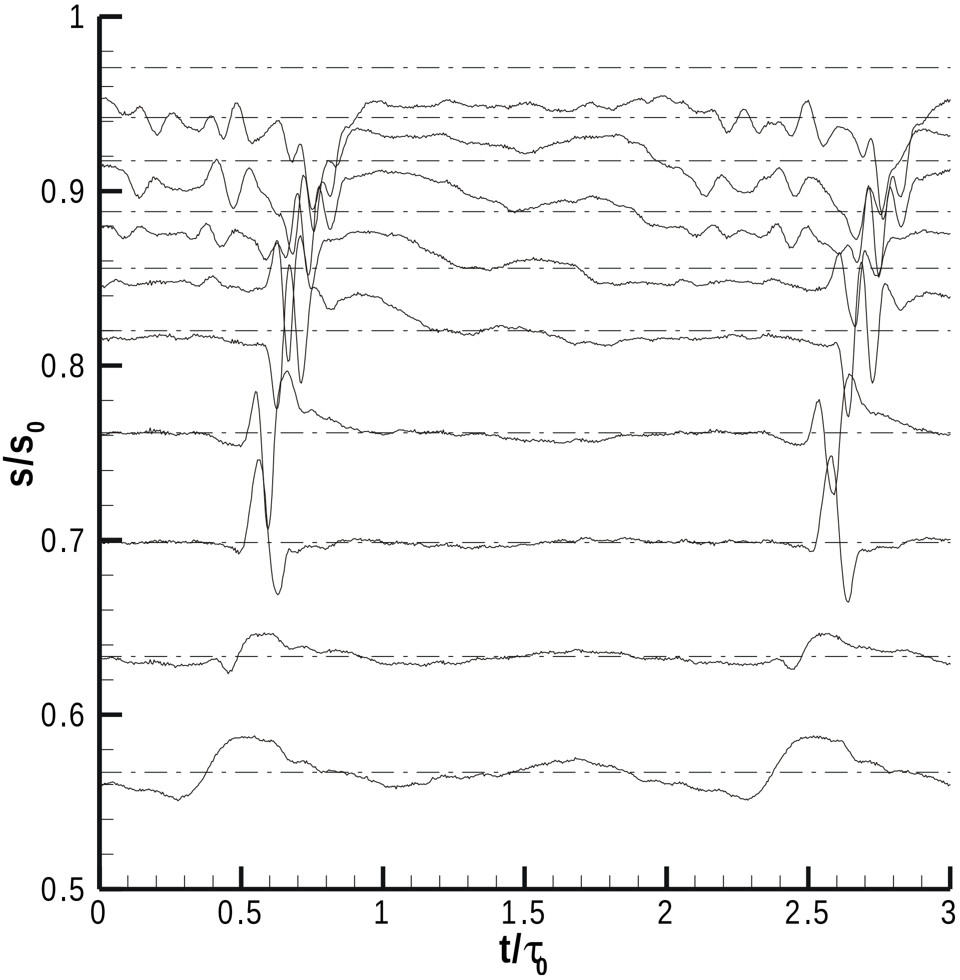

Figure 6-6: Measured ensemble averaged unsteady surface pressure distribution over rear suction surface of T106 LP turbine cascade. ***$Re_{2C}=1.6\times10^5$, $\phi=0.83$, $d_{bar}=2.05mm$, $s_b/s_c=2$, $f_r=0.34$*.** **Time is normalised by bar passing period for $s_b/s_c=1$.**

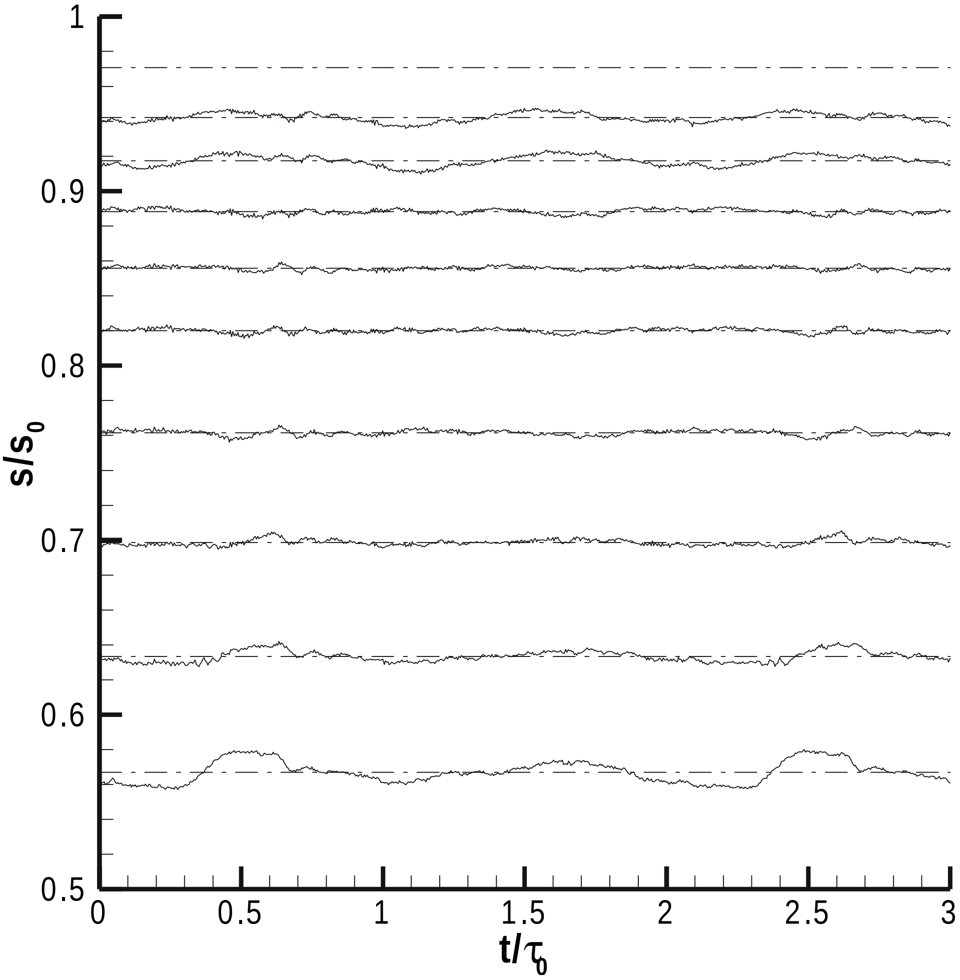

Figure 6-7: Measured ensemble averaged unsteady surface pressure distribution over rear suction surface of T106 LP turbine cascade with the boundary layer tripped at s/s$_0$=0.44. ***Re_{2C}=1.6×10^5, ϕ=0.83, d_{bar}=2.05mm, s_b/s_c=2, f_r=0.34*****. Time is normalised by bar passing period for s_b/s_c=1.**

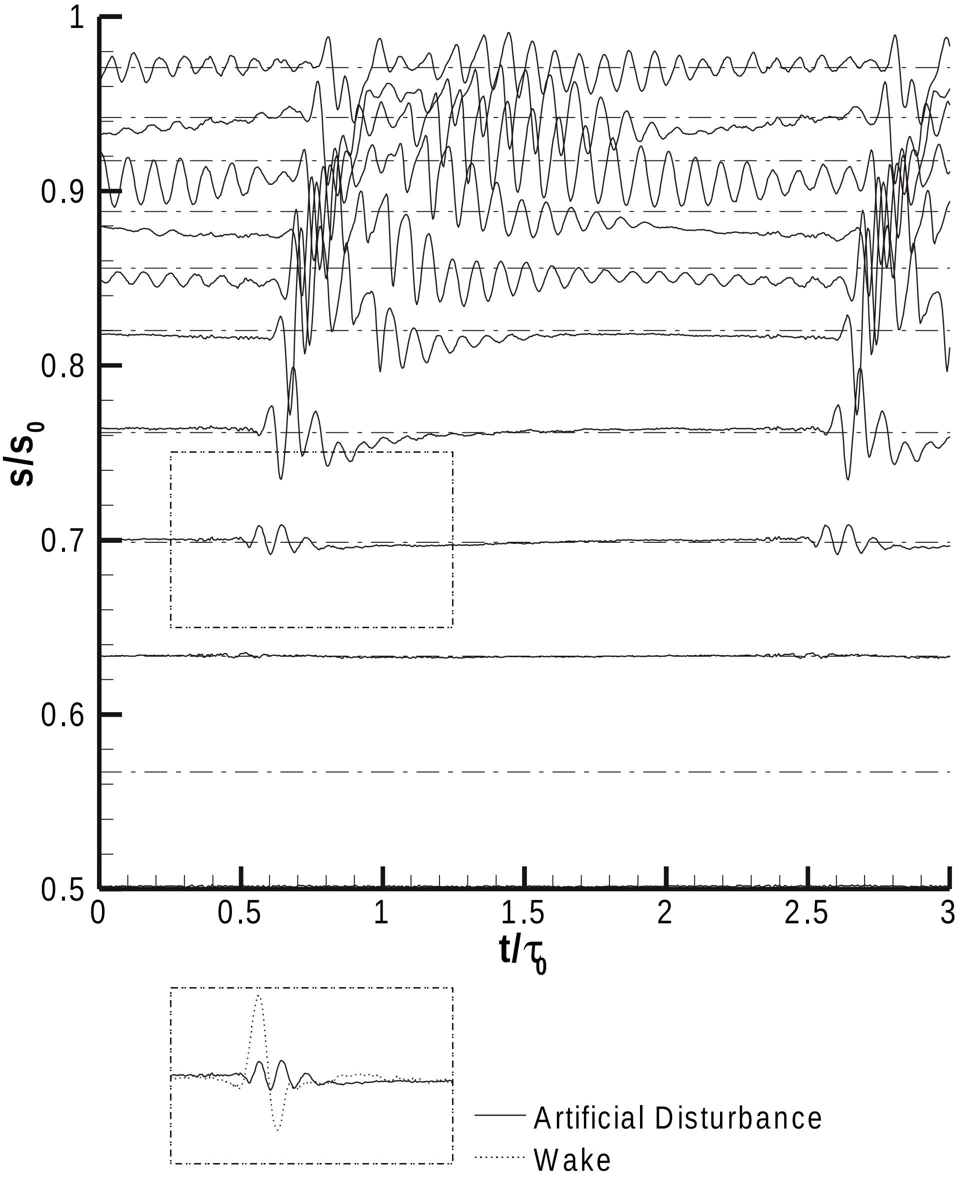

Figure 6-8: Measured ensemble averaged unsteady surface pressure distribution over rear suction surface of T106 LP turbine cascade with disturbances triggered in the boundarylayer at s/s_0=0.57. $Re_{2C}=1.6\times10^5$, $\phi=0.83$. Time is normalised by bar passing period for s_b/s_c=1.

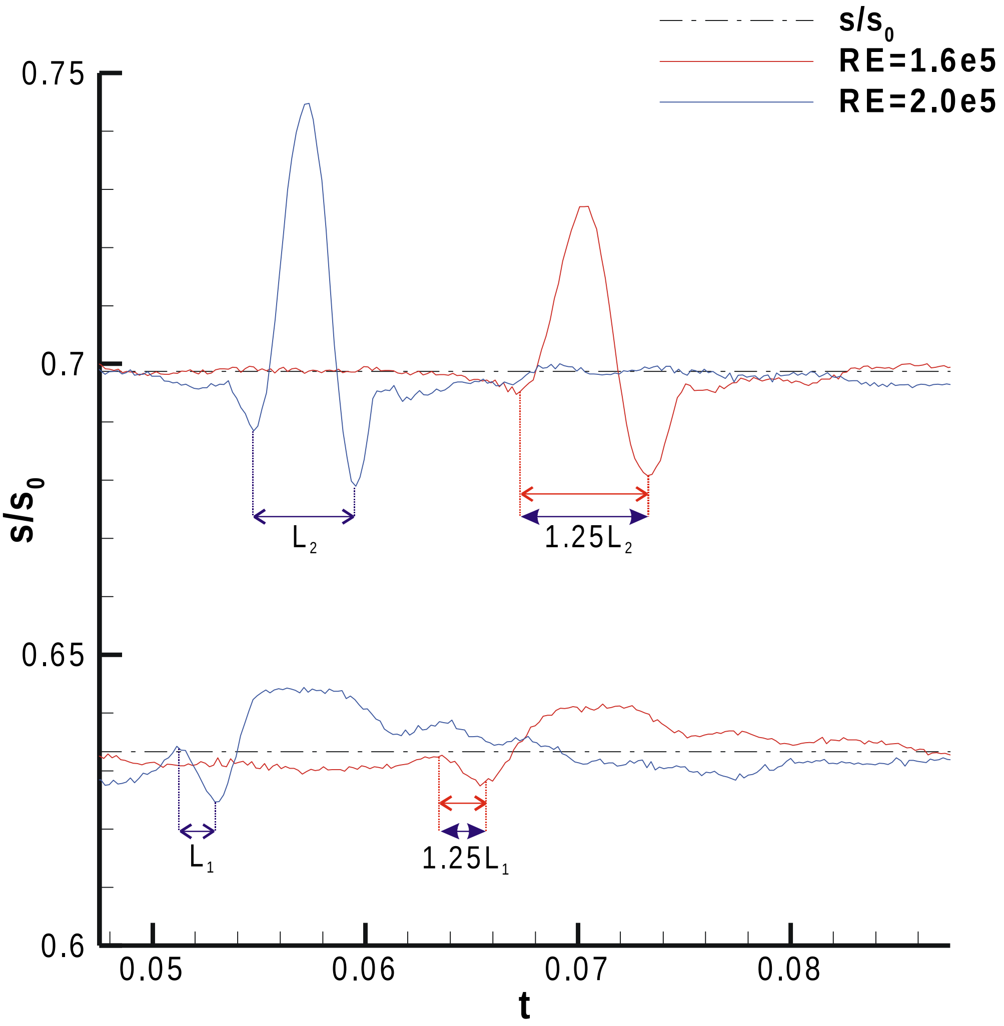

Figure 6-9: Effect of Reynolds number. Measured ensemble averaged unsteady surface pressure distribution over rear suction surface of T106 LP turbine cascade. ***$Re_{2C}=1.6\times10^5$, $\phi=0.83$, $d_{bar}=2.05mm$, $s_b/s_c=2$, $f_r=0.34$.***

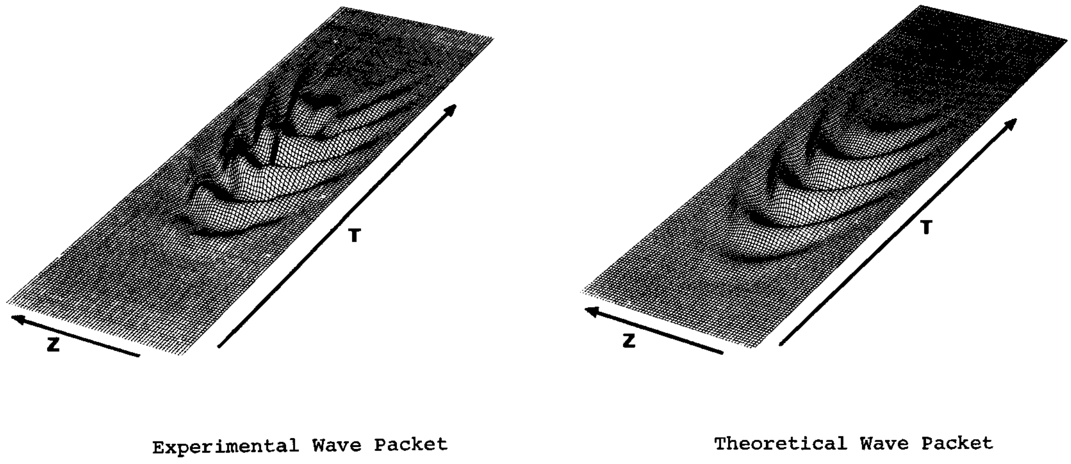

Figure 6-10: Measured and computed wave packet in a Blasius boundary layer (Gaster, 1981).

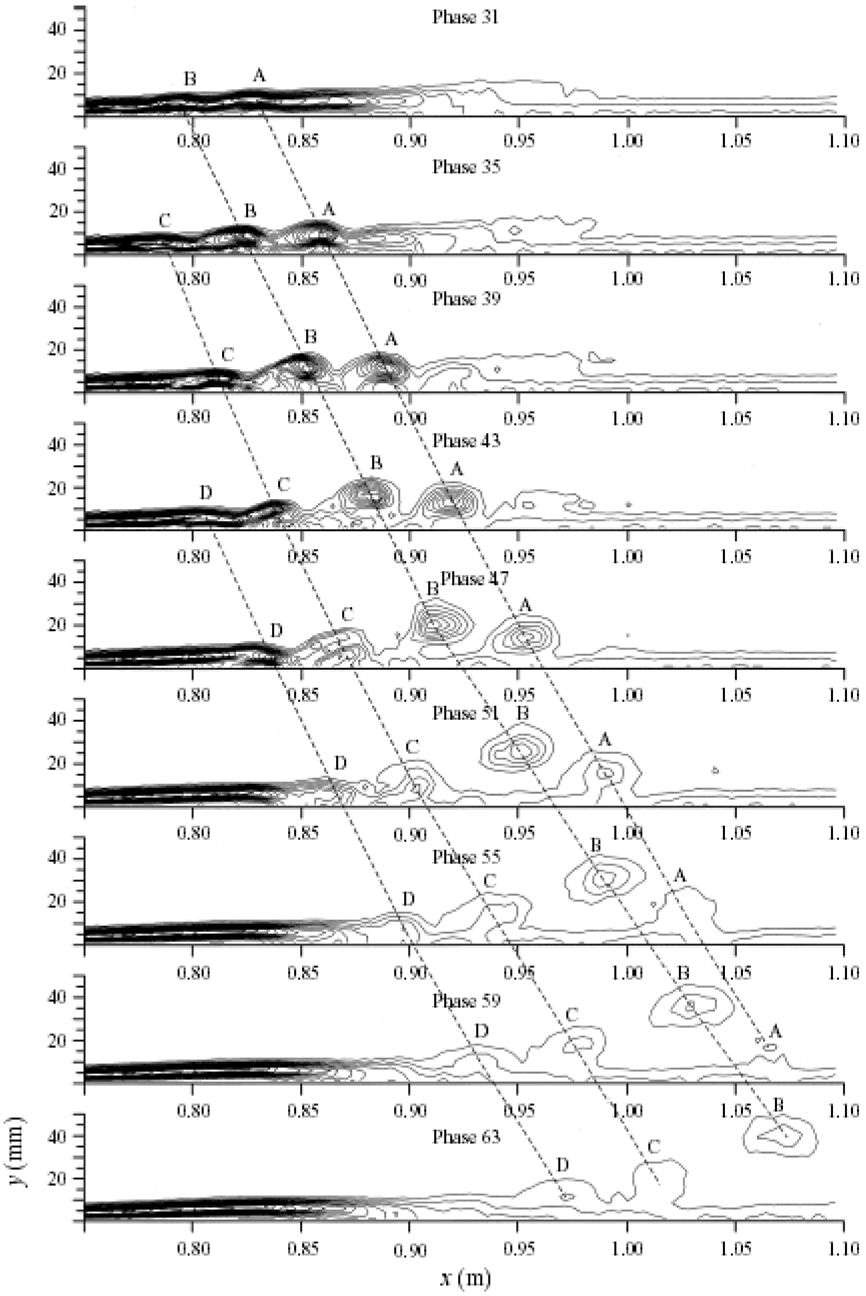

Figure 6-11: Sequence of phase averaged spanwise vorticity contours measured on the spot centre line for the interaction of an artificial disturbance and a separation bubble. Reproduced from Watmuff (1999)

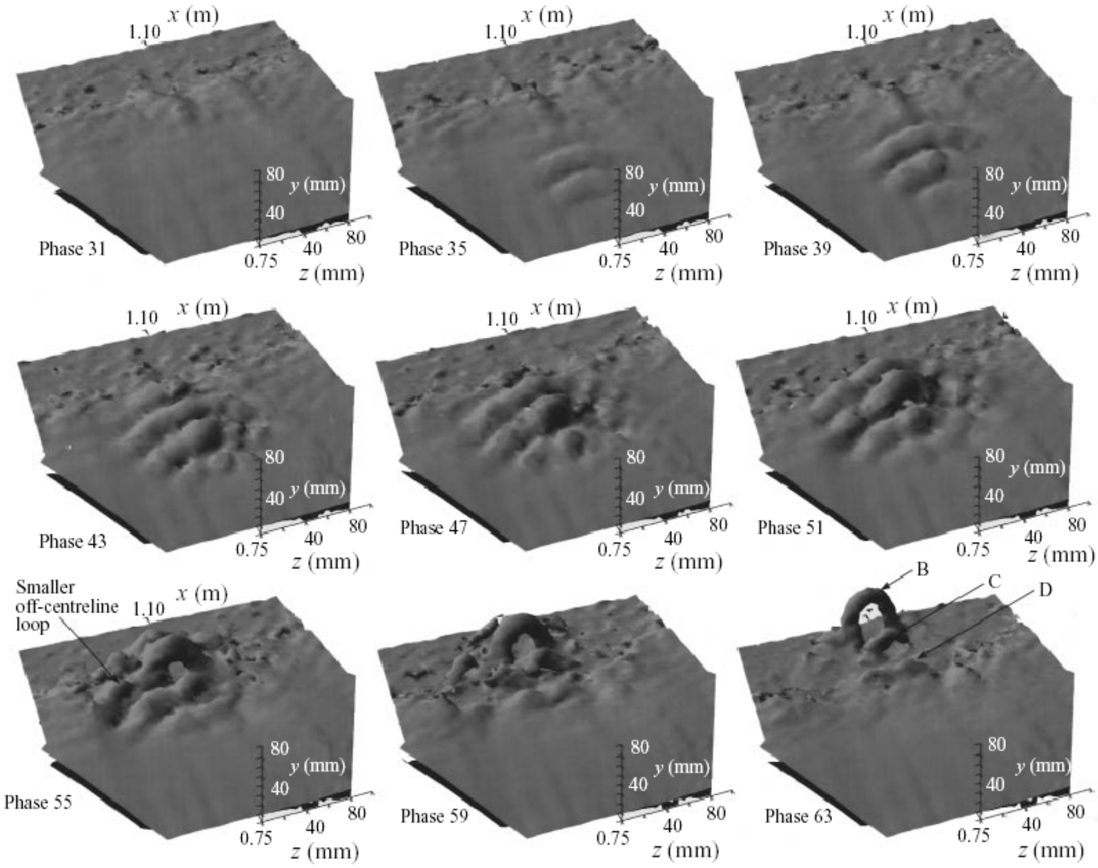

Figure 6-12: Three-dimensional surface contour of phase averaged vorticity magnitude showing the evolution of vortex loops that result from the interaction of an artificial disturbance and a separation bubble. Reproduced from Watmuff (1999).

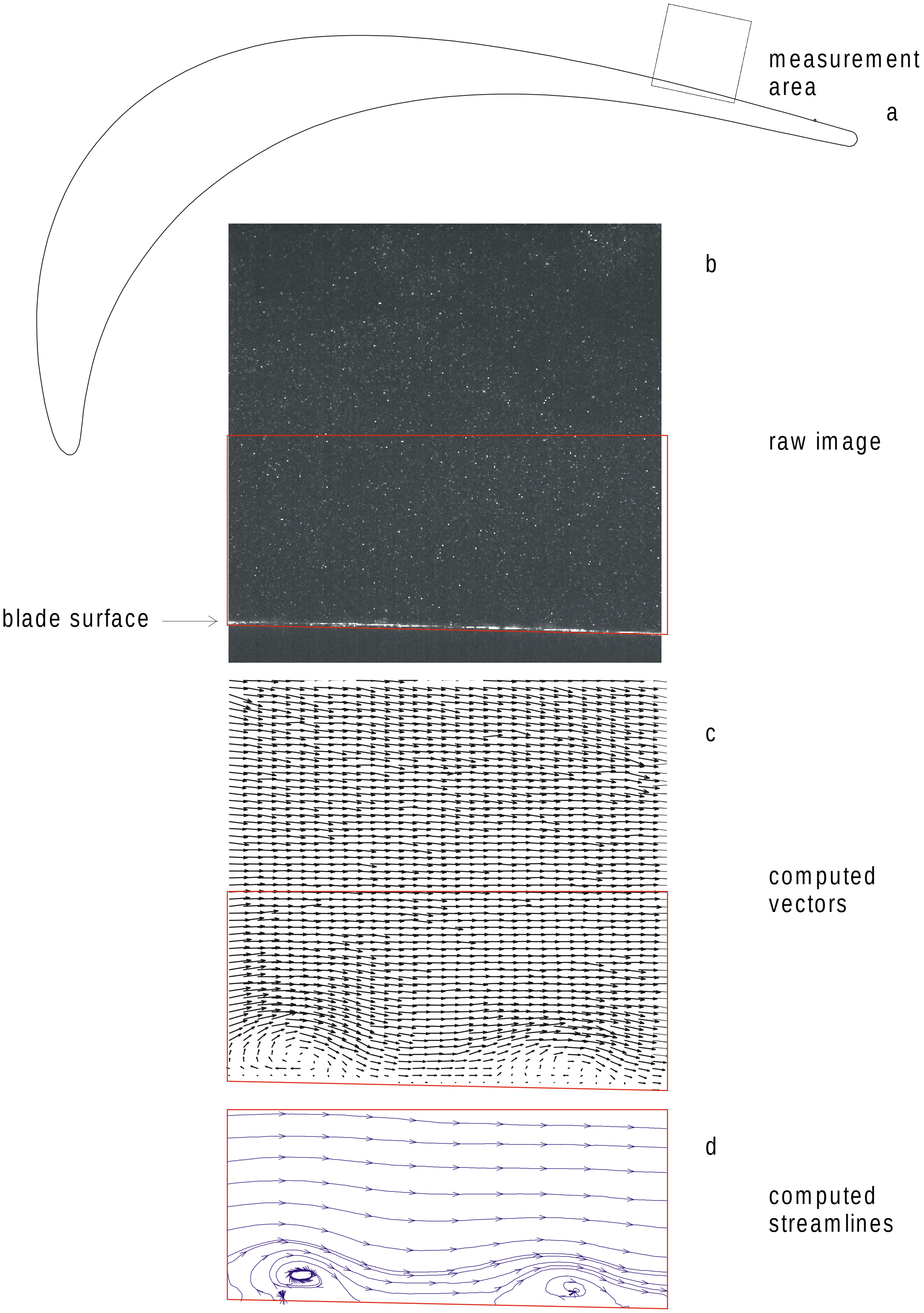

Figure 6-13: Results from PIV measurement showing location of measurement region, raw image of flow, and the resulting vector map. The bottom plot shows streamlines computed for the boxed portion of the vector map.

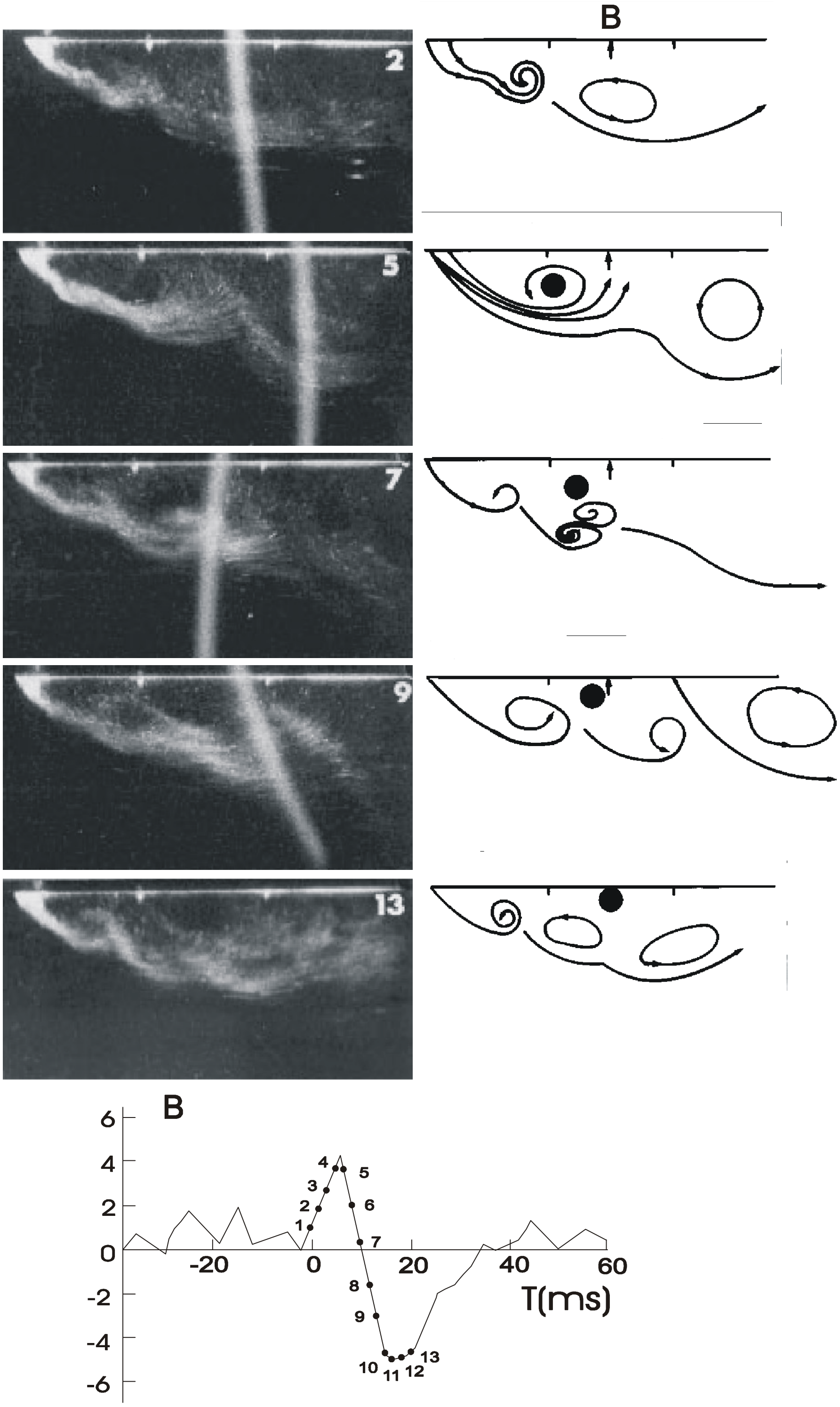

Figure 6-14: Sequence of flow visualisation pictures and accompanying sketches of the flow structure reproduced from Saathoff and Melbourne (1997). The bottom plot is a simultaneously measured time trace of pressure with the numbered symbols corresponding to the time of the flow visualisation pictures.

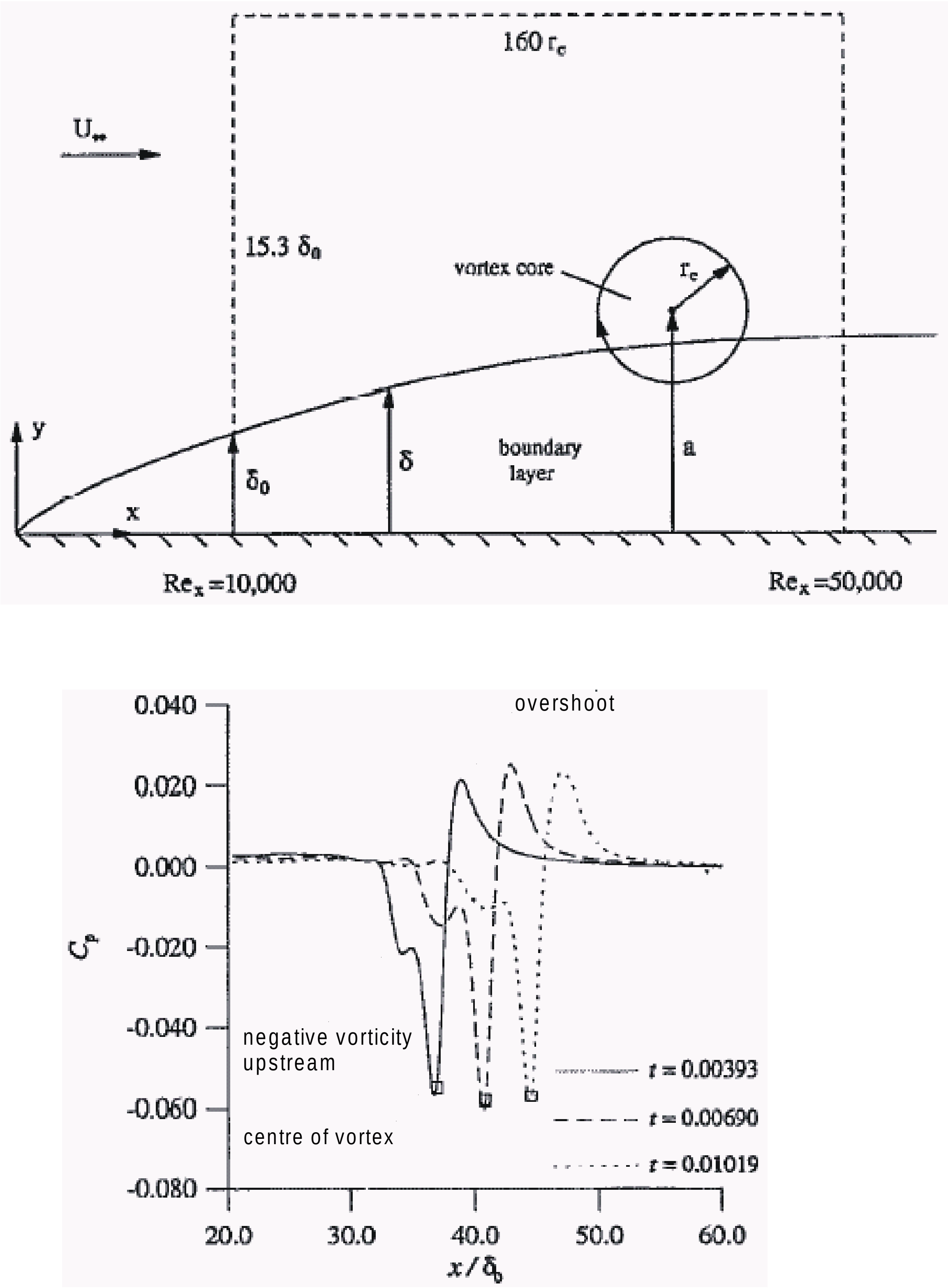

Figure 6-15: Schematic of computed flow and calculated surface pressure distribution of Luton et al (1995).

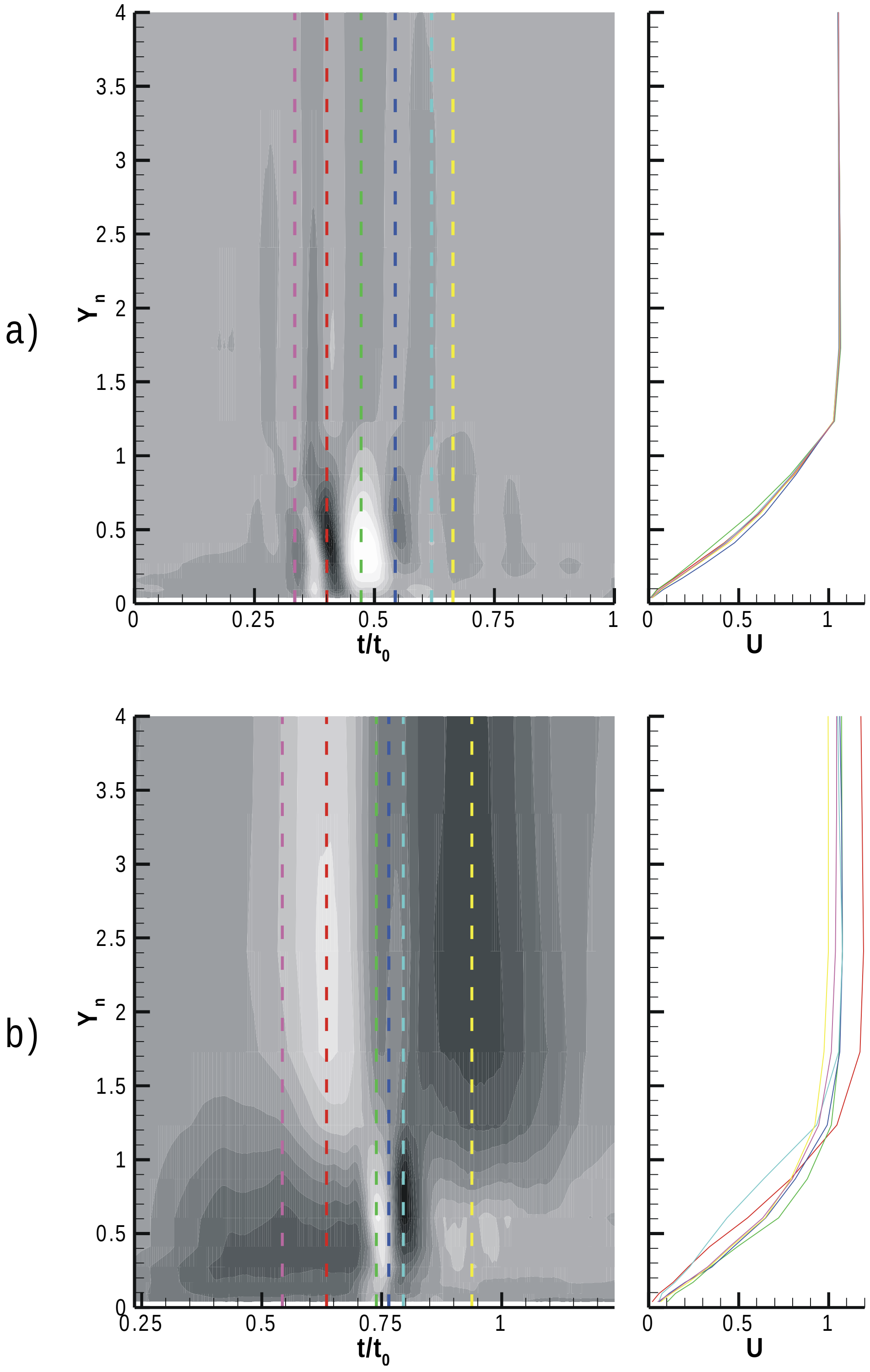

Figure 6-16: Hot wire traverses at s/s_0=0.70 for a) the artificial disturbance and b) wake passing. Contours of the ensemble averaged perturbation velocity are shown adjacent the measured velocity profiles. The colour coded dashed lines on the contour plots indicate the phase of selected velocity profiles.

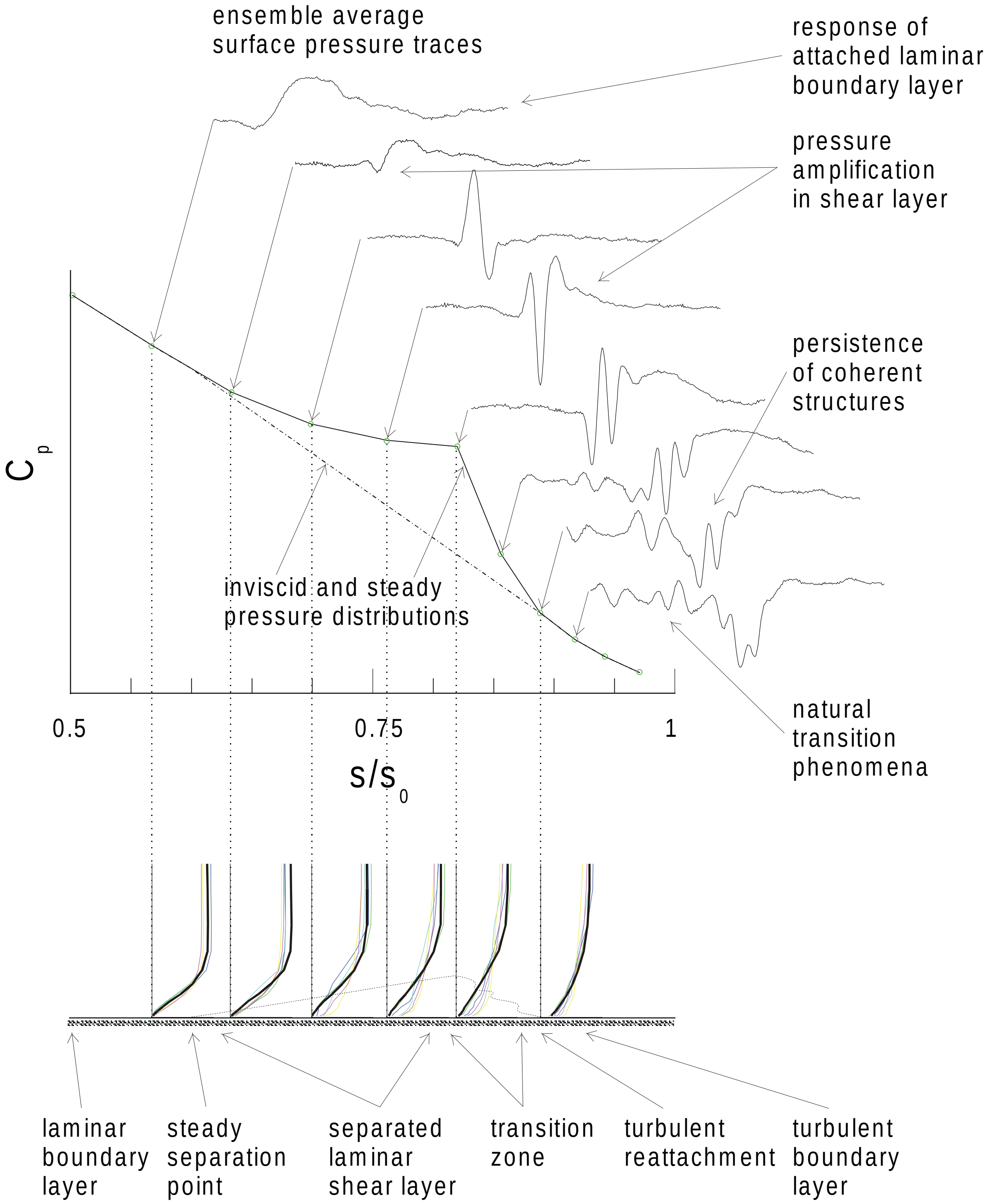

Figure 6-17: Sketch of measured pressure fluctuations and boundary layer profiles showing their locations relative to the pressure distribution for a steady separation bubble.

Chapter 7: Boundary layer measurements on the T106 LP turbine cascade

7.1 Introduction

The large amplitude unsteady surface pressure fluctuations that were presented in Chapter 6 represent a newly discovered aspect of wake boundary layer interaction. In order to gain a better understanding of this interaction and the cause of the large amplitude pressure fluctuations, a series of boundary layer traverses were performed using 2D LDA.

The results, presented as S-T diagrams of the boundary layer measurements, provide a new insight into the wake-induced transition mechanisms found on LP turbine blades with inflexional boundary layer profiles associated with separation bubbles. The traditional wake-induced bypass transition path lags the passing of the wake in the freestream, however, when the wake passes over regions of inflexional boundary layer profiles, the traditional bypass transition is preceded by an interaction that occurs immediately beneath the passing wake. Coherent structures resulting from this interaction are identified on the S-T diagrams.

The boundary layer state is then investigated at three representative phases during the wake passing cycle and this identifies the coherent structures to be vortices embedded in the boundary layer that are formed as the wake passes over regions of inflexional profiles. The production and dissipation of turbulent kinetic energy (*TKE*) calculated from the LDA measurements show that these vortices are regions of very high production and dissipation of *TKE* within the boundary layer.

Finally, a detailed view of the shear layer breakdown induced by the passing wake is presented. A cat’s eye pattern is identified in the measured vorticity contours of the separated shear layer and this provides evidence that the breakdown of the separated shear layer is by an inviscid Kelvin-Helmholtz mechanism that results in the formation of rollup vortices.

7.2 Details of 2D LDA boundary layer measurements

A series of boundary layer traverses were performed on the suction surface of the T106 LP turbine cascade. The measurement grid is shown in Figure 7-1. Each traverse was performed perpendicular to the local blade surface. The blade was painted matt black to minimise reflections from the intersecting laser beams except for a strip at midspan, which was left unpainted to avoid contamination of the static pressure tappings. For this reason the traverses were performed at 45% span as in Chapter 5. The first traverse point was *0.1mm* from the blade surface and the first *16* points were exponentially distributed within the boundary layer. The final *4* of the *20* traverse points were evenly spaced from the boundary layer edge to a point 16mm from the blade surface. In the streamwise direction *25* measurement locations were used. These were selected based on previous measurements.

The Reynolds number based on chord and time mean isentropic exit velocity was $Re_{2C}=1.6\times10^5$ and the flow coefficient was $\phi=0.83$. The bar pitch matched the cascade pitch so that $s_b/s_c=1$ ($f_r=0.68$). This flow condition matches those presented in Chapter 5 and Chapter 6. Ensemble averaging of the LDA data was performed as described in Chapter 3.

7.3 Wake induced transition schematic for LP turbines

The transition process occurring on LP turbine blades is multi-modal and unsteady. Although described by a number of authors (e.g. Mayle (1991), Walker (1993), Addison and Hodson (1992), Schulte (1995)), perhaps the most comprehensive study is that of Halstead et al (1997 a-d). To facilitate their description of the boundary layer development, they presented S-T diagrams as schematics highlighting the boundary layer state during the wake-induced transition. The same approach is adopted here.

Two schematics are presented. Firstly, the traditional view of wake-induced transition for attached boundary layers on LP turbine blades is presented. Then the wake-induced transition process involving the interaction of the wake and the inflexional boundary layer profiles associated with a separation bubble is shown. The experimental basis of the second schematic follows in §7.4 .

7.3.1 A traditional schematic of wake induced transition

Following the description of Halstead et al (1997 a), two generic transition paths may be identified on the blade surface. The wake-induced path, labelled *1* in the schematic of Figure 7-2, arises when the turbulent wake from an upstream bladerow washes over the blade surface. High levels of turbulence convect with the wake in the freestream, the trajectory of which is denoted by line *3*. The wake turbulence diffuses into the boundary layer, which then undergoes a bypass transition. This bypass transition is initiated by a transitional region where isolated turbulent spots may intermittently form, prior to their merging into the wake-induced turbulent strip. The wake-induced bypass transition happens along trajectory line *4* and lags behind the trajectory of the wake in the freestream. This was observed in the measurements presented in Chapter 4. The turbulent strip resulting from the wake-induced transition describes a wedge shape on the S-T diagram due to the trailing edges of the turbulent strip convecting slower than the leading edge. The elevated turbulence of the wake causes the wake-induced bypass transition to occur nearer to the leading edge than the undisturbed transition location. The wake induced and natural transition locations are marked on Figure 7-2.

The transition path between the wakes is labelled *2* in Figure 7-2 and is characterised by the calmed region and a natural transition process. After the wake has passed, the stimulus for early transition is removed and the turbulent boundary layer upstream of the natural transition location relaxes to its pre-transition state. This relaxation process results in the calmed region, which is characterised by low levels of dissipation and full velocity profiles that suppress boundary layer separation. The calmed region spreads as it convects downstream due to the different convection velocities for the trailing edge of turbulent spots and the trailing edge of the clamed region. After the influence of the clamed region has decayed, the blade surface boundary layer undergoes natural transition, which for LP turbines at cruise condition may be incomplete at the trailing edge.

7.3.2 Schematic of wake-induced transition with inflexional boundary layer profiles

A schematic for the transition process resulting from the interaction of a turbulent wake and the inflexional profiles of a separating boundary layer is shown in Figure 7-3. As before the wake induced path is labelled *1*, and the path between the wakes is labelled *2*.

In Chapter 6 it was shown that the interaction of the wake and the inflexional boundary layer profiles resulted in rollup vortices being formed. These rollup vortices were found to form as the wake passed over the region where a separation bubble formed in the absence of wakes. Further evidence of this is presented in §7.4 .

In Figure 7-3, the wake-induced path, labelled *1*, differs to that in Figure 7-2. There is no lag between the wake passing in the freestream (trajectory line *3*) and the response of the boundary layer. The rollup of vortices resulting from the interaction of the wake and inflexional profiles occurs by an inviscid mechanism. The diffusion of turbulence into the boundary layer is thus not a necessary precursor to the rollup of the shear layer and thus there is no time lag between the wake passing and the boundary layer response. The inviscid interaction resulting in the formation of roll-up vortices is represented in the schematic of Figure 7-3 as a series of wedges originating beneath the centre of the wake. The rollup vortices break down and a region of turbulent boundary layer follows the inviscid rollup process.

After the inviscid interaction of the wake and the inflexional profiles, the wake turbulence diffuses into the boundary layer and induces a bypass transition as described in §7.3.1 above. This bypass transition is indicated in the schematic of Figure 7-3 by the wake-induced transitional and turbulent strips occurring along trajectory *4*.

The transition path between the wakes is labelled *2* and is initially controlled by the calmed region that follows the wake induced turbulent strip. However, after the influence of the calming has passed, the boundary layer profiles become inflexional and begin to separate under the strong adverse pressure gradient. The trailing edge of this inflexional region initially follows the trajectory of the trailing edge of the calmed region. Thereafter, the inflexional or separating flow undergoes transition, however, as shown in Chapter 4, this is not the highly dissipative transition process associated with separation bubbles found in steady flows. Immediately prior to the arrival of the wake, the separation location is observed to move fractionally upstream. This is the influence of the negative jet, which alters the pressure gradient locally and is a precursor to the inviscid rollup occurring beneath the wake.

7.4 An S-T view of the measured boundary layer

The measurements supporting the schematic of wake-induced transition with inflexional boundary layer profiles is now presented. The 2D LDA boundary layer traverse data is presented in S-T diagrams in Figure 7-4 to Figure 7-8. To aid visualisation of the unsteady process the data is copied onto three wake passing periods as it was in Chapter 4.

7.4.1 Boundary Layer Edge Velocity

The boundary layer edge is defined as the wall normal distance where the velocity is *98%* of the maximum velocity measured in the ensemble-average profile at that location and time. The velocity at this point is the boundary layer edge velocity, measurements of which are plotted as an S-T diagram in Figure 7-4. Three trajectory lines denoted *A*, *B* and *E*, are drawn at the time average boundary layer edge velocity. Line *A* marks the peak velocity due to the negative jet of the approaching wake. Line *B* is approximately at the centre of the wake. Line *E* marks the minimum velocity, which occurs after the negative jet of the wake has passed.

Two further lines, labelled *C* and *D*, are drawn to mark two distinct features originating along the wake centre at $s/s_0 \approx 0.70$ and $s/s_0 \approx 0.80$. These perturbations to the boundary layer edge velocity have not previously been observed. They are attributed to the rollup vortices that form as the wake interacts with the inflexional boundary layer as described in Chapter 6. The rollup vortices can be seen to follow trajectories slower than the local freestream. Indeed, dashed lines *C* and *D* are drawn with a trajectory of half the freestream velocity. The vortex closer to the leading edge initially convects more slowly than this. These observations are in agreement with the findings of Chapter 6.

7.4.2 TKE thickness

Due to practical constraints, the boundary layer state on turbomachinery blading is typically inferred from measurements made with hot-film anemometers. The results are thus qualitative, however, it is not the quasi-shear stress, but rather the random unsteadiness (ensemble average RMS), which is used to indicate the boundary layer state. This is possible as transitional and turbulent boundary layers have far higher levels of random unsteadiness than laminar boundary layers.

D'Ovidio et al (2001 b) sought to recover the familiarity of using RMS as an indicator of boundary layer state while using all the data from hot wire boundary layer traverses. They made use of the Blackwelder parameter, which was defined as the integral of the RMS velocity through the boundary layer thickness non-dimensionalised by the time average displacement thickness. A similar approach is adopted for the current measurements. The parameter δ' is defined as the integral of *TKE* through the boundary layer. Thus

$$\left\langle \delta' \right\rangle = \frac{1}{\left\langle U_{98} \right\rangle^{2}} \int_{y=0}^{\delta_{98}} \tfrac{1}{2}\left(\left\langle u'^{2} \right\rangle + \left\langle v'^{2} \right\rangle\right) dy \qquad (7\text{-}1)$$

An S-T diagram of δ' is shown in Figure 7-5. The trajectory lines and labels are copied from Figure 7-4.

Upstream of $s/s_0=0.70$, δ' is low throughout the wake passing cycle. In this region, the boundary layer is laminar and is not significantly influenced by the passing wakes.

Downstream of $s/s_0=0.70$, the wake-induced path is characterised by very high levels of δ'. The onset of elevated δ' lies along the wake centre at line *B* and does not lag behind the wake. The lack of a lag time corresponds to the region where the rollup vortices were observed in Figure 7-4 at labels *C* and *D*. This provides experimental evidence that the inviscid rollup occurs at the wake centre and does not lag behind the passing wake. The coherent rollup vortices follow trajectories of approximately $0.5U_\infty$ before merging into a region of high δ' that persists to the trailing edge.

A second strip of elevated δ' is seen to originate at label H. This strip lags behind the passing of the wake and is a result of a wake-induced bypass transition. Also shown in Figure 7-5 is line *F* drawn with a trajectory of $0.5U_\infty$ and line *G* drawn with a trajectory of $0.3U_\infty$. These lines, drawn from the trailing edge of the wake induced turbulent strip, mark the trajectory of the trailing edge of turbulent spots and the trailing edge of the calmed region respectively.

At the traverse location closest to the trailing edge, four distinct levels of δ' are distinguishable. The highest levels occur between lines *B* and *E* and originate from the interaction of the wake and the inflexional profiles of the separating boundary layer. The next highest region of δ' occurs between lines *E* and *F* and results from the turbulent strip formed by the wake induced bypass transition. The lowest region of δ' occurs between lines *F* and *G*. This region corresponds to the calmed region and shows that the calmed region persists to the trailing edge. Finally between *G* and *A* of the following cycle the level of δ' is again elevated due to the natural transition that occurs once the influence of the calmed region has passed.

7.4.3 Integral Parameters

The ensemble average integral parameters were calculated from the measured velocity profiles. The displacement thickness, δ^*, and momentum thickness, θ, are presented in Figure 7-6 and Figure 7-7 respectively. Figure 7-8 presents an S-T diagram of the boundary layer shape factor, H_{12}. Trajectory lines and labels are repeated from previous S-T diagrams.

The rollup vortices labelled *C* and *D* change the boundary layer profiles and thus affect the integral parameters. A close inspection of Figure 7-6 reveals that in the region of the rollup vortices a series of peaks and troughs of δ^* are formed. The trajectories *C* and *D* lie along regions of reduced δ^* while between these trajectories regions of elevated δ^* are measured. However, Figure 7-7 reveals generally elevated levels of θ with no distinct features. The rollup vortices thus influence δ^* more than θ. This is highlighted in Figure 7-8 where trajectories *C* and *D* lie in distinct wedge shaped regions of reduced H_{12} protruding into the elevated H_{12} of the inflexional flow.

In Figure 7-7, two regions of elevated θ are identified. The first, originating at *C*, is due to the turbulent boundary layer that results from the breakdown of the rollup vortices. The second region of elevated θ is seen to form at label *H*. This corresponds to the second region of elevated δ' that was previously identified to result from the wake-induced bypass transition in Figure 7-5.

A region of calmed flow bounded by lines *F* and *G* follows the wake induced turbulent strip. The calming is associated with low levels of δ^* and θ observed in this region. The reduced θ region is seen to persist to the trailing edge and identifies the calmed region with low losses as shown by Howell (1999). After the calmed region has passed, both δ^* and θ increase gradually. In this region H_{12} increases as δ^* increases more rapidly than θ. This describes the process whereby the calmed boundary layer relaxes back to the inflexional profiles and a separating boundary layer under a strong adverse pressure gradient.

The effect of the wake's negative jet on the boundary layer is apparent between lines *A* and *B*. As the wake approaches θ decreases while δ^* is unaffected. The result of this is to produce more inflexional boundary layer profiles with increased H_{12}. The separation point thus moves marginally upstream.

The values of θ at the blade trailing edge were used by Howell (1999) to compare the boundary layer losses at different phases through the wake passing cycle. Between lines *B* and *E*, the trailing edge momentum thickness is highest. The S-T diagram shows that this region of high θ is the turbulent fluid that results from the breakdown of the rollup vortices formed due to the inviscid interaction of the wake and the separation bubble. A second region of high θ at the trailing edge occurs between lines *E* and *F*. This results from the turbulent spots formed by the wake induced bypass transition. These observations show the same character as those made from the trailing edge levels of δ'.

7.5 Unsteady boundary layer development

Further details of the 2D LDA boundary layer traverses are presented to gain a better understanding of the interaction of the wake and separating boundary layer. To achieve this understanding, a series of phases through the wake passing cycle were selected for analysis.

A collage of the mean and turbulent flow quantities measured through the boundary layer at each of these selected phases are presented in Figure 7-10 to Figure 7-13. The mean flow is described by vector plots of the mean and perturbation velocities and a contour plot of vorticity calculated from the measured velocity field. The mean velocity vectors show the boundary layer profile and character while the perturbation velocity vectors highlight the unsteady components of the velocity field, in particular, the wall normal velocity components and the position of the wake. Plots of vorticity enable the identification of vortical structures embedded in the sheared fluid of the boundary layer. Further information about the nature of the boundary layer profiles is also available as the peaks of vorticity away from the wall highlight the inflexional profiles and free shear layers.

Contour plots of the ensemble average turbulent quantities are also presented at each of the selected phases. The turbulent kinetic energy (*TKE*) is calculated directly from the measured velocity fluctuations. The production of *TKE* is calculated from the measured Reynolds stresses and mean velocity gradients as in Chapter 5. Finally, the dissipation of *TKE* is presented. This was calculated simply as the difference in *TKE* flux and *TKE* production. Details of the calculation of the dissipation of *TKE* are described in Appendix III.

Figure 7-9 shows the selected phases superimposed on the S-T schematic of wake induced transition with a separating boundary layer that was presented in Figure 7-3. Phases *i*, *ii* and *iii* are equally spaced through the inviscid interaction with *i* just prior to the interaction. The sequence depicts the rollup of the separated shear layer induced by the wake passing. Phase *iv* is near the end of the calmed region and depicts the boundary layer state between wakes.

7.5.1 Boundary layer state before the interaction of the wake and inflexional profiles

The boundary layer state at phase *i* can be inferred from the schematic of Figure 7-9. Upstream of the separation point, *1*, the boundary layer is laminar and attached while downstream of *1* the boundary layer profiles are inflexional. The separating boundary layer undergoes transition from point *2* and reattaches at position *3*. The position of the wake in the freestream is immediately upstream of the separation point, *1*. These labels are transferred to the collage of boundary layer measurements at phase *i* which is presented in Figure 7-10.

Figure 7-10 (a) shows the ensemble average velocity vectors at phase *i*. The inflexional profiles of the separating boundary layer are evident in the region between *1* and *2*. These inflexional profiles have their maximum vorticity levels displaced from the wall (Figure 7-10 (c)), which is indicative of a free shear layer between *1* and *2*. At this phase, the shear layer is not perturbed. This is confirmed by the absence of wall normal components of the perturbation velocity vectors in Figure 7-10 (b). Also evident from Figure 7-10 (b) is the position of the wake, the centre of which is located immediately upstream of *1* and is marked by a filled circle.

The reattachment process that results from the transition of the inflexional profiles occurs between *2* and *3*. This region is characterised by the velocity profiles becoming fuller and turbulent in character. In the vorticity contour plots, this process is characterised by the disappearance of the peak displaced from the wall and by reduced levels of vorticity in the outer boundary layer as the profiles become fuller and more turbulent.

The transition associated with the free shear layer is accompanied by increased levels of *TKE*. This increase in *TKE* is seen to start at *2* in Figure 7-10 (d) and extend to the trailing edge. The increased levels of *TKE* coincide with increased levels of production and dissipation of *TKE* as shown by Figure 7-10 (e) and (f). The velocity profiles downstream of *3* are full and so the velocity gradients are low. The *TKE* production thus results primarily from increased levels of Reynolds stresses in the turbulent boundary layer. The dissipation and production are of similar levels and occur at the same location, however, the reduced streamwise resolution compromises the quality of the measurements in this region.

7.5.2 Interaction of wake and inflexional boundary layer

It was shown in Chapter 6 that the inviscid rollup of the separated shear layer is triggered by the wake passing. The schematic of Figure 7-9 shows that the boundary layer at phase *ii* is representative of this inviscid rollup. The interaction of the wake and inflexional profiles occurs between *4* and *6*. Downstream of *6* the boundary layer is still inflexional as the wake has not yet reached this location. The transition and reattachment of the inflexional profiles occurs between *7* and *8*. These labels have been transferred to Figure 7-11, which presents the boundary layer state measured at this phase.

The mean velocity profiles of Figure 7-11 (a) differ from those at phase *i*. At *4* the profiles are inflexional and this is confirmed by the vorticity contours in Figure 7-11 (c) which show a peak detached from the wall. However, between *4* and *5*, the velocity profiles are full and at *5* the profiles are again inflexional. Between *5* and *6* the profiles are again full while at *6* the profiles are again inflexional. This rapid change with distance along the blade surface is attributed to the rollup of the shear layer induced by the wake. Indeed, rollup vortices may be identified at *4*, *5* & *6* in Figure 7-11 (c) as regions of high vorticity embedded within the boundary layer. The boundary layer edge can be inferred from the edge of the elevated vorticity region. From this the rollup vortices can be seen to thicken the boundary layer locally, particularly at *5*. This was also observed in the S-T diagram of δ^* shown in Figure 7-8. The perturbation velocity vectors of Figure 7-11 (b) show significant wall normal velocities associated with the rollup vortices. The rollup vortex with its centre at *5* may be identified in the perturbation velocity vectors. It is clear that the rollup vortex at *5* induces large local flow curvature and it is this flow curvature that is responsible for the large pressure oscillations measured at the wall in Chapter 6.

Downstream of the wake, between *6* and *7*, the velocity profiles are inflexional and the vorticity contours show a peak detached from the wall. This region has not yet been affected by the wake passing. The transition and reattachment of the inflexional profiles between *7* and *8* occurs as in phase *i*.

Figure 7-11 (d) shows contours of *TKE* at phase ii. The elevated turbulence associated with the wake (see contour level 0.001) can be seen to extend from 4 to the trailing edge and the boundary layer *TKE* is elevated throughout this region. Three regions of elevated *TKE* are distinguishable at labels 4,5 & 6 and correspond to the centres of the rollup vortices previously identified. The highest levels of *TKE* are located at *5* which is the largest and most distinct of the rollup vortices. The reduced levels of *TKE* at *7* corresponds to the inflexional profiles that have not yet interacted with the wake. Downstream of this, the elevated *TKE* is a result of the natural transition of the inflexional profiles.

The production and dissipation of *TKE* are presented in Figure 7-11 (e)&(f). These follow the distribution of *TKE* with elevated production and elevated dissipation at the centre of the vortices at *4*, *5* & *6*. The peak levels of production and the peak levels of dissipation are located at the centre of the vortex at *5*. The natural transition downstream of *8* is also associated with elevated levels of *TKE* production and dissipation. In this region, the dissipation extends further from the wall then the production.

7.5.3 Boundary layer after wake interaction

From Figure 7-9, it can be seen that at phase *iii* the boundary layer is dominated by the wake induced turbulent strip. The wake-induced strip can be further decomposed into three regions. Between *9* and *10*, the boundary layer is transitional, between *10* and *11* the boundary layer is turbulent due to the wake induced bypass transition and downstream of *11* the boundary layer is turbulent as a result of the breakdown of the rollup vortices formed by the interaction of wake and the inflexional profiles. These labels are transferred to Figure 7-12.

The mean velocity profiles are shown in Figure 7-12 (a). Upstream of *9* the boundary layer profiles are laminar. Between *9* and *10* the boundary layer profiles have the shape of attached laminar profiles but the levels of *TKE* in this region are elevated (see Figure 7-12 (d)). This indicates that the profiles are transitional in this region.

Downstream of *10* the velocity profiles have a turbulent shape. However, the levels of *TKE* downstream of *11* are far higher than between *10* and *11*. This is attributed to the breakdown of the rollup vortices. An isolated region of elevated *TKE* can be identified in Figure 7-12 (d) at *11*. Although not evident in the vorticity contours, this is attributed to a rollup vortex and is accompanied by elevated production and elevated dissipation that accompanied the rollup vortices identified at phase *ii* (see Figure 7-12 (e)&(f)). The levels of production measured at the vortex centre are lower than those measured previously at phase *ii*. The vortex is now further from the wall where the boundary layer velocity gradients are smaller and this reduces the production of *TKE* at the vortex centre. The reduced streamwise resolution of the measurements downstream of *11* causes streaks in the contours and this prevents the identification of further rollup vortices downstream of this location.

The boundary layer between *10* and *11* is due to the wake-induced bypass transition and is characterised by elevated *TKE* together with elevated production and dissipation. The production in this region is of similar magnitude to that of the vortex centred at *11*, however, the extent is smaller. The peak dissipation in this region is slightly higher than that associated with the rollup vortex at *11* and again the extent is smaller than that of the vortex. The area of elevated dissipation is greater than the area of elevated production. This is also true for the rollup vortex.

7.5.4 Calmed boundary layer

After the passage of the wake, the boundary layer relaxes back to its pre-transitional state. Phase *iv* is representative of this. The sketch of Figure 7-9 shows that the boundary layer is laminar upstream of *13*. Between *13* and *14* the boundary layer is calmed while downstream of *14*, the boundary layer is turbulent. The boundary layer measurements, shown in Figure 7-13, have these positions marked on them.

The velocity profiles along the blade surface are shown in Figure 7-13 (a). Upstream of *12* the boundary layer is laminar and attached. Between *12* and *13*, the boundary layer is laminar and in the forward part of this region, the profiles are inflexional. This is emphasised by the vorticity peak detached from the wall. Over the rear portion of the region between *12* and *13* the boundary layer profiles are fuller and more like the calmed profiles that are observed between *13*and *14*. The profiles between *12* and *13* describe the process whereby the calmed profiles become inflexional and start to separate under the strong adverse pressure gradient.

The *TKE* at phase *iv* is shown in Figure 7-13 (d). The levels of *TKE* are observed to be low. The elevated region between *13* and *14* is due to the decaying boundary layer turbulence in the calmed region, while downstream of *14* the turbulence is due to the turbulent boundary layer.

The production and dissipation of *TKE* are presented in Figure 7-13 (e) & (f). The levels of production and dissipation are very low throughout the measurement domain with only a small region of low production at *14* and a similar level of dissipation between *13* and *14*. These low levels of production and dissipation of *TKE* again point to the loss reducing mechanism associated with the calmed region as described in Chapter 4.

7.6 Kelvin-Helmholtz breakdown of the shear layer

The rollup of the separated shear layer associated with the interaction of the wake and the inflexional profiles is shown in Figure 7-14. Measurements of the vorticity over a small region of the boundary layer are presented as a sequence of contour plots at an interval of *1/64* of the wake passing cycle.

In the first frame, *1*, the ensemble average velocity vectors are superimposed on the vorticity contours. The peak vorticity is away from the blade surface typifying the separated shear layer of the inflexional profiles. At this phase, there is no perturbation to the shear layer. The next two frames, *2* & *3*, show the development of a perturbation to the shear layer, which forms a cat’s eye pattern in the measured vorticity field. This cat’s eye pattern of vorticity is typical of the inviscid Kelvin-Helmholtz mechanism. The measurements of Watmuff (1999) exhibit a similar pattern that enabled the author to infer the inviscid nature of the instability governing the growth of a wave-packet in a laminar separation bubble. The following frames, *4*, *5* & *6*, describe the growth and convection of the rollup vortex.

7.7 Conclusions

The ensemble-average 2D LDA measurements of the boundary layer on the T106 LP turbine cascade provide new insight into the wake induced transition mechanism. The measurements confirm the mechanism proposed in Chapter 6 and show the separated shear layer associated with the inflexional profiles of the re-establishing separation bubble to form rollup vortices beneath the passing wake. The vortices were formed by an inviscid Kelvin-Helmholtz mechanism. Due to the inviscid nature of the rollup mechanism, there was no delay between the wake passing and the boundary layer response. The rollup vortices were observed to breakdown into highly turbulent flow that convected along the blade surface. The rollup vortices embedded in the boundary layer are responsible for the measured pressure oscillations that were discussed in Chapter 6.

The transition mechanism described above was observed on the T106 cascade and not on the flat plate. The differences are attributed to the relative positions of the transition onset location and the separation location. For the flat plate, wake induced transition occurred before the separation point. The turbulent boundary layer fluid formed as a result then simply convects into and suppresses the separation bubble. This is akin to the mechanism described by Schulte and Hodson (1994). By contrast, the mechanism described above results when no wake induced turbulent spots are formed upstream of the separation location. The turbulent wake then convects over the inflexional profiles of the separating boundary layer and the inviscid breakdown described above results.

The production and dissipation of *TKE* were determined from the measured Reynolds stress components and mean velocity gradients. The centres of the rollup vortices were identified to have high levels of *TKE*, *TKE* production and *TKE* dissipation.

7.8 Figures

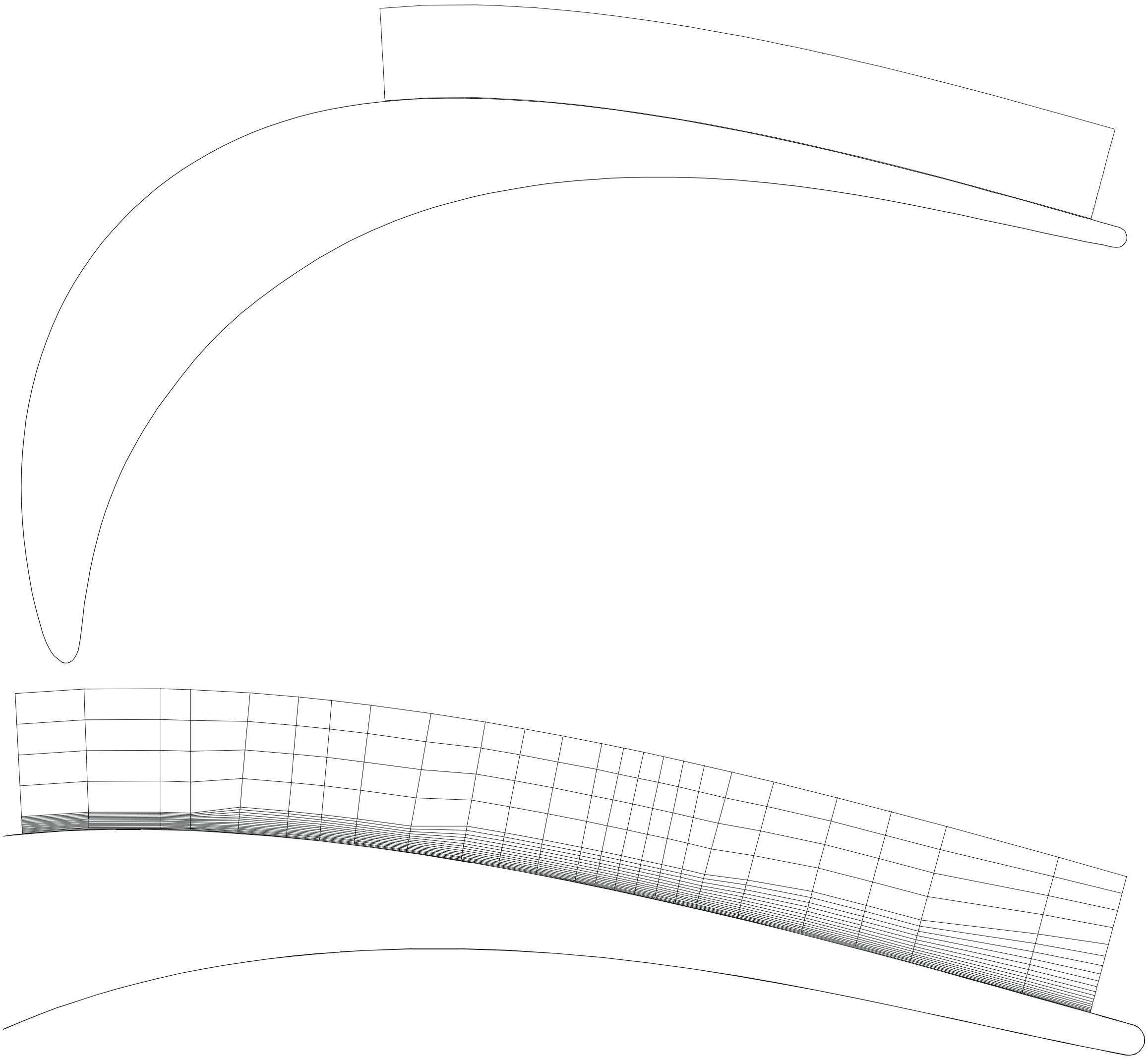

Figure 7-1: Measurement grid for boundary layer of T106 LP turbine cascade.

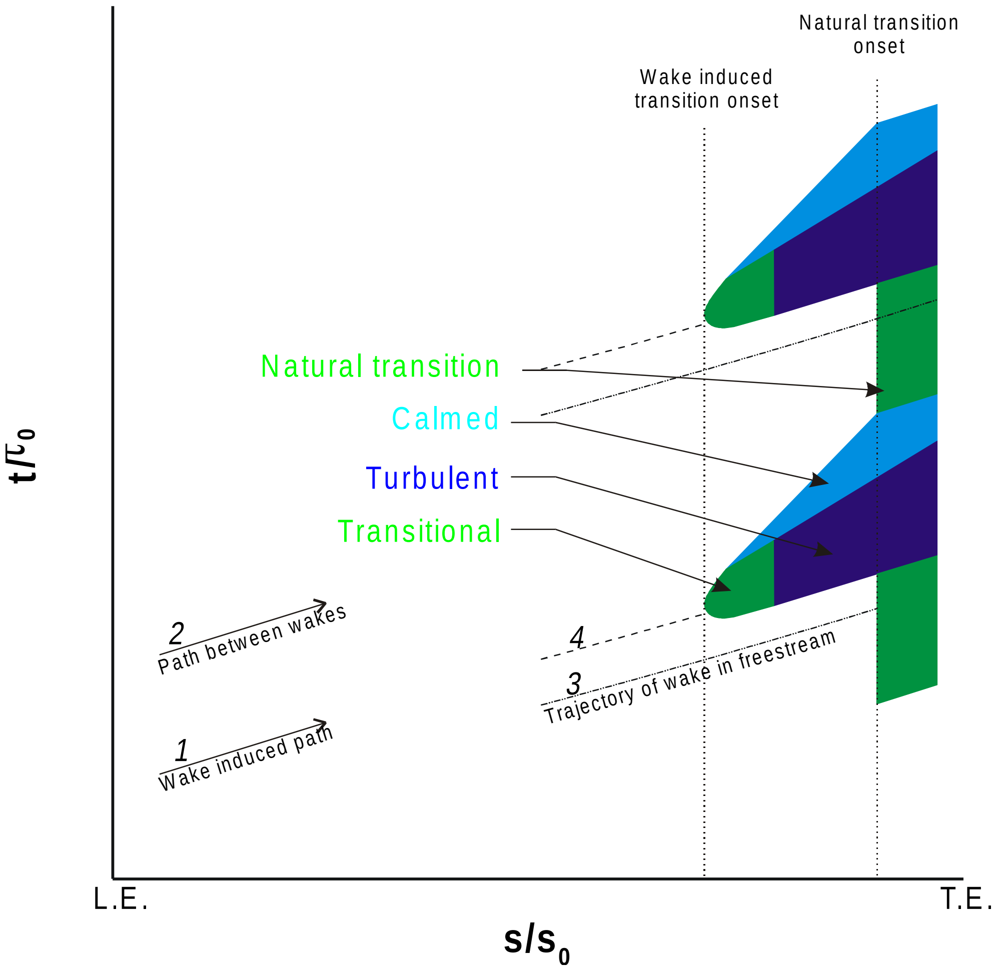

Figure 7-2: Simplified S-T sketch of wake induced transition in an axial turbine exhibiting bypass transition of the attached boundary layer under the wake.

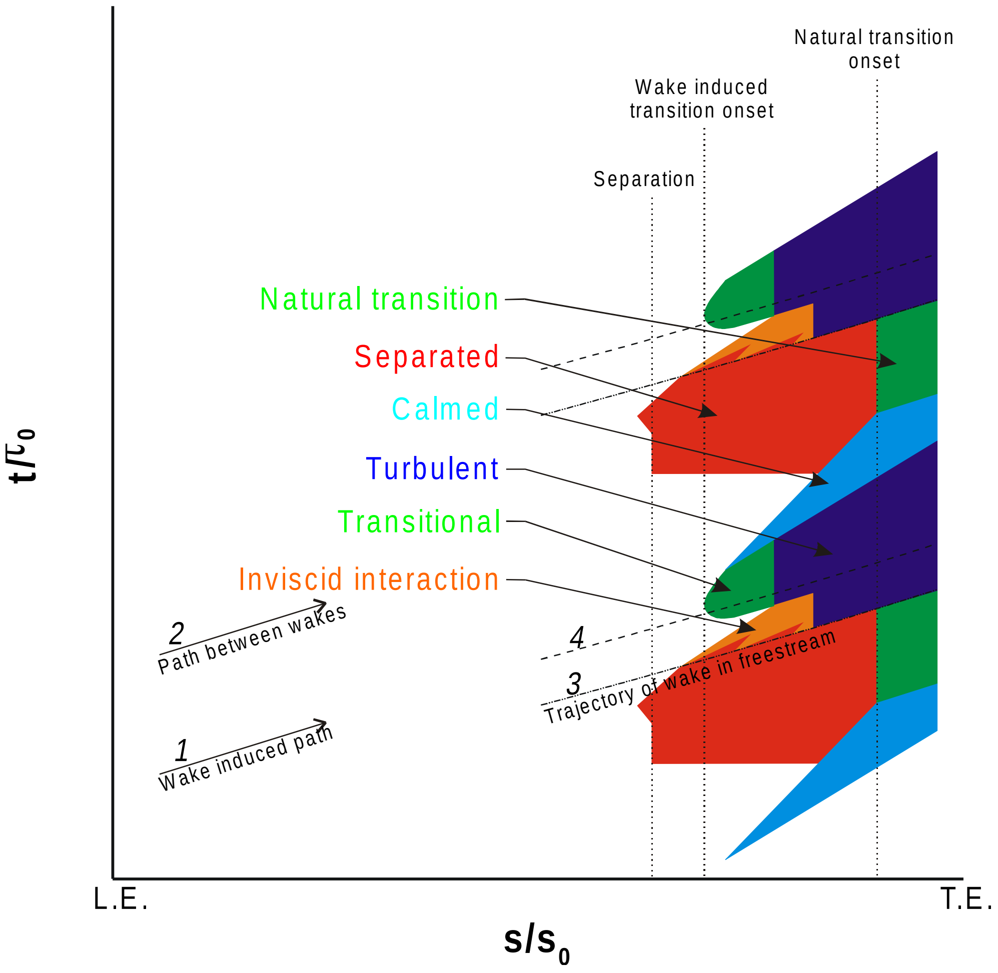

Figure 7-3: Simplified S-T sketch of wake induced transition in axial turbines with wake separation bubble interaction.

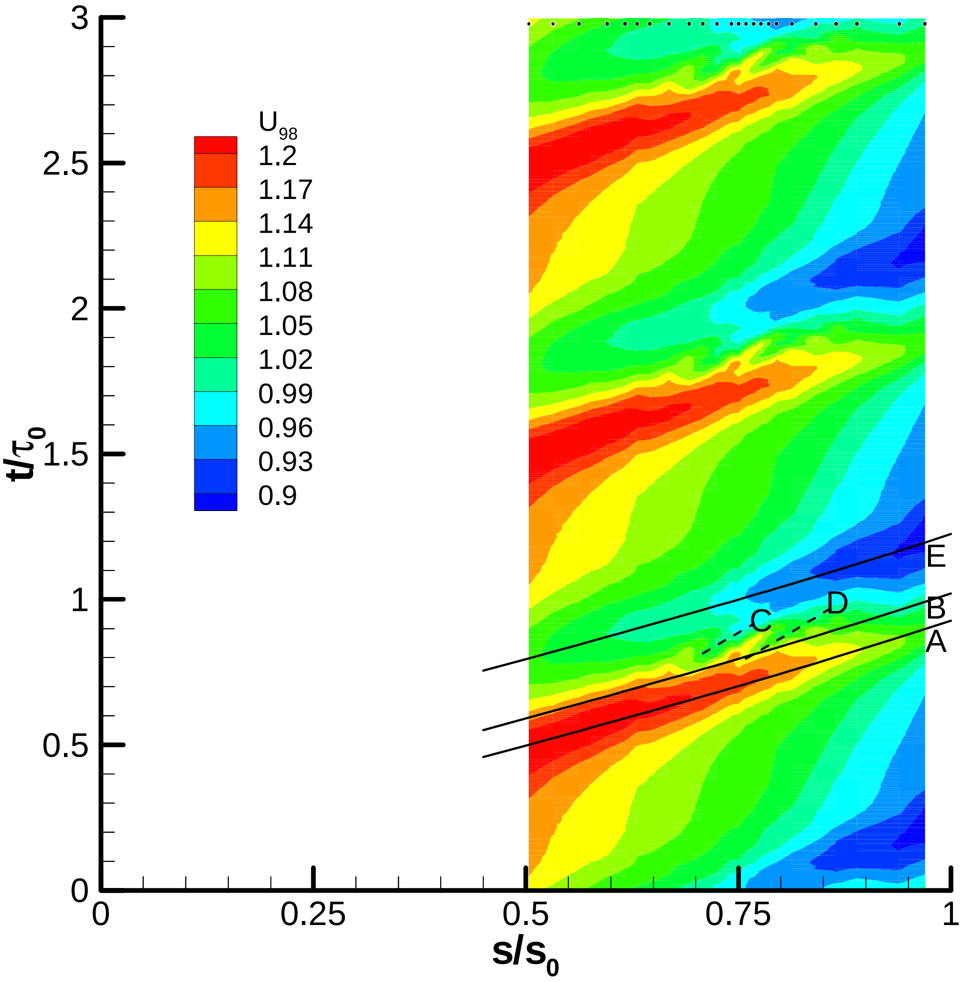

Figure 7-4: S-T diagram of measured boundary layer edge velocity, *U_{98}*. *$Re_{2C}=1.6\times10^5$ $\phi=0.83$ $s_b/s_c=1$, $f_r=0.68$.*

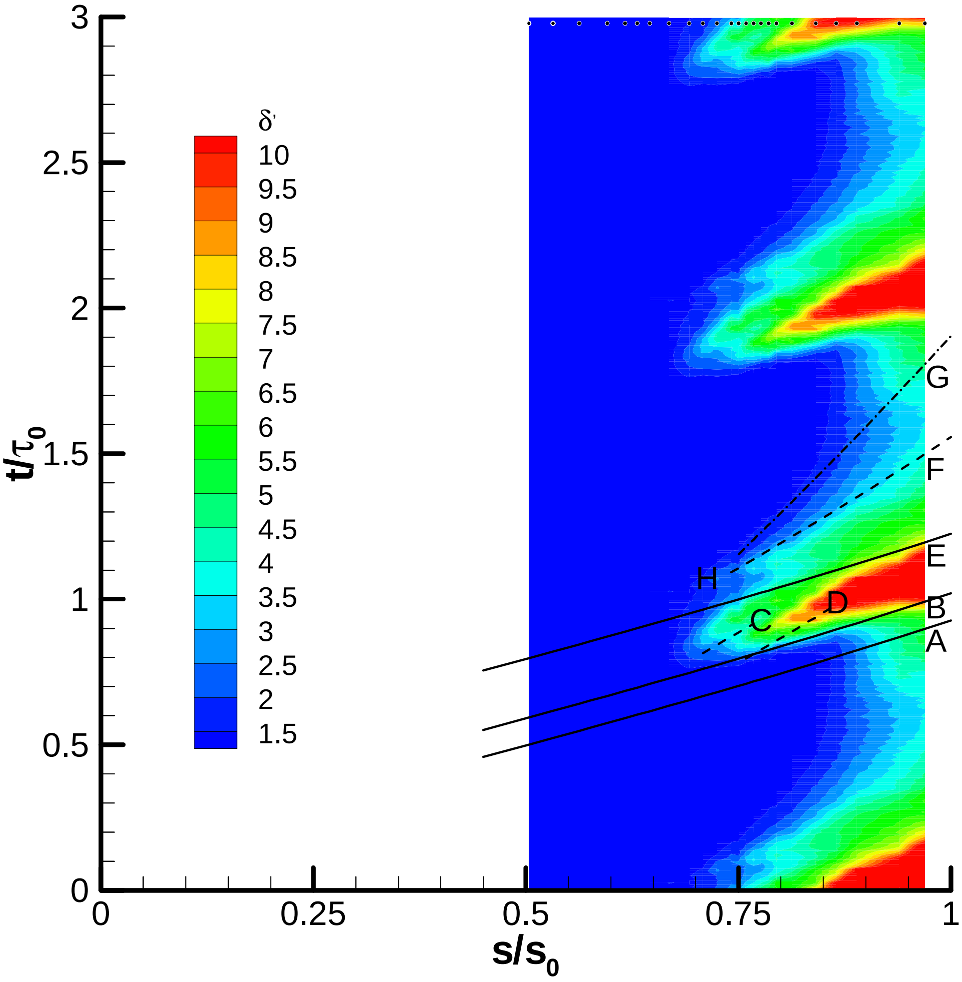

Figure 7-5: S-T diagram of TKE integrated through the boundary layer, δ'. *$Re_{2C}=1.6\times10^5$ $\phi=0.83$ $s_b/s_c=1$, $f_r=0.68$.*

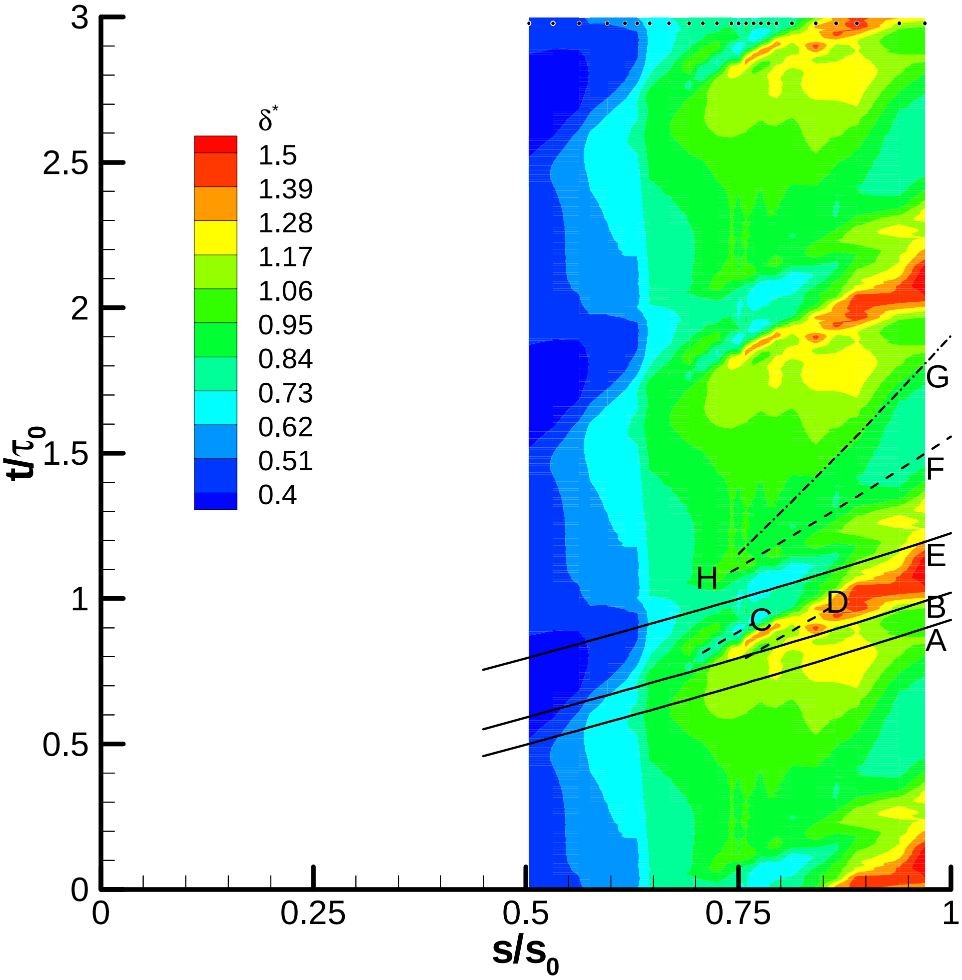

Figure 7-6: S-T diagram of measured displacement thickness, δ^*. $Re_{2C}=1.6\times10^5$ $\phi=0.83$ $s_b/s_c=1$, $f_r=0.68$.

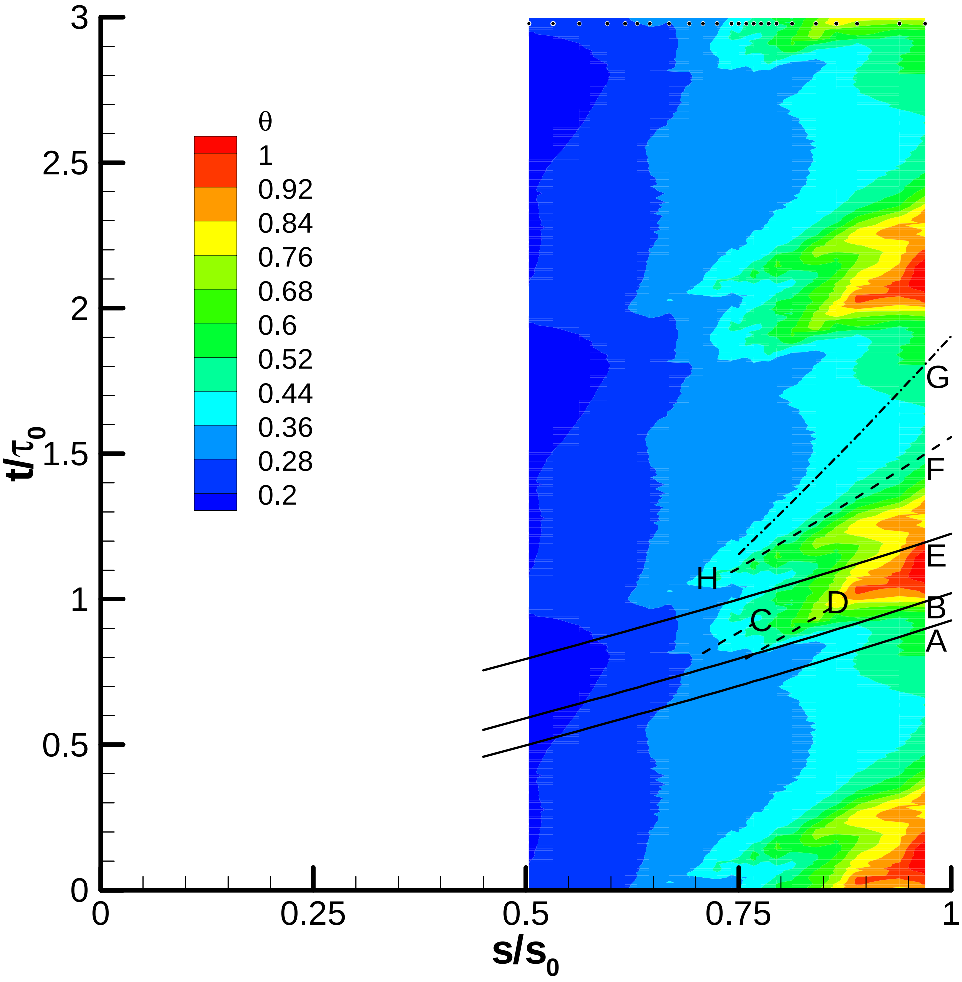

Figure 7-7: S-T diagram of measured momentum thickness, *θ. $Re_{2C}=1.6\times10^5$ $\phi=0.83$ $s_b/s_c=1$, $f_r=0.68$.*

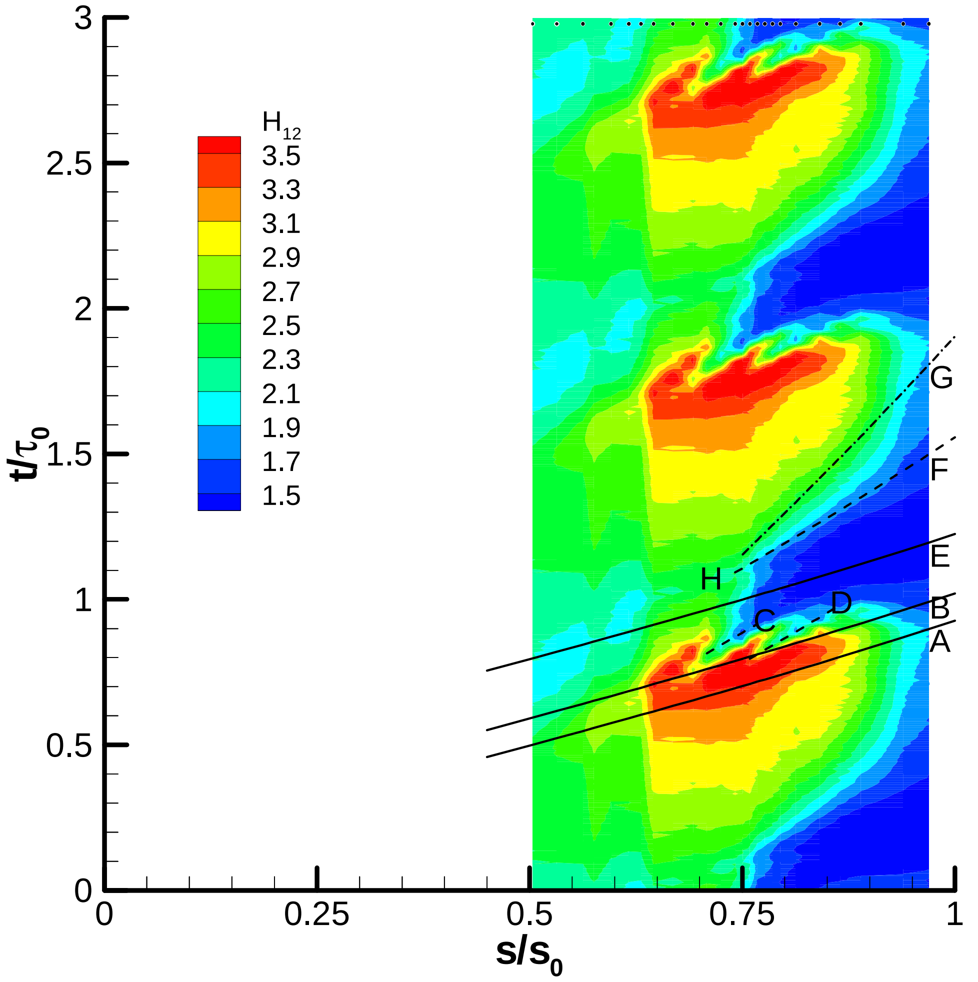

Figure 7-8: S-T diagram of measured shape factor, H_{12}. $Re_{2C}=1.6\times10^5$ $\phi=0.83$ $s_b/s_c=1$, $f_r=0.68$.

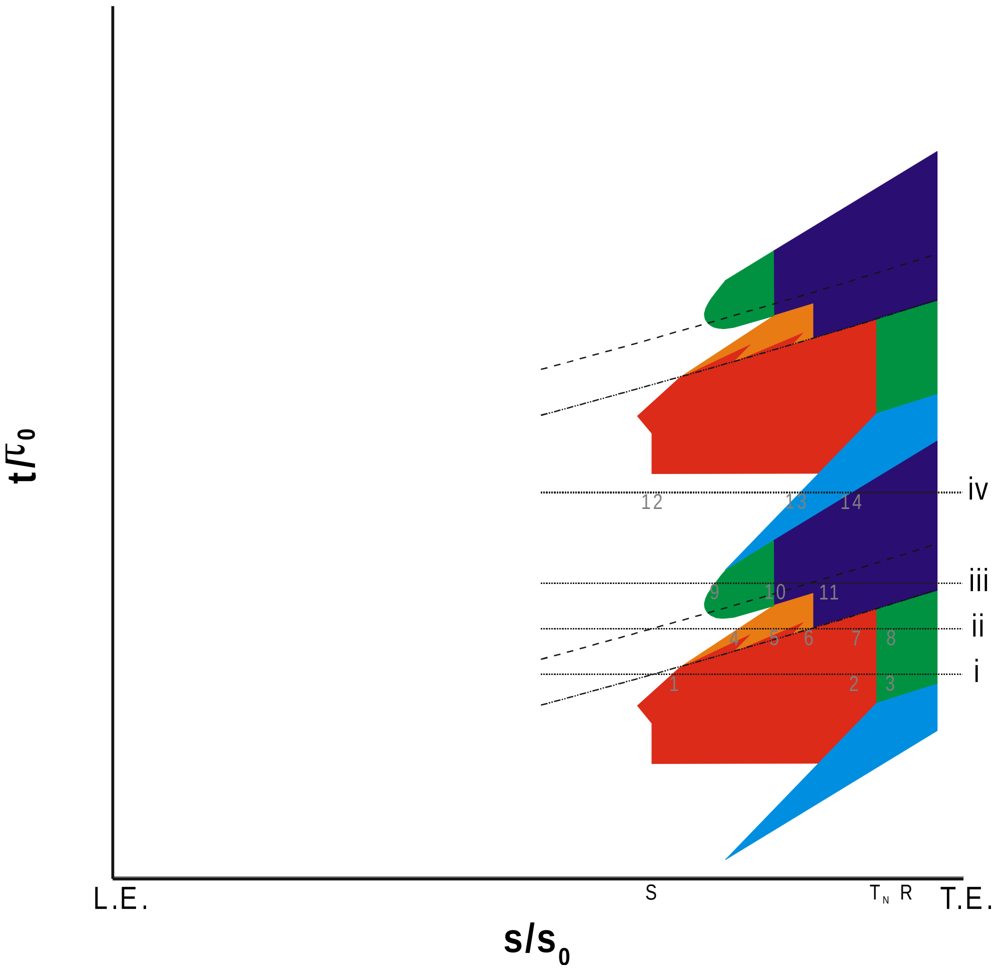

Figure 7-9: Sketch showing selected phases for boundary layer collages.

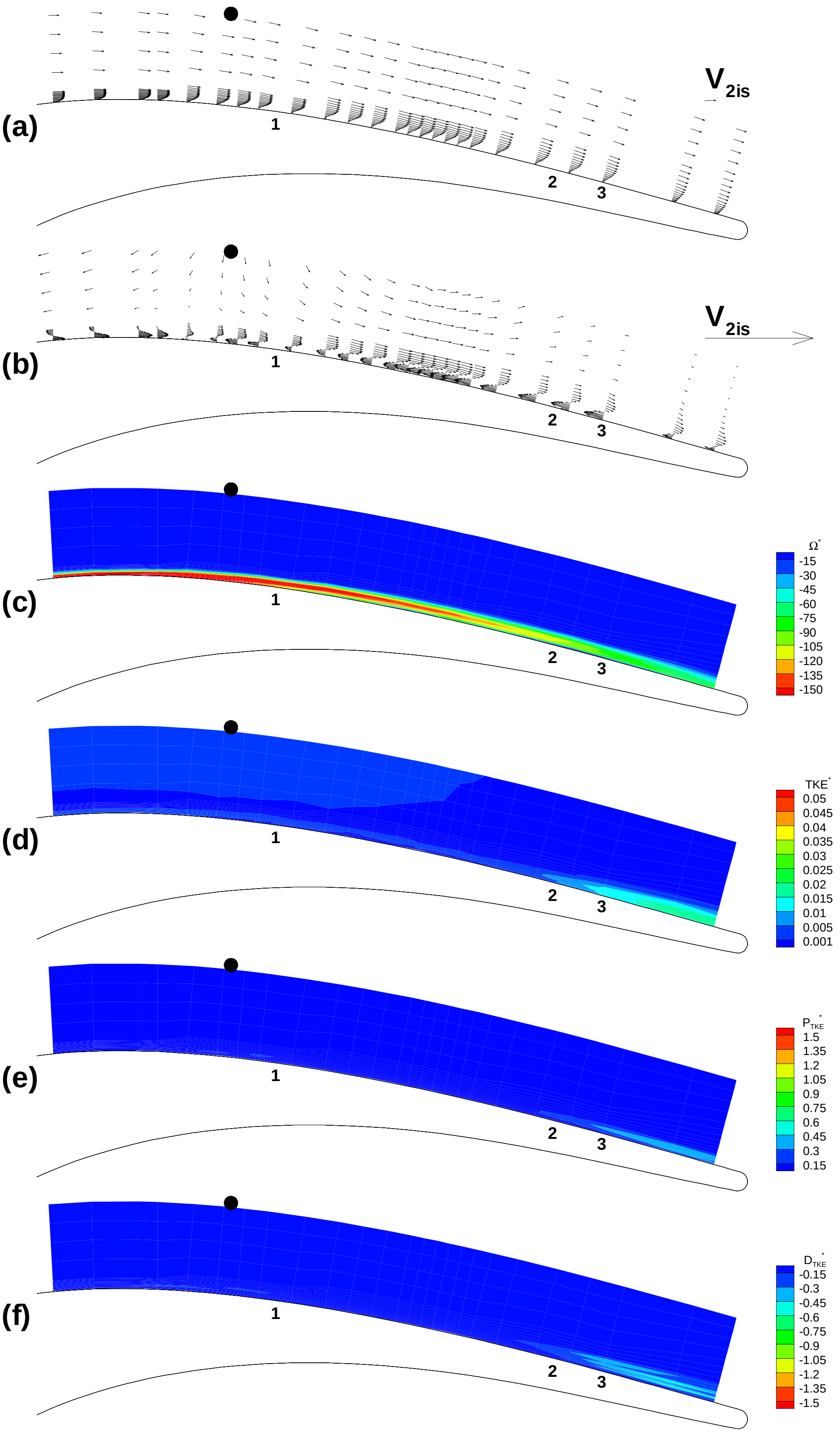

Figure 7-10: Collage of 2D LDA boundary layer measurements at phase *i*, before the wake passes the separation point. $t/\tau_0=0.70$; $Re_{2C}=1.6\times10^5$; $\phi=0.83$; $s_b/s_c=1$, $f_r=0.68$.

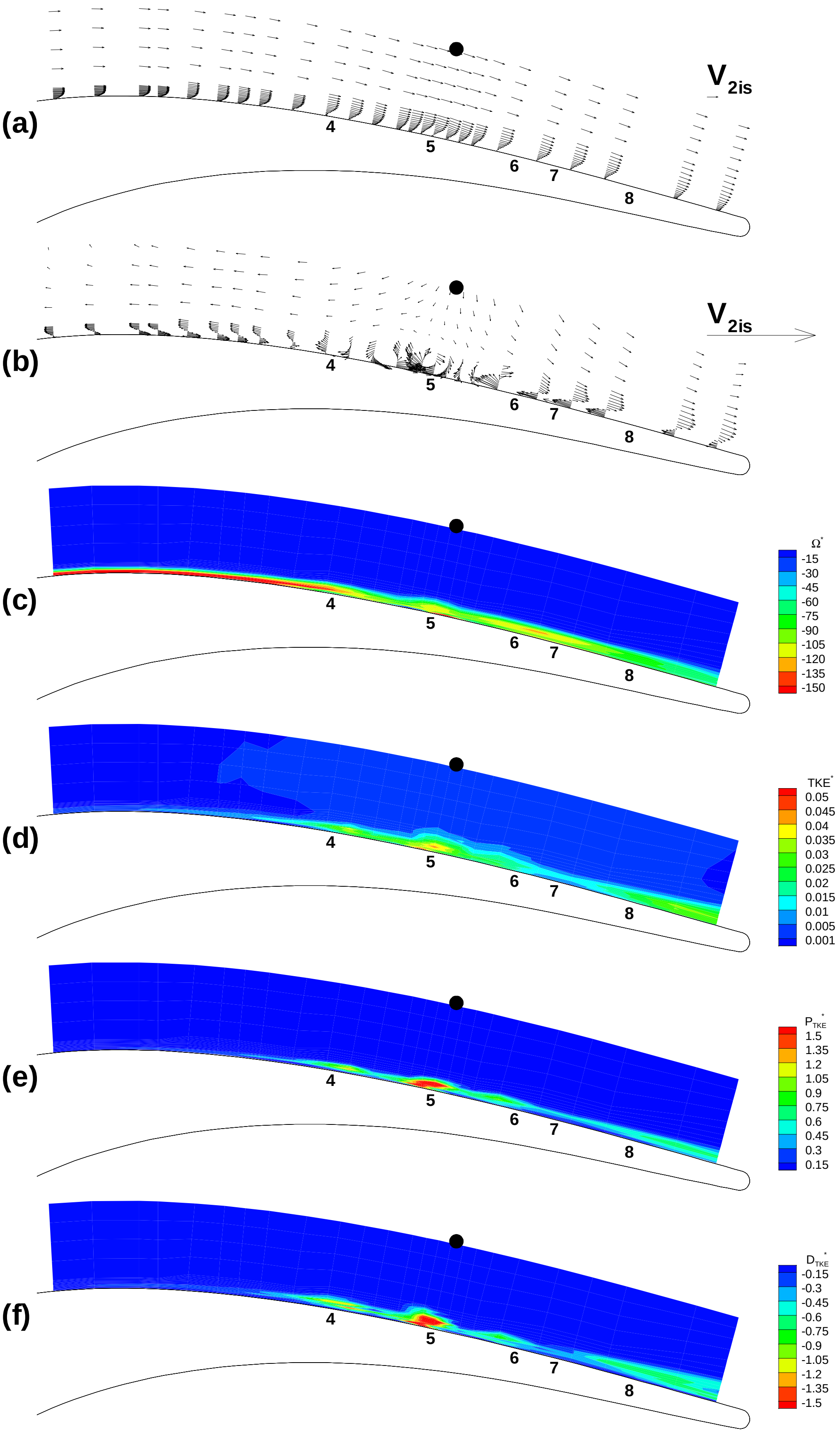

Figure 7-11:Collage of 2D LDA boundary layer measurement at phase *ii*, during the interaction of the wake with the inflexional profiles. $t/\tau_0=0.86$; $Re_{2C}=1.6\times10^5$; $\phi=0.83$; $s_b/s_c=1$, $f_r=0.68$.

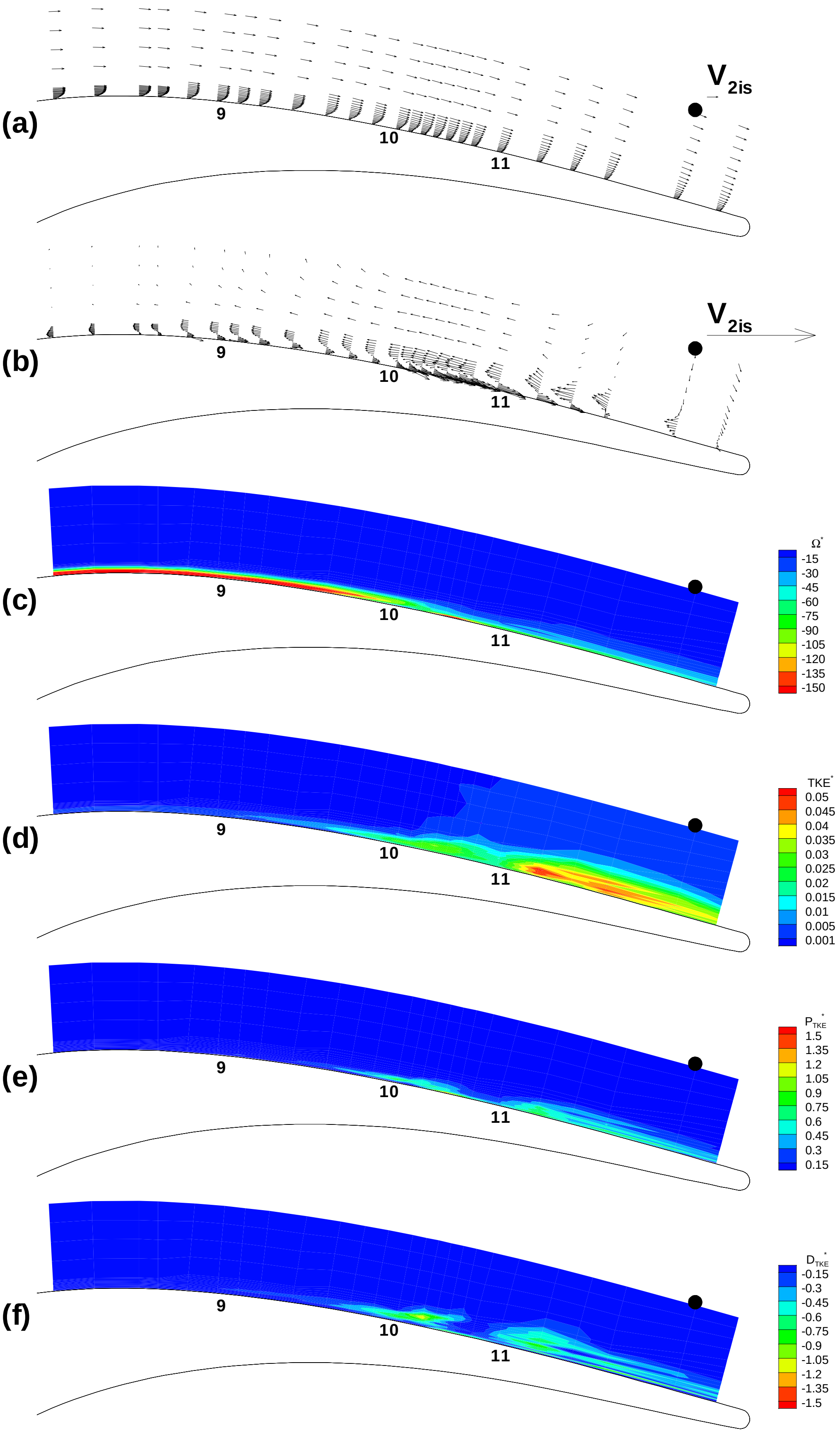

Figure 7-12: Collage of 2D LDA boundary layer measurements at phase *iii*, showing the turbulent boundary layer resulting from the interaction of wake and inflexional profiles. $t/\tau_0=0.01$; $Re_{2C}=1.6\times10^5$; $\phi=0.83$; $s_b/s_c=1$, $f_r=0.68$.

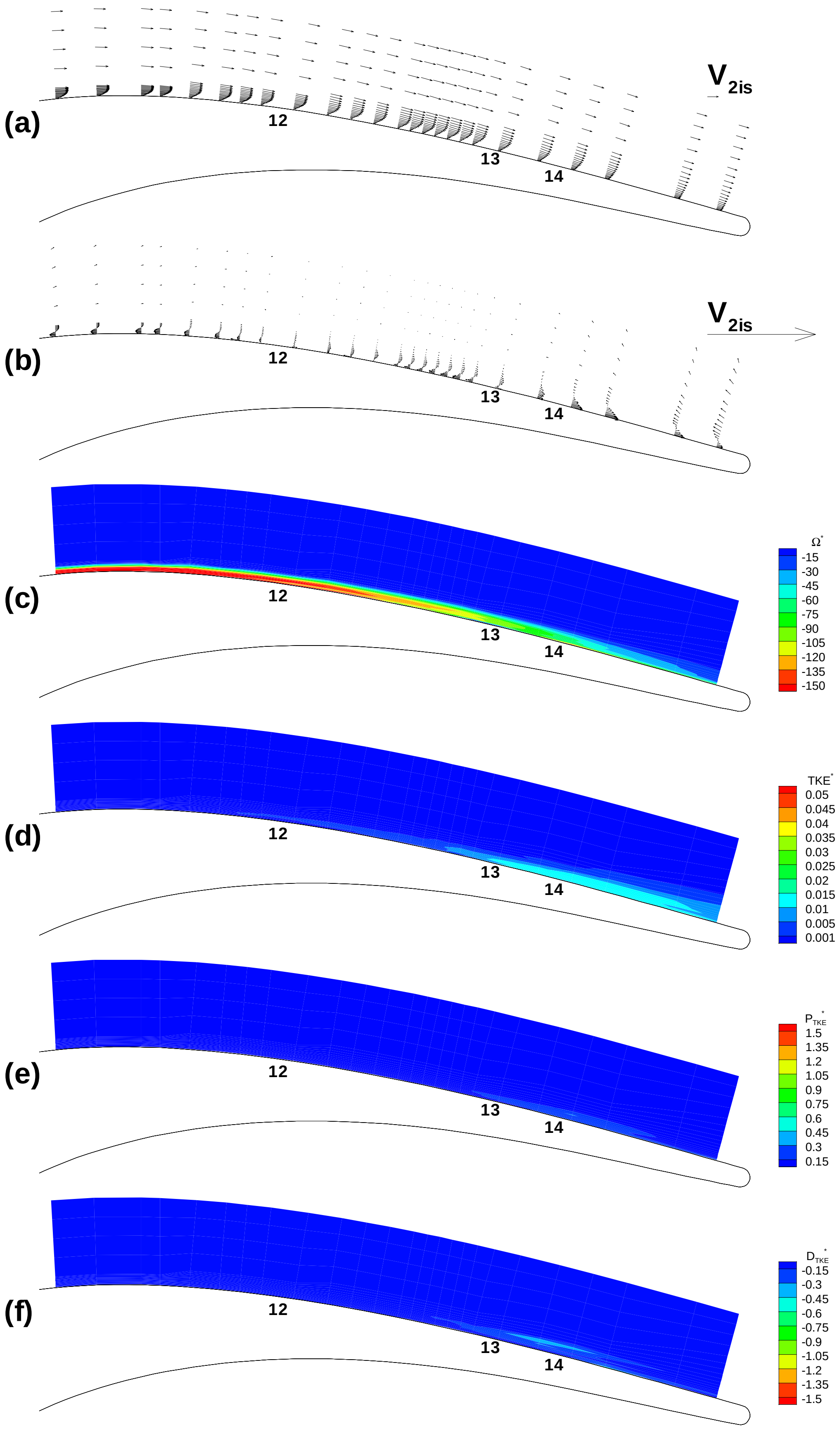

Figure 7-13: Collage of 2D LDA boundary layer measurements at phase *iv*, in the calmed region after the wake interaction of the wake with the inflexional profiles. $t/\tau_0=0.32$; $Re_{2C}=1.6\times10^5$; $\phi=0.83$; $s_b/s_c=1$, $f_r=0.68$.

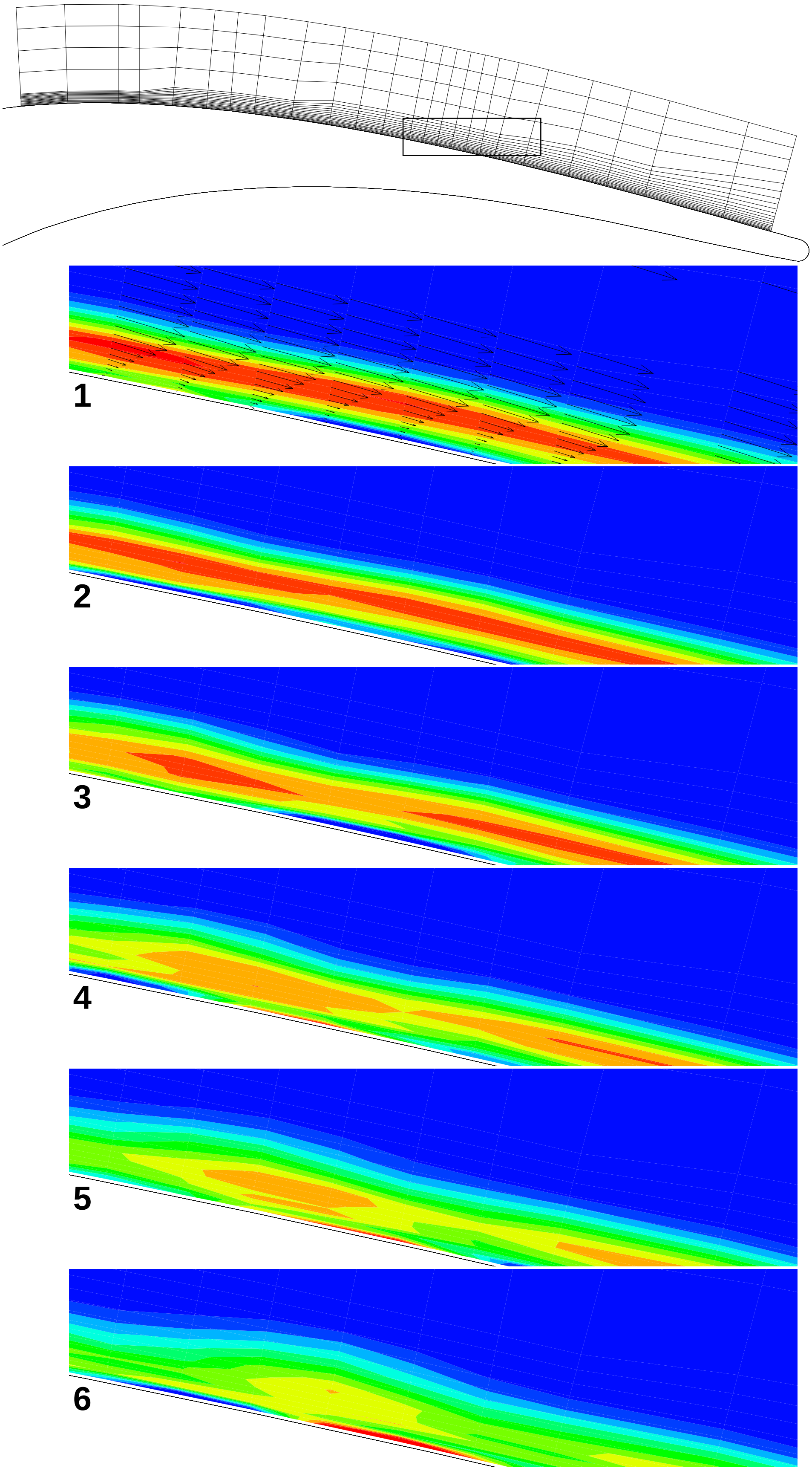

Figure 7-14: Measurements of vorticity in the boundary layer detailing the Kelvin-Helmholtz breakdown of the separated shear layer.

Chapter 8: Conclusions and recommendations for future work

8.1 Conclusions

8.1.1 Flat Plate

The boundary layer of a flat plate subject to a pressure distribution matched to the T106 LP turbine cascade was measured using 1D LDA and a novel technique to determine the 2D Reynolds stresses. The unsteady flow conditions were created by a wake generator using cylindrical bars traversed across the inlet. The bars produced strong wakes, which resulted in bypass transition upstream of the steady flow separation point. The wake induced turbulent strip suppressed the separation bubble. A calmed region followed the wake induced turbulent strip and continued to suppress separation. As the influence of calming decayed, the boundary layer relaxed to its pre-transition state and began to separate. During this process, instability waves were observed in the ensemble average boundary layer measurements. This provides evidence of deterministic natural transition phenomena arising between wake passing events. The unsteady flow field provides conditions where the boundary layer is most susceptible to unstable disturbances for a short time period. Disturbances entering during this time evolve preferentially and form deterministic structures of wave-packets in the boundary layer. This phenomenon was observed by Obremski and Morkovin (1969) for an unsteady flow with a sinusoidal fluctuation of the freestream.

From measurements of the ensemble average mean flow and the full ensemble average 2D Reynolds stress tensor, it was possible calculate the boundary layer dissipation on the flat plate. This direct measure of the rate of entropy production in the boundary layer highlighted the loss reducing mechanisms associated with wake-induced transition. As expected high levels of dissipation were measured in the wake induced turbulent strip and low levels in the laminar boundary layer. The calmed region following the turbulent strip was shown to have laminar levels of dissipation, as was the separating boundary layer. This confirms that the loss reduction associated with the interaction of a wake and separation bubble is due to the substitution of the highly dissipative steady separation bubble flow with calmed and re-establishing separation flows that are characterised by low dissipation.

8.1.2 T106 LP turbine cascade

Measurements of the convection of a wake through the T106 LP turbine cascade were made using 2D LDA and a measurement grid of unprecedented resolution. These detailed measurements of the 2D Reynolds stresses are intended to provide a database for the validation of numerical predictions.

Increased levels of *TKE* were seen to originate about the peak suction location. This was attributed to the interaction of the elevated turbulent stresses in the wake passing through a region of strained fluid and thereby acting as a region of *TKE* production. Subsequent to this region of high *TKE* production, the turbulence associated with the wake was seen to become more isotropic.

A novel adaptation of traditional wavelet transform algorithms allowed an ensemble averaged wavelet analysis of the randomly sampled LDA data. Results showed that the Reynolds stress components of the blade-to-blade flow were not dominated by any particular eddy size.

Unsteady blade surface pressure measurements revealed unexpected high frequency pressure oscillations with a peak-to-peak magnitude approximately *30%* of the exit dynamic head. The pressure oscillations originated as the wake passed over the region of the steady flow separation bubble.

Subsequent detailed 2D LDA measurements in the boundary layer revealed the source of the pressure oscillations to be a series of convected rollup vortices that formed by an inviscid Kelvin-Helmholtz mechanism when the wake perturbed the inflexional profiles. These vortices were identified as being localised regions of elevated production and dissipation of TKE.

Understanding of the mechanism by which the interaction of the wake and separation bubble results in transition is a crucial element in developing models for wake-induced transition in highly decelerated boundary layers.

8.2 Recommendations for future work

The evidence of instability waves in the ensemble averaged flat plate data indicates the presence of deterministic natural transition structures. Based on the ability of the simple quasi-steady e^n transition model of Obremski and Morkovin (1969) to predict the evolution of wave packets in a flow with sinusoidal freestream oscillations, it is suggested that such an approach may be applicable in determining transition in blade surface boundary layers between wake passing events.

No intermittency measurements are presented in this thesis. This is due to the subjective nature of the threshold selection in highly decelerated flows. It is proposed that a rigorous intermittency algorithm could be developed based on wavelet spectra. The instantaneous wavelet spectra could be compared to representative turbulent or laminar spectra and the intermittency determined on a suitable continuous scale. It should, however, be borne in mind that the concept of intermittency arose from transition studies in zero pressure gradient boundary layers where the turbulent and laminar portions of flow are distinct and may be discriminated in a binary manner. In separated flows, this simplistic view of turbulence may be misleading and obscure the true physics of the flow.

The detailed database of wake convection through the T106 LP turbine cascade is intended for the evaluation of CFD codes. The anisotropy associated with the wake turbulence suggests that Reynolds stress transport models may be most suited to correctly reproducing this phenomenon. However, as with all engineering calculations, the ability of k-ε models and algebraic models to adequately estimate the convection of turbulent parameters relevant to unsteady by-pass transition prediction calculations must be determined.

The increased levels of *TKE* that result from the production of *TKE* within the blade passage may prove beneficial in multistage LP turbine environments. The increasing levels of turbulence may prove more effective in suppressing separations formed by stronger adverse pressure gradients particularly as the Reynolds number drops through the machine, which further increases the danger of separation.

The new insights into the transition mechanism resulting from the interaction of a wake and separating boundary layer should be included in transition models in an attempt to improve design tools for highly loaded LP turbines. Moreover, understanding of the transition mechanism may assist in further increasing blade loading thus further reducing blade counts.

The formation of rollup vortices during the wake-induced transition suggests that traditional RANS calculations used for turbomachinery design and analysis will not have sufficient resolution to capture these flow features. In light of this, high-resolution calculations such as DNS or LES may be necessary to suitably predict the flow. However, the ability of RANS calculations with fine meshes should also be evaluated as a potential design tool while LES and DNS remain impractical for design purposes.

The current design process for LP turbine profiles involves simplistic calculations typically with prescribed intermittency models followed by cascade tests. Despite the complex transition mechanism involving the rollup of the separated shear layer, the results of Chapter 7 show that the trajectories of the wake induced turbulent regions may be adequately described by the correlations of Gostelow et al (1996). It is proposed that the pressure distribution may be optimised by modelling the onset location and spot celerities with existing correlations, the starting pressure distribution could then be adjusted by a numerical optimiser to find the optimal pressure distribution. Subsequent high-resolution calculations may be used to analyse these designs and take the place of preliminary cascade testing. As a result, fewer candidate designs will be tested reducing the development cost and time scale.

Unsteady transition measurements for turbomachines, including those presented here, have typically been performed at a single spanwise location. As a result, no information about the spanwise structure of the transition process is available. This should be investigated using a spanwise array of hot-film gauges and investigating the cross-correlations between various sensors. The flat plate and cascade facilities used for the current investigation are only capable of simulating a two-dimensional flow field. In real machines, the flow field is three-dimensional. In particular, the wakes are skewed resulting in different wake arrival times along the span of the blade. The effect of the different arrival times on the transition process and the interaction between wake and separating boundary layer is unknown. This could be investigated by orientating the wake generator at an angle to a cascade or flat plate and performing simultaneous measurements at more than one spanwise location.

The discovery of rollup vortices formed due to the interaction of the wake and separating boundary layer and their influence on the measured unsteady blade surface pressures has implications on other areas of aero-engine design. In light of current demands to reduce air traffic noise, the contribution of the rollup vortices to turbine noise should be investigated.

References

Abu-Ghannam, B.J., and Shaw, R., 1980, "Natural transition of boundary layers - the effects of turbulence, pressure gradient and flow history," J. Mech. Eng. Sci., Vol. 22, No. 5, pp 213-228.

Addison, J.S. and Hodson, H.P., 1990 a, “Unsteady Transition in an Axial Flow Turbine, Part 1: Measurements on the Turbine Rotor”, ASME Jnl. of Turbomachinery, Vol.112, No2, April 1990, pp206-214.

Addison, J.S. and Hodson, H.P., 1990 b, “Unsteady Transition in an Axial Flow Turbine, Part 2: Cascade measurements and modelling”, ASME Jnl. of Turbomachinery, Vol.112, No2, April 1990, pp215-221.

Addison, J.S., and Hodson, H.P., 1992, "Modelling of Unsteady Transitional Boundary Layers", ASME Jnl. of Turbomachinery, Vol. 114, No. 3, pp 580-589, Jul.

Alam, M. and Sandham, N.D., 2000, “Direct numerical simulation of short laminar separation bubbles with turbulent reattachment”, J. Fluid. Mech., Vol. 410, pp1-28

Banieghbal, M.R., Curtis, E.M., Denton, J.D., Hodson, H.P., Huntsman, I., Schulte, V., Harvey, N.W. and Steele, A.B., 1995, “Wake passing in LP Turbine Blades”, presented at the AGARD conference, Derby, UK, 8.5-12.5.

Bearman, P.W., 1971, “Correction for the effect of ambient temperature drift on hot-wire measurements in incompressible flow”, DISA Information, No. 11, pp. 25-30

Bell, W.A., 1983, “Spectral Analysis Algorithms for the Laser Velocimeter: A Comparative Study”, AIAA Journal, Vol. 21, No. 5

Betchov, R. and Criminale, W.O., “Stability of Parallel Flows”, Academic Press, 1967

Brunner, S., Fottner, L., Schiffer, H-P., 2000, “Comparison of Two Highly Loaded Low Pressure Turbine Cascades under the Influence of Wake-Induced Transition”, ASME 2000GT-268

Chen, K.K. and Thyson, N.A., 1971, "Extension of Emmons” Spot Theory to Flows on Blunt Bodies", AIAA Journal, Vol. 9, No 5, pp 821-825

Cicatelli, G., Hodson, H.P., Dawes, W.N., 1998, BRITE/EURAM CT96-0143, 30 Month Report, May 98- December 98

Cobley, K., Coleman, N., Siden, G., Arndt, N., 1997, “Design of new three stage low pressure turbine for BMW Rolls-Royce BR715 engine”, ASME 97-GT-419

Cox, R.N., 1957, “Wall Neighborhood Measurements in Turbulent Boundary Layers using a Hot-Wire Anemometer”, A.R.C. Report 19191, Feb

Curtis, E.M., Hodson, H.P., Banieghbal, M.R., Denton, J.D. and Howell, R.J., 1996, “Development of blade profiles for low pressure turbine applications”, ASME paper 96-GT-358, International Gas Turbine and Aeroengine Congress and Exposition, Birmingham, UK

D’Ovidio, A., Harkins, J. A., Gostelow, J. P., 2001 a, “Turbulent spots in strong adverse pressure gradients: Part 1 – Spot Behavior”, Proceedings of ASME TURBO EXPO 2001, June, 4-7, 2001, New Orleans, 2001-GT-0406.

D’Ovidio, A., Harkins, J.A., Gostelow, J.P., 2001 b “Turbulent spots in strong adverse pressure gradients part 2- Spot propagation and spreading rates”, Proceedings of ASME Turbo Expo 2001, June 4-7 2001, New Orleans, 2001-GT-0406

Dovgal, A.V., and Kozlov, V.V., 1990, “Hydrodynamic instability and receptivity of small scale separation regions”, In Laminar-Turbulent Transition, Proc. IUTAM Symp., pp. 523-531, Springer

Dambach, R. and Hodson, H.P., 1999, “ A new Method of Data Reduction for Single-Sensor Pressure Probes”, ASME Paper number 99-GT-304, Presented at the International Gas Turbine and Aeroengine Congress and Exhibition, Indianapolis, Indiana. June 7-10.

Dantec, 1999, “BSA Flow Software Installation and User’s Guide”, Dantec Measurement Technology A/S, Publication Number 9040115712, 4 January 1999.

Denton, J.D., 1993, ”Loss mechanisms in turbomachines”, ASME Journal of Turbomachinery, Vol. 115, No. 4, pp 621-656

Dhawan, S, Narasimha, R, 1958, “Some Properties of Boundary Layer Flow during Transition from Laminar to Turbulent Motion”, J. Fluid Mech. 3, pp. 418-436.

Doorly, D.L. and Oldfield, 1985, “Simulation of the effects of shock wave passing on a turbine rotor blade”, ASME paper No. 85-GT-112

Doorly, D.J., 1988, “Modelling of Unsteady Flow in a Turbine Rotor Passage”, J. Turbomachinery, 110, pp. 27-37.

Dunham, J., 1972, “Predictions of Boundary Layer Transition on Turbomachinery Blades”, AGARD AGARDoGRAPH AG-164, pp55-71

Emmons, H.W., 1951, “The laminar-turbulent transition in a boundary layer- Part 1”, Journal of Aerospace Science, Vol. 18, No7, pp490-498

Farge, M., 1992, “Wavelet transforms and their applications to turbulence”, Annu. Rev. Fluid Mech., Vol. 24, pp395-457

Fujita, H and Kovasznay, LSH, 1969, “Measurements of Reynolds Stress by a Single Rotated Hot Wire Anemometer”, Rev. Sci. Instrum., Vol 39, pp 1351-1355

Gaster, M, 1967, “The Structure and Behaviour of Separation Bubbles” reports and Memo No. 3595, March 1967

Gaster, M., “On transition to turbulence in boundary layers”, in “Transition and Turbulence”, ed. R. E. Meyer, Proceedings of a Symposium, Conducted by the The Mathematics Research Centre, The University of Wisconsin-Maddison, October 13-15, 1980, Academic Press, 1981.

George, W.K., 1975, “Limitations to measuring accuracy inherent in the laser-Doppler signal”, Proc. LDA Symp., Copenhagen

Gibson, W.H., 1970, in “Flow research on blading”, Elsevier Publishing Company

Giles, M.B., 1987, “Calculation of Unsteady Wake/Rotor Interactions”, AIAA Paper 87-0006, presented at AIAA 25th Aerospace Sciences Meeting, Reno, Nevada, 1987

Gostelow, J.P., Blunden, A.R., Walker, G.J., 1994, “Effects of free-stream turbulence and adverse pressure gradients on boundary layer transition”, ASME Journal of Turbomachinery, Vol. 116, pp 392-404, July

Gostelow, J.P., Melwani, N. and Walker, G.J., 1996, “Effects of streamwise pressure gradients on turbulent spot development”, ASME Journal of Turbomachinery, Vol. 118, pp. 737-743

Halstead, D.E., Wisler, D.C., Okiishi, T.H., Walker, G.J., Hodson, H.P., Shin, H.-W., 1997 a, “Boundary layer development in axial compressors and turbines: Part 1 of 4 – Composite Picture” Journal of Turbomachinery, vol. 119, pp114-127, January

Halstead, D.E., Wisler, D.C., Okiishi, T.H., Walker, G.J., Hodson, H.P., Shin, H.-W., 1997 b, “Boundary layer development in axial compressors and turbines: Part

2 of 4 – Compressors” Journal of Turbomachinery, vol. 119, pp114-127, January

Halstead, D.E., Wisler, D.C., Okiishi, T.H., Walker, G.J., Hodson, H.P., Shin, H.-W., 1997 c, “Boundary layer development in axial compressors and turbines: Part 3 of 4 – LP Turbines” Journal of Turbomachinery, vol. 119, pp114-127, January

Halstead, D.E., Wisler, D.C., Okiishi, T.H., Walker, G.J., Hodson, H.P., Shin, H.-W., 1997 d, “Boundary layer development in axial compressors and turbines: Part 4 of 4 – Computations and Analyses” Journal of Turbomachinery, vol. 119, pp114-127, January

Haselbach, F., Schiffer, H-P., Horsman, M., Dressen, S., Harvey, N., Read, S., 2001, "The application of Ultra high Lift Blading in the BR715 LP Turbine”, Proceedings of ASME TURBO EXPO 2001New Orleans, Louisiana, USA, June 4-7, 2001, 2001-GT-0436.

Hatman, A and Wang, T, 1998 a, “Separated-flow Transition. Part 1 – Experimental Methodology and Mode Classification” Presented at ASME Turbo Expo, Stockholm Sweden, 1998

Hatman, A and Wang, T, 1998 b, “Separated-flow Transition. Part 2 – Experimental Results”, Presented at ASME Turbo Expo, Stockholm Sweden, 1998

Hatman, A and Wang, T, 1998 c, Separated-flow Transition. Part 3 – Primary Modes and Vortex Dynamics”, Presented at ASME Turbo Expo, Stockholm Sweden, 1998

Hatman, A and Wang, T, 1998 d, A Prediction Model for Separated Flow Transition”, Presented at ASME Turbo Expo, Stockholm Sweden, 1998

Hodson, H.P., 1984, “Boundary layer and loss measurements on an axial flow turbine”, ASME Jnl. of Engineering for Gas Turbines and Power, Vol. 106, April

Hodson, H.P., 1985, “A Blade-to-Blade Prediction of Wake-Generated Unsteady Flow”, ASME Jnl. of Engineering for Gas Turbines and Power, vol. 107, April 1985

Hodson, H.P., 1989, “Modelling of Unsteady Transition and its Effect on Profile Loss”, in “Unsteady Aerodynamic Phenomena in Turbomachines”, AGARD CP 468

Hodson, H.P., Addison, J.S., and Shepherdson, C.A., 1992, “Models for unsteady wake-induced transition in axial turbomachines”, J. Phys. III France, Vol. 2, No. 4, pp545-574

Hodson, HP and Gostelow, JP, 1999, “Similarities in the development between Triggered Turbulent Spots and Wake-Induced Turbulent Patches”, 37th AIAA Aerospace Sciences Meeting and Exhibit, January 11-14, 199, Reno, NV

Hodson, HP and Schulte. V, 1998, “PUIM users manual”, Whittle Laboratory, Cambridge University

Hodson, HP, 1998, “Bladerow Interactions In Low Pressure Turbines”, in VKI Lecture Series No. 1998-02 *Blade Row Interference Effects Axial Turbomachinery Stages*, Von Karman Institute, Feb 9-12

Horton, HP, 1969, “A semi-Empirical Theory for the growth and Bursting of Laminar Separation Bubbles”, ARC CP 1073

Hourmouziadis, J, 1989, "Aerodynamic Design of Low Pressure Turbines", AGARD Lecture Series, 167

Howell, R.J., 1999, “Wake-separation bubble interactions in low Reynolds number turbomachinery”, Ph.D. Thesis, Cambridge University Engineering Department

Howell, R.J., Ramesh, O.N., Hodson, H.P., Harvey, N.W., Schulte, V., 2000, “High Lift and Aft Loaded Profiles for Low Pressure Turbines”, ASME 2000-GT-261.

Howell, R.J., Hodson, H.P., Schulte, V., Schiffer, H-P., Haselbach, F., Harvey, N.W., 2001, “Boundary Layer Development on the BR710 and BR715 LP Turbines – The Implementation of High Lift and Ultra High Lift Concepts”, ASME Paper 2001-GT-0441, Proceedings of the ASME Turbo Expo 2001, June 4-7, New Orleans, LA

Hughes, J.D., Walker, G.J., 2000, “Natural transition phenomena on an axial compressor blade”, Presented at the International Gas Turbine and Aeroengine Congress and Exhibition, Munich, Germany, May 8-11, 2000-GT-264

Jacobs, R.G. and Durbin, P.A., 2001, “Simulations of bypass transition”, J. Fluid Mech., Vol. 428, pp. 185-212

Johnson, M.W., 1993, “A bypass transition model for boundary layers”, 93-GT-90, Presented at the international Gas Turbine and Aeroengine Congress and Exposition, Cincinnati, Ohio, May 24-27

Johnson, M. W., 1998, “Turbulent spot characteristics in boundary layers subjected to streamwise pressure gradient”, 98-GT-124, Presented at the International Gas Turbine and Aeroengine congress and exhibition, Stockholm, Sweden, 2-5 June

Johnson, M.W. and Dris, A., 2000, “The origin of turbulent spots”, ASME Journal of Turbomachinery, Vol. 122, pp88-92, January

Johnson, M.W. and Ercan, A.H., 1996, “A boundary layer transition model”, ASME paper 96-GT-444

Johnson, M.W., Fashifar, A., 1994, “Statistical properties of turbulent bursts in transitional boundary layers”, Int. J. Heat ad Fluid Flow, Vol. 15, No. 4, pp 283-290, August

Klebanoff, P.S., Tidstrom, K.D., Sargent, L.M., 1962, “The Three-Dimensional Nature of Boundary Layer Instability”, J. Fluid Mech., Vol. 12, pp.1-24

Knapp, CF and Roache, PJ, 1968, “A Combined Visual and Hot-Wire Anemometer Investigation of Boundary Layer Transition”, AIAA Journal, Vol 6, Jan 1968, pp 29-36.

Kool, P, 1979, “Determination of Reynolds Stress tensor with a Single Slanted Hot wire in Periodically Unsteady Turbomachinery Flow” ASME Paper 79-GT-130, March.

Kuroumaru, M, Inoue, M, Higki, T, Abd-Elkhalek, FA-E and Ikui, T, 1982, “Measurement of Three Dimensional Flow Field behind an Impeller by means of Periodic Multi-sampling with a Slanted Hot wire”, Bulletin of JSME, Vol. 25, No 209, Nov.

La Graff, J.E., Ashworth, D.A. and Schultz, D.L., 1989, “Measurements and Modelling of the Gas Turbine Blade Transition Process as Disturbed by Wakes”, ASME Jnl. of Turbomachinery, July 1989, vol. 111, pp315-322

LaVision, 2001, ‘DaVis Flowmaster’ v. 6.03, February 2001, LaVision GmbH, Anna-VandenHoeck-Ring 19, 37081 Goettingen, FRG

Li, F. and Widnall, S.E., 1989, “Wave patterns in plane Poiseuille flow created by concentrated disturbances”, J. Fluid Mech., Vol. 208, pp 639-656

Lin, C.C., 1957, “Motion in the boundary layer with a rapidly oscillating external flow”, Proc. 9th Int. Congress Appl. Mech., Brussels, Vol. 4, pp 155-167

Liu, X. and Rodi, W., 1991, “Experiments on transitional boundary layers with wake-induced unsteadiness”, J. Fluid Mech., Vol. 231, pp. 229-256

Lou, W., Hourmouziadis, J., 2000, “Separation bubbles under steady and periodic-unsteady main flow conditions”, The 45th ASME International Gas Turbine & Aeroengine Technical Congress, Munich Germany May 8-11, paper 2000-GT-0270

Luton, A., Ragab, S., Telionis, D,. 1995, “Interaction of spanwise vortices with a boundary layer”, Phys. Fluids, vol. 7, no. 11, November

Malkiel, E, and Mayle, RE, 1995, “ Transition in a separation bubble”, ASME 95-GT-32.

Mayle, R.E., Schulz, A., 1997, “The path to predicting bypass transition”, ASME Journal of Turbomachinery, vol. 119, pp 405-411, July

Mayle, R.E., 1991, “The role of laminar-turbulent transition in gas turbines engines”, ASME Journal of turbomachinery, Vol. 113 October , 13/509.

Mayle, R.E., 1998, “A Theory for Predicting the Turbulent-Spot Production Rate”, ASME Paper number 98-GT-256

Mayle, R.E., and Dullenkopf, K., 1989, “A Theory for Wake Induced Transition”, ASME paper number 91-GT-57

Merzkirch, W., 1974, “Flow Visualisation”, Academic Press, New York, NY

Meyer, R.X. 1958, “The Effects of Wakes on the Transient Pressure and Velocity Distributions in Turbomachines”, ASME Journal of Basic Engineering, October, pp 1544-1552

Michalike, A., 1991, “On the Stability of Wall Boundary Layers Close to Separation” IUTAM Symposium on Separated Flows and Jets, Springer-Verlag, Berlin, pp. 557-564.

Narasimha, R., 1957, "On the Distribution of Intermittency in the Transition Region of a Boundary Layer", Journal of Aerospace Science, Vol. 24, pp 711-712

Narasimha, R., 1985, “The Laminar Turbulent Transition Zone in the Boundary Layer”, Progress in Aerospace Science, Vol. 22, pp29-80

Narasimha, R., 1998, “Minniwbrook II – 1997 Workshop on boundary layer transition in turbomachines: Post workshop summary”, NASA conference publication 206958, pp. 485-495

Obremski H.J. and Fejer, A.A., 1967, “Transition in oscillating boundary layer flows” Journal of Fluid Mechanics, vol. 29, part 1, July 1967, pp. 93-111.

Obremski, H.J., and Morkovin, M.V., 1969, “Application of quasi-steady stability model to periodic boundary layer flows”, AIAA Journal, Vol. 7, No. 7, pp 1298-1301, July

Obremski, H.J., Morkovin, M.V. and Landhal, M., 1969, “A Portfolio of Stability Characteristics of Incompressible Boundary Layers”, AGARDograph 134, March

Pauley, L.P., Moin, P. and Reynolds, W.C., 1990, “The structure of two-dimensional separation”, J. Fluid Mech. Vol. 220, pp. 397-411

Pfeil, H. and Herbst, R., 1979, “Transition Procedure of Instationary Boundary Layers”, ASME Paper 79-GT-128.

Pfeil, H., and Eifler, J., 1976, “Turbulenzverhaltnisse hinter rotierenden Zylindergittern”, *Forschung im Ingeneiurswesen*, vol. 42, pp 27-32.

Pfeil, H., Herbst, R. and Schröder, T., 1982, “Investigation of the laminar-turbulent transition of boundary layers disturbed by wakes”, ASME paper 82-GT-124

Ramesh, O.N. and Hodson, H.P., 1999, "A new intermittency model incorporating the calming effect", Third European Conference on Turbomachinery: Fluid Dynamics and Thermodynamics, Volume B, 2-5 March 1999, Royal National Hotel, London, UK.

Roberts, W.B., 1980, "Calculation of Laminar Separation Bubbles and their effect of Airfoil Performance", AIAA Journal, Vol., 18, January

Saathoff, P.J., and Melbourne, W.H., 1997, "Effects of free-stream turbulence on surface pressure fluctuations in a separation bubble", J. Fluid. Mech., vol. 337, pp1-24

Schlichting, H., 1979, "Boundary-layer Theory", McGraw-Hill, 7th Edition.

Schlichting, H. and Das, A., 1969, "On the influence of turbulence level on the aerodynamic losses of axial turbomachines", Proceeding of The Symposium on Flow Research on Blading, Baden, Switzerland

Schubauer, G.B., and Klebanoff, P.S., 1955, "Contributions on the Mechanics of Boundary Layer Transition", NACA TN 3489 (1955) and NACA Rep. 1289 (1956).

Schubauer, G.B. and Skramstad, H.K., 1947, "Laminar boundary-layer oscillations and transition on a flat plate", NACA Report No. 909, 1947

Schulte, V., 1995, "Unsteady Separated Boundary Layers in Axial-flow Turbomachinery", PhD Dissertation, Cambridge University.

Schulte, V. and Hodson, H.P., 1994, "Wake-Separation Bubble Interaction in Low Pressure Turbines", AIAA/SAE/ASME/ASEE 30th Joint Propulsion Conference and Exhibit, Indianapolis, Indiana

Schulte, V. and Hodson, H.P., 1996, "Unsteady wake-induced boundary layer transition in high lift LP turbines", ASME Journal of Turbomachinery. vol. 120, pp28-35. January 1998

Schulte, V. and Hodson, H.P., 1999, "Predicting unsteady wake induced transition", Submitted to ASME 1999.

Smith, L.H., 1966, "Wake Dispersion in Turbomachines", ASME Journal of Basic Engineering, Vol. 88

Solomon, W.J., Walker, G.J., 1995, "Observations of Wake-Induced Transition on an Axial Compressor Blade", ASME paper 95-GT-381

Solomon, W.J., Walker, G.J., Gostelow, J.P., 1996, "Transition length prediction for flows with rapidly changing pressure gradients", ASME Journal of Turbomachinery, Vol. 118, pp 744-751, October

Spiegel, M.R., "Theory and Problems of Vector Analysis and an introduction to Tensor Analysis", McGraw-Hill, 1974

Stieger, R.D. and Hodson, H.P., 2001, "Reynolds stress measurement with a single component Laser Doppler Anemometer", submitted to AIAA Journal

Tani, I., 1964, "Low speed Flows involving separation bubbles", Progress in Aeronautical Science, Pergamon Press.

Tennekes, H., and Lumley, J.L., "A first course in turbulence", The MIT Press, eleventh printing, 1987

Thwaites, B., 1949, Approximate Calculation of the Laminar Boundary Layer", The Aeronautical Quarterly, Vol. 1, pp. 245-280.

Torrence, C. and Compo, G.P., 1998, "A Practical guide to wavelet analysis", Bulletin of the American Meteorological Society, vol. 79, No. 1, January

Truckenbrodt, E., 1952, " A method of Quadrature for the calculation of laminar and turbulent boundary layers in Plane and Rotational Symmetric Flow", Ingenieur-Archiv, Vol. 20, translated as NACA TM 1379

Villermaux, E., 1998, “On the role of viscosity in shear instabilities”, Phys. Fluids, vol. 10, no. 2, February

Volino, R.J., 1998, “Wavelet analysis of transitional flow data under high free-stream turbulence conditions”, 98-GT-289, Presented at the International Gas Turbine & Aeroengine Congress & Exhibition, Stockholm, Sweeden, 2-5 June

Walker, G.J., 1974, “The Unsteady Nature of Boundary Layer transition on an Axial-Flow Compressor Blade”, ASME Paper 74-GT-135

Walker, G.J., 1975, “Observations of Separated Laminar Flow on Axial Compressor Blading”, ASME Paper number 75-GT-63

Walker, G.J., 1987, “Transitional Flow on Axial Turbomachine Blading”, AIAA J. Vol. 27, pp 595-602

Walker, G.J., 1989, “Transitional flow in axial turbomachine blading”, AIAA Journal, vol. 27, no. 5, May

Walker, G.J., 1993, “The role of laminar turbulent transition in gas turbine engines: a discussion”, ASME Jnl. Turbomachinery, Vol. 115, pp 207-217, April

Walker, G.J., and Gostelow, J.P., 1989, “The effect of adverse Pressure Gradients on the Nature and Length of Boundary Layer transition”, ASME Paper number 89-GT-274

Walker, GJ, Subroto, PH and Platzer, MF, 1988, “Transition Modelling Effects on Viscous/Inviscid Interaction Analysis of Low Reynolds Number Airfoil Flows Involving Laminar Separation Bubbles”, ASME Paper number 88-GT-32

Watmuff, J. H., 1999, “Evolution of a wave packet into vortex loops in a laminar separation bubble”, J. Fluid Mech., vol. 397, pp119-169

White, F.M., 1991, “Viscous Fluid Flow”, McGraw-Hill, 2nd Edition.

Williams, J. C., 1999, Private communication

Wu, X., Jacobs, R.G., Hunt, J.C.R., Durbin, P.A., 1999,”Simulation of boundary layer transition induced by periodically passing wakes”, J. Fluid Mech., Vol. 398, pp109-153

Zhong, S., Kittichaikarn, C., Hodson, H. P. & Ireland, P. T. 1998, “Visualisation of turbulent spots under the influence of adverse pressure gradients”, In Proc. 8th Intl Conf. on Flow Visualistion, Italy

Appendix I: T106 LP Turbine Profile

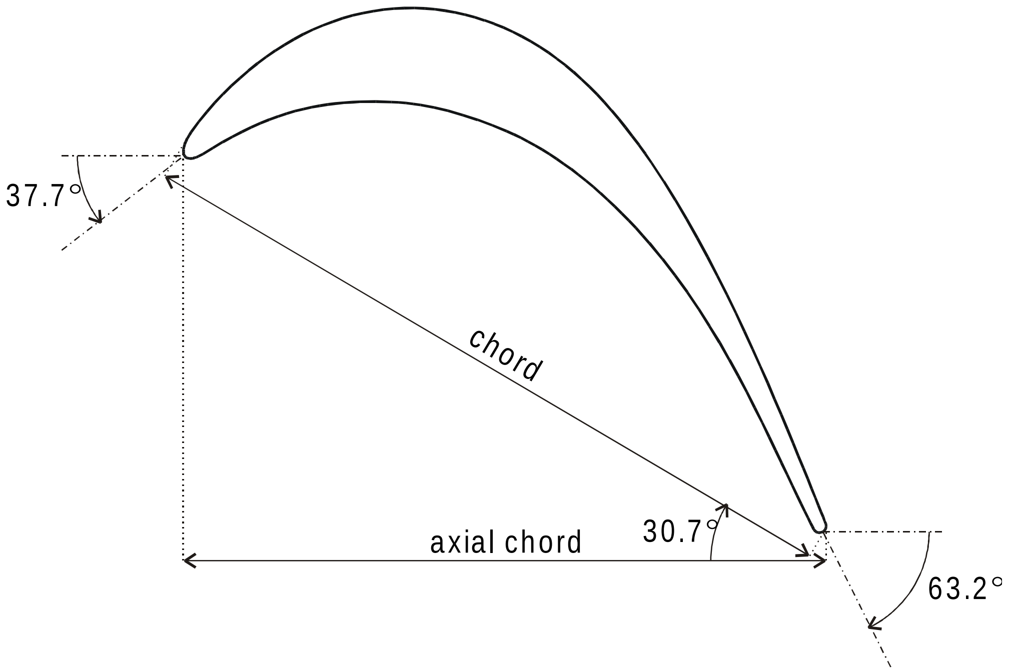

Figure I-1: T106 LP turbine blade

Number of blades		5
Chord	[mm]	198
Axial chord	[mm]	170
Blade stagger	[°]	30.7
Pitch	[mm]	158
Span	[mm]	375
Suction surface length	[mm]	264.7
Pressure surface length	[mm]	230.0
Inlet flow angle	[°]	37.7
Design exit flow angle	[°]	63.2

Table I-1: T106 Cascade specifications.

Table I-2: T106 blade co-ordinates.

x/c	y/c	x/c	y/c	x/c	y/c	x/c	y/c	x/c	y/c
0.852022	-0.499894	0.590809	0.041609	0.134837	0.151909	0.114539	0.051907	0.566712	-0.054864
0.854287	-0.499152	0.581625	0.052984	0.122597	0.144092	0.126483	0.056272	0.576342	-0.063994
0.856024	-0.497879	0.572194	0.064157	0.110472	0.135697	0.137856	0.059993	0.585810	-0.073291
0.857388	-0.496202	0.562565	0.075027	0.098656	0.126874	0.149354	0.063309	0.595251	-0.082951
0.858425	-0.494252	0.552660	0.085647	0.086915	0.117442	0.160399	0.066097	0.604502	-0.092792
0.858921	-0.492134	0.542536	0.095906	0.075496	0.107622	0.171531	0.068513	0.613686	-0.102927
0.858849	-0.489945	0.532108	0.105857	0.064090	0.097111	0.182359	0.070508	0.622688	-0.113225
0.858336	-0.487832	0.521465	0.115384	0.053025	0.086239	0.193243	0.072168	0.640270	-0.134439
0.856981	-0.484433	0.510501	0.124541	0.041933	0.074534	0.203964	0.073488	0.657151	-0.156283
0.854884	-0.479210	0.499342	0.133204	0.031245	0.062457	0.214716	0.074522	0.673265	-0.178579
0.852085	-0.472232	0.487867	0.141440	0.020435	0.049183	0.225362	0.075276	0.688595	-0.201154
0.848607	-0.463560	0.476249	0.149133	0.010278	0.035401	0.236021	0.075789	0.703073	-0.223816
0.844469	-0.453274	0.464341	0.156368	0.007569	0.031203	0.257060	0.076098	0.716738	-0.246414
0.839713	-0.441446	0.452322	0.163044	0.005124	0.026842	0.277659	0.075493	0.729583	-0.268769
0.834337	-0.428134	0.440047	0.169240	0.003235	0.022872	0.287634	0.074850	0.741636	-0.290734
0.828372	-0.413425	0.427639	0.174893	0.001625	0.018778	0.297594	0.074004	0.752938	-0.312161
0.821836	-0.397388	0.415012	0.180039	0.000631	0.015282	0.307184	0.072977	0.763519	-0.332903
0.814726	-0.380103	0.402272	0.184630	0.000000	0.011694	0.316734	0.071626	0.773423	-0.352847
0.807069	-0.361644	0.389355	0.188696	0.000088	0.008846	0.335108	0.068196	0.782696	-0.371894
0.798872	-0.342097	0.376273	0.192225	0.000351	0.006020	0.353287	0.063847	0.791327	-0.389909
0.790120	-0.321545	0.363052	0.195189	0.001225	0.003898	0.373463	0.058063	0.799366	-0.406804
0.780839	-0.300063	0.349624	0.197578	0.002663	0.002099	0.393279	0.051654	0.806821	-0.422490
0.771018	-0.277748	0.336102	0.199358	0.004054	0.001048	0.412745	0.044491	0.813669	-0.436886
0.760651	-0.254690	0.322457	0.200535	0.005660	0.000389	0.431923	0.036586	0.819910	-0.449898
0.749746	-0.230987	0.308772	0.201087	0.007649	0.000031	0.441443	0.032270	0.825496	-0.461463
0.738285	-0.206733	0.294991	0.201010	0.009663	0.000000	0.450826	0.027661	0.830405	-0.471509
0.726255	-0.182047	0.281229	0.200303	0.012095	0.000289	0.460367	0.022685	0.834580	-0.479967
0.713682	-0.156981	0.267419	0.198967	0.014480	0.000826	0.469785	0.017480	0.837962	-0.486768
0.700516	-0.131702	0.253684	0.197008	0.017259	0.001730	0.479443	0.011805	0.840543	-0.491860
0.686776	-0.106292	0.239943	0.194412	0.019942	0.002874	0.488953	0.005886	0.842197	-0.495145
0.672425	-0.080891	0.226333	0.191202	0.025860	0.006081	0.498720	-0.000528	0.843535	-0.497014
0.657461	-0.055603	0.212761	0.187358	0.039158	0.014055	0.508326	-0.007180	0.845263	-0.498560
0.641855	-0.030573	0.199372	0.182919	0.052488	0.021970	0.518154	-0.014344	0.846593	-0.499318
0.625580	-0.005925	0.186068	0.177858	0.065205	0.029003	0.527832	-0.021709	0.848086	-0.499770
0.617178	0.006200	0.172994	0.172231	0.078096	0.035710	0.537943	-0.029707	0.849626	-0.499988
0.608581	0.018188	0.160048	0.166003	0.090332	0.041618	0.547860	-0.037944	0.852022	-0.499894
0.599805	0.029981	0.147370	0.159246	0.102755	0.047127	0.557378	-0.046301		

Appendix II: The use of 1D LDA to measure the full 2D Reynolds Stress Tensor

II.1 Introduction

The measurement of the full 2D Reynolds Stress tensor typically requires multi-axis anemometry systems. By simultaneously measuring multiple velocity components, it is possible to directly calculate the correlation between the components of velocity fluctuation and thus to calculate the Reynolds Stress tensor. However, if the flow is time invariant, or if it is phase locked, it is possible to combine a series of measurements made at different probe orientations and derive the time averaged or ensemble averaged Reynolds Stress tensor. This has been demonstrated by Fujita and Kovasznay (1969), Kuroumaru et al.(1982) and Kool et al.(1979) who have used the technique in thermal anemometry.

This note details the adaptation of the method of Fujita and Kovasznay (1969) to Laser Doppler Anemometry (LDA). It is demonstrated that the directional response of LDA makes it most suitable to this form of measurement. Moreover, the range of possible measurements obtainable from a 1D system is greatly enhanced with significant financial savings on equipment purchase. The data collected at multiple probe angles can also be utilised to enhance the mean flow measurements.

II.2 Derivation

The velocity measured by LDA is the component of velocity in the plane of the intersecting beams and normal to the fringe pattern. If the plane of the beams is rotated relative to the instantaneous flow velocity vector, *U*, then only the instantaneous component of velocity in the plane of the intersecting beams, *M*, will be measured according to the cosine relationship

$$M = U\cos(\theta) \tag{II-1}$$

where θ is defined in Figure II-2.

The instantaneous velocity component measured by the LDA can also be written in terms of the instantaneous flow vector components normal and parallel to the local mean flow (see Figure II-2)

$$M = (\overline{U} + u)\cos(\overline{\theta}) - v\sin(\overline{\theta}) \tag{II-2}$$

The mean measured velocity, $\overline{M}$, may be written in terms of the mean flow velocity, $\overline{U}$, and mean flow angle $\overline{\theta}$

$$\overline{M} = \overline{U}\cos(\overline{\theta}) \qquad \text{(II-3)}$$

A relationship between the variance of the measured velocity, $\overline{m'^2}$, and the Reynolds Stress tensor (aligned to the mean flow direction) may be obtained by subtracting (II-3) from (II-2), squaring the result and averaging.

$$\overline{m'^2} = \overline{u'^2}\cos^2(\overline{\theta}) + \overline{v'^2}\sin^2(\overline{\theta}) - 2\overline{u'v'}\sin(\overline{\theta})\cos(\overline{\theta}) \qquad \text{(II-4)}$$

If data is acquired at three probe angles then the Reynolds stress tensor may be calculated directly from (II-4). If more than three probe angles are used, then for a given number of acquired data points, the quality of the measurement can be improved by a least squares fit to the data obtained by solving the following linear system

$$\sum_{i=1}^{N} A(\overline{\theta}_i)\cdot\begin{bmatrix}\overline{u'^2}\\ \overline{v'^2}\\ \overline{u'v'}\end{bmatrix} = \sum_{i=1}^{N}\overline{m_i{}^2}\begin{bmatrix}\cos^2(\overline{\theta}_i)\\ \sin^2(\overline{\theta}_i)\\ \cos(\overline{\theta}_i)\sin(\overline{\theta}_i)\end{bmatrix} \qquad \text{(II-5)}$$

where

$$A(\overline{\theta}_i) = \begin{bmatrix}\cos^4(\overline{\theta}_i) & \cos^2(\overline{\theta}_i)\sin^2(\overline{\theta}_i) & \cos^3(\overline{\theta}_i)\sin(\overline{\theta}_i)\\ \cos^2(\overline{\theta}_i)\sin^2(\overline{\theta}_i) & \sin^4(\overline{\theta}_i) & \cos(\overline{\theta}_i)\sin^3(\overline{\theta}_i)\\ \cos^3(\overline{\theta}_i)\sin(\overline{\theta}_i) & \cos(\overline{\theta}_i)\sin^3(\overline{\theta}_i) & \cos^2(\overline{\theta}_i)\sin^2(\overline{\theta}_i)\end{bmatrix}$$

Using a least squares fit to more than three probe angles also removes the need of an a priori knowledge of the flow, as data acquired at all probe angles is used to enhance the measurement quality.

Since the measurement of the turbulent quantities requires measurements at multiple probe angles, the quality of the mean flow measurements can be improved as suggested by Dambach and Hodson (1999). This involves minimising the error (S) between the mean velocity measured at the N probe angles and the functional relationship for the angular response of the LDA (II-1). The resulting function to be minimised in this case, is therefore

$$S = \sum_{i=1}^{N} \left(\overline{M}_i - \overline{U} \cos(\overline{\theta}_i) \right)^2 \qquad \text{(II-6)}$$

This minimisation may be performed numerically as the function is non-linear in the variables of interest namely $\overline{U}$ and $\overline{\theta}$.

With knowledge of the mean flow direction, it is possible to transform the Reynolds stresses, calculated in the direction of the mean velocity vector, to any co-ordinate system using a standard transformation.

The derivation presented above is for a stationary flow, but can be extended to a phase locked flow if conventional phase averaging techniques are employed.

II.3 Evaluation of Technique

In order to validate the experimental technique, the flow at the inlet to a turbine cascade downstream of a moving bar wake generator was measured using the rotated 1D LDA technique described above and using conventional 2D LDA.

The wake generator consisted of a series *2mm* diameter stainless steel bars suspended between two belts. A variable speed DC motor was used to drive the belts through a system of pulleys so that the bars traversed the inlet to the cascade. The experimental facility is sketched in Figure II-2 and further details may be found in Schulte and Hodson (1996) and in Chapter 3.

The cascade and bars were set at an incidence of *37.7°* to the inlet flow. The bars were spaced *158* diameters apart and *35* diameters axially upstream of the cascade. The bar passing frequency was set to *22.3Hz* and the ratio of bar speed to inlet flow speed was set to $\phi=0.83$. The measurement station was in the plane of the blade leading edges and at mid pitch of the cascade (see Figure II-3). The Reynolds number based on relative flow velocity and bar diameter was $Re=1.7\times10^3$.

The Dantec LDA and seeding systems described in Chapter 3 were used. At each probe orientation, *120 000* samples were collected over a maximum of *5000* wake passing events. A trigger signal, generated at each bar passing, was used to time stamp the collected data. Ensemble averaging of the measured signal was then performed by dividing the wake passing period into *128* time bins and calculating the mean and variance for each time bin. Only the 514.5nm beam was used for the rotated 1D measurements. For the 2D measurements, coincidence filtering was performed by software with a coincidence interval of *0.005ms* and the Reynolds stress was calculated for each time bin.

The ensemble averaged results of the 1D rotated LDA and the 2D LDA are compared in Figure II-4 with only the portion of the period in which the wake passes shown and the Reynolds stress tensor aligned with the x-y axes of Figure II-3. Excellent agreement is evident for the ensemble mean data of the two techniques. For the turbulent statistics, however, the agreement is seen to improve as the number of angles and thus the total number of samples increases. Estimating the error of the rotated 1D technique as the average variance from the 2D LDA measurement and defining the cost of the measurement as the total number of samples used, it is possible to plot the error of the 1D measurements as a function of cost. Figure II-5 shows the error in ensemble average Reynolds stress, <u'v'>, for a range of numbers of probe angles, *N*. Similar results were obtained for the ensemble averaged velocity variances $<u'^2>$ and $<v'^2>$.The highest errors, at all costs, were obtained for case with *N=3*. This demonstrates the benefit of using the least squares approach to improve the quality of the measurements. However, the case of highest *N* does not give the lowest error. This indicates that there is an optimum *N* for a given cost. For a constant cost experiment, increasing *N* will reduce the number of samples in each bin from which statistics are calculated. With inaccurate statistics, the quality of the least squares fit is compromised.

II.4 Discussion

Although the form of (II-4) matches that presented by Fujita and Kovasznay (1968), it is more precise because the angular response of the LDA is known. The derivation presented by Fujita and Kovasznay (1969) employed a calibrated functional fit for the angular response of the hot wire therefore, their derivation required a Taylor expansion and a small angle approximation. This requires the fluctuation to be small relative to the mean. However, when the functional response is known exactly, there is no such limitation and the technique is applicable to flows with large fluctuations relative to the mean. It should be noted that the least squares formula presented by Fujita and Kovasznay (1969) assumes that the probe angles are symmetrically distributed about the flow. The least squares fit presented in (II-5) is a more general case and places no restriction on the selection of probe angles.

This technique retains significant advantages over rotated hot-wires as discussed by Fujita and Kovasznay (1969). The spatial resolution of the rotated 1D LDA is far superior to that of a rotated single hot wire and indeed a X-wire. The measuring volume of the rotated LDA is the same as that for a single orientation and has a diameter of 0.077mm whereas a rotated single wire sweeps out a circle with diameter equal to the wire length normal to the flow direction where a typical hot wire is 1mm long. This means that the rotated hot wire cannot be used to make boundary layer measurements except in very large-scale experiments, which are impractical for turbomachinery research. Furthermore, unlike the hot wire technique, there is no directional ambiguity in the LDA measurements and this remains true for the technique described here.

II.5 Conclusions

A technique for using a single component LDA system to measure the 2D Reynolds Stress tensor has been presented and found to be in excellent agreement with the conventional 2D LDA measurements. This technique allows the functionality of 2D LDA at a capital cost comparable to a single component system.

II.6 Figures

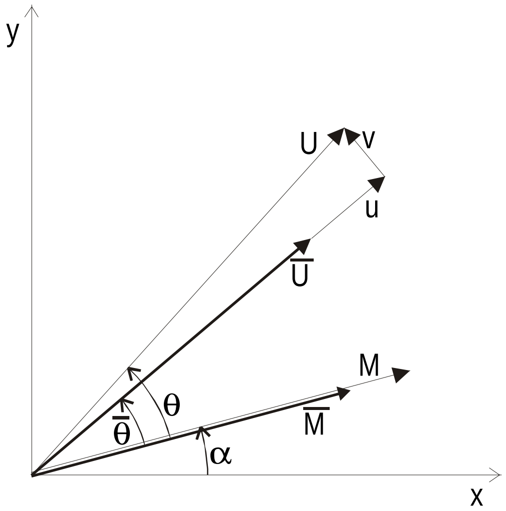

Figure II-1:Decomposition of velocity vector.

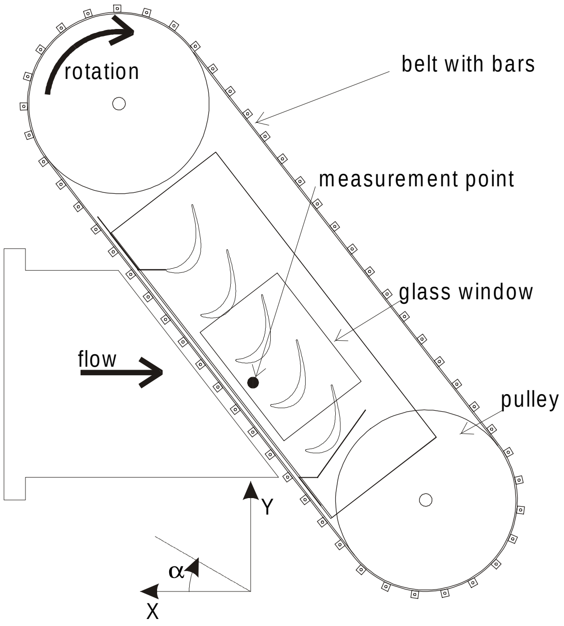

Figure II-2: Sketch of moving bar wake generator.

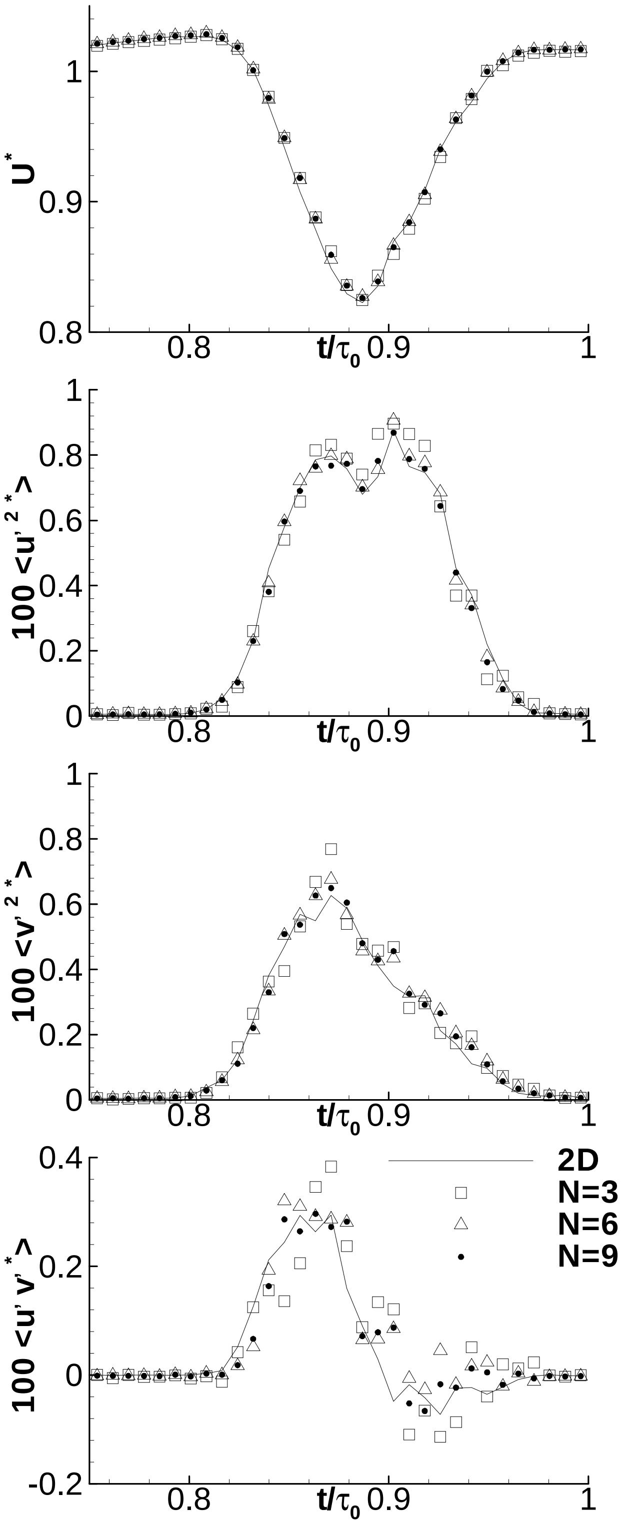

Figure II-3: Comparison of conventional 2D LDA measurements and rotated 1D LDA for 3, 6 and 12 probe angles. The measurements are ensemble-averaged data taken at one measurement location.

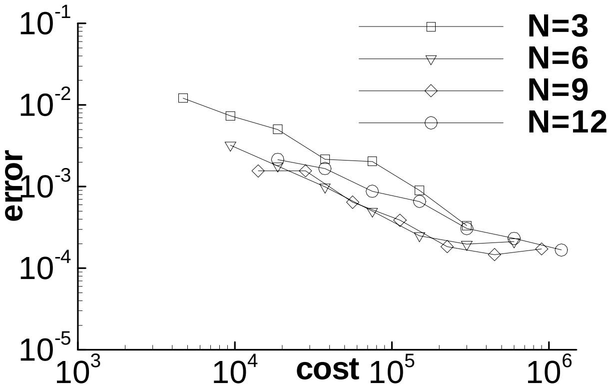

Figure II-4: Error in <u'v'> for rotated 1D LDA for different numbers of probe angles. The 2D LDA measurement is taken as the datum.

Appendix III: A wavelet algorithm for LDA data

III.1 Introduction

The wavelet transform of a discrete sequence is defined as the convolution of the signal with an analysing wavelet (see Torrence and Compo, 1989 or Farge, 1992). The analysing wavelet is scaled and translated in time to build up a picture of the frequency content of the signal at different times thereby providing a time–frequency decomposition of a signal. Traditional methods of computing wavelet transforms rely on fast Fourier transform (FFT) techniques to reduce computational time. However, the use of FFT techniques requires evenly sampled data and so these techniques are not applicable to LDA data where the sampling is dictated by seeding of the flow and is thus random.

Spectral analysis of LDA is typically performed by re-sampling of acquired data to achieve an evenly sampled data set on which FFT techniques may be employed (see Bell, 1983). However, to the author's knowledge no previous attempts have been made to perform a wavelet analysis on LDA data.

For this reason, a novel technique is presented. This technique first directly calculates the Fourier transform of the LDA data at a series of selected frequencies. This Fourier transform is then used in conjunction with the traditional FFT algorithms to realise the wavelet transform.

III.2 Wavelet Algorithm for LDA data

Following Torrence and Compo (1989), the continuous wavelet transform, W, of a discrete sequence, x_n, is defined at a given scale, s, as the convolution of x_n with a scaled and translated version of the analysing wavelet $\varphi_0(\eta)$ as

$$W_n(s) = \sum_{n'=0}^{N-1} x_{n'} \varphi^{\bullet}\left[\frac{(n'-n)\delta t}{s}\right] \tag{III-1}$$

where $\varphi^{\bullet}$ is the complex conjugate of the scaled wavelet and n the localised time index. Calculating (III-1) directly is computationally intensive, however, the convolution theorem may be used to calculate all N convolutions simultaneously in Fourier space according to

$$W_n(s) = \sum_{k=0}^{N-1} \hat{x}_k \hat{\varphi}^{\bullet}(s\omega_k) e^{i\omega_k n\delta t} \tag{III-2}$$

where (^) indicates the Fourier transform and the angular frequency is

$$\omega_k = \begin{cases} \dfrac{2\pi k}{N\delta t} & \cdots \quad \cdots \quad k \le \dfrac{N}{2} \\ -\dfrac{2\pi k}{N\delta t} & \cdots \quad \cdots \quad k > \dfrac{N}{2} \end{cases} \tag{III-3}$$

To ensure unit energy of the analysing wavelet at each scale the analysing wavelet, φ_0, is normalised according to

$$\hat{\varphi}(s\omega_k) = \sqrt{\frac{2\pi s}{\delta t}}\hat{\varphi}_0(s\omega_k) \tag{III-4}$$

For evenly sampled data, the wavelet transform described above may be performed using Fast Fourier Transform (FFT) techniques. The FFT of x_n is computed and multiplied by $\varphi^\bullet$ which is typically an analytic function. The wavelet transform at a given wavelet scale is then found as the inverse FFT of this product.

However, for LDA, the data acquisition is controlled by seeding and is therefore random. This precludes the use of traditional FFT technique for computing the discrete Fourier transform of the LDA signal. Rather than incurring the computational cost of performing the convolution of (III-1) directly, the wavelet transforms may be obtained by a hybrid method.

The discrete Fourier transform of the LDA signal must first be calculated directly according to

$$\hat{x}_k = \frac{\sum_{l=1}^{NL} x_l t_{rl} e^{-i2\pi k \frac{t_l}{t_{\max}}}}{\sum_{l=1}^{NL} t_{r\,l}} \tag{III-5}$$

where the weighting factor t_r is the residence (transit) time of the LDA sample and is used to remove statistical biasing inherent in LDA data (Buchhave et al, 1979). The number of LDA samples ($l=1,2 \ldots NL$) is typically greater than the number of frequencies ($k=0 \ldots N-1$) at which the Fourier transform is calculated.

The time of the LDA sample, t_l , is used in conjunction with the maximum time stamp t_{max}. For periodic unsteady data, t_{max} is taken as the period time, τ_0; otherwise, the last time stamp t_{NL} may be used. The definition used here overcomes the problem of unevenly sampled data thereby eliminating the need to resample the LDA data. Consequentially, no spectral noise is added to the wavelet transform.[20]

The number of frequencies, N, at which the Fourier transform is calculated dictates the frequency resolution of the wavelet transform. To facilitate the use of FFT techniques N is chosen such that $N=2^n$ where n is a natural number.

Having calculated the Fourier transform of the LDA data sequence with (III-5) it is possible to calculate the wavelet transform. The convolution is performed in Fourier space by multiplying the Fourier transform by the Fourier transform of the analysing wavelet as in equation (III-2). The inverse Fourier transform necessary to complete the convolution is then performed by in inverse FFT, which is made possible by the choice of N.

---

[20] For an evenly sampled sequence x_n, the discrete Fourier transform is given by $\hat{x}_n = \frac{1}{N}\sum_{n=1}^{N} x_n e^{-i2\pi k\frac{n}{N}}$. Thus equation (III-5) is identical to this except the factor n/N is replaced by the factor t/t_{max} for the unevenly sampled data

Appendix IV: Determination of mean velocity derivatives and the dissipation of TKE

IV.1 Calculation of derivatives

Taking derivatives of experimental data typically amplifies noise present in the measurements. By contrast, integration of experimental data tends to reduce noise. Thus in order to calculate derivatives of the measured mean velocity field Green's theorem (see Spiegel (1974)) was used to calculate derivatives by the evaluation of line integrals.

Green's theorem in a plane states

$$\oint_C M dx + N dy = \iint_R \left(\frac{\partial N}{\partial x} - \frac{\partial M}{\partial y} \right) dx dy \qquad \text{(IV-1)}$$

where *C* is a closed curve about the region *R*. Treating each component separately, the derivatives over the region *R* may be independently evaluated as

$$\frac{\partial M}{\partial y} = \frac{-1}{A} \oint_C M dx \qquad \text{(IV-2)}$$

and

$$\frac{\partial N}{\partial x} = \frac{1}{A} \oint_C N dy \qquad \text{(IV-3)}$$

The LDA measurement grid can be considered to consist of quadrilateral elements made up of four measurement points as shown in Figure IV-1. For each quadrilateral, line integrals were calculated assuming a linear variation of velocity across each face. The area was calculated as shown in Figure IV-1 from the known positions of the vertices. The cell centred derivatives were then calculated from equation (IV-2) and equation (IV-3). The derivatives at the measurement points were then determined by distributing the cell centred values to the vertices of the cell.

IV.2 Calculation of turbulent dissipation

The dissipation of turbulent kinetic energy may be estimated very simplistically as the difference between the *TKE* flux and the production of *TKE*.

The flow field constructed from a series of measurement points does not necessarily conserve mass due to imperfections in the measurements. These imperfections may arise from drift in tunnel conditions or measurement noise for example. The flux of *TKE* used to estimate dissipation must thus be accounted for.

Consider the 2D flow element, *A*, shown in Figure IV-2 that comprises four measurement points. The flow properties on each face of the element are taken as the average of the values at the vertices and the projection of the element face in the x and y directions are denoted dS_x and dS_y respectively as shown in Figure IV-2. The net mass flux through the faces of the element can be calculated by summation over all the faces of the element according to

$$\frac{\partial \rho}{\partial t} \approx \frac{\Delta \rho}{\Delta t} = \frac{1}{A}\sum_{faces} \rho V_x \cdot dS_x + \rho V_y \cdot dS_y \qquad \text{(IV-4)}$$

Similarly, the TKE flux can be obtained,

$$\frac{\partial(\rho \cdot TKE)}{\partial t} \approx \frac{\Delta(\rho \cdot TKE)}{\Delta t} = \frac{1}{A}\sum_{faces} \rho \cdot TKE_f \cdot V_x \cdot dS_x + \rho \cdot TKE_f \cdot V_y \cdot dS_y$$

(IV-5)

however, by applying the chain rule it becomes obvious that there is a contribution to the measured *TKE* flux due to changes in mass within the element, which is given by the last term of

$$\frac{\partial(\rho \cdot TKE)}{\partial t} = \rho \cdot \frac{\partial TKE}{\partial t} + TKE \cdot \frac{\partial \rho}{\partial t} \qquad \text{(IV-6)}$$

By rearranging (IV-6), the *TKE* flux due only to the production and dissipation of *TKE* within the computational cell can be found.

The production of *TKE*, P_{TKE}, can be found directly from

$$P_{TKE} = \overline{u'^2}\frac{\partial U}{\partial x} + \overline{v'^2}\frac{\partial V}{\partial y} - \overline{u'v'}\left(\frac{\partial U}{\partial x} + \frac{\partial V}{\partial y}\right) \qquad \text{(IV-7)}$$

using the measured Reynolds stresses values and the velocity derivatives calculated as described above.

Finally, the dissipation of *TKE* may be estimated by

$$D_{TKE} \approx \frac{\partial TKE}{\partial t} - P_{TKE} \qquad \text{(IV-8)}$$

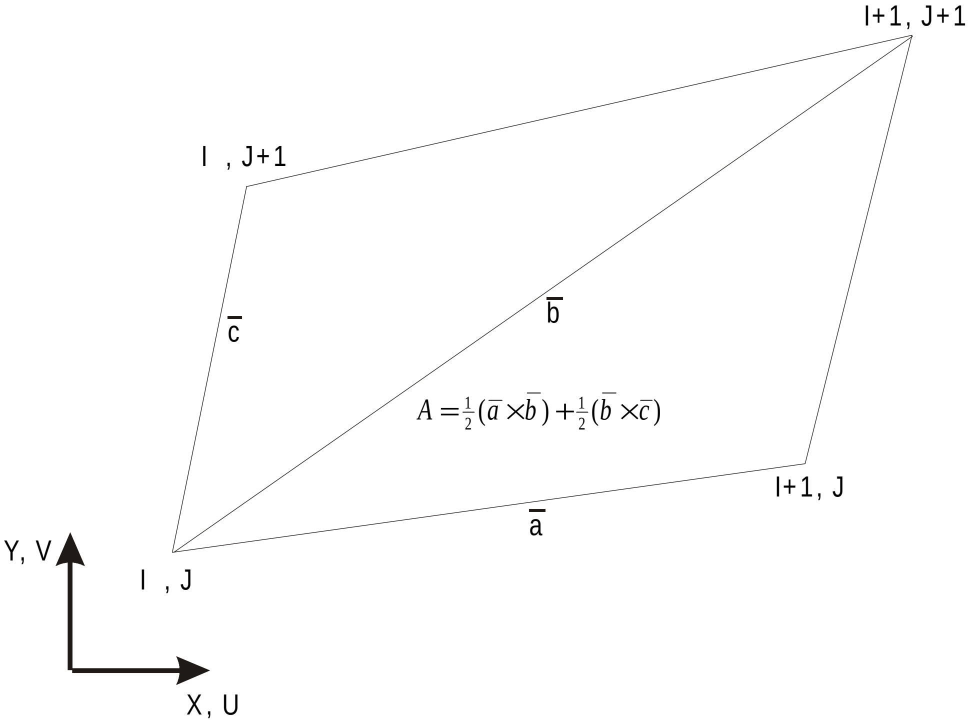

Figure IV-1: Computational element for the calculation of derivatives using Green's theorem

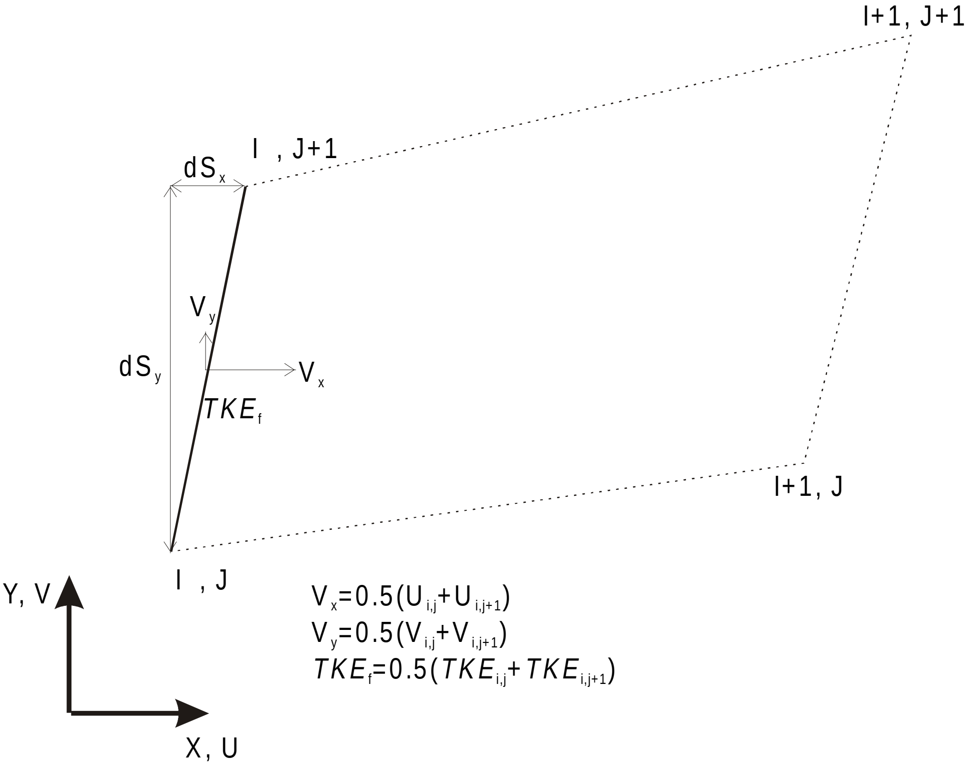

Figure IV-2: Computational element for calculation of flux